frontiers

Green and sustainable chemistry editor's pick 2024

Edited by
James Clark

Published in
Frontiers in Chemistry

ISSN 2296-2646
ISBN 978-2-8325-5798-3
DOI 10.3389/978-2-8325-5798-3

About Frontiers

Frontiers is more than just an open access publisher of scholarly articles: it is a pioneering approach to the world of academia, radically improving the way scholarly research is managed. The grand vision of Frontiers is a world where all people have an equal opportunity to seek, share and generate knowledge. Frontiers provides immediate and permanent online open access to all its publications, but this alone is not enough to realize our grand goals.

Frontiers journal series

The Frontiers journal series is a multi-tier and interdisciplinary set of open-access, online journals, promising a paradigm shift from the current review, selection and dissemination processes in academic publishing. All Frontiers journals are driven by researchers for researchers; therefore, they constitute a service to the scholarly community. At the same time, the *Frontiers journal series* operates on a revolutionary invention, the tiered publishing system, initially addressing specific communities of scholars, and gradually climbing up to broader public understanding, thus serving the interests of the lay society, too.

Dedication to quality

Each Frontiers article is a landmark of the highest quality, thanks to genuinely collaborative interactions between authors and review editors, who include some of the world's best academicians. Research must be certified by peers before entering a stream of knowledge that may eventually reach the public - and shape society; therefore, Frontiers only applies the most rigorous and unbiased reviews. Frontiers revolutionizes research publishing by freely delivering the most outstanding research, evaluated with no bias from both the academic and social point of view. By applying the most advanced information technologies, Frontiers is catapulting scholarly publishing into a new generation.

Green and sustainable chemistry editor's pick 2024

Topic editor
James Clark — University of York, United Kingdom

Citation
Clark, J., ed. (2025). *Green and sustainable chemistry editor's pick 2024*. Lausanne: Frontiers Media SA. doi: 10.3389/978-2-8325-5798-3

We are pleased to introduce the collection Frontiers in Chemistry – Green and Sustainable Editor's Pick 2024. This collection showcases most well-received spontaneous articles from the past couple of years, and have been specially handpicked by our Chief Editor.

The work presented here highlights the broad diversity of research performed across the section, and aims to put a spotlight on the main areas of interest. All research presented here displays strong advances in theory, experiment and methodology with applications to compelling problems.

This collection aims to further support Frontiers' strong community by recognizing highly deserving authors.

Table of contents

frontiers | Frontiers in Chemistry

TYPE Editorial
PUBLISHED 07 January 2025
DOI 10.3389/fchem.2024.1546377

OPEN ACCESS

EDITED AND REVIEWED BY
Steve Suib,
University of Connecticut, United States

*CORRESPONDENCE
James Clark,
james.clark@york.ac.uk

RECEIVED 16 December 2024
ACCEPTED 23 December 2024
PUBLISHED 07 January 2025

CITATION
Clark J (2025) Editorial: Green and sustainable chemistry editor's pick 2024.
Front. Chem. 12:1546377.
doi: 10.3389/fchem.2024.1546377

Editorial: Green and sustainable chemistry editor's pick 2024

James Clark*

Green Chemistry Centre of Excellence, University of York, York, United Kingdom

KEYWORDS

waste feedstocks, waste water, biomass, calcium carbonate, clean synthesis

Editorial on the Research Topic
Green and sustainable chemistry editor's pick 2024

Green and Sustainable chemistry is at the heart of the global movements towards a circular economy and a more sustainable society. Green Chemistry became a recognised term 30 years ago and largely built on many years of process chemistry improvements that led to safer and more efficient chemical manufacturing. The early movement was strongly focussed on avoiding where possible, the more hazardous chemical substances and reducing toxic chemical waste. While these remain as core components, there is now a more holistic view of the chemical space with feedstocks, process and products sharing the limelight. Frontiers Green and Sustainable Chemistry seeks to embrace all key stages in the life-cycle of chemical products and including key subjects including renewable resources and the valorisation of waste, clean synthesis and alternative technologies, and product performance, as well as environmental impact and recyclability. We seek high quality research articles that address these subjects in the context of important products across all key sectors, including advanced materials, pharmaceuticals and other bio-actives, electronics, and home and personal care products. We have selected 10 outstanding research articles from 2024 that reflect these principles and values.

In the article *Transformation of struvite from wastewater to a hydrogen fuel storage compound ammonia borane*, the interesting and important future source of hydrogen, ammonia-borane is synthesised from wastewater (Dingra et al.). This not only opens the door to a new use of a widespread waste, it can also help alleviate the growing concerns about adequate treatment of wastewater.

A more widely recognised use of organic wastes is their pyrolysis to produce useful oils, such as those that can be co-fed with traditional crude oil feedstocks. However, the biggest problem with such pyrolysis oils is often their poor quality. In *Processing renewable and waste-based feedstocks with fluid catalytic cracking: Impact on catalytic performance and considerations for improved catalyst design*, the optimisation of solid catalysts in FCC is shown to enable pyrolysis oils to be used as replacements for fossil oils with little impact on performance (Mastry et al.).

One of the largest volume but little exploited natural resources is lignin which remains more of a waste than a feedstock despite its chemical potential. In *Biocatalytic selective acylation of technical lignins: a new route for the design of new biobased additives for industrial formulations*, technical soda lignins are chemically modified using a biocatalytic process (Sarieddine et al.). The resulting materials have useful properties that suggest possible real industrial application value.

Many modern vaccines require the addition of adjuvants which are chemical entities that can induce a strong but controlled immune response. Despite their rapidly growing value, the rate of innovation of vaccine adjuvants has been very slow. In *Cleaner synthesis of preclinically validated vaccine adjuvants*, synthetic glycophospholipids have been developed (Romerio and Peri). These not only have promising activity and low toxicity, they can be made using good clean synthesis techniques including regio- and chemo-selective reactions.

The valorisation of biomass feedstocks is likely to become a vital part of the future chemical industry and we need to prove alternative technologies for this that go beyond traditional methods like pyrolysis. In the review article, *Mechanochemistry and oleochemistry: a green combination for the production of high-value small chemicals*, the little utilised mechanochemistry technique for oleochemistry is demonstrated in a number of recent articles (Len et al.). This includes original work aimed at creating new and efficient routes to important products including biodiesel, benzoxazine and solketal.

Deep eutectic solvents are attracting increasing interest as green solvents but their use in biocatalysis has been little reported. In *Harnessing the potential of deep eutectic solvents in biocatalysis: design strategies using CO_2 to formate reduction as a case study*, these fascinating solvents are successfully demonstrated in the important reduction of carbon dioxide to formate (Logarušić et al.). This is achieved by a powerful combination of experimental screening and computational tools.

The removal of lead from water is an important clean water strategy. In *Improvement of magnetite adsorption performance for Pb (II) by introducing defects*, the ability of natural magnetite to adsorb lead is improved by surface defect engineering specifically by calcination under argon (Li et al.). The creation and effects of surface vacancies are studied by equilibrium and kinetic adsorption experiments.

Organic pollutants are of increasing concern to water purity and are becoming more common with the growth of many industries. Among the most worrying are organic dyes which are currently dumped in multi-thousand ton quantities around the world. In *Kinetics and thermodynamics investigations of efficient and eco-friendly removal of alizarin red S from water via acid-activated Dalbergia sissoo leaf powder and its magnetic iron oxide nanocomposite*, a new cost-effective natural adsorbent is proven for the adsorption of the hazardous dye alizarin red S from water (Nawaz et al.).

The complex behaviour of pollutants in water needs good mathematical modelling to aid field remediation planning. In *Modelling and optimization study on degradation of organic contaminants using nZVI activated persulfate based on response surface methodology and artificial neural network: a case study of benzene as the model pollutant*, the degradation effects of activated persulfate on the common groundwater contaminant benzene are modelled and then used to optimise the process parameters and maximise benzene removal (Luo et al.).

Calcium carbonate is one of the most common natural substances on our planet and is made even more important because of its role in helping to abate the CO_2 crisis and help combat ocean acidification. We need to make more use of this compound. In *Improvements in the utilization of calcium carbonate in promoting sustainability and environmental health*, both well-known and less well-known applications for $CaCO_3$ are described (Comes et al.). Utilization of pre-consumer and post-consumer recycled calcium carbonate is on rise and can help customers achieve their circular economy objectives.

Author contributions

JC: Writing–original draft, Writing–review and editing.

Funding

The author(s) declare that no financial support was received for the research, authorship, and/or publication of this article.

Conflict of interest

The author declares that the research was conducted in the absence of any commercial or financial relationships that could be construed as a potential conflict of interest.

The author(s) declared that they were an editorial board member of Frontiers, at the time of submission. This had no impact on the peer review process and the final decision.

Generative AI statement

The author(s) declare that no Generative AI was used in the creation of this manuscript.

Publisher's note

frontiers | Frontiers in Chemistry

TYPE Original Research
PUBLISHED 19 January 2023
DOI 10.3389/fchem.2023.1067488

OPEN ACCESS

EDITED BY
Roger Gläser,
Leipzig University, Germany

REVIEWED BY
Konstantinos Triantafyllidis,
Aristotle University of Thessaloniki, Greece
George Manos,
University College London,
United Kingdom

*CORRESPONDENCE
Bilge Yilmaz,
bilge.yilmaz@basf.com

SPECIALTY SECTION
This article was submitted to Green and Sustainable Chemistry,
a section of the journal
Frontiers in Chemistry

RECEIVED 11 October 2022
ACCEPTED 06 January 2023
PUBLISHED 19 January 2023

CITATION
Mastry MC, Dorazio L, Fu JC, Gómez JP, Sedano S, Ail SS, Castaldi MJ and Yilmaz B (2023), Processing renewable and waste-based feedstocks with fluid catalytic cracking: Impact on catalytic performance and considerations for improved catalyst design.
Front. Chem. 11:1067488.
doi: 10.3389/fchem.2023.1067488

Processing renewable and waste-based feedstocks with fluid catalytic cracking: Impact on catalytic performance and considerations for improved catalyst design

Melissa Clough Mastry[1], Lucas Dorazio[1], James C. Fu[1], Juan Pedro Gómez[2], Sergio Sedano[3], Snehesh S. Ail[4], Marco J. Castaldi[4] and Bilge Yilmaz[1]*

[1]BASF Corporation, Iselin, NJ, United States, [2]Consultant, Madrid, Spain, [3]Neoliquid Advanced Biofuels and Biochemicals, Guadalajara, Spain, [4]Chemical Engineering, City College of New York, New York, NY, United States

Refiners around the globe are either considering or are actively replacing a portion of their crude oil inputs originating from fossil sources with alternative sources, including recycled materials (plastics, urban waste, mixed solid waste) and renewable materials (bio-mass waste, vegetable oils). In this paper, we explore such replacement, specifically focusing on the fluid catalytic cracking (FCC) operation. Five pyrolysis oils, obtained from municipal solid waste (MSW) and biogenic material (olive stones/pits), were fully characterized and tested at 10% loading against a standard fluid catalytic cracking (FCC) vacuum gasoil (VGO) feed in a bench scale reactor using an industrially available fluid catalytic cracking catalyst based on ultrastable Y zeolite to simulate fluid catalytic cracking co-processing. Despite having unique feed properties, including high Conradson carbon (e.g., up to 19.41 wt%), water (e.g., up to 5.7 wt%), and contaminants (e.g., up to 227 ppm Cl) in some cases, the five pyrolysis oils gave similar yield patterns as vacuum gasoil. Gasoline was slightly (*ca*. 1 wt%) higher in all cases and LPG slightly (*ca*. 1 wt%) lower. Olefinicity in the LPG streams were unchanged, bottoms and light cycle oil (LCO) showed no significant changes, while dry gas was slightly (up to −0.2 wt%) lower. Coke selectivity was also unchanged (maximum −7.7 wt%, relatively), suggesting minimal to no heat balance concerns when co-processing in an industrial fluid catalytic cracking unit. The results demonstrate the applicability of municipal solid waste and biogenic originating pyrolysis oils into a refinery. A catalyst design concept is explored, based on higher rare Earth oxide exchange and/or utilization of ZSM-5 zeolite, that would further minimize the impacts of replacing fossil oils with pyrolysis oils, namely one that shifts the 1% higher gasoline into LPG.

KEYWORDS

fluid catalytic cracking, sustainability, renewable feedstocks, pyrolysis oil, biofuels, waste to energy, biomass upgrading, industrial waste

Introduction

The valorization of waste and renewable streams has been studied for many years (Tuck et al., 2012) (Sheldon, 2014) (Ragaert et al., 2017) (Kiran et al., 2014) (Dermeche et al., 2013) (Dahiya et al., 2018). However, more recently this concept is quickly gaining traction in industrial practices as more companies are trying to implement such strategies. In addition, from a consumer and regulatory perspective, the demand and push, respectively, for cleaner and more sustainable energy and material sources is increasing. Importantly, this includes the Renewable Energy Directive II (RED II), redefined in 2018, requiring 32% of renewable energy in the European Union by the year 2030 (European Commission, 2018), and more recently RED III, redefined again in 2022, requiring 45% renewable energy within the same time frame.

Renewable and recyclable waste can be broadly categorized into three categories: plastic waste, agricultural waste, and municipal solid waste (MSW), with the latter typically comprised of both plastic and agricultural wastes, among other materials. Dedicated plastic recycling can be done either mechanically or chemically; mechanical recycling is a proven viable option, while chemical recycling (Ragaert et al., 2017) [sometimes called advanced recycling and/or ChemCycling™ (Grauke et al., 2021)] offer other pathways, allowing for the decomposition of polymeric material into virgin molecules (i.e., ethylene and propylene). Chemical recycling is typically done thermochemically and can involve steam gasification (Saebea et al., 2020) or pyrolysis, with the ultimate goal to produce monomers and/or fuels (Lopez et al., 2017) (Wong et al., 2015). Steam gasification typically results in more chemical building blocks, whereas pyrolysis processes result in more fuel-range building blocks (Antelava et al., 2021).

Agricultural waste can be disposed of or re-used in a variety of ways. Common pathways include animal feed, composting, or landfilling, with pyrolysis upgrading becoming more prevalent (Lahijani et al., 2022). Many sources of agricultural waste and biomass have been studied *via* the pyrolysis pathway, including woodchips (Pinho et al., 2017) (Lutz et al., 2022) and food waste (Dahiya et al., 2018) (Kiran et al., 2014). In Europe, the waste from olive mills accounts for 9.6 million tons per year, with half of the European production originating in the southern part of Spain, Andalucía (Berbel and Posadillo, 2018). Most of this waste goes toward very low value-added processes, including the generation of heat and electricity, with only 5% going towards higher value-added processes including animal feed. In the median of the value addition scale is the generation of biofuels and chemicals (Berbel and Posadillo, 2018), suggesting that the transformation into biofuels and biochemicals is an attractive pathway.

At the intersection of plastic and agricultural waste is MSW, whose generation is nearly 2.0 billion metric tons and is expected to increase in the future, with some projecting MSW to comprise a large portion of the future biofuels market (Gelder et al., 2022). The investigation into MSW valorization is complex, given its diversity. Its composition varies with respect to region, waste management practices, and sorting complexity. Importantly, plastic in MSW on a global scale is approximately 12 percent by weight and, therefore, can be a significant source for chemical and fuel manufacture. The renewable portion, excluding yard and food waste, comprises about 34 wt% and represents a truly renewable path to fuels and chemicals. Various researchers and companies also investigate the use of more specific unique streams, including waste tires (Tian et al., 2022; Pyrum Innovations, 2022) and waste biological products (Shim et al., 2022). Laboratory experiments have been conducted on carefully prepared MSW-like materials (Sorum et al., 2001) and the pyrolysis of MSW has been studied in detail by many groups (Chen et al., 2014; Du et al., 2021). However, the post-processing of the resulting MSW-pyrolysis oil to generate valuable fuels and chemicals is less studied.

In this paper, we focus on the usage of pyrolysis oils from MSW and biomass waste in an FCC unit. The FCC is at the heart of the refinery and is one of the more flexible processes in the refinery, making it an ideal candidate for the processing of unique streams. By utilizing pilot scale laboratory testing, the impact of alternative feed sources on FCC product yields can be quantified by replacing a portion of the fossil-based feed. Given the flexibility of the FCC process and its ability to handle unique feedstocks and contaminants, it remains a very valuable tool when considering outlets for pyrolysis oil upgrading (Lappas et al., 2009; Fogassy et al., 2011). Previous literature exploring the co-processing of biogenic pyrolysis oils utilize lab-created pyrolysis oils (Magrini et al., 2022; Seiser et al., 2022). The novelty in this paper lies in the direct application to industry and the unique nature of the pyrolysis oils that are from an industrial scale operation and are already being sold into the open market. The utilization of industrially available pyrolysis oils and catalysts in this paper demonstrates the applicability of previous works to real life scenarios. The post-processing of the resulting pyrolysis oils is evaluated using an industrially available FCC catalyst. Further, the application of the pyrolysis oil is such that the co-processing level is industrially relevant, i.e., tested at a level that a typical refiner would also consider/utilize at scale. The work presented supports refiners' goals to use existing equipment and infrastructure to answer the latest question around sustainability. These concepts (yield impacts, feed characterization, and contaminant handling) are of paramount importance to enable the refining industry's partial or full replacement of fossil fuels.

Experimental

Pyrolysis oils were obtained from the industrial plant of Neoliquid in Guadalajara (Spain) and from the industrial plant of Neoliquid/Preco in Toledo (Spain) and used without further pre-processing. Notably the BIO1 material is the oil product from pyrolysis, whereas the aqueous fraction (wood vinegar) obtained from pyrolysis was separated into a different product stream. Both plants operate using the pyrolysis technology of Neoliquid Biofuels and Advanced Biochemicals. The municipal solid waste (MSW) processed in these plants has previously been processed to remove glass, metal, and minerals. The feed samples spent 18 days in transit (in ambient and cold temperatures during ground and air transport) before being analyzed. All were dark and viscous liquids at room temperature. Upon arrival at the testing lab, they were stored in a freezer (0°C). In addition to the five pyrolysis oils, a standard vacuum gasoil (VGO) feed was also used. The oils were used as-received, without the use of stabilizing agents.

Six oils were included in this study, with descriptions listed below:

Standard: VGO representative of an FCC feed used in a typical US gulf coast FCC unit.

MSW1: Pyrolysis oil from MSW, containing 70%–90% mixed plastics and 10%–30% paper, cardboard, biomass, and textile waste.

MSW2: Heavy liquid fraction from the MSW1 pyrolysis process.

MSW3: Pyrolysis oil from MSW, containing 70%–90% mixed plastics (with a high fraction of polyolefins) and 10%–30% paper, cardboard, biomass, and textile waste.

BIO1: Pyrolysis oil from biomass waste (olive stones/pits).

MIX1: A 10% BIO1 and 90% MSW1.

The catalyst used in the cracking evaluations was a porous zeolite-based *in-situ* catalyst (McLean, 2003) containing a high ultrastable Y (USY) content designed for resid applications. The properties for fresh catalyst are found in Table 1. The catalyst was deactivated under hydrothermal conditions (100% steam, 788 C, 24 h) and this deactivated catalyst, properties for which are found in Table 2, was used for all catalytic evaluations.

Elemental analysis of the catalysts was conducted by X-ray Florescence (XRF) using a Philips PW2400 spectrometer, with fused pellet specimens; data were accurate within 1% relative abundance. BET (TSA) surface area was determined using N_2 adsorption data acquired using a Micromeretics Galaxy 3,060 sorptometer. T-plot external area (MSA) was calculated from the same N_2 isotherms. Results have a precision of about ±2% relative.

Unit cell size was determined following ASTM D3942. X-Ray diffraction data were collected using a PANalytical MPD X'Pert Pro diffractometer, with Cu radiation and Si was used as an internal standard. The unit cell size uncertainty of our estimate ranges from 0.004 to 0.01 Å.

Catalytic measurements were made using an Advanced Catalytic Evaluation (ACE™) fluid bed reactor (Kayser, 1997). The ACE was operated using a steam-deactivated catalyst, at a temperature of 529°C, 60 s injection time, 1.125 inch injector height, and using a constant time on stream protocol to vary catalyst to oil ratios of 4, 5, 6, and 7. Pyrolysis oils were tested at 10% loading with the balance of 90% as a standard FCC feed. This approach is being considered by early adopters from a refinery perspective, with many opting to co-process alternative (e.g., pyrolysis) oils at 1%–10% loading. Gasoline product was defined as C_5 to 232°C, diesel as 232°C–360°C, and bottoms as 360 °C and higher. API gravity, refractive index, and viscosity were measured at 16, 25, and 99°C, respectively. PIONA were not collected on the syncrude materials.

High temperature simulated distillation (HT SIMDIS ASTM 7500 method) of oil samples were conducted on an Agilent 7890 B GC equipped with a SIMDIS capillary column capable of reaching up to 430°C. This method starts at −20°C using cryogenic nitrogen and then ramps up to 430°C. Helium was used as carrier gas. Before oil samples were introduced to the GC, they were first diluted with carbon disulfide (CS_2) at 1:50 ratio (0.02 g sample with 1 g CS_2). The HT SIMDIS ASTM 7500 method was used to determine boiling point distribution for samples that could not elute completely by ASTM 2887 method and can determine boiling points from n-C5 to n-C120 distribution.

Water content in the oil samples were measured by a Karl Fischer titrator (Mettler Toledo V30S). A sample is added to dry methanol (no water present) and the mixture is titrated with a titrant (Composite 5) until it reaches the end point which is determined using bi-voltametric indication, i.e., the potential at the polarized double-platinum-pin electrode falls below a certain value (e.g., 100 mV). The water content of the sample is calculated from the amount of titrant used.

CHN (carbon, hydrogen and nitrogen) was measured by a LECO CHN628 analyzer. It is a combustion elemental carbon, hydrogen and nitrogen instrument that uses pure oxygen to completely combust a sample. Helium carrier gas sweeps the combustion gas to separate IR cells for detection of CO_2 and H_2O. A TCD (thermal conductivity detector) is used to detect nitrogen. Oxygen is calculated from balancing to 100. Other elements in oils were determined by ICP (inductively coupled plasma) using a method similar to ASTM D7691. The ICP instrument uses two-point calibration (blank and 1 ppm) and sample preparation involves kerosene as the diluent.

TABLE 1 Fresh catalyst properties.

Parameter	Fresh catalyst property
Total surface area, m^2/g	311
Zeolite surface area, m^2/g	225
Matrix surface area, m^2/g	86
Rare earth oxide, wt%	2.2
SiO_2, wt%	50.2
Al_2O_3, wt%	44.6
Na2O, wt%	0.22
UCS, Å	24.59
APS, μ	80

In addition to the physical and chemical analyses, a more detailed analysis of the hydrocarbons comprising each feedstock oil was performed using an Agilent 7890B gas chromatograph equipped with an Agilent 5977A mass spectrometer. For these measurements, the pyrolysis oil was dissolved in cyclohexane solvent at a ratio of 1:100 and the hydrocarbon spectra were characterized using a slightly polar SHRX5LB column.

For catalytic testing, the pyrolysis oils were mixed with standard feed at 10/90 weight ratio without the use of emulsifiers. Upon mixing, the two oils were miscible with no phase separation noted, distinctly different from other accounts of immiscibility of biogenic oils and standard petroleum-based oils (Seiser et al., 2022). The homogeneous feeds were then injected into the catalytic reactor through a singular injection line.

Results and discussion

First, we examine catalyst and oil characterizations. For the catalyst, because the continuous operation of FCC units results in an aged distribution of particles, we must examine both fresh and deactivated catalysts. Fresh and steam deactivated catalysts tested are noted below.

Table 3 below describes the full (neat) feed analyses. The API gravities of the MSW and MIX1 pyrolysis oils are comparable to the standard VGO feed. The BIO1 pyrolysis oil gave a negative API value suggesting a heavy feed, confirmed by distillation. In terms of Conradson carbon, BIO1 oil gives values that are much higher than those currently being processed in FCC units globally while the MSW1-3 and MIX1 oils falling in a more traditional range (BASF benchmarking database). However, when considering the later evaluation at the 10% co-processing scenario, the resulting weighted average even with the BIO1 oil is well within typical FCC feeds. Not surprisingly, the BIO1 feed gives considerable water content, typical of bio-based feedstocks (Magrini et al., 2022), while

TABLE 2 Steam deactivated catalyst properties.

Parameter	Deactivated catalyst property
Total surface area, m^2/g	133
Zeolite surface area, m^2/g	88
Matrix surface area, m^2/g	45
UCS, Å	24.29

the MSW and MIX1 feeds have more typical water content. The very high viscous nature of the BIO1 sample precluded its viscosity from being accurately measured. Similarly, the pour points for MSW3 and BIO1 were not measured because portions of these two samples remain as liquid at lowest temperature (−6 C) achievable for the instrument.

The pyrolysis oils bring halogen contaminants, particularly Cl which range between 190 and 230 ppm for the MSW-originating oils (MSW1-3 and MIX1). The purely biogenic feed (BIO1) brings lower

TABLE 3 Properties of feeds used in this study.

	Standard	MSW1	MSW2	MSW3	BIO1	MIX1
Physical properties						
API (specific) gravity	23.79 (0.91)	33.71 (0.86)	24.86 (0.91)	31.16 (0.87)	−5.35 (1.12)	31.58 (0.87)
Conradson carbon (wt%)	0.43	1.09	3.85	0.44	19.41	1.65
Pour point (°C)	38	4	38	NM[b]	NM[b]	10
Aniline point (°C)	77	>93	>93	>93	>93	>93
Sulfur (wt%)	0.72	ND[a]	ND[a]	ND[a]	0.02	ND[a]
Refractive index	1.51	1.48	1.51	1.50	1.56	1.49
Viscosity (cSt)	7.43	1.14	5.64	1.37	NM[b]	3.53
Flash point (°C)	>149	38	>149	45	>149	38
Water (wt%)	0.07	0.01	0.17	0.22	5.72	0.08
Elemental analyses						
C (wt%)	86.4	84.5	85.7	84	67.9	84.6
H (wt%)	12.5	11.2	11.5	10.4	7.3	10.8
N (wt%)	0.11	0.08	0.19	0.08	0.32	0.13
O (wt%)	0.38	3.55	2.05	4.85	24.04	3.85
Br (ppm)	<1.5	16.3	22.3	7.1	<0.5	13.6
Ca (ppm)	<0.1	0.4	0.5	45.1	4.9	0.4
Cl (ppm)	<0.0001	198	227	205	17	194
Cu (ppm)	<0.1	0.2	0.4	0.8	1.2	0.2
Fe (ppm)	<0.1	9	8	43	61	2
K (ppm)	21	9	7	15	51	9
Mg (ppm)	<0.1	<0.1	0.1	7.2	1.0	<0.1
Na (ppm)	0.3	3	3	23	26	3
Ni (ppm)	0.3	0.2	0.9	0.4	0.6	0.2
P (ppm)	<0.1	11.1	35.1	5.5	6.2	11.2
Si (ppm)	0	90.8	36.4	60.2	4.7	93.4
V (ppm)	0.2	<0.1	<0.1	<0.1	<0.1	<0.1
GC Distillation (°C)						
Initial BP	251	61	147	43	96	99
5%	294	114	227	115	141	118
10%	338	138	272	139	187	137
20%	365	150	311	147	211	153
30%	388	177	343	148	236	193
40%	409	217	376	183	257	232
50%	428	253	410	238	288	268
60%	449	289	442	303	333	299
70%	472	329	481	369	363	341
75%	484	361	501	403	389	370
80%	496	393	522	437	416	399
85%	511	437	549	476	446	438
90%	526	482	576	516	477	476
95%	571	545	614	566	549	557
Final BP	616	643	665	642	622	637

[a]ND, not detected.
[b]NM, not measured.

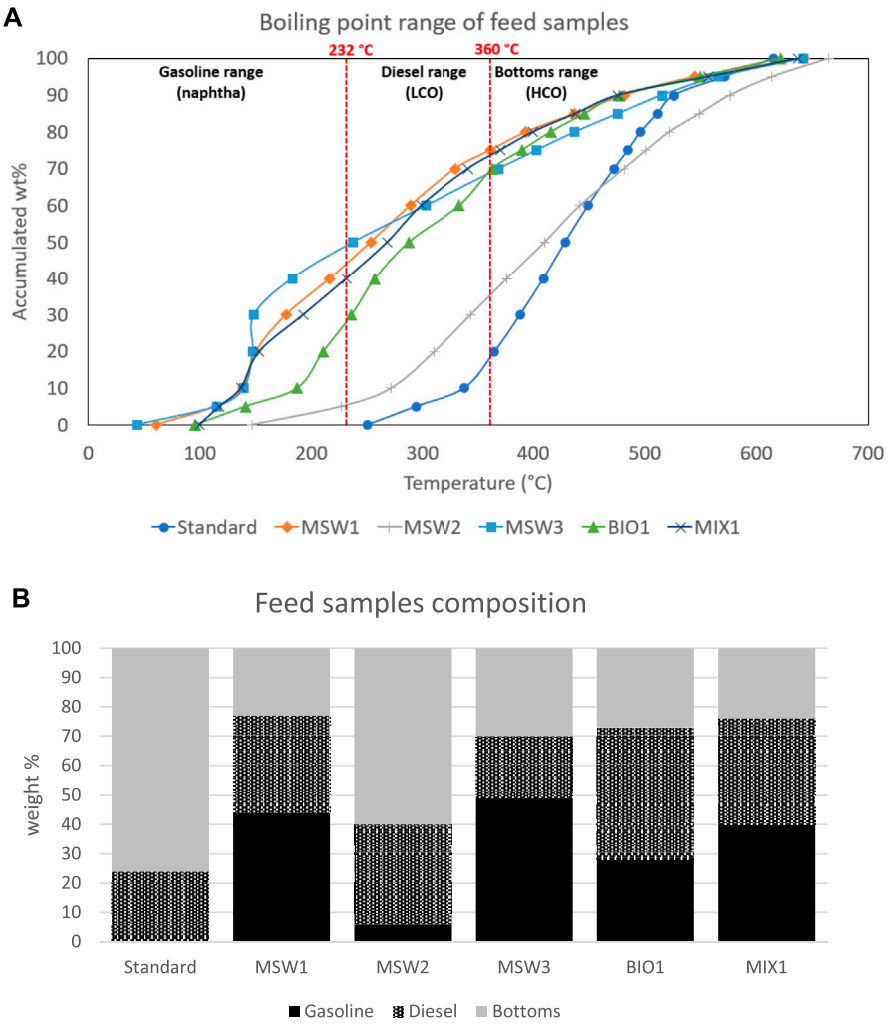

FIGURE 1
Standard and pyrolysis oil feed distillation curves **(A)**, top and component breakdown **(B)**, bottom.

Cl at 17.3 ppm. The effects of Cl in FCC have been previously examined by our group (Senter et al., 2021). We do not expect to observe any effects in lab-scale testing considering the lack of nickel contaminant. In a refinery setting, care must be taken in case of nickel reactivation and chloride deposits downstream of the FCC unit.

The feed distillation is depicted graphically to provide a visual comparison. In Figure 1A, the pyrolysis oil distillations are plotted along with the standard feed. In most cases, the pyrolysis oils are lighter than the standard feed, with the exception of the MSW2 sample. This is not surprising considering that this is the heavy fraction from the pyrolysis process corresponding to MSW1. The feeds were further analyzed by the composition breakdown into gasoline, diesel, and bottoms using 232°C and 360°C cut points between the naphtha/LCO and LCO/HCO products, respectively, and are also depicted below in Figure 1B. The standard FCC feed contains a majority amount of bottoms product. Refiners typically process the standard feeds upstream to remove as much of the upgraded products as possible. However, in the case of the pyrolysis oils, we observe significant amounts, sometimes up to 75%, of the lighter gasoline and diesel products.

In addition to the bulk properties, GC-MS analyses were also conducted on the 5 pyrolysis oils to characterize their molecular makeup. The hydrocarbon spectra and the list of dominant compounds are provided in the Supplementary data (Supplementary Figures S1–S5; Supplementary Table S3). For the purposes of this analysis, MIX1 is characterized as an MSW-derived pyrolysis oil given the larger content of MSW1 *versus* BIO1. The MSW-derived pyrolysis oils contain aromatic, aliphatic, and oxygenated hydrocarbons, whereas the BIO1 sample is characterized by large fractions of cyclic-oxygenated hydrocarbons and small fractions of linear-oxygenated hydrocarbons. The distribution of these classes of hydrocarbons in the five pyrolysis oil samples are shown in Figures 2A,B.

Upon further analysis, not surprisingly, the biogenic oil BIO1 is distinctly different from the MSW oils. BIO1 was derived from olive pits/stones, which is a typical example of lignocellulose waste. In general, all lignocellulose waste will be comprised of lignin, hemicellulose, and cellulose. During pyrolysis, these highly oxygenated structural components of the biomass will undergo deconstruction and are expected to yield a highly diverse mixture of oxygenated hydrocarbons (Huber et al., 2006; Liu et al., 2014). Lignin will primarily yield phenols and guaiacols. Cellulose and

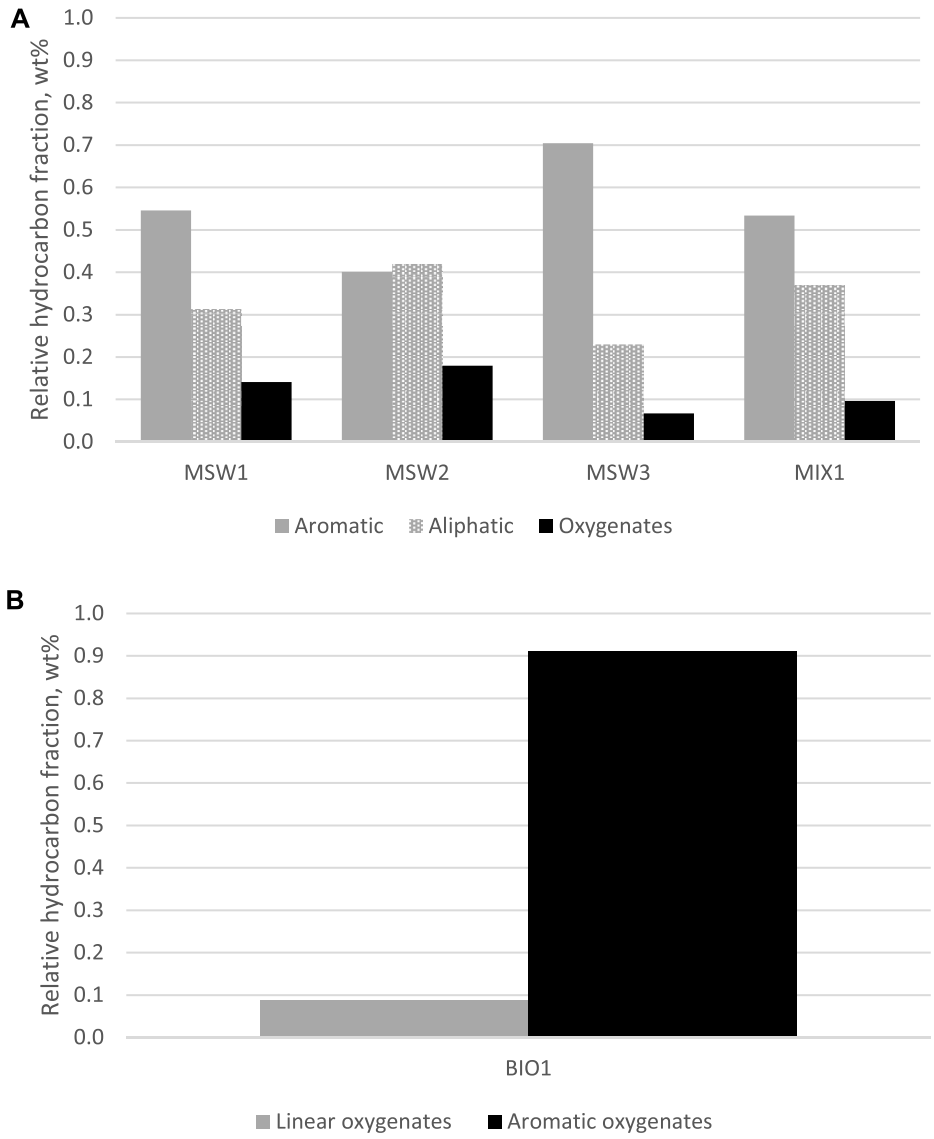

FIGURE 2
Dominant compounds found in pyrolysis oils; relative aromatic, aliphatic, and oxygenate hydrocarbon distribution in MSW-derived pyrolysis oils **(A)**, top and relative linear and aromatic oxygenate hydrocarbon distribution in biomass-derived pyrolysis oil **(B)**, bottom.

hemicellulose will yield a diverse mixture of smaller carbonyl compounds and sugar derived compounds such as furfural and furan/pyran ring structures. Our analysis of BIO1, which is illustrated in the Supplementary data, is consistent with these expectations and shows the presence of phenolic molecules (phenol and substituted phenols) and other oxygenated hydrocarbons including ketones, fatty acids, and caffeine. There is a notable absence of light water-soluble compounds, i.e., those found after pyrolysis of cellulosic materials; this is likely explained by the separation of BIO1 oil from the aqueous fraction as explained in the experimental section. The composition of the MSW derived oils is quite different. Consistent with their oxygen content, there was a limited presence of oxygenates that included molecules such as large linear alcohols and esters. The bulk of the oil was comprised of aromatic and aliphatic hydrocarbons. Consistent with the oil Conradson carbon and specific gravity reported in Table 3, MSW 2 was comprised of larger aliphatic hydrocarbons and multiring aromatic structures.

Next, we examine the catalytic cracking evaluations, all of which were done using the deactivated catalyst as described in the experimental section. In the refining industry, it is customary to discuss catalyst activity in terms of the conversion to gasoline and lighter products, which is defined as 100—LCO—bottoms. At a constant catalyst to oil of 7, the conversion of all oils were slightly higher than the standard feed, which gave 75.8 wt% conversion. MSW1, MSW2, MSW3, BIO1, and MIX1 gave conversion levels of 76.2, 75.9, 76.1, 76.3, and 76.2 wt%, respectively. This is likely due to already converted material (i.e., naphtha range molecules) entering as feed in all cases. To examine the effects on product selectivities, the cracking evaluations are examined at iso conversion (75 wt%), obtained by regression of raw data. This conversion value was chosen since it is the median value of all tests and does not require extrapolation. Compared to the standard feed, all pyrolysis oils gave an increase in gasoline yield and a decrease in LPG yield. It is likely this

10.3389/fchem.2023.1067488

TABLE 4 Catalytic cracking evaluation of all feeds at constant conversion (75 wt%).

	Standard	MSW1	MSW2	MSW3	BIO1	MIX1
Process variables						
Catalyst to oil ratio, wt/wt	6.65	6.38	6.50	6.30	6.35	6.41
Hydrocarbon yields						
H_2, wt%	0.08	0.08	0.08	0.08	0.07	0.08
Methane, wt%	0.88	0.82	0.84	0.79	0.86	0.81
Ethane, wt%	0.59	0.55	0.59	0.55	0.58	0.57
Ethylene, wt%	0.81	0.76	0.78	0.75	0.84	0.77
Propane, wt%	1.07	0.99	1.01	0.96	1.03	0.97
Propylene, wt%	5.83	5.55	5.72	5.49	5.67	5.56
n-Butane, wt%	0.89	0.82	0.84	0.81	0.86	0.81
i-Butane, wt%	4.11	3.84	3.88	3.76	3.95	3.75
n-Butenes, wt%	5.32	5.11	5.33	5.11	5.20	5.20
i-Butylene, wt%	2.26	2.22	2.34	2.24	2.24	2.30
Gasoline, wt%	50.42	51.63	50.86	51.94	50.96	51.59
LCO, wt%	15.18	15.23	15.36	15.22	15.29	15.34
Bottoms, wt%	9.82	9.77	9.64	9.78	9.71	9.66
Coke, wt%	2.73	2.64	2.75	2.52	2.74	2.59
Calculated values						
Total valuable liquids[a], wt%	85.08	85.39	85.33	85.54	85.20	85.52
Total dry gas, wt%	2.36	2.20	2.28	2.16	2.35	2.23
Total LPG, wt%	19.49	18.53	19.11	18.38	18.95	18.59
LPG olefinicity, wt/wt	0.69	0.70	0.70	0.70	0.69	0.70
Total C4=, wt%	7.58	7.33	7.67	7.36	7.44	7.50
C3 olefinicity, wt/wt	0.84	0.85	0.85	0.85	0.85	0.85
C4 olefinicity, wt/wt	0.60	0.61	0.62	0.62	0.61	0.62
Non-hydrocarbon yields						
CO, wt%	0.05	0.04	0.06	0.05	0.09	0.06
CO_2, wt%	0.26	0.31	0.28	0.24	0.26	0.25
H_2O, wt%	0.82	0.75	0.81	0.42	1.15	0.31

[a]Total valuable liquids defined as LPG + gasoline + LCO.

shift is the result of higher aromatic content in the naphtha fraction of the pyrolysis oils relative to the standard gasoil. During catalytic cracking, these aromatics will be relatively inert and ultimately collected within the gasoline product fraction. Coke selectivity is the same or lower for all pyrolysis oils compared to the standard oil, suggesting that major heat balance issues in an FCC unit would not arise or would be minimal with the co-processing of these oils. In the case of minimal heat balance selectivity (e.g., with MSW3 at −7.7% on a relative basis), delta coke in the unit could be increased. The small shift in LCO and bottoms yield is likely the result of the higher natural fractions of naphtha and LCO sized molecules contained in the pyrolysis oil feedstocks. Unlike other studies of biogenic pyrolysis oil coprocessing in an FCC (Pinho et al., 2017), the processing of the biogenic material (BIO1 coming from olive stones/pits) did not result in lower liquid yields.

The olefinicity, which is the ratio of cracking (olefin producing) and hydrogen-transfer reactions (olefin consuming) is an important metric in FCC analysis. The LPG selectivities (LPG olefinicity, C3 olefinicity, and C4 olefinicity) are not affected in any of the pyrolysis oil co-processing scenarios. Dry gases are either similar (BIO1) or lower than the standard feed, suggesting that dry gas handling during a co-processing event in an FCC unit would not be a concern. Yields of products of deoxygenation, i.e., CO, CO_2, and H_2O, are also listed in Table 4. The oxygen content of the standard gasoil and yields of CO, CO_2, and H_2O should approach zero. Yields of these products reported in Table 4 are the result of either measurement error and/or atmospheric water inadvertently introduced into the recovered syncrude liquid as it is prepared for external analysis. The yields of CO, CO_2, and H_2O for the standard feed should be considered a zero baseline to compare the other feedstocks against. For all cases, the yields of CO and CO_2 are similar to that of the standard gasoil. This suggests that at least for the case where the co-processing is limited to 10%, deoxygenation through decarbonylation (yielding CO) or decarboxylation (yielding CO_2) is not significant enough to be detected in product yields. Yield of water is consistent with the oxygen content of the feedstock where the water yield from the lower oxygen containing feedstocks were similar to the standard gasoil. Only for the case of BIO1 was the water yield higher, suggesting the preferred pathway for deoxygenation was likely dehydration. In terms of FCC co-processing, the production of water would translate to more wastewater treatment and processing. In terms of FCC chemistry, production of water would consume hydrogen and potentially lead to higher coke yields, although this was not observed for the 10% co-processing of BIO1. Not explored in this paper are potential impacts on equipment corrosion and fouling in an industrial FCC unit.

There is a correlation ($R^2 = 0.91$) between the amount of gasoline-range molecules in the neat pyrolysis oil (presented in Figure 1 above)

and the delta gasoline yield *versus* standard feed (presented in Table 4 above). The pyrolysis oil coming with the highest amount of gasoline-range molecules (MSW3, 49%) also gives the highest delta gasoline yield (+1.52 wt%) *versus* the standard feed in the catalytic cracking evaluation. There also is a similarly good correlation (R^2 = 0.94) between the amount of gasoline-range molecules in the neat pyrolysis oil and the delta LPG yield *versus* standard feed, in this case showing a negative trend. Both correlations are shown below in Figure 3. Other possible correlations between diesel content in the pyrolysis oils, bottoms content in the pyrolysis oils, LPG + gasoline delta yields, and bottoms delta yields, were determined to not have relevant (R^2 > 0.90) correlations, suggesting that gasoline-range molecules in the pyrolysis oil is the most relevant bulk property in terms of resulting catalytic cracking differences. We theorize that the gasoline made from the pyrolysis oils are distinctly different from the gasoline made from the VGO oil. The data suggest that the naphtha fraction from the pyrolysis oil does not undergo significant further cracking into LPG. This theory is supported by the above observations of high aromatics content of the pyrolysis oils. Since FCC units do not crack aromatic compounds, the aromatics remain in the gasoline product cut as a high-octane naphtha molecule. The expected difference in gasoline composition is important for a refiner to understand, especially if further cracking by additional zeolites, i.e. ZSM-5, are used. Since ZSM-5 works mainly on linear and near linear naphtha molecules, the higher presence of aromatic content within the naphtha range will result in lower secondary cracking.

For refiners and researchers who prefer to examine the data at constant catalyst-to-oil ratio and at constant coke, we offer the full cracking evaluation data in Supplementary Tables S1 and S2 as part of the supporting information. As expected in the constant coke cases, the small coke selectivity differences are translated in different conversion levels, with all pyrolysis oils being higher than the standard oil.

We further evaluated various pragmatic cases in terms of pyrolysis oil crackability, an exercise that a refining organization might likely perform themselves during the planning stages of such an undertaking. In this analysis, we examined two cases.

- Scenario 1: in which we assumed pure carry-over of the pyrolysis oil components and no further conversion
- Scenario 2: in which we assumed standard conversion of the unconverted products in the pyrolysis oils

For all scenarios, the catalyst to oil of 7 data were used, in which the standard oil delivered a conversion of 75.8 wt%. As an illustration of scenario 1, the MSW1 contains 56 wt% unconverted products (i.e., diesel and bottoms). Applying a 75.8 wt% conversion to that figure, the remaining diesel and bottoms content of a pure MSW1 would be 13.6 wt% [i.e., 56—(56 * 0.758)]. The theoretical conversion of the co-processed MSW1 is then a weighted average of the VGO conversion (75.8 wt%) and of the pyrolysis conversion (100—13.6 wt%), giving a value of 76.9 wt%. These calculations were repeated for the other pyrolysis oils.

To illustrate scenario 2, the natural conversion level (i.e., naphtha content) of the pyrolysis oil was considered. For MSW1, this natural conversion level is 44 wt%. The theoretical conversion therefore is a weighted average of the VGO conversion (75.8 wt%) and the natural conversion level of the pyrolysis oil (44 wt%), giving a value conversion of 76.9 wt%.

The two scenarios were then compared to the experimental (observed) conversion to give further insight into the pyrolysis oil reactivity, with the key data summarized in Figure 4. The full data tables explaining these calculations and estimates can be found in Supplementary data (Supplementary Table S3).

We found that the experimental conversion was always higher than scenario 1 and lower than scenario 2. The higher observed conversions *versus* scenario 1 conversions illustrate that the pyrolysis oils are indeed

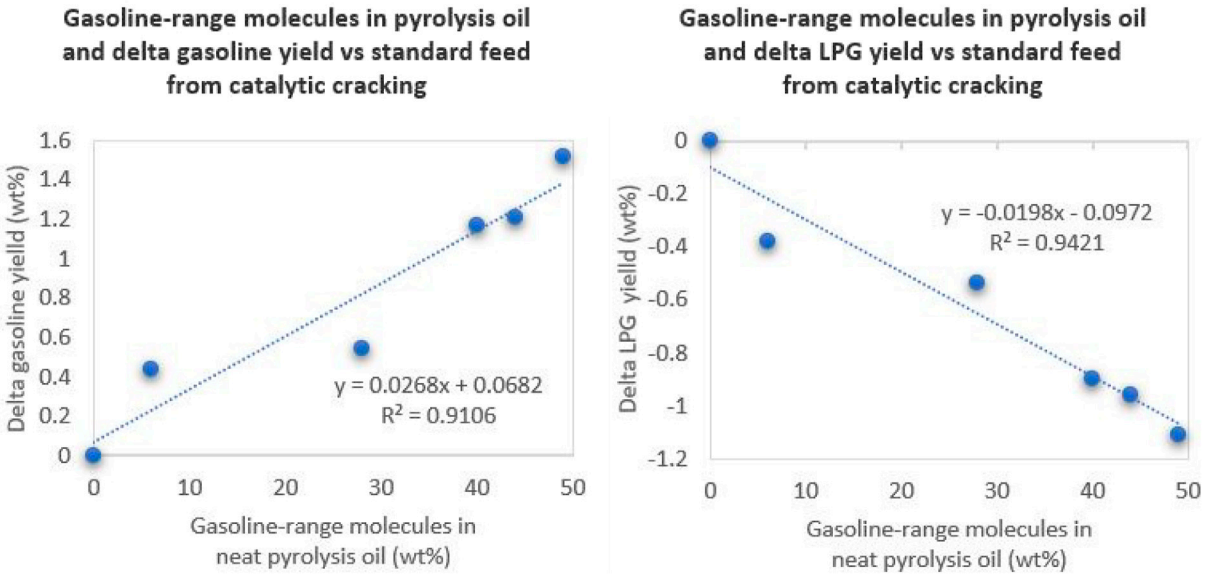

FIGURE 3
Correlations between gasoline-range molecules in the pyrolysis oils and resulting gasoline (left) and LPG (right) yield deltas from the catalytic cracking evaluations.

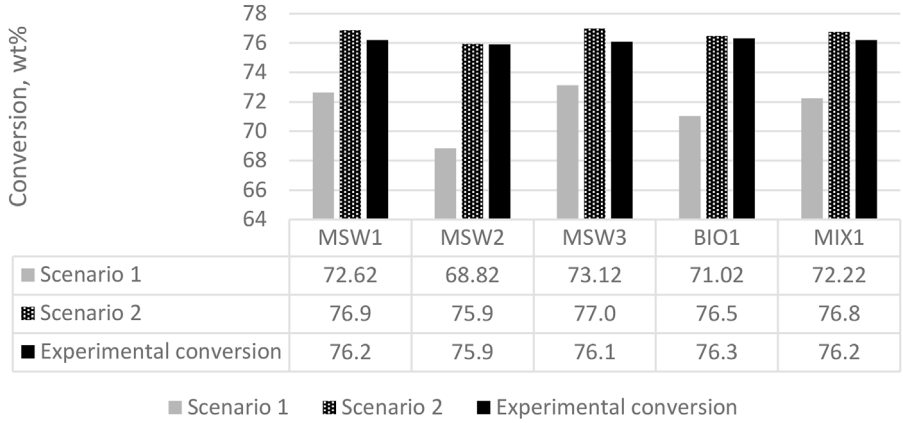

FIGURE 4
Pragmatic conversion estimates using two scenarios compared to observed experimental conversion.

undergoing cracking reactions, rather than a pure carry-over of existing converted and heavy products. The lower observed conversion *versus* scenario 2 conversions illustrates that the heavy fractions from the pyrolysis oils are more difficult to convert than the standard VGO, which is supported by the high aromaticity of the pyrolysis oils.

Conclusions

Five pyrolysis oils originating from MSW and/or biogenic materials (olive stones/pits) were compared against a standard VGO material for FCC co-processing applications. The pyrolysis oils were mixed with standard oil at 10/90 ratio with no issues with miscibility. The catalytic results show very favorable outcomes for the co-processing of MSW and bio- originating pyrolysis oils with minimal impacts. An increase in valuable liquids was observed, likely due to the high qualities/properties of BIO1 compared to other biomass pyrolysis liquids. In fact, all pyrolysis oils gave higher total valuable liquid yields. This catalytic evaluation suggests that the co-processing of the 5 pyrolysis oils studied could be rather straight forward for some refineries and FCC units with respect to yield selectivities. Some impacts on product qualities are expected, namely a more aromatic naphtha product. Further considerations for a refinery would be the handling of any unique contaminants that cannot be assessed in small scale laboratory settings, such as the effect of chlorides and possible corrosion or fouling in an FCC unit. The pragmatic conversions estimate analysis suggests that the pyrolysis oils are indeed undergoing further cracking of the heavy (diesel and bottoms) fractions and not simply exhibiting a carryover effect. The experimental conversion was lower than the scenario 2 case, suggesting that the heavy molecules in pyrolysis oils are slightly more difficult to crack than the standard VGO.

Given the impact on product selectivities have been mainly towards gasoline and LPG, considerations for catalyst design are feasible. In the case where the refinery desires similar yields, i.e., ca. 1 wt% lower gasoline and ca. 1 wt% higher LPG to better mimic the standard feed case, a simple catalyst reformulation and/or usage of an LPG olefins additive would be beneficial, however taking into consideration the possibility of lower light olefins in the naphtha product fraction for further cracking by ZSM-5. Importantly, this study describes the "drop-in scenario", i.e., co-processing pyrolysis oils without pre-treatment. In some cases, a refinery might elect to pre-treat the pyrolysis oil (through hydrotreating or another method) to lower contaminants going into the FCC unit. In another scenario, a refiner might elect to first process the pyrolysis oil using separation methods (i.e., distillation) to first remove the valuable fractions (i.e., gasoline and diesel) and feed the remaining heavy portions into the FCC unit.

Data availability statement

The original contributions presented in the study are included in the article/Supplementary Material, further inquiries can be directed to the corresponding author.

Author contributions

MM: Conceptualization, Methodology, Investigation, Formal analysis, Data curation, Writing—original draft. LD: Conceptualization, Methodology, Investigation, Formal analysis, Data curation. JF: Investigation, Formal analysis, Resources, Data curation, Writing—review and editing. JG: Resources, Writing—review and editing. SS: Resources, Writing—review and editing. SA: Investigation, Formal analysis, Data curation, Writing—review and editing. MC: Investigation, Formal analysis, Data curation, Writing—review and editing. BY: Conceptualization, Investigation, Resources, Writing—review and editing.

Acknowledgments

We thank BASF for funding this work, providing catalyst samples, and granting permission to publish it. We thank Neoliquid Advanced

Biofuels and Biochemicals for providing the pyrolysis oil and for granting permission to publish this work. We thank the Combustion and Catalysis Laboratory at the City College of New York for performing GC-MS analyses and for granting permission to publish the work.

Conflict of interest

Authors MM, LD, JF, and BY were employed by BASF Corporation. SS was employed by Neoliquid Advanced Biofuels and Biochemicals.

The remaining authors declare that the research was conducted in the absence of any commercial or financial relationships that could be construed as a potential conflict of interest.

The authors declare that this study received funding from BASF. The funder had the following involvement in the study: study design, collection, analysis, interpretation of data, the writing of the article, and the decision to submit it for publication.

Publisher's note

Supplementary material

The Supplementary Material for this article can be found online at: https://www.frontiersin.org/articles/10.3389/fchem.2023.1067488/full#supplementary-material

References

Antelava, A., Jablonska, N., Constantinou, A., Manos, G., Salaudeen, S. A., Dutta, A., et al. (2021). Energy potential of plastic waste valorization: A short comparative assessment of pyrolysis versus gasification. *Energy fuels.* 35 (5), 3558–3571. doi:10.1021/acs.energyfuels.0c04017

BASF benchmarking database. Iselin, NJ USA.

Berbel, J., and Posadillo, A. (2018). Review and analysis of alternatives for the valorisation of agro-industrial olive oil by-products. *Sustainability* 10, 237. doi:10.3390/su10010237

Chen, D., Lijie Yin, H. W., and He, P. (2014). Pyrolysis technologies for municipal solid waste: A review. *Waste Manag.* 32 (12), 2466–2486. doi:10.1016/j.wasman.2014.08.004

Dahiya, S., Kumar, A. N., Chatterjee, S., Omprakash, S., and Mohan, S. V. (2018). Food waste biorefinery: Sustainable strategy for circular bioeconomy. *Bioresour. Technol.* 248, 2–12. doi:10.1016/j.biortech.2017.07.176

Dermeche, S., Nadour, M., Larroche, C., Moulti-Mati, F., and Michaud, P. (2013). Olive mill wastes: Biochemical characterizations and valorization strategies. *Process Biochem.* 48 (10), 1532–1552. doi:10.1016/j.procbio.2013.07.010

Du, Y., Ju, T., Meng, Y., Lan, T., Han, S., and Jiang, J. (2021). A review on municipal solid waste pyrolysis of different composition for gas production. *Fuel Process. Technol.* 224, 107026. doi:10.1016/j.fuproc.2021.107026

European Commission (2018). EU science hub European commission. Available at: https://joint-research-centre.ec.europa.eu/welcome-jec-website/reference-regulatory-framework/renewable-energy-recast-2030-red-ii_en [Accessed September 9 2022].

Fogassy, G., Thegarid, N., Schuurman, Y., and Mirodatos, C. (2011). From biomass to bio-gasoline by FCC co-processing: Effect of feed composition and catalyst structure on product quality. *Energy and Environ. Sci.* 4, 5068. doi:10.1039/c1ee02012a

Gelder, A., Venter, G., McManus, G., and Bailey, G. (2022). Wood mackenzie. Available at: https://view.ceros.com/wood-mackenzie/horizons-edition-august-2022-2/p/1?heightOverride=17970&mobileHeightOverride=29930 [Accessed September 8 2022].

Grauke, R., Schunk, S. A., Hanf, S., Kelkar, C., Köpke, D., Finger, E.-E., et al. (2021). "Maximizing olefin yields: Fluid catalytic cracking as conversion technology for pyrolysis-oils from plastic waste," in DGMK conference on chemical recycling - beyond thermal use of plastic and other waste, 06-07.10.2021.

Huber, G. W., Iborra, S., and Corma, A. (2006). Synthesis of transportation fuels from biomass: Chemistry, catalysts, and engineering. *Chem. Rev.* 106, 4044–4098. doi:10.1021/cr068360d

Kayser, J. C. (1997).Versatile fluidized bed reactor. US Patent US6069012A.

Kiran, E. U., Trzcinski, A. P., Ng, W. J., and Liu, Y. (2014). Bioconversion of food waste to energy: A review. *Fuel* 134, 389–399. doi:10.1016/j.fuel.2014.05.074

Lahijani, P., Mohammadi, M., Mohamed, A. R., Ismail, F., Lee, K. T., and Amini, G. (2022). Upgrading biomass-derived pyrolysis bio-oil to bio-jet fuel through catalytic cracking and hydrodeoxygenation: A review of recent progress. *Energy Convers. Manag.* 268, 115956. doi:10.1016/j.enconman.2022.115956

Lappas, A. A., Bezergianni, S., and Vasalos, I. A. (2009). Production of biofuels via co-processing in conventional refining processes. *Catal. Today* 145, 55–62. doi:10.1016/j.cattod.2008.07.001

Liu, C., Wang, H., Karim, A. M., Sun, J., and Wang, Y. (2014). Catalytic fast pyrolysis of lignocellulosic biomass. *Chem. Soc. Rev.* 43, 7594–7623. doi:10.1039/c3cs60414d

Lopez, G., Artexe, M., Amutio, M., Bilbao, J., and Olazar, M. (2017). Thermochemical routes for the valorization of waste polyolefinic plastics to produce fuels and chemicals. A review. *Renew. Sustain. Energy Rev.* 73, 346–368. doi:10.1016/j.rser.2017.01.142

Lutz, H., Buchele, M., Knaus, F., Reichhold, A., Vollenhofer, W., and Venderbosch, R. (2022). Wood derived fast pyrolysis bio-liquids as co-feed in a fluid catalytic cracking pilot plant: Effect of hydrotreatment on process performance and gasoline quality. *Energy and Fuels* 36 (17), 10243–10250. doi:10.1021/acs.energyfuels.2c01736

Magrini, K., Olstad, J., Peterson, B., Jackson, R., Parent, Y., Kukarakate, C., et al. (2022). Feedstock and catalyst impact on bio-oil production and FCC Co-processing to fuels. *Biomass Bioenergy* 163, 106502. doi:10.1016/j.biombioe.2022.106502

McLean, J. (2003). *Distributed matrix structures - a technology platform for advanced FCC catalyst solutions*. San Antonio, TX USA: NPRA.

Pinho, A. d. R., Almeida, M. B. d., Mendes, F. L., Casavechia, L. C., Talmadge, M. S., Kinchin, C. M., et al. (2017). Fast pyrolysis oil from pinewood chips co-processing with vacuum gas oil in an FCC unit for second generation fuel production. *Fuel* 188, 462–473. doi:10.1016/j.fuel.2016.10.032

Pyrum Innovations (2022). From end-of-life tyre to door handle: Pyrum, BASF and Mercedes-Benz close the recycling loop. Available at: https://www.pyrum.net/en/about-us/news/news-detail/news/vom-altreifen-zum-tuergriff-pyrum-basf-und-mercedes-benz-schliessen-wertstoffkreislauf/?tx_news_pi1%5Bcontroller%5D=News&tx_news_pi1%5Baction%5D=detail&cHash=f577f0d10d022c7b16c68ea1935274f4 [Accessed September 13, 2022].

Ragaert, K., Delva, L., and Geem, K. V. (2017). Mechanical and chemical recycling of solid plastic waste. *Waste Manag.* 69, 24–58. doi:10.1016/j.wasman.2017.07.044

Saebea, D., Ruengrit, P., Amornchai Arpornwichanop, Y. P., and Patcharavorachot, Y. (2020). Gasification of plastic waste for synthesis gas production. *Energy Rep.* 6 (1), 202–207. doi:10.1016/j.egyr.2019.08.043

Seiser, R., Olstad, J. L., Magrini, K. A., Jackson, R. D., Peterson, B. H., Christensen, E. D., et al. (2022). Co-processing catalytic fast pyrolysis oil in an FCC reactor. *Biomass bioenergy* 163, 106484. doi:10.1016/j.biombioe.2022.106484

Senter, C., Mastry, M. C., Zhang, C. C., Maximuck, W. J., Gladysz, J. A., and Yilmaz, B. (2021). Role of chlorides in reactivation of contaminant nickel on fluid catalytic cracking (FCC) catalysts. *Appl. Catal. A General* 611, 117978. doi:10.1016/j.apcata.2020.117978

Sheldon, R. A. (2014). Green and sustainable manufacture of chemicals from biomass: State of the art. *Green Chem.* 16 (3), 950–963. doi:10.1039/c3gc41935e

Shim, J.-W., Pyo, S., Lam, S. S., Jae, J., Jeon, B.-H., Khan, M. A., et al. (2022). Catalytic pyrolysis of chicken manure over various catalysts. *Fuel* 322, 124241. doi:10.1016/j.fuel.2022.124241

Sorum, L., Gronli, M. G., and Hustad, J. E. (2001). Pyrolysis characteristics and kinetics of municipal solid wastes. *Fuel* 80, 1217–1227. doi:10.1016/s0016-2361(00)00218-0

Tian, X., Han, S., Wang, K., Shan, T., Li, Z., Li, S., et al. (2022). Waste resource utilization: Spent FCC catalyst-based composite catalyst for waste tire pyrolysis. *Fuel* 328, 125236. doi:10.1016/j.fuel.2022.125236

Tuck, C. O., Perez, E., Horvath, I., Sheldon, R. A., and Poliakoff, M. (2012). Valorization of biomass: Deriving more value from waste. *Science* 337 (6095), 695–699. doi:10.1126/science.1218930

Wong, S. L., Ngadi, N., Abdullah, T. A. T., and Uniwa, I. M. (2015). Current state and future prospects of plastic waste as source of fuel: A review. *Renew. Sustain. Energy Rev.* 50, 1167–1180. doi:10.1016/j.rser.2015.04.063

frontiers | Frontiers in Chemistry

TYPE Original Research
PUBLISHED 24 February 2023
DOI 10.3389/fchem.2023.1137246

OPEN ACCESS

EDITED BY
Sining Yun,
Xi'an University of Architecture and Technology, China

REVIEWED BY
Kaixin Zhu,
Dalian Maritime University, China
Buzuayehu Abebe,
Adama Science and Technology University, Ethiopia

*CORRESPONDENCE
Libing Liao,
clayl@cugb.edu.cn

SPECIALTY SECTION
This article was submitted to Green and Sustainable Chemistry, a section of the journal Frontiers in Chemistry

RECEIVED 04 January 2023
ACCEPTED 16 February 2023
PUBLISHED 24 February 2023

CITATION
Li Y, Lv G, Liu H, Liu X and Liao L (2023), Improvement of magnetite adsorption performance for Pb (II) by introducing defects.
Front. Chem. 11:1137246.
doi: 10.3389/fchem.2023.1137246

Improvement of magnetite adsorption performance for Pb (II) by introducing defects

Yuxin Li[1], Guocheng Lv[1], Hao Liu[2], Xin Liu[1] and Libing Liao[1]*

[1]Engineering Research Center of Ministry of Education for Geological Carbon Storage and Low Carbon Utilization of Resources, Beijing Key Laboratory of Materials Utilization of Nonmetallic Minerals and Solid Wastes, National Laboratory of Mineral Materials, School of Material Sciences and Technology, China University of Geosciences (Beijing), Beijing, China, [2]School of Science, China University of Geosciences (Beijing), Beijing, China

Surface defect engineering is an efficient strategy to enhance the adsorption properties of materials. After calcination in argon, the adsorption capacity of natural magnetite to Pb (II) is significantly improved. The Rietveld refinement, Mössbauer spectrum, and XPS were used to prove the existence of oxygen and cation vacancies in the crystal structure of magnetite after calcination, and it is found that the vacancy content is linearly related to the adsorption amount of Pb (II). This indicates that the increase in the adsorption performance of magnetite after calcination is determined by the vacancy. The adsorption capacity increases from 8 to 26 mg/g when the calcination temperature reaches 700°C. The equilibrium adsorption process of Pb (II) on magnetite can be well fitted to the Langmuir model, and the kinetic adsorption followed a pseudo-second-order mechanism. The improvement of the adsorption performance of magnetite is mainly due to the change in its structure, which depends on the oxidation degree and surface effect of magnetite in the calcination process. This work also provides a theoretical basis for the broad application of magnetite as environmental material.

KEYWORDS

magnetite, adsorption, oxygen vacancy, cation vacancy, Pb (II)

1 Introduction

Magnetite crystallizes in the so-called inverse spinel structure (Space group, Fd3m). The chemical formula is often written as $[Fe^{3+}]_A$ $[Fe^{3+}, Fe^{2+}]_B$ O_4. This formulation shows that O atoms form a closed-packed cubic lattice, Fe^{3+} ions are located in the tetrahedral sites, and a 1:1 mixture of Fe^{2+} and Fe^{3+} ions fill the octahedral sites. The rapid electron hopping process occurs between Fe^{2+} and Fe^{3+} ions (Noh et al., 2015; Schöttner et al., 2019). Magnetite is a metal-deficient oxide with high electronic conductivity under high oxygen pressure (Castle and Surman, 1969; Nakamura A, et al., 1978). The self-diffusion coefficient of oxyanion is far less than that of cations. The non-stoichiometric feature of magnetite is the existence of cation vacancies in its structure. This is caused by the oxidation of Fe (II) at octahedral sites to Fe (III), which leads to an imbalance of charge, thus removing additional Fe (II) from the structure (Cervellino et al., 2014). The concentration of point defects in metal oxides is usually controlled by introducing a small number of foreign ions with different valences or changing the partial pressure of oxygen. (Nakamura et al., 1978). In binary oxide crystals, by introducing an appropriate external gas atmosphere, the defect concentration can be changed in a certain way. According to the reaction between oxygen and magnetite,

cation vacancy is formed (Becker and Litterst, 1990). With the increase in temperature, the distribution of cation vacancies will also change, which researchers have learned using the Mössbauer spectroscopy (Wiβmann et al., 1998). In the temperature range of 1,100°C–1,400°C, the shape of the spectral line is affected by the cation diffusion process. Also, the exact lattice parameters and stoichiometry of nano ferric oxide can be used to determine the vacancy distribution of magnetite by synchronous X-ray scattering and Debye function analysis (Cervellino et al., 2014). The results show a small number of vacancies at tetrahedral stations, which is at most 3%–4% of the total. When magnetite nanoparticles are oxidized, the cation diffusion comes from removing iron ions from the octahedral site.

The defects in magnetite are not only cationic vacancies but also oxygen vacancies (Castle and Surman, 1969; Millot and Niu, 1997). It is well known that oxygen vacancies usually exist in metal oxides, especially in the oxidation process of some variable valence metal oxides (Lv et al., 2011; Greiner et al., 2012; Choudhury et al., 2015). Oxygen will also diffuse in Fe_3O_4 and during the diffusion process, oxygen defects will be generated under low oxygen pressure, and cation and anion vacancy pairs will be developed under the condition of high oxygen pressure, namely, Schottky defects (Vaari, 2015). Under reducing conditions, the formation of oxygen vacancies on the surface leads to reduced iron nearby (Santos-Carballal et al., 2014). In fact, oxygen vacancies created by ultra-high vacuum annealing are likely to reduce ferric iron to divalent iron (Rioult et al., 2016).

Magnetite is a common component in soil and sediment and has high adsorption capacity for dissolved metal ions such as Pb (II) (Bargar et al., 2004). It is increasingly used in groundwater pollution and soil remediation (Filip et al., 2014). Its surface defects are widely regarded as the active site of the reaction process (Gorski et al., 2010; Li et al., 2014; Lesiak et al., 2019). Much adsorptive behavior between contaminant and adsorbent is strongly affected by surface defects (such as point defects and step edges) of the adsorbent (Li et al., 2015; Yong et al., 2021; Li et al., 2022). Although calcination will cause aggregation of some materials, this phenomenon usually occurs on nanoparticles (there are interactions between nanoparticles) (Ding et al., 2009), it can still be used to introduce defects in micron-scale materials to improve the reaction activity in this paper and avoid aggregation reaction. Bui et al. engineered Fe_3O_4 surface defects by doping 1% mol Cr without affecting the magnetic properties of Fe_3O_4, and experimental analysis showed that defect control significantly impacted the photocatalytic performance of Fe_3O_4, making them efficient photocatalysts (Bui et al., 2020). Kim S et al. calcined magnetite in a reducing atmosphere for the decomposition of CO_2 to effectively reduce CO_2 in the atmosphere. With the increase of reduction temperature, the number of defect sites on the sample surface increased, providing reaction sites for decomposing CO_2 (Kim et al., 2012).

There are abundant iron oxide minerals in nature, which have high adsorption and removal capacity of Pb (II) and affect the migration of Pb (II) on the Earth (Liang et al., 2017). Calcination is an effective strategy for introducing defects in the crystal structure (Nandi and Das, 2019; Li et al., 2020b), so we calcined magnetite in an inert atmosphere to improve the removal effect of magnetite on Pb (II) from water. In this work, we have done deep work with calcined magnetite in argon to study the changes in oxygen vacancy and iron vacancy. Natural magnetite was used as the precursor to obtain a mineral material with more defects to remove Pb (II) from water. The adsorption process was studied by equilibrium and kinetic adsorption experiments, and the effect of vacancies on adsorption capacity was invested.

2 Experimental details

2.1 Materials and reagents

The lead nitrate used in the experiment was purchased from Beijing Chemical Plant. A stock solution of Pb (II) was prepared by dissolving 1.599 g of solid Pb $(NO_3)_2$ (AR grade) in 1 L of deionized (DI) water. The natural magnetite was selected from Jinling Iron Mine in Zibo, Shandong Province. The sample was sieved through 200 mesh and then was prepared by magnetic separation to remove the impurities. And the obtained raw magnetite was named after Mag-25. After that, the obtained high-purity magnetite powder sample was calcined at 300°C, 500°C, 700°C, and 900°C in a tube furnace in argon at a heating rate of 5°C/min for 2 h and the samples were denoted as Mag-300, Mag-500, Mag-700, and Mag-900, respectively. All the chemicals used were analytical reagent grade without further purification, and DI water was used in all experiments.

2.2 Characterizations

The phase composition and crystal structure of the samples were affirmed by X-ray diffraction (XRD) on an X-ray powder diffractometer (D8 Advance, Bruker, Germany) with Cu $K\alpha 1$ (λ = 1.5406 Å) radiation at 40 kV and 100 mA, a scanning speed of 1.2° 2θ/min, and a step size of 0.02° 2θ from 5° to 130°. Scanning electron microscopy (SEM, ZEISS, sigma 300, Germany) was used to characterize the morphologies of the samples. X-Ray fluorescence spectrometer (XRF, Thermo electron corporation, ARLADVANT X, United States) was used to determine the chemical composition of the sample. The Brunauer-Emmet-Teller (BET) specific surface area was determined from N_2 adsorption-desorption isotherms using an automated gas sorption instrument (Micro Active for ASAP 2460, United States). The removal amount of Pb (II) was measured and calculated using an Inductively coupled plasma spectrometer (ICP-OES, Thermo scientific, iCAP 7,600, United States). The electron paramagnetic resonance (EPR) measurements were performed on a Bruker EMX plus model spectrometer operating at the X-band frequency (9.4 GHz) to investigate the oxygen vacancies at room temperature. The proportion of different valence elements in the sample was obtained by X-ray photoelectron spectroscopy (XPS, Thermo Scientific, ESCALab250, United States) test. The ^{57}Fe Mössbauer spectra were recorded on a SEE Co W_3O_4 Mössbauer spectrometer, using a^{57}Co/Rh source in transmission geometry. The data were fitted by using the MössWinn 4.0 software. The content of the different valent Fe was determined from the spectra.

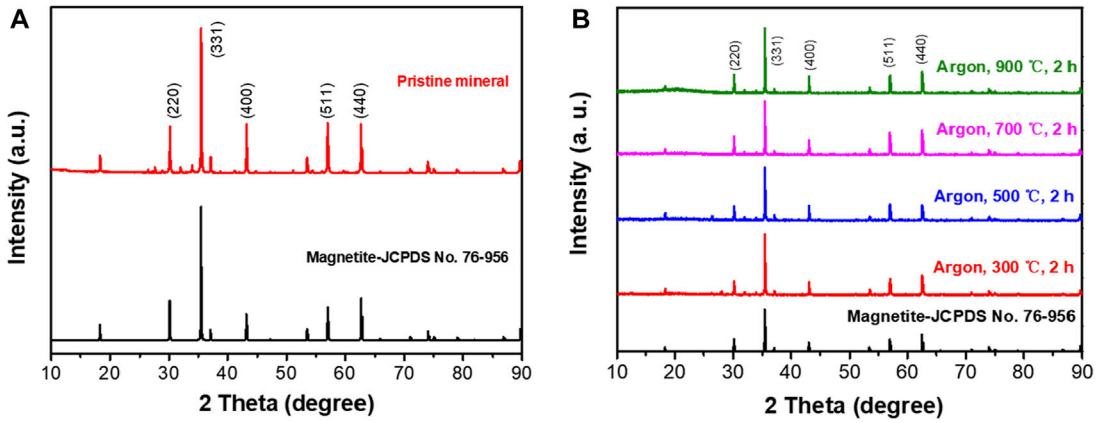

FIGURE 1
XRD patterns of magnetite ore **(A)** and its calcined products in argon atmosphere **(B)**.

TABLE 1 X-Ray Fluorescence results of pristine magnetite.

Element	Fe	O	Mg	Si	Al	C	Ca	Other
Result (mass%)	69.9	27.5	0.966	0.427	0.270	0.588	0.117	0.142

2.3 Removal of Pb^{2+}

Batch adsorption experiments were carried out to remove Pb (II) using magnetite and its calcined products by changing the initial Pb (II) concentration and contact time at a fixed amount of adsorbent dosage of 5 g/L. A mass of 0.1 g magnetite and a volume of 20 mL Pb (II) solutions were used in all batch experiments. They were mixed in 50 mL centrifuge tubes in duplicates for each condition. The stock solution was diluted to obtain the standard solution of concentrations 5, 10, 20, 40, 80, 120, 160, and 200 mg/L. The pH of the solution was adjusted to 5.5, which was consistent with the pH of the natural environment without precipitation. The mixture of adsorbent and solution was shaken on a reciprocal shaker at 150 rpm for 24 h. After being centrifuged for 10 min at 8,000 rpm, the suspension was analyzed for equilibrium Pb (II) concentration. With an initial Pb (II) concentration of 200 mg/L, the mixture was shaken on a reciprocal shaker at 150 rpm for 0.1, 0.5, 1, 2, 3, 6, 9, 12, and 18 h. The suspensions were then analyzed for equilibrium Pb (II) concentrations at these specific times. The residual Pb (II) concentration in the solution was determined with ICP.

3 Results and discussion

3.1 Characterization of magnetite and calcined products

The magnetite and its calcined products were analyzed by XRD, and the results are shown in Figure 1. The natural magnetite is mainly composed of Fe_3O_4 (Figure 1A), which is consistent with the diffraction pattern of Magnetite (JCPDS: 76-956). The content of each element in mineral materials was tested by XRF. The results were listed in Table 1, which were almost 97% iron oxide. It showed that the magnetite was of high purity, and some weak peaks not assigned in the XRD spectra might be caused by some very trace impurities in the raw ore, which were ignored in the experiment.

After calcination in argon, the XRD patterns are shown in Figure 1B. The product is still magnetite after calcined at 300°C, 500°C, 700°C and 900°C in Ar for 2 h, which has apparent characteristic diffraction peaks at 30.16°, 35.51°, 43.12°, 57.01° and 62.59°. All the diffraction peaks can be indexed to the standard pattern of magnetite, and no new substances were generated.

SEM analysis was carried out so as to explore the effect of heat treatment at different temperatures on the morphology of magnetite, and the pictures of natural magnetite and its calcined products in argon are shown in Figure 2. The information we can get from the figure is that the size of the untreated magnetite is mostly 1~5 μm, without any pores on the surface. As the calcination temperature increased in argon, the surface of the sample gradually changed, as shown in Figures 2C–F, which indicated the morphology of the samples at different temperatures.

As the temperature rised, some nano-pores are gradually formed on the surface of the mineral. At 300°C, the surface was still smooth without morphological changes; at 500°C, the surface had small deformation, and there were some tiny pits; at 700°C, the surface micropores gradually became larger; at 900°C, the surface melted and blocked the pores.

In general, the surface area of the adsorbent affected its adsorption performance, so the specific surface area of this series of materials was tested. As shown in Figure 3, the specific surface areas of Mag-25, Mag-300, Mag-500, Mag-700, and Mag-900 were 0.53, 0.52, 0.42, 0.57, and 0.28 $m^2 g^{-1}$, respectively. When the temperature is below 700°C, the specific surface area of the sample had no noticeable change. Once the temperature reaches 900°C, the specific surface area dropped sharply to 0.28, which was also consistent with the conclusion of SEM. High temperature resulted in the surface melting of magnetite, thus leading to the decrease of specific surface area.

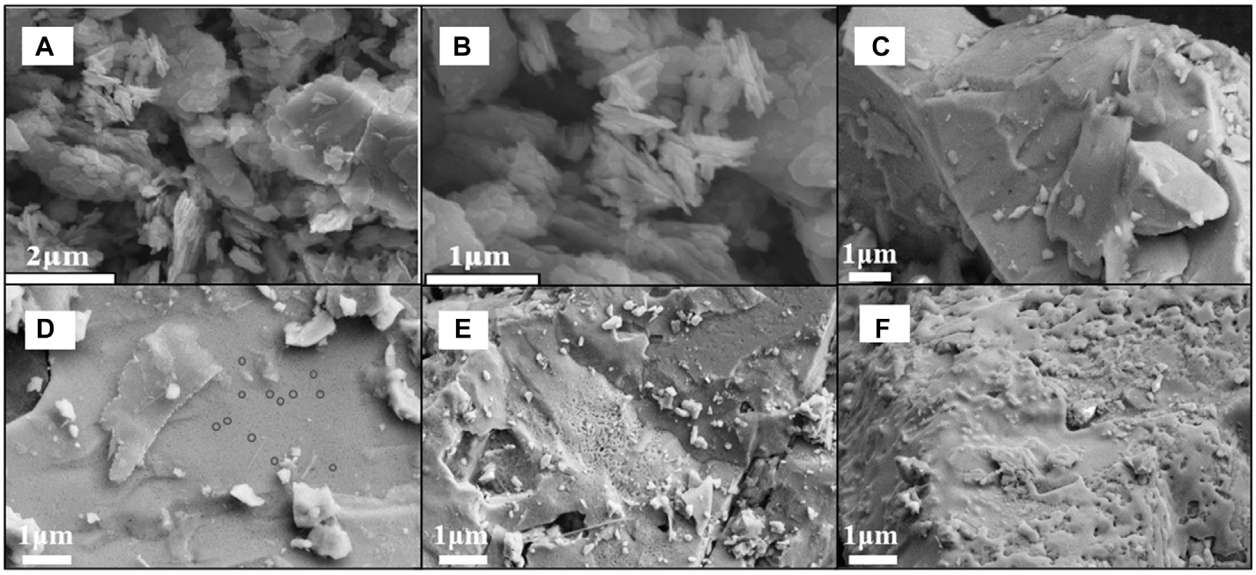

FIGURE 2
SEM images of magnetite **(A, B)** and its calcined products in argon at 300°C **(C)**, 500°C **(D)**, 700°C **(E)**, 900°C **(F)**.

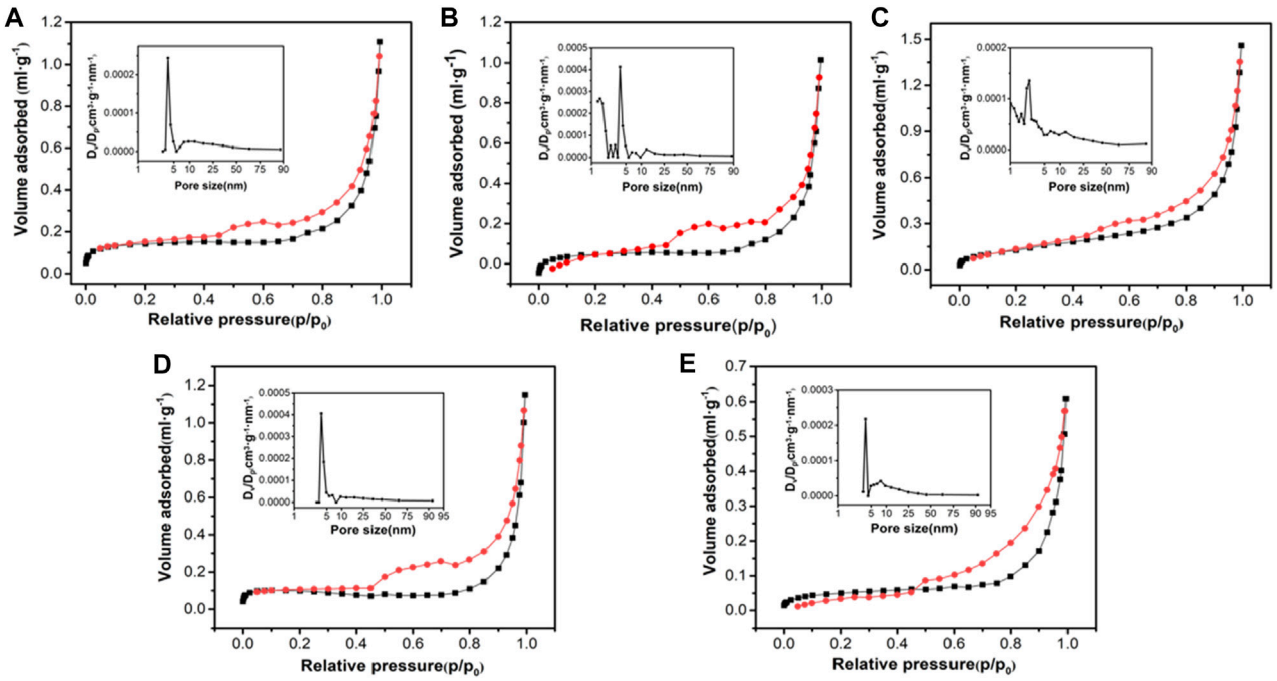

FIGURE 3
N_2 adsorption-desorption isotherms and pore size distribution curves of Mag-25 **(A)**, Mag-300 **(B)**, Mag-500 **(C)**, Mag-700 **(D)**, and Mag-900 **(E)**.

3.2 Adsorption isotherm

The raw magnetite had poor adsorption performance on Pb (II). The adsorption capacity was about 8 mg/g and accorded with the Langmuir adsorption model (Figure 4A). To improve its adsorption performance, the raw minerals were treated at different temperatures to obtain a series of samples. The effect of pH on Pb (II) adsorption was vital. The adsorption of Pb (II) onto magnetite was found to be enhanced as pH increased (Trivedi et al., 2003; Liang et al., 2017). This was because the

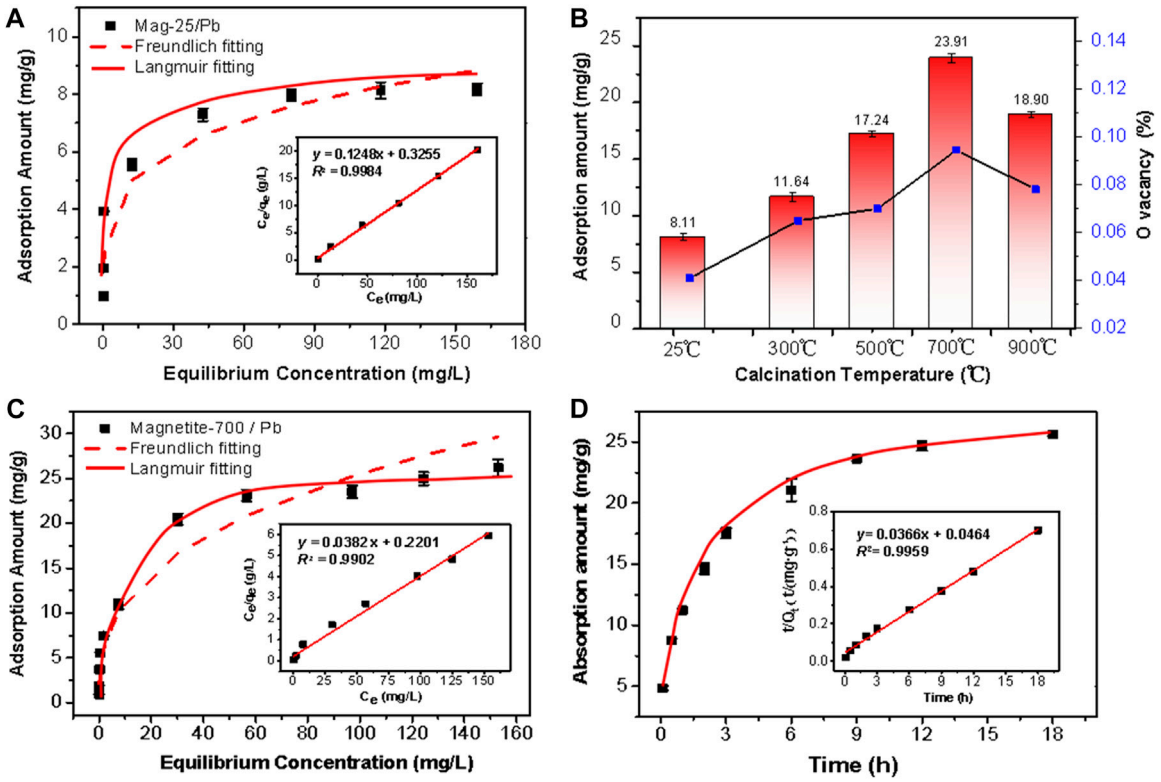

FIGURE 4
Pb(II) adsorption by **(A)** Mag-25, **(B)** magnetite at different calcination temperatures and the correlation with Oxygen vacancy, **(C)** Mag-700. The data were fitted to the Langmuir (solid line) and Freundlich (dashed line) isotherm models **(A, C)**. The insert is Langmuir adsorption isotherms model fitting. **(D)** Kinetics of Pb(II) adsorption by Mag-700 fitted to the pseudo-second-order kinetics (solid line). The insert is the linear plot of the pseudo-second-order reaction.

deprotonation of magnetite is promoted in alkaline solutions. Pb (II) adsorption onto magnetite was favored when the surface charge of the mineral was negative (Bradl, 2004; Mamindy et al., 2009). The initial concentration of Pb (II) was 200 mg/L, and the experiment was conducted at pH 5.5 to eliminate the impact of precipitation on the removal rate at a high pH (Karami, 2013). In Figure 4B, the adsorption capacity of Mag-25 was the lowest among the series of materials. As the increase in calcination temperature, the adsorption performance of the material was significantly improved and reached its highest when the calcination temperature reached 700°C. Subsequently, the adsorption performance of Mag-900 decreased slightly. (The correlation between adsorption capacity and oxygen vacancy content would be discussed in Section 3.4.3) Mag-700 was selected for the next adsorption experiment of Pb (II). The adsorption capacity and affinity of the adsorbent were obtained by adsorption isotherm. The amount of Pb (II) ion adsorbed per unit of adsorbent at equilibrium could be gained by isotherm study. Langmuir and Freundlich isotherm models were used to analyze the batch experimental data with initial Pb (II) concentrations ranging from 5 to 200 mg/L at pH ≈ 5.5.

The Langmuir isotherm applies to the monolayer adsorption sites on an energetically homogenous surface with a finite number of identical sites (Nemr et al., 2008). No further adsorption can occur once a site is occupied (Yuan et al., 2013). The Freundlich isotherm is an empirical equation describing a heterogeneous system (Qiu et al., 2015; Abebe et al., 2021). The linear forms of Langmuir and Freundlich isotherm models are described by Equations 1, 2:

$$\frac{C_e}{q_e} = \frac{1}{q_{max}b} + \left(\frac{1}{q_{max}}\right)C_e \quad (1)$$

$$ln\,q_e = ln\,K_f + \frac{1}{n}ln\,C_e \quad (2)$$

where C_e and q_e are the equilibrium concentration (mg/L), and the amount of Pb (II) adsorbed per Gram of adsorbent (mg/g), respectively. The q_{max} and b are the adsorption capacity of the adsorbent (mg/g) and the Langmuir affinity constant (L/mg) of the binding sites, respectively. K_f (mg/g) and n (g/L) are the empirical Freundlich constants representing the bond strength and the adsorption intensity of the heterogeneous surface. As can be seen from Table 2, the adsorption reaction was favorable as the n was

TABLE 2 Comparison of isotherm models of Pb (II) adsorption by Mag-700 at different concentrations.

T/K	Langmuir			Freundlich		
	q_{max}/mg g^{-1}	b	R^2	lnK_f	n	R^2
293	26.18	0.1735	0.9902	0.9215	2.61	0.9283

TABLE 3 Comparison of Pb (II) adsorption properties of magnetite in different references.

Adsorbent	Q_0 (mg/g)	Surface area (m^2/g)	pH	Concentration (mg/L)	Dosage (g/L)	References
Magnetite nanoparticles	22.9	115.3	5	0.5–5 (mmol/L)	10	Wang et al. (2010)
Magnetite nanoparticles	20.14	125.77	3.8	10–100	4	Wang et al. (2014)
Magnetite nanospheres	19	11.3	5	0–100	2	Kumari et al. (2015)
Magnetite	9.8	28	5	10–160	2	Liang et al. (2017)
Magnetite/kaolin granules	0.9	—	—	10–100	5	Lankathilaka et al. (2021)
Calcined magnetite	26.21	0.57	5.5	5–200	5	This work

TABLE 4 Comparison of kinetic parameters of Pb (II) adsorption onto Mag-700.

C_0 (mg/L)	$q_{e(exp)}$ (mg/g)	Pseudo-first-order kinetic model			Pseudo-second-order kinetic model		
		$q_{e(cal)}$ (mg/g)	K_1 (1/h)	R^2	$q_{e(cal)}$ (mg/g)	K_2 (g/mg/h)	R^2
200	26.21	27.20	0.378	0.9327	27.32	0.029	0.9959

2.61, which lied between 1 and 10 (Zhao et al., 2013). Besides the above findings, the experimental R^2 value (0.9902) of the Langmuir model was better (Figure 4C). The essential features of Langmuir isotherm can be expressed in terms of dimensionless constant known as separation factor or equilibrium parameter (R_L) using Eq. 3. The value of R_L between 0 and 1 indicates favorable adsorption; $R_L > 1$ indicates unfavorable adsorption; $R_L = 1$ represents the linear adsorption, and the adsorption operation is irreversible if $R_L = 0$ (Arulkumar et al., 2012).

$$R_L = \frac{1}{1 + bC_0} \tag{3}$$

where b (L/mg) and C_0 (mg/L) are the Langmuir affinity constant and initial concentration of Pb (II). Table 2 indicated the positive value of R_L is 0.03 and it is within 0 and 1. Thus, it indicated the adsorption was favorable and also feasible onto Mag-700.

Thus, a conclusion could be drawn that the adsorption of Pb (II) onto Mag-700 was not a multi-molecular adsorption process, and its equilibrium adsorption capacity was 26.21 mg/g. Compared with other magnetite materials, the adsorption performance of lead is even better than that of nanoparticle magnetite (Table 3) (Wang et al., 2010; Wang et al., 2014; Kumari et al., 2015; Liang et al., 2017; Lankathilaka et al., 2021). According to the adsorption and BET test results of the series of materials, the improvement of adsorption performance does not correlate with the specific surface area.

3.3 Adsorption kinetics

In the research field of solid-liquid adsorption, the pseudo-first-order (Lagergren, 1998) and pseudo-second-order kinetic models (Ho and McKay, 1999) are applied to the adsorption data obtained. The integral forms of these two models are expressed using the following Eqs 4, 5:

$$\ln(q_e - q_t) = ln\, q_e - k_1 t \tag{4}$$

$$\frac{t}{q_t} = \frac{1}{k_2 {q_e}^2} + \frac{1}{q_e} t \tag{5}$$

where q_e (mg/kg) is the amount of Pb (II) adsorbed at equilibrium, and q_t (mg/kg) is the amount of Pb (II) adsorbed on adsorbent at any time. k_1 (1/min) is the rate constant of the adsorption reaction. k_2 (g/mg/min) is the rate constant of the second-order reaction.

The kinetic model parameter values and regression coefficients (R^2) obtained from each kinetic plots (Figure 4D) are given in Table 4. The value of R^2 of the pseudo-second-order kinetic model was relatively higher (0.9959) than that of the pseudo-first-order model (0.9327). Therefore, the adsorption of Pb (II) onto Mag-700 could be described in terms of the pseudo-second-order kinetics. The adsorption equilibrium was reached after 9 h.

3.4 Mechanism

Ions diffuse in metal oxides through point defects. According to the vacancy mechanism, vacancies jump into neighboring lattice sites, and ions on the sites jump in reverse (Nakamura et al., 1978). The magnetite in this work is very likely to form such defects after high-temperature calcination, which may also be the reason for the improvement of adsorption performance. Therefore, XRF, EPR, Rietveld refinement, Mössbauer spectrum, and XPS were used to verify the adsorption mechanism of magnetite.

First, according to the XRF results in Table 1, more than 97% was iron oxide. In addition, there were trace impurities such as magnesium, silicon, and aluminum. However, in the crystal structure of magnetite, the Mg may replace some of the Fe^{2+}, given the relatively high magnesium content of the impurity. It thus affected its charge distribution, so the influence of magnesium was taken into account when calculating the chemical formula. Based on the atomic ratio of Fe, O, and Mg, the chemical formula of magnetite was determined as $Fe_{2.90}Mg_{0.09}O_4$ if there was no oxygen vacancy.

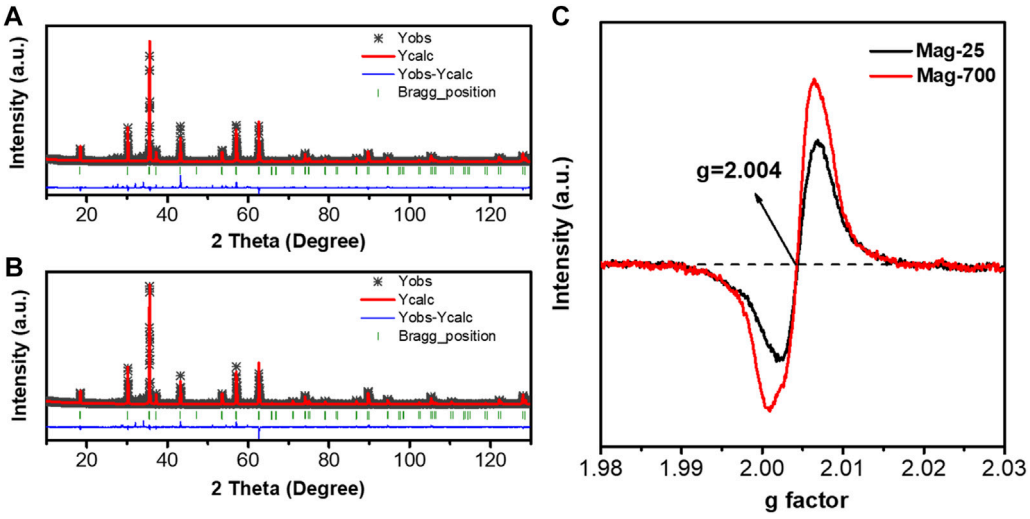

FIGURE 5
Rietveld refinement of the XRD patterns for **(A)** Mag-25; **(B)** Mag-700 and EPR spectra measured at room temperature **(C)**.

TABLE 5 Magnetite refinement parameters were obtained from the Rietveld refinement using X-ray powder diffraction data at room temperature.

Samples	Mag-25	Mag-700
Space group	Fd3m	Fd3m
Crystal system	Cubic	Cubic
a/b/c (nm)	8.397865 (55)	8.398043 (46)
α/β/γ	90°	90°
V (Å^3)	592.252 (12)	592.290 (10)
R-Bragg	8.18920665	6.85563089
R_{exp}	14.66	13.24
R_{wp}	4.81	5.10
R_p	10.07	8.78
χ^2	3.05	2.60

TABLE 6 The occupancy parameters of Mag-25 and Mag-700.

Samples	Occ-Fe (tet)	Occ-Fe (oct)	Occ-O	beq
Mag-25	1	0.995	0.987	14.66
Mag-700	0.986	1	0.978	13.24

3.4.1 Crystal structure

To further identify the occupancies of iron and oxygen elements in the crystal structure of magnetite, these two samples Mag-25 and Mag-700, were used for the XRD Rietveld refinement, performed using the TOPAS V7.11 package (Bruker, 2009). The structure model was acquired using the JCPDS No.76-956 card. Figures 5A, B show the Rietveld refinement of Mag-25 and Mag-700, where the black asterisk, solid red line, short green vertical line, and solid blue line in the bottom represent the XRD measurement data, the calculated pattern, the Bragg position, and the distinction between the observed and the calculated patterns, respectively. The refinement parameters for magnetite obtained from the Rietveld refinement are shown in Table 5. The final refinement was stable and convergent well with low residual factors R_p = 10.07%, χ^2 = 3.05 and R_p = 8.78%, χ^2 = 2.60, indicating no unidentified diffraction peaks due to impurity. The occupancies of Fe (oct) were almost constant, while the Fe (tet)'s declined obviously (Table 6). And the occupancies of O also declined from 0.987 to 0.978. The occupation fraction from Rietveld refinement illustrates that Fe cation vacancies in tetrahedrons and O vacancies are generated in Mag-700.

The single-featured EPR spectra have been identified as oxygen vacancy at g = 2.004 (Fan J, et al., 2020), so the EPR was applied to determine further the number of O vacancies in Mag-25 and Mag-700, which was shown in Figure 5C. The value of the free electron *g*-factor varies with the nature of the defect and the surroundings, and it is usually calculated using quantum electrodynamic methods (Lu D, et al., 2022). Only one type of signal (g = 2.004) was exhibited in Mag-25 and Mag-700 samples arising from the O vacancies. For Mag-25, the weak peak reflected a small number of vacancies. The signal for Mag-700 significantly intensified and showed 1.6 times that of mag-25, indicating elevated content of O vacancies in Mag-700.

3.4.2 Mössbauer spectroscopy

Also, the change of the occupation of Fe^{2+} and Fe^{3+} in magnetite needs to be confirmed to determine the structural formula of magnetite, so the Mössbauer spectrum tests were carried out for Mag-25 and Mag-700. The fitted spectra for the lowest and highest temperatures are shown in Figure 6, and the hyperfine parameters in the form are shown in Table 7.

10.3389/fchem.2023.1137246

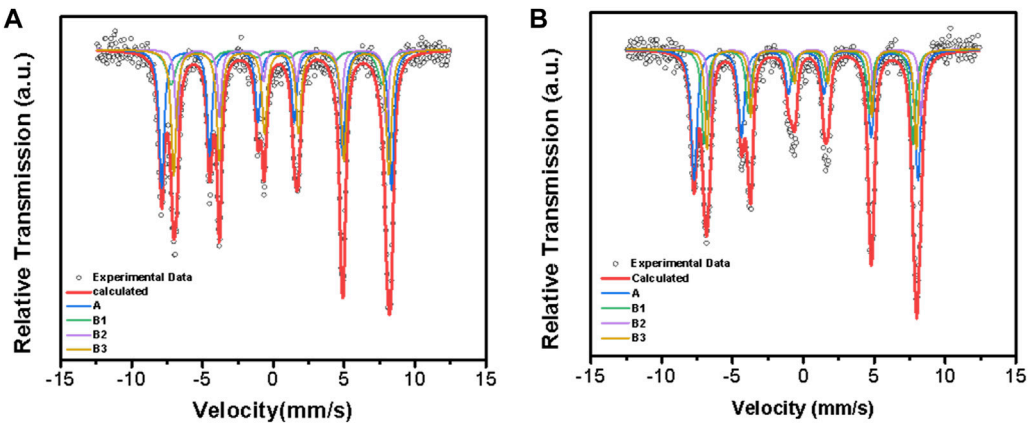

FIGURE 6
Room temperature Mössbauer spectra of Mag-25 **(A)** and Mag-700 **(B)**. The black circles stand for the experimental data, and the thick red line stands for the calculated data, Fe^{3+} **(A)** sextet is shown in blue, Fe^{3+} (B1), Fe^{2+} (B2) and Fe^{2+} (B3) sextets are shown in blue, green, purple and yellow, respectively.

TABLE 7 Parameters of the hyperfine structure.

Sample	Position	IS (mm/s)	QS (mm/s)	H (T)	Γ (mm/s)	Area (%)	Valence-state
Mag-25	A	0.21	0.03	50.40	0.42	38.5	$8\times Fe^{3+}$
	B1	0.11	0.26	46.36	0.81	28.7	$8\times Fe^{3+}$
	B2	0.54	0.11	45.96	0.33	11.1	$5\times Fe^{2+}$
	B3	0.57	−0.02	47.22	0.43	21.7	$3\times Fe^{2+}$
Mag-700	A	0.19	−0.03	49.12	0.48	36.9	$8\times Fe^{3+}$
	B1	0.38	−0.01	45.86	0.43	26.8	$8\times Fe^{3+}$
	B2	0.76	0.18	46.27	0.31	13.1	$5\times Fe^{2+}$
	B3	0.57	0.03	45.92	0.35	23.2	$3\times Fe^{2+}$

Note: IS, means isomer shift; QS, means quadrupole splitting, H stands for the hyperfine magnetic field, and Γ stands for line broadening.

The electron charge density of the iron nuclei is represented in the Mössbauer spectrum as an isomer shift relative to the metal bcc α-Fe as a reference substance. The nuclear charge densities of 8 non-equivalent A sites and 16 non-equivalent B sites can be determined by the calculation of DFT (Řezníček et al., 2015; Řezníček et al., 2017; Chlan et al., 2018). The four sextets correspond to the tetrahedral (A) sites and the octahedral (B) magnetic sublattice, and the spectral analysis was based on those considerations (Sorescu et al., 1998; Sorescu et al., 2003). The trimeron model adequately described the electronic structure and grouped the B sites in an 8:5:3 ratio (Senn et al., 2011; Řezníček et al., 2015). The first group contains Fe^{3+}-like ions, defined as B1, while the other groups are occupied by Fe^{2+}-like ions. C (Řezníček et al., 2017).

The area ratios of the four groups of lines A, B1, B2, and B3 represent the ratios of ions at different positions. There is a decrease in the proportion of the Fe^{3+} at positions A and B1 of the two materials before and after the calcination of magnetite while the area ratio of B2 and B3 increased, which shows that the content of Fe^{2+} in the sample is relatively increased after calcination at 700 °C. Since the oxidation and reduction of magnetite are carried out in the range of its non-stoichiometric composition, vacancies will also appear in the materials (Nakamura et al., 1978). The non-stoichiometric characteristics of magnetite are the presence of oxygen vacancy in the structure. This is due to the rearrangement of the internal Fe atoms. The proportion of Fe^{2+} in the octahedron increases, and the content of Fe^{3+} in the tetrahedron and octahedron decreases, resulting in an imbalance of charge that removes additional O atoms from the structure. From the ratio of Fe^{2+} to Fe^{3+} in the Mössbauer spectrum and the results of Rietveld refinement, the structural formulae of Mag-25 and Mag-700 can be written as $Fe^{3+}[Fe^{2+}_{0.951}Mg_{0.090}Fe^{3+}_{0.949}]O_{3.965}$ and $Fe^{3+}_{0.990}$ $[Fe^{2+}_{1.053}Mg_{0.090}Fe^{3+}_{0.857}]O_{3.914}$, respectively. It can be seen that there are oxygen vacancies in magnetite, which was consistent with Rietveld refinement results.

3.4.3 XPS analysis

XPS is considered a highly efficient and reliable method for determining the ratio of Fe^{2+} to Fe^{3+} on active surface atoms (Liu et al., 2016). In order to explore the reason why the adsorption effect of Mag-700 was stronger than that of raw magnetite, XPS analysis

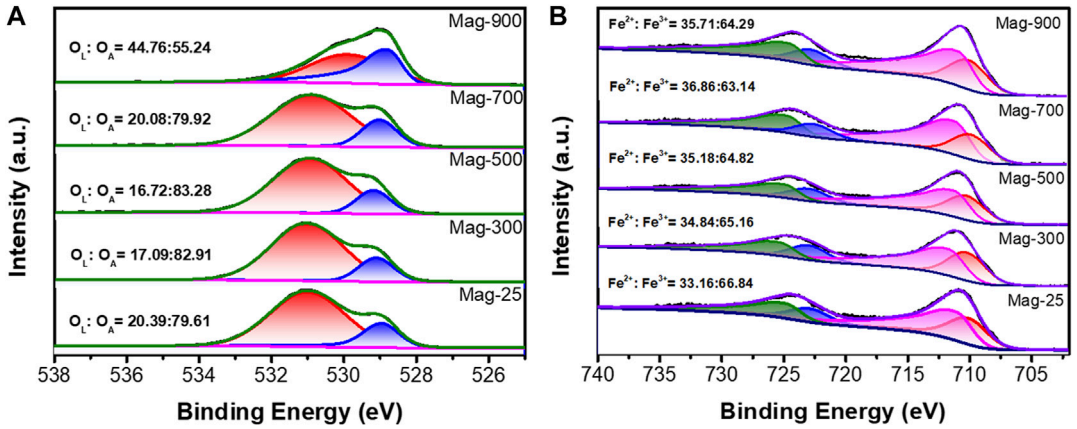

FIGURE 7
O 1s XPS spectra **(A)** and Fe 2p spectra **(B)** of magnetite at different temperatures.

TABLE 8 Related content of Fe^{2+} and Fe^{3+} in series materials and the given structural formulae.

Samples	Fe 2p 1/2 (eV)		Fe 2p 3/2 (eV)		Atom ratio Fe^{2+}/Fe^{3+}	Chemical formulae
	710	723	711.7	725.3		
Mag-25	24.25	8.91	43.49	23.35	33.16/66.84	$Fe^{2+}_{0.962}Fe^{3+}_{1.983}Mg^{2+}_{0.090}O_{3.959}$
Mag-300	24.63	10.21	47.63	17.54	34.84/65.16	$Fe^{2+}_{1.010}Fe^{3+}_{1.890}Mg^{2+}_{0.090}O_{3.935}$
Mag-500	24.87	40.34	12.87	21.90	35.18/64.82	$Fe^{2+}_{1.020}Fe^{3+}_{1.880}Mg^{2+}_{0.090}O_{3.930}$
Mag-700	24.52	12.37	46.89	16.30	36.86/63.14	$Fe^{2+}_{1.069}Fe^{3+}_{1.831}Mg^{2+}_{0.090}O_{3.9055}$
Mag-900	24.53	11.18	44.64	19.65	35.17/64.29	$Fe^{2+}_{1.036}Fe^{3+}_{1.864}Mg^{2+}_{0.090}O_{3.922}$

was carried out on raw magnetite and a series of materials calcined at different temperatures to study the effect of calcination in argon on the valence state of iron in the mineral.

Surface composition and valence states of O and Fe have been investigated by X-ray photoelectron spectroscopy, as shown in Figures 7A, B. The binding energy at 531.8 eV was attributed to surface adsorbed oxygen (O_A), and the photoelectron peak of the surface lattice oxygen (O_L) had binding energy at around 529 eV (Deng et al., 2016). The intensity of the O_L peak decreased to the minimum when the calcination temperature was up to 500 °C and then increased with the temperature further rising. In Mag-900, the ratio of O_L/O_A increased to 44.76/55.24. The increase in O_L peak intensity may be due to the oxygen vacancies caused by the high temperature (Chen et al., 2017). When the calcination temperature was above 700 °C, the relative content of lattice oxygen in the sample increased sharply, which may be caused by the release of the surface adsorbed oxygen at higher temperatures.

As shown in Figure 7B, Fe 2p3/2 of Fe_3O_4 has no satellite peak, and distinct two peaks of Fe2p with binding energies at 710.7 and 724.2 eV were assigned to spin-orbit peaks Fe 2p3/2 and Fe 2p1/2 of Fe_3O_4 respectively (Yamashita and Hayes, 2008; Farghali et al., 2015). The main peaks of Fe^{3+} 2p1/2 and Fe^{3+} 2p1/2 are located at 711.7 eV and 725.3 eV (Wang et al., 2017). Moreover, by fitting Fe 2p double peak, another two peaks yield at 710 eV and 724 eV, which belongs to Fe^{2+} 2p3/2 and Fe^{2+} 2p1/2 (Hou et al., 2016; Jia et al., 2018; Li et al., 2020a). The peak position does not shift significantly with the temperature change. When the temperature increases to 700°C, the proportion of Fe^{2+} increases from 33.16% to 36.86%, and the content of Fe^{3+} decreases by reducing to Fe^{2+}. However, its ratio decreases when the temperature rises to 900°C, and the oxidation reaction plays a dominant role.

In light of these results, it can be concluded that heating magnetite under an inert atmosphere will cause the appearance of oxygen vacancies, which leads to the increase of the proportion of Fe^{2+} to maintain the overall charge balance. However, the ratio of Fe^{2+} in the Mag-900 sample is abnormal, which may be due to the oxidation of the sample at a very high temperature. The total amount of Fe did not change according to Fe occupancy in Rietveld refinement. The chemical formula for the surface of magnetite can be obtained from the ratio of Fe^{2+}/Fe^{3+} in XPS. Table 8 shows that there are Fe and O vacancies in the pristine Mag-25, and the amount of O vacancies increased to a maximum in Mag-700, then decreased slightly in Mag-900. In the chemical formulae obtained from XPS results, the variation trend of oxygen vacancy content is consistent with the experimental results of Pb (II) removal (Figure 4B), indicating that oxygen vacancy plays a significant role in the adsorption reaction. In addition, the

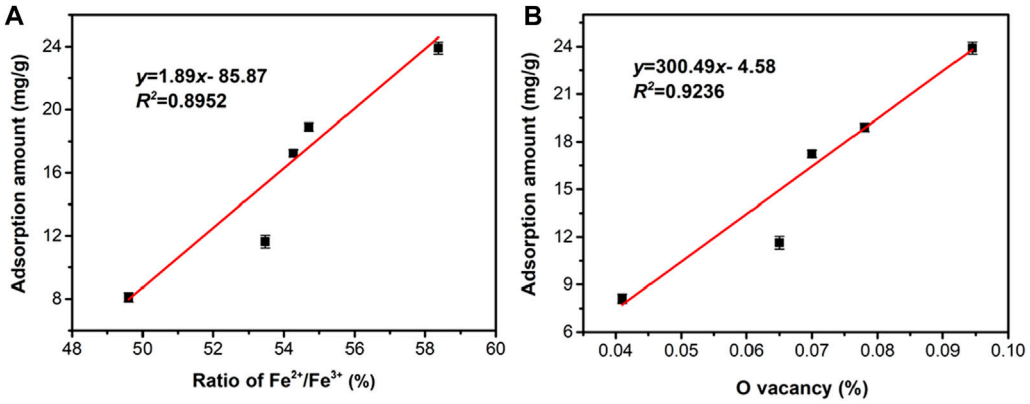

FIGURE 8
Correlation analysis of adsorption capacity with **(A)** proportion of Fe^{2+}; and **(B)** oxygen vacancy content in series magnetite.

adsorption amount of Pb (II) has a good correlation with the proportion of Fe^{2+} (Figure 8A) and the content of oxygen vacancy content (Figure 8B) in magnetite. The introduction of oxygen vacancy can be the result of the rearrangement of iron atoms, which directly improves the adsorption capacity of magnetite to Pb (II).

3.4.4 Surface complexes

The mechanism of magnetite adsorption for Pb (II) has been widely studied. It has been suggested that Pb (II) is adsorbed onto the surface of magnetite by electrostatic attraction and forms surface complexes with the functional group (≡FeOH) generated by the protonation and deportation reactions (Giraldo et al., 2013; Wang et al., 2014). However, according to the pH_{pzc} of the magnetite, magnetite is positively charged, and the adsorption of Pb (II) should not depend on electrostatic bonding, mainly through the complexation of Pb (II) with deprotonated surface hydroxyl groups. Pb (II) acts as Lewis acid while the functional surface hydroxyl group (≡FeOH) serves as the Lewis base in deprotonated form (≡FeO-) to bind the Lewis acid Pb (II) cation (Liang et al., 2014). Pb (II) ions were mainly adsorbed on the surface of magnetite by inner-sphere complexation, and the adsorbed Pb (II) species showed a bidentate binuclear corner-sharing geometry (Liang et al., 2017). The inner-sphere complexes are more stable than the outer-sphere complexes. This is because the former has the coordination covalent bonds as the main force, while the latter has an electrostatic bond as the dominant force. As Lewis basis, the hydroxyl group on the surface of magnetite is a critical functional group for adsorbing Pb (II). In this work, the calcined Mag-700 has more defects, especially cationic vacancies and oxygen vacancies, which makes the magnetite exposed more functional groups and more reactive active sites (Li et al., 2014; Ali et al., 2021), and increases the contact field between the surface of magnetite and Pb (II), which is the main reason for improving the adsorption performance of Pb (II).

4 Conclusion

In conclusion, calcination in argon effectively increases the oxygen vacancy content in the crystal structure of magnetite, which plays a vital role in improving the removal of Pb (II). The results show that, compared with natural magnetite, high temperature significantly influences the defect density and affinity for Pb (II) of magnetite under low oxygen pressure. The defect contents and structural formulae of the magnetite samples were determined successfully through Rietveld refinement and the ratio of Fe^{2+} and Fe^{3+}. In general, the defect degree of magnetite is linearly related to the removal capacity of Pb (II). Magnetite has a broad application prospect in wastewater remediation due to its simple defect engineering method, superior Pb (II) removal ability, rapid kinetics, and recyclability.

Data availability statement

The original contributions presented in the study are included in the article/supplementary material, further inquiries can be directed to the corresponding author.

Author contributions

YL carried out the experiment and wrote the manuscript. GL contributed to data analysis and discussed the mechanism. HL contributed to the software. XL contributed to the discussion of mechanism and proofread. LL supervised the experiment and proofread the manuscript.

Funding

This research was supported by National Natural Science Foundation of China (Grants 41831288).

Conflict of interest

The authors declare that the research was conducted in the absence of any commercial or financial relationships that could be construed as a potential conflict of interest.

Publisher's note

References

Abebe, B., Murthy, H. C., and Zereffa, E. A. (2021). Multifunctional application of PVA-aided Zn-Fe-Mn coupled oxide nanocomposite. *Nanoscale. Res. Lett.* 16 (1), 1–9. doi:10.1186/s11671-020-03464-0

Ali, S., Zuhra, Z., Abbas, Y., Shu, Y., Ahmad, M., and Wang, Z. (2021). Tailoring defect density in UiO-66 frameworks for enhanced Pb (II) adsorption. *Langmuir* 37 (46), 13602–13609. doi:10.1021/acs.langmuir.1c02032

Arulkumar, M., Thirumalai, K., Sathishkumar, P., and Palvannan, T. (2012). Rapid removal of chromium from aqueous solution using novel prawn shell activated carbon. *Chem. Eng. J.* 185, 178–186. doi:10.1016/j.cej.2012.01.071

Bargar, J. R., Trainor, T. P., Fitts, J. P., Chambers, S. A., and Brown, G. E. (2004). *In situ* grazing-incidence extended X-ray absorption fine structure study of Pb (II) chemisorption on hematite (0001) and (1-102) surfaces. *Langmuir* 20 (5), 1667–1673. doi:10.1021/la0354133

Becker, K., and Litterst, F. (1990). Mössbauer study of high-temperature diffusion in magnetite. *Hyperfine. Interact.* 56 (1), 1431–1435. doi:10.1007/bf02405453

Bradl, H. (2004). Adsorption of heavy metal ions on soils and soils constituents. *J. Colloid. Interface. Sci.* 277 (1), 1–18. doi:10.1016/j.jcis.2004.04.005

Bruker, A. (2009). *Topas V4. 2: General profile and structure analysis software for powder diffraction data*. Karlsruhe, Germany: Bruker AXS.

Bui, H., Im, S., Kim, K., Kim, W., and Lee, H. (2020). Photocatalytic degradation of phenolic compounds of defect engineered Fe_3O_4: An alternative approach to solar activation via ligand-to-metal charge transfer. *Appl. Surf. Sci.* 509, 144853. doi:10.1016/j.apsusc.2019.144853

Castle, J., and Surman, P. (1969). Self-diffusion of oxygen in magnetite. Effect of anion vacancy concentration and cation distribution. *J. Phys. Chem.* 73 (3), 632–634. doi:10.1021/j100723a025

Cervellino, A., Frison, R., Cernuto, G., Guagliardi, A., and Masciocchi, N. (2014). Lattice parameters and site occupancy factors of magnetite-maghemite core-shell nanoparticles. A critical study. *J. Appl. Crystallogr.* 47 (5), 1755–1761. doi:10.1107/s1600576714019840

Chen, D., He, D., Lu, J., Zhong, L., Liu, F., Liu, J., et al. (2017). Investigation of the role of surface lattice oxygen and bulk lattice oxygen migration of cerium-based oxygen carriers: XPS and designed H_2-TPR characterization. *Appl. Cata. B Environ.* 218, 249–259. doi:10.1016/j.apcatb.2017.06.053

Chlan, V., Żukrowski, J., Bosak, A., Kąkol, Z., Kozłowski, A., Tarnawski, Z., et al. (2018). Effect of low Zn doping on the verwey transition in magnetite single crystals: Mössbauer spectroscopy and X-ray diffraction. *Phys. Rev. B* 98, 125138125138–125138. doi:10.1103/physrevb.98.125138

Choudhury, B., Chetri, P., and Choudhury, A. (2015). Annealing temperature and oxygen-vacancy-dependent variation of lattice strain, band gap and luminescence properties of CeO_2 nanoparticles. *J. Exp. Nanosci.* 10 (2), 103–114. doi:10.1080/17458080.2013.801566

Deng, W., Dai, Q., Lao, Y., Shi, B., and Wang, X. (2016). Low temperature catalytic combustion of 1, 2-dichlorobenzene over CeO_2-TiO_2 mixed oxide catalysts. *Appl. Cata. B Environ.* 181, 848–861. doi:10.1016/j.apcatb.2015.07.053

Ding, P., Orwa, M. G., and Pacek, A. W. (2009). De-agglomeration of hydrophobic and hydrophilic silica nano-powders in a high shear mixer. *Powder. Technol.* 195 (3), 221–226. doi:10.1016/j.powtec.2009.06.003

Fan, J., Zuo, M., Ding, Z., Zhao, Z., Liu, J., and Sun, B. (2020). A readily synthesis of oxygen vacancy-induced in $(OH)_3$/carbon nitride 0D/2D heterojunction for enhanced visible-light-driven nitrogen fixation. *Chem. Eng. J.* 396, 125263. doi:10.1016/j.cej.2020.125263

Farghali, M., El-Din, T., Al-Enizi, A., and El Bahnasawy, R. (2015). Graphene/magnetite nanocomposite for potential environmental application. *Int. J.* Electrochem. Sci. 10, 529–537.

Filip, J., Karlický, F., Marusõák, Z., Lazar, P., Cernik, M., Otyepka, M., et al. (2014). Anaerobic reaction of nanoscale zerovalent iron with water: Mechanism and kinetics. *J. Phys. Chem. C* 118 (25), 13817–13825. doi:10.1021/jp501846f

Giraldo, L., Erto, A., and Moreno-Piraján, J. (2013). Magnetite nanoparticles for removal of heavy metals from aqueous solutions: Synthesis and characterization. *Adsorption* 19 (2), 465–474. doi:10.1007/s10450-012-9468-1

Gorski, C., Nurmi, J., Tratnyek, P., Hofstetter, T., and Scherer, M. (2010). Redox behavior of magnetite: Implications for contaminant reduction. *Environ. Sci. Technol.* 44, 55–60. doi:10.1021/es9016848

Greiner, M., Chai, L., Helander, M., Tang, W. M., and Lu, Z. H. (2012). Transition metal oxide work functions: The influence of cation oxidation state and oxygen vacancies. *Adv. Funct. Mat.* 22 (21), 4557–4568. doi:10.1002/adfm.201200615

Ho, Y., and McKay, G. (1999). Pseudo-second order model for sorption processes. *Process. Biochem.* 34, 451–465. doi:10.1016/s0032-9592(98)00112-5

Hou, L., Wang, L., Royer, S., and Zhang, H. (2016). Ultrasound-assisted heterogeneous Fenton-like degradation of tetracycline over a magnetite catalyst. *J. Hazard. Mat.* 302, 458–467. doi:10.1016/j.jhazmat.2015.09.033

Jia, D., Sun, S., Wu, Z., Wang, N., Jin, Y., Dong, W., et al. (2018). TCE degradation in groundwater by chelators-assisted fenton-like reaction of magnetite: Sand columns demonstration. *J. Hazard. Mat.* 346, 124–132. doi:10.1016/j.jhazmat.2017.12.031

Karami, H. (2013). Heavy metal removal from water by magnetite nanorods. *Chem. Eng. J.* 219, 209–216. doi:10.1016/j.cej.2013.01.022

Kim, S., Lee, S., and Hong, S. (2012). A study on the reaction characteristics of CO_2 decomposition using iron oxides. *J. Ind. Eng. Chem.* 18 (2), 860–864. doi:10.1016/j.jiec.2011.11.141

Kumari, M., Pittman, C. U., Jr, and Mohan, D. (2015). Heavy metals [chromium (VI) and lead (II)] removal from water using mesoporous magnetite (Fe_3O_4) nanospheres. *J. Colloid. Interface. Sci.* 442, 120–132. doi:10.1016/j.jcis.2014.09.012

Lagergren, S. (1998). About the theory of so-called adsorption of solution substances. *K. Sven. Vetenskapsaka-demiens Handl. Band.* 24, 1–39.

Lankathilaka, K., de Silva, R., Mantilaka, M., and de Silva, K. N. (2021). Magnetite nanoparticles incorporated porous kaolin as a superior heavy metal sorbent for water purification. *Groundw. Sustain. Dev.* 14, 100606. doi:10.1016/j.gsd.2021.100606

Lesiak, B., Rangam, N., Jiricek, P., Gordeev, I., Toth, J., Kover, L., et al. (2019). Surface study of Fe_3O_4 nanoparticles functionalized with biocompatible adsorbed molecules. *Front. Chem.* 7, 642. doi:10.3389/fchem.2019.00642

Li, H., Li, R., Niu, J., Gan, K., and He, X. (2022). Defect chemistry of electrocatalysts for CO_2 reduction. *Front. Chem.* 10, 1067327. doi:10.3389/fchem.2022.1067327

Li, J., Chen, C., Zhang, S., and Wang, X. (2014). Surface functional groups and defects on carbon nanotubes affect adsorption-desorption hysteresis of metal cations and oxoanions in water. *Environ. Sci. Nano.* 1 (5), 488–495. doi:10.1039/c4en00044g

Li, X., Cui, K., Guo, Z., Yang, T., Cao, Y., Xiang, Y., et al. (2020a). Heterogeneous Fenton-like degradation of tetracyclines using porous magnetic chitosan microspheres as an efficient catalyst compared with two preparation methods. *Chem. Eng. J.* 379, 122324. doi:10.1016/j.cej.2019.122324

Li, X., Li, H., and Yang, G. (2015). Promoting the adsorption of metal ions on kaolinite by defect sites: A molecular dynamics study. *Sci. Rep.* 5 (1), 14377–14413. doi:10.1038/srep14377

Li, X., Zhao, J., Hong, X., Yang, Y., Tang, X., Zhu, Y., et al. (2020b). Calcination-dependent surface defect variation and antibacterial activity of magnesium oxide nanoplates. *ChemistrySelect* 5 (11), 3201–3207. doi:10.1002/slct.201904853

Liang, X., He, Z., Wei, G., Liu, P., and Zhong, Y. (2014). The distinct effects of Mn substitution on the reactivity of magnetite in heterogeneous Fenton reaction and Pb (II) adsorption. *J. Colloid. Inter. Sci.* 181-189.

Liang, X., Wei, G., Xiong, J., Tan, F., He, H., Qu, C., et al. (2017). Adsorption isotherm, mechanism, and geometry of Pb (II) on magnetites substituted with transition metals. *Chem. Geo.* 470, 132–140. doi:10.1016/j.chemgeo.2017.09.003

Liu, H., Wei, G., Xu, Z., Liu, P., and Li, Y. (2016). Quantitative analysis of Fe and Co in Co-substituted magnetite using XPS: The application of non-linear least squares fitting (NLLSF). *Appl. Surf. Sci.* 389, 438–446. doi:10.1016/j.apsusc.2016.07.146

Lv, K., Xiang, Q., and Yu, J. (2011). Effect of calcination temperature on morphology and photocatalytic activity of anatase TiO_2 nanosheets with exposed {0 0 1} facets. *Appl. Catal. B* 104 (3-4), 275–281. doi:10.1016/j.apcatb.2011.03.019

Mamindy, P., Hurel, C., Marmier, N., and Romeo, M. (2009). Arsenic adsorption onto hematite and goethite. *C R. Chim.* 12 (8), 876–881. doi:10.1016/j.crci.2008.10.012

Millot, F., and Niu, Y. (1997). Diffusion of O^{18} in Fe_3O_4: An experimental approach to study the behavior of minority defects in oxides. *J. Phys. Chem. Solids* 58 (1), 63–72. doi:10.1016/s0022-3697(96)00101-1

Nakamura, A., Yamauchi, S., Fueki, K., and Mukaibo, T. (1978). Vacancy diffusion in magnetite. *J. Phys. Chem. Solids.* 39 (11), 1203–1206. doi:10.1016/0022-3697(78)90097-5

Nandi, P., and Das, D. (2019). Photocatalytic degradation of Rhodamine-B dye by stable ZnO nanostructures with different calcination temperature induced defects. *Appl. Surf. Sci.* 465, 546–556. doi:10.1016/j.apsusc.2018.09.193

Nemr, A., Khaled, A., Abdelwahab, O., and El-Sikaily, A. (2008). Treatment of wastewater containing toxic chromium using new activated carbon developed from date palm seed. *J. Hazard. Mat.* 152, 263–275. doi:10.1016/j.jhazmat.2007.06.091

Noh, J., Osman, O., Aziz, S., Winget, P., and Bredas, J. L. (2015). Magnetite Fe_3O_4 (111) surfaces: Impact of defects on structure, stability, and electronic properties. *Chem. Mat.* 27 (17), 5856–5867. doi:10.1021/acs.chemmater.5b02885

Qiu, B., Xu, C., Sun, D., Wang, Q., Gu, H., Zhang, X., et al. (2015). Polyaniline coating with various substrates for hexavalent chromium removal. *Appl. Surf.* 334, 7–14. doi:10.1016/j.apsusc.2014.07.039

Řezníček, R., Chlan, V., Štěpánková, H., and Novák, P. (2015). Hyperfine field and electronic structure of magnetite below the Verwey transition. *Phys. Rev. B* 91, 125134. doi:10.1103/physrevb.91.125134

Řezníček, R., Chlan, V., Stepankova, H., Novak, R., Zukrowski, J., Kozlowski, A., et al. (2017). Understanding the mössbauer spectrum of magnetite below the verwey transition: *Ab initio* calculations, simulation, and experiment. *Phys. Rev. B* 96, 195124. doi:10.1103/physrevb.96.195124

Rioult, M., Stanescu, D., Fonda, E., Barbier, A., and Magnan, H. (2016). Oxygen vacancies engineering of iron oxides films for solar water splitting. *J. Phys. Chem. C* 120 (14), 7482–7490. doi:10.1021/acs.jpcc.6b00552

Santos-Carballal, D., Roldan, A., Grau-Crespo, R., and de Leeuw, N. H. (2014). A DFT study of the structures, stabilities and redox behaviour of the major surfaces of magnetite Fe_3O_4. *Phys. Chem. Chem. Phys.* 16 (39), 21082–21097. doi:10.1039/c4cp00529e

Schöttner, L., Nefedov, A., Yang, C., Heissler, S., Wang, Y., and Woll, C. (2019). Structural evolution of α-Fe_2O_3 (0001) surfaces under reduction conditions monitored by infrared spectroscopy. *Front. Chem.* 7, 451. doi:10.3389/fchem.2019.00451

Senn, M., Wright, J., and Attfield, J. (2011). Charge order and three-site distortions in the Verwey structure of magnetite. *Nature* 481, 173–176. doi:10.1038/nature10704

Sorescu, M., Mihaila-Tarabasanu, D., and Diamandescu, L. (1998). Mössbauer and magnetic study of substituted magnetites. *Appl. Phys. Lett.* 72 (16), 2047–2049. doi:10.1063/1.121260

Sorescu, M., Tarabasanu-Mihaila, D., and Diamandescu, L. (2003). A Mössbauer study of manganese-doped magnetite. *Mat. Lett.* 57, 1867–1869. doi:10.1016/s0167-577x(02)01092-3

Trivedi, P., Dyer, J. A., and Sparks, D. L. (2003). Lead sorption onto ferrihydrite. 1. A macroscopic and spectroscopic assessment. *Environ. Sci. Technol.* 37 (5), 908–914. doi:10.1021/es0257927

Vaari, J. (2015). Molecular dynamics simulations of vacancy diffusion in chromium (III) oxide, hematite, magnetite and chromite. *Solid. State. Ionics* 270, 10–17. doi:10.1016/j.ssi.2014.11.027

Wang, F., Li, M., Yu, L., Sun, F., Wang, Z., Zhang, L., et al. (2017). Corn-like, recoverable γ-Fe_2O_3@ SiO_2@ TiO_2 photocatalyst induced by magnetic dipole interactions. *Sci. Rep.* 7 (1), 6960. doi:10.1038/s41598-017-07417-z

Wang, T., Jin, X., Chen, Z., Megharaj, M., and Naidu, R. (2014). Simultaneous removal of Pb (II) and Cr (III) by magnetite nanoparticles using various synthesis conditions. *J. Ind. Eng. Chem.* 20, 3543–3549. doi:10.1016/j.jiec.2013.12.047

Wang, X., Lu, H., Zhu, L., Liu, F., and Ren, J. J. (2010). Adsorption of lead (II) ions onto magnetite nanoparticles. *Adsorpt. Sci. Technol.* 28 (5), 407–417. doi:10.1260/0263-6174.28.5.407

Wiβmann, S., Wurmb, V. V., Litterst, F. J., Dieckmann, R., and Becker, K. (1998). The temperature-dependent cation distribution in magnetite. *J. Phys. Chem. Solids.* 59 (3), 321–330. doi:10.1016/s0022-3697(97)00219-9

Yamashita, T., and Hayes, P. (2008). Analysis of XPS spectra of Fe^{2+} and Fe^{3+} ions in oxide materials. *Appl. Surf. Sci.* 254, 2441–2449. doi:10.1016/j.apsusc.2007.09.063

Yong, X., Zhang, J., Ma, X., and He, W. (2021). Efficient N_2-and O_2-sensing properties of $PtSe_2$ with proper intrinsic defects. *Front. Chem.* 9, 676438. doi:10.3389/fchem.2021.676438

Yuan, X., Wang, Y., Wang, J., Zhou, C., Tang, Q., and Rao, X. (2013). Calcined graphene/MgAl-layered double hydroxides for enhanced Cr (VI) removal. *Chem. Eng. J.* 221, 204–213. doi:10.1016/j.cej.2013.01.090

Zhao, Y., Yang, S., Ding, D., Chen, J., Zhang, Z., Lei, Z., et al. (2013). Effective adsorption of Cr (VI) from aqueous solution using natural Akadama clay. *J. Colloid. Interface. Sci.* 395, 198–204. doi:10.1016/j.jcis.2012.12.054

frontiers | Frontiers in Chemistry

TYPE Original Research
PUBLISHED 21 July 2023
DOI 10.3389/fchem.2023.1239479

OPEN ACCESS

EDITED BY
Florent Allais,
AgroParisTech Institut des Sciences et Industries du Vivant et de L'environment, France

REVIEWED BY
Stephane Grelier,
Université de Bordeaux, France
Kalavathy Rajan,
The University of Tennessee, United States

*CORRESPONDENCE
Paul-Henri Ducrot,
paul-henri.ducrot@inrae.fr

RECEIVED 13 June 2023
ACCEPTED 12 July 2023
PUBLISHED 21 July 2023

CITATION
Sarieddine A, Hadjiefstathiou C, Majira A, Pion F and Ducrot P-H (2023), Biocatalytic selective acylation of technical lignins: a new route for the design of new biobased additives for industrial formulations.
Front. Chem. 11:1239479.
doi: 10.3389/fchem.2023.1239479

Biocatalytic selective acylation of technical lignins: a new route for the design of new biobased additives for industrial formulations

Aya Sarieddine[1,2], Caroline Hadjiefstathiou[1,3], Amel Majira[1], Florian Pion[1] and Paul-Henri Ducrot[1]*

[1]Université Paris-Saclay, Institut national de la recherche agronomique, AgroParisTech, Institut Jean-Pierre Bourgin (IJPB), Versailles, France, [2]FARE Laboratory, Institut national de la recherche agronomique, Université de Reims Champagne Ardenne, Reims, France, [3]URCOM Laboratory, Université Le Havre Normandie, Le Havre, France

In this article, we describe a proof of concept of the potential use of a biocatalytic process for the functionalization of technical soda lignins from wheat straw through the selective acylation of primary hydroxy groups of lignin oligomers by acetate or hexanoate, thus preserving their free, unreacted phenols. The selectivity and efficiency of the method, although they depend on the structural complexity of the starting material, have been proven on model compounds. Applied to technical lignins, the acylation yield is only moderate, due to structural and chemical features induced by the industrial mode of preparation of the lignins rather than to the lack of efficiency of the method. However, most of the physicochemical properties of the lignins, including their antioxidant potential, are preserved, advocating the potential use of these modified lignins for industrial applications.

KEYWORDS

soda technical lignins, *Candida antarctica* lipase B, selective acylation, lipophilisation, transmethylation

1 Introduction

Due to the expected gradual depletion of fossil resources, industries have turned to the introduction of polymers, cosmetics, pure natural compounds, or mixtures resulting from the fractionation of the biomass into their formulations. For applications with high added values, the strong consumer demand for environmentally friendly processes and formulations, and a wish for naturalness in commonly used compounds, especially for cosmetics, have strongly stimulated research efforts. Among these compounds and beside secondary metabolites (Vaishnav and Demain, 2011), polysaccharide fractions have received much attention from researchers due to their homogeneity in terms of physicochemical properties and chemical reactivity (Benna-Zayani et al., 2008; Bouyer et al., 2012; Robertson et al., 2017; Arca et al., 2018; Yu et al., 2018). Therefore, industries involved in biomass fractionation have mostly favored "polysaccharides first" biorefinery processes.

Regrettably, due to the research of optimized polysaccharide or secondary metabolite recovery yields, biomass fractionation processes mostly involve drastic acidic or basic treatments with or without sulfur-containing reagents. Other components of the biomass

may be strongly modified structurally, thus highly degrading their chemical structure and their main physicochemical properties of interest. For instance, this is the case with lignins (Sharma et al., 2020; Yao et al., 2022), which represent the major biopolymer in vertical terrestrial plants after cellulose (Ralph et al., 2004). These heterogeneous assemblies of polyphenolic oligomers result in plants from the oxidative coupling of *p*-hydroxy cinnamic alcohols (mainly coniferyl and sinapyl alcohols) and acids (Figure 1) (Liu et al., 2018; Sternberg et al., 2021). Thanks to this unique polyphenolic structure, they exhibit protective properties (such as antioxidant, antimicrobial, and anti-UV) and thus play the role of defensive barriers in plants.

The main treatments of lignocellulosic biomass for polysaccharide recovery and lignin residue availability at an industrial scale for further applications are the Kraft (Chakar and Ragauskas, 2004; Gellerstedt, 2015), bisulfite (Duval et al., 2013; Miles-Barrett et al., 2017), soda (Takada et al., 2020), and organosolv (de la Torre et al., 2013) treatments, which at the end of the process all involve an acidic treatment for the recovery of lignins through precipitation. Thus, large amounts of lignins are produced from paper industries and emerging cellulosic 2G bioethanol industries every year. More than 50 million tons of lignins are produced each year by pulp and paper industries alone (Bezerra and Ragauskas, 2016; Maldhure and Ekhe, 2017; Robertson et al., 2017), and up to now, lignins were considered more as a residue than as a valuable material, and were mainly burned to produce energy because of their high calorific power (Zakzeski et al., 2010; Chen et al., 2017).

In order to complete the biorefinery concept by valorizing all the biomass fractions, the resulting lignins must now be considered as potential candidates for industrial chemical applications. With this aim in mind, low-added value applications such as a filler in asphalt (Wu et al., 2021), additive for mineral wool (Allais et al., 2016; Lucia et al., 2020), and board binders (Gravitis et al., 2010) have emerged. Nevertheless, higher added value applications such as in carbon fibers or as antioxidant additives in polymers and cosmetic formulations have to be explored for technical lignins, which have already shown antioxidant (Pouteau et al., 2003; Vinardell et al., 2008; Ponomarenko et al., 2015; Majira et al., 2019), antimicrobial (Alzagameem et al., 2019; Cresnar et al., 2022), and emulsion stabilizing properties (Czaikoski et al., 2020). For these later applications, incorporation of lignins into most of the usual polymer matrices still faces constraints due to their heterogeneous and complex structure and poor miscibility in apolar matrices, where they show a tendency to form aggregates (Lora and Glasser, 2002; Zhang et al., 2015; Romhányi et al., 2018; Dias et al., 2019). To overcome these problems, it seems that chemical modification of the lignin structure remains the best solution. Degradative depolymerization of lignin has been intensively investigated in past decades (Weng et al., 2021; Roy et al., 2022; Zhou et al., 2022) but requires, whatever the conditions used, final separative processes to recover pure fractions (or, at least, homogeneous in terms of molar mass). Alternatively, another route to minimize their heterogeneity can be solvent fractionation (Majira et al., 2019; Zhou et al., 2022). Some of our previous articles highlighted the potential of phenolic compounds or phenolic fractions derived from lignins

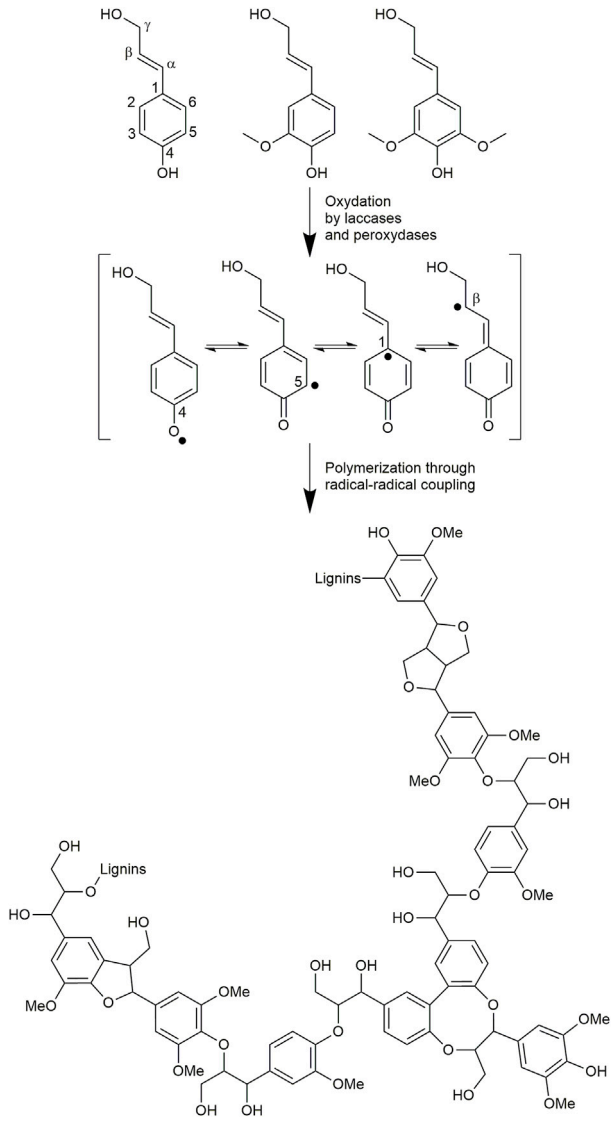

FIGURE 1
p-Hydroxy cinnamic alcohols involved in lignins biosynthesis and putative structure of the resulting biopolymer.

constituents as antioxidants (Reano et al., 2016) or as building blocks for polymer chemistry (Pion et al., 2013), and also reported the design of innovative processes for the transformation of technical lignins from various botanical sources and diverse industrial separation processes into valuable fractions (Thierry et al., 2018; Majira et al., 2019; Lu et al., 2021; Jin et al., 2022). In addition, direct modification of lignins to tune their properties may be also a promising pathway, taking into account their valuable chemical functionalities. One example is the acylation of lignin hydroxy groups in order to increase their lipophilicity. Chemical acylation processes in the presence of base catalysts such as 4-dimethyl amino pyridine (DMAP) (Zhao et al., 2017) lead to the formation of byproducts such as carboxylic acids and require organic solvents such as 1,4-dioxane or pyridine. However, most importantly, in such processes, the reactivity

of phenolic hydroxyls is higher than that of aliphatic ones, inducing a disappearance of free phenol content and thus a loss of their related properties.

The goal of our project was to target antioxidant additive applications mainly for polymer chemistry; we faced the problem of improving the compatibility of lignins with apolar matrices while not affecting their free phenol content. That is why this project aimed to selectively acylate the primary aliphatic hydroxy groups of some lignin fractions using either acetate or hexanoate groups, thus preserving their antioxidant properties afforded by the presence of the free phenolic groups. We therefore turned to the use of *Candida antarctica* lipase B (CAL-B) as a transesterifying biocatalyst (Cassani et al., 2007; Zhang et al., 2020). This enzyme is indeed known to be inactive toward phenols (Pion et al., 2013; Weissbach et al., 2017) and to be active in a large range of experimental conditions (solvents and temperatures) (Cassani et al., 2007). CAL-B is commercially available in different forms (expression in *Aspergillus niger* (Mustranta et al., 1993) or in yeast (Graber et al., 2003)), either as free enzyme or immobilized on resins (Miletic et al., 2010) in order to allow its easy separation from the reaction mixture by simple filtration. Other groups succeeded with a similar aim of selective acylation of lignins biocatalyzed by CAL-B, involving either ionic liquid as the reaction media (Hulin et al., 2015) or technical lignins that were post-depolymerized through catalytic hydrogenation (Martinez-Garcia et al., 2023). The present work differs in the sense that it involves technical lignin fractions in the solvent MEK, both being industrially common. Moreover, these published works estimated the resulting acylation yields through the disappearance of the acyl donor in the reaction media (by HPLC) or through the decrease of aliphatic hydroxy groups using ^{31}P NMR. However, based on our practical experience on lignins analyses and their reactivity, we must consider unpredicted artefacts in such methodologies. Indeed, the lignin spontaneous reactivity that is often noticed in the literature but is not yet fully understood, can generate side-reactions and thus analytical artefacts, leading to misinterpretation. That is why, in this article we furthermore transposed one of the most commonly used method for the quantification of fatty acid composition in complex matrices: transmethylation followed by GC-MS. We follow a robust analytical procedure that is less impacted by the potential biases induced by the unusual chemical reactivity of lignin derivatives upon chemical or thermic treatments. This article describes the feasibility of the combination of a solvent fractionation process and biocatalytic acylation of technical wheat straw alkali lignins (Protobind 1000) to convert them into valuable antioxidant additives for polymers and cosmetic applications as well as a robust analytic methodology to quantify the yield of the acylation step.

2 Material and methods

2.1 Chemicals

Dimer guaiacylglycerol-β-guaiacyl ether (GGE, Purity >97.0% (GC)) was purchased from TCI Chemicals. Other reagents, laccase (from *Trametes versicolor*, 13 U/mg), and recombinant lipase from *Candida* antarctica supported on acrylic resin (expressed in *Aspergillus niger*, ≥5,000 U/g, (1 U corresponds to the amount of enzyme which liberates 1 μmol of butyric acid per minute at pH 7.5°C and 40°C, from tributyrin as substrate)) were purchased from Sigma Aldrich. Solvents and sulfuric acid (96%) were purchased from Carlo Erba and used as received. Soda technical lignins Protobind 1000 (grass mixture of wheat straw and sarkanda) were purchased from Green Value LLC.

2.2 Substrate preparation

2.2.1 Dehydrogenative polymer preparation (DHPs)

S monolignol and syringaresinol were synthesized according to procedure described in one of our previous articles (Jaufurally et al., 2016). 0.4 g of syringaresinol (0.96 mmol) was placed in a 500 mL flask and dissolved in 180 mL of ethanol (EtOH). Then, 200 mL of deionized water was added (1 g/L of total solvents) prior the introduction of 17.6 mg of laccase (0.1 U/mg regarding total substrates). 2 g of S monolignol (9.51 mmol) was dissolved in 20 mL of EtOH (100 g/L) and added dropwise at 0.9 mL/h using a syringe pump. The mixture was stirred in the dark at ambient temperature for 24 h. EtOH was removed under reduced pressure, the mixture was cooled to 0°C, and was then filtered on a glass filter. The same procedure was repeated 10 times and the products gathered in order to obtain a sufficient batch that was dissolved in acetone, then precipitated into diethyl ether. After filtration, the recovered S-DHPs (approximately 10 g) were dried under vacuum.

2.2.2 Fractionation of lignins

Alkali lignins Protobind 1000 (PB1000) was magnetically stirred in ethyl acetate (10 L/kg) for 1 h at room temperature. The mixture was then filtered and flushed with ethyl acetate on a glass filter. The procedure was repeated a second time and the filtrates were combined prior to evaporation under reduced pressure to eliminate ethyl acetate and recover **F1** as a brown solid (36% wt.). The dried insoluble residue was magnetically stirred in methyl ethyl ketone (MEK) (10 L/kg) for 1 h at room temperature. The mixture was then filtered and flushed with MEK on a glass filter. The procedure was repeated a second time and the filtrates were combined prior to evaporation under reduced pressure to eliminate MEK and recover **F2** as a brown solid (26% wt.) and an insoluble residue **F3** (37% wt.).

2.3 Procedures for functionalization

2.3.1 Typical procedure for enzymatic acetylation

The substrate to be acetylated (200 mg) was placed in the presence of supported CAL-B (20 mg, 10% mass of the substrate) and mixed with ethyl acetate:acetonitrile (1:1 vol, 20 mL, 10 g/L) in a 25 mL round bottom flask equipped with a Dean–Stark apparatus. The mixture was magnetically stirred under reflux for 24 h and aliquots were periodically collected for kinetics study. After cooling to room temperature, the mixture was filtered to recover the supported lipase and the filtrate was concentrated under reduced pressure to recover the acetylated compound.

2.3.2 DHPs chemical acetylation

S-DHPs (200 mg) was placed in a 25 mL round bottom flask under argon flow in the presence of anhydrous pyridine (2 mL). After cooling to 0°C, acetic anhydride (2 mL, 10 mL/g) was added and the mixture was magnetically stirred at room temperature for 18 h. The reaction was cooled at 0°C before adding methanol dropwise (2 mL). Toluene (2 mL) was then added and the solvents were evaporated under reduced pressure to recover the acetylated DHPs.

2.3.3 Typical procedure for enzymatic hexanoylation

The substrate to be hexanoylated was placed in a round bottom flask in the presence of ethyl hexanoate (1:1 mass ratio to substrate), supported CAL-B (10% mass of substrate), and MEK (25 g/L). The mixture was magnetically stirred under reflux for 24 h using a Dean–Stark apparatus. After cooling to room temperature, the mixture was filtered to recover the supported lipase and the filtrate was concentrated under reduced pressure. In the case of the lignins substrate, the mixture was then precipitated into hexane under magnetic stirring and hexanoylated lignins were recovered by filtration on a glass filter, then dried under vacuum overnight. The parameters that have been changed for the purpose of the study are indicated in the discussion.

2.4 Analytical methods

2.4.1 Nuclear magnetic resonance spectroscopy

All NMR spectra were recorded on an Ascend™ 400 spectrometer (Bruker).

2.4.1.1 2D NMR

^{1}H-^{13}C HMBC and HSQC NMR spectra were recorded using $CDCl_3$ (calibrated at 7.26 ppm/77.16 ppm) or pyridine-d_5 (calibrated at 8.71 ppm/149.9 ppm) as solvent and using standard Topspin 3.2 pulse sequences.

2.4.1.2 31P NMR

Approximately 20 mg of sample and 20 mg of triphenylphosphine (TPP, internal standard) were accurately weighted and dissolved in 0.5 mL of a mixture of $CDCl_3$/pyridine (1/1.6) prior to phosphorylation using 2-chloro-4,4,5,5-tetramethyl-1,3,2-dioxaphospholane as the phosphorylating reagent (50 µL). ^{31}P spectra were recorded at 160 MHz (128 scans, with a relaxation time of 6 s) and calibrated to the hydrolyzed phosphorylating reagent singlet peak at 132.2 ppm. The following regions were integrated: aliphatic hydroxyls (149.1–144.2 ppm), phenolic hydroxyls (143.8–137.0 ppm), and acid region (136.6–133.6 ppm), normalized to TPP (−5.0 ppm). Each spectrum was treated only when an excess of phosphorylation reagent was observed as a singlet at approximately 175 ppm, and sample analysis was validated if an error below 5% was observed between two duplicates.

2.4.2 Liquid chromatography

Liquid chromatography analyses were performed using a HPLC system (Thermo Fisher Scientific) equipped with an ACCELA 600 pump, an ACCELA auto sampler, a C18 column EC 50/2 Nucleoshell RP 18, 2.7 µm (Macherey-Nagel), and an ACCELA photodiode array (PDA) detector recording over the range 250–450 nm. Samples were dissolved in acetonitrile (ACN) at 1 mg/mL, filtered on a 0.45 µm PET microdisk (Macherey-Nagel), and 1 µL was analyzed using a mobile phase consisting of water/ACN +1‰ HCOOH eluted at 250 µL/min, applying a gradient from 80/20 to 30/70 within 15 min.

2.4.3 Size exclusion chromatography

10 mg of samples was weighed and tetrahydrofuran (THF) containing 5% of toluene (internal standard) was added in order to reach a concentration of 5 mg/mL. After 5 min of shaking, samples were filtered on 0.45 µm GHP microfilters (PALL) prior to analysis by size-exclusion chromatography (SEC). SEC analyses were performed using THF stabilized with BHT as the eluent at 1 mL/min (Ultimate 3000 Pump, Dionex). 10 µL was injected (Ultimate 3000 Autosampler, Dionex) on either a PLgel Mixed C column (5 µm, 7.5 mm × 600 mm, Agilent) in the case of DHPs, or a PLgel Mixed E column (3 µm, 7.5 mm × 600 mm, Agilent) in the case of lignins, and the signal was observed at 280 nm (Ultimate 3000 UV/vis detector, Dionex). The molar mass distributions were determined using a calibration curve based on 10 polystyrene standards ranging from 580 to 364,000 g/mol (Agilent) for the Mixed C column (Supplementary Figure S1) or from 162 to 22,290 g/mol (Agilent) for the Mixed E column (Supplementary Figure S2).

2.4.4 Quantification of hexanoylation yield through transmethylation followed by GC-MS

2.4.4.1 Standard solutions

Different standard solutions have been used in order to allow good accuracy of the calibration curves and an overall good reproducibility of the method. Approximately 500 mg of each internal standard (ethyl pentanoate, methyl heptanoate, methyl octanoate, and tetradecane) was accurately weighed in a 100 mL volumetric flask and mixed with methanol to obtain a stock solution at 5 mg/mL. This stock solution was then diluted by 100 using a 2.5 mL glass syringe and 250 mL volumetric flasks to obtain standard solutions at 0.05 mg/mL in methanol in the presence of 5%vol H_2SO_4 (MQS, solution for methyl hexanoate quantification after transmethylation) or not (EQS, solution for residual ethyl hexanoate quantification). In the same manner, a calibration solution (CS) containing methyl hexanoate and ethyl hexanoate, at 5 mg/mL each, in methanol was prepared.

2.4.4.2 Transmethylation procedure

Approximately 20 mg of sample to be analyzed was accurately weighed in a 15 mL Pyrex test tube and 2 mL of internal standard solution containing 5%vol H_2SO_4 (**MQS**, 0.05 mg/mL) was added. The capped tube was heated at 80°C for 2 h. After cooling to room temperature, 2 ml of hexane and 1 mL of water were added, the capped tube was agitated vigorously by orbital shaking for 20 min, and then centrifuged at 4°C at 4,800 rpm for 10 min. The upper phase was collected and analyzed directly by GC-MS. Samples were prepared in duplicates and each vial injected twice.

2.4.4.3 Quantification of residual ethyl hexanoate

Approximately 20 mg of sample to be analyzed was accurately weighted in a 15 mL Pyrex test tube and 2 mL of internal standard solution (**EQS**, 0.05 mg/mL) was added. 2 ml of hexane and 1 mL of water were added, the capped tube was agitated vigorously by orbital shaking for 20 min, and then centrifuged at 4°C at 4,800 rpm for 10 min. The upper phase was collected and analyzed directly by GC-MS. Samples were prepared in duplicates and each vial injected twice.

2.4.4.4 Calibration curves

In a 15 mL capped Pyrex test tube, 5–100 µL of the calibration solution **CS** at 5 mg/mL in methanol was added to 2 mL of the internal standard solution **EQS** at 0.05 mg/mL in methanol. 2 ml of hexane and 1 mL of water were added, the capped tube was agitated vigorously by orbital shaking for 20 min, and then centrifuged at 4°C at 4,800 rpm for 10 min. The upper phase was collected and analyzed directly by GC-MS. Each calibration point was prepared in duplicate and injected three times. The vial was validated when an error below 3% was observed between the three injections, and calibration was validated when an error below 5% was observed between the two vials when considering the peak area ratio of compound to quantify over methyl heptanoate. Plotting the determined molar ratio of both compounds to quantify (methyl and ethyl hexanoate) over the methyl heptanoate standard as a function of the corresponding peak area ratios gave their two calibration curves and the corresponding linear equations: [molar ratio (compound/methyl heptanoate)] = f ([peak areas ratio (compound/methyl heptanoate)]) (Supplementary Figure S3).

2.4.4.5 Hexanoylation yield calculation

The chromatogram was validated if 1) the peak area ratio of methyl heptanoate over methyl octanoate was between 0.85 and 0.93 in order to ensure the wellness of the GC-MS system, 2) the peak area ratio of tetradecane over methyl octanoate was between 1.29 and 1.41, in order to ensure the absence of volatiles loss during sample preparation, and 3) in the case of transmethylated samples, no residual ethyl pentanoate was observed in order to ensure complete transmethylation. For a sample to be analyzed, the peak area ratio of the compound to quantify (methyl or ethyl hexanoate) over the methyl heptanoate internal standard was inserted into the equation of its respective calibration curve to determine its concentration. Normalization by sample weight gave its molar amount per Gram of sample to be analyzed. The vial was validated when an error below 5% was observed between the two injections and the sample was validated when an error below 10% was observed between the two vials. The molar amount of residual ethyl hexanoate per Gram of sample was subtracted from the molar amount of methyl hexanoate per Gram of sample quantified after transmethylation to calculate the hexanoylation yield, which was expressed in µmol of hexanoate chains per Gram of sample.

2.4.4.6 Gas chromatography-mass spectrometry procedure

Gas chromatography-mass spectrometry (GC-MS) analyses were performed using a 6890 Series GC system (Agilent). 0.5 µL of sample was injected through a 7683 Series Injector (Agilent) with a split ratio of 30 and the inlet set at 250°C. Elution was by helium N60 at 0.7 mL/min through a DB-Wax UI column (Agilent) with dimensions 30.0 m × 250 µm x 0.25 µm. The oven temperature was maintained at 50°C for 4 min, then increased up to 95°C at 5°C/min, and finally up to 180°C at 70°C/min with a hold of 5 min. Eluted compounds were detected by a quadrupole 5973 Mass Selective Detector (Hewlett Packard) operating over the scanning range 50–650 m/*z*, with electron-impact ionization at 70 eV, the transfer line at 250°C, and the source at 230°C. Identification of compounds was based on pure compound injection and mass spectra comparison. The peak areas of each compound were determined from the total ion chromatogram.

3 Results and discussion

3.1 Feasibility and selectivity of enzymatic acylation

3.1.1 Acetylation of dimer model compound

In order to test the feasibility and selectivity of the reaction, the CAL-B activity was first tested on commercial guaiacylglycerol-β-guaiacyl ether dimer, which is commonly used as representative of the β-*O*-4 linkage between two coniferyl alcohols found in lignin oligomers as the major linkage between two *p*-hydroxycinnamic subunits. This commercial stereopure dimer exhibits a free phenolic group and both primary and secondary aliphatic hydroxy groups. The acetylation of the dimer (Figure 2) was first investigated in the presence of ethyl acetate and supported CAL-B (10% wt of

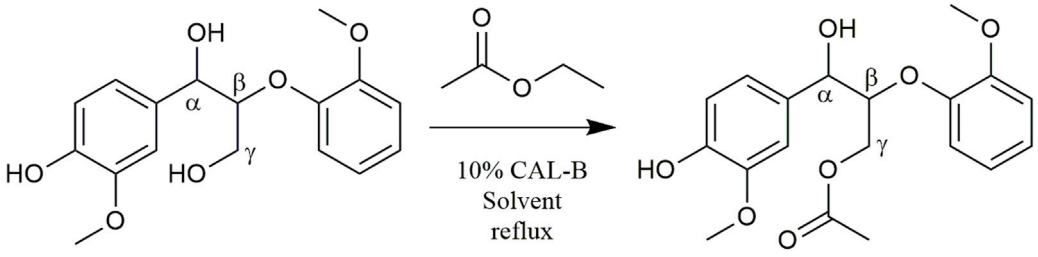

FIGURE 2
Guaiacylglycerol-β-guaiacyl ether enzymatic acetylation.

dimer) in acetonitrile (10 g/L, 50:50 acetonitrile:ethyl acetate) and with continuous removal of the by-produced ethanol by azeotropic distillation. The reaction was easily followed by HPLC and ^{1}H NMR (Supplementary Figure S4). These first results showed only acetylation of the primary hydroxyl in approximately 90% yield after 8 h of reaction. The reaction could also be monitored by ^{31}P NMR after phosphorylation (Supplementary Figure S5), where the relative integration of the signal corresponding to the phosphorylated primary OH (triplet at 147.5 ppm) progressively decreased, while the integration of secondary (doublet at 148.2 ppm) and phenolic OH (singlet at 139.5 ppm) remained equal, even if their chemical shift slightly increased (to 148.3 and 139.6 ppm, respectively), thus confirming the selectivity. To further ensure this selectivity, the reaction was conducted over a longer time period (13 days): no peracetylated product was observed by HPLC, ^{1}H NMR, or ^{31}P NMR. If CAL-B is well-known to be strictly inactive toward phenols, it may induce acylation of secondary hydroxyls (Pion et al., 2013). In this current case, inactivity toward the secondary hydroxyl might be due either to stereoselectivity toward the involved stereopure commercial dimer, or to the proximity of the hindered phenolic moiety (Uppenberg et al., 1995). Acetonitrile, first selected because it is known for being tolerated by CAL-B (Dutta Banik et al., 2016) has however a rather low ability to solubilize lignins. Thus, it was thereafter replaced by methyl ethyl ketone (MEK), showing similar acetylation kinetics on the commercial dimer (Figure 3). MEK was therefore chosen as the reaction solvent for this process and to efficiently solubilize a large fraction of Protobind 1000 (60% wt), which is our targeted lignin substrate.

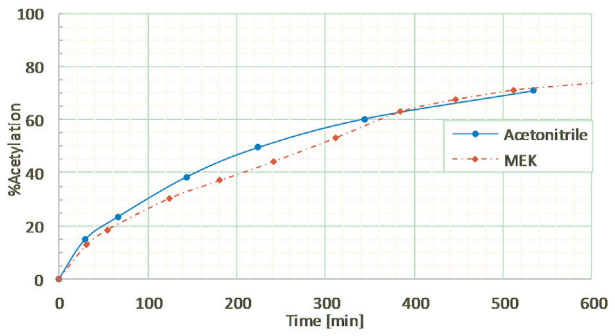

FIGURE 3
Kinetics of guaiacylglycerol-β-guaiacyl ether (GGE) enzymatic acetylation under reflux in acetonitrile or in MEK (10 g/L), followed by HPLC.

3.1.2 Complexification of the model substrate: DHPs acetylation

However, direct monitoring of the reaction on lignins fractions by ^{1}H NMR or HPLC would be unfeasible due to the complexity of the lignins' structure and their poor solubility in the appropriate solvents (Wen et al., 2013; Wurzer et al., 2021). Therefore, to challenge further analytical methodologies (SEC, ^{31}P NMR), we turned to the acetylation of a substrate of intermediate complexity: dehydrogenative dehydropolymers (DHPs) (Lahive et al., 2020) of sinapyl alcohol (Figure 4). Such S-type DHPs, exhibiting only two types of inter subunit linkages (β-*O*-4 and syringaresinol types), are indeed good candidates to adapt our analytical procedures to a more complex substrate representative of lignins.

DHPs were treated in the presence of CAL-B (10% wt compared to DHPs) in ethyl acetate:MEK (50:50 vol, 10 g/L) under reflux for 2 days. Afterwards, the mixture was cooled to room temperature, filtered to recover supported CAL-B, and the solvent evaporated under vacuum to obtain the resulting acetylated DHPs.

For the purpose of analytical comparisons, completely acetylated DHPs were prepared through a chemical procedure in pyridine using acetic anhydride. From ^{1}H-^{13}C HMBC NMR (in C_5D_5N) of the chemically acetylated DHPs, three acetate groups were observed: one phenolic (2.29 ppm/168.5 ppm) and two aliphatic, corresponding to primary and secondary hydroxyls (1.94 ppm/170.6 ppm and 2.13 ppm/170.0 ppm, respectively), while the enzymatically acetylate showed a single primary aliphatic acetate signal (1.94 ppm/170.6 ppm, Supplementary Figure S6). This confirmed the transposability of the selective enzymatic process to more complex substrates, where acetylation is restricted to primary aliphatic hydroxyls. In addition, another characteristic signal was observed at 2.11 ppm/173.3 ppm, corresponding to residual acetic acid (confirmed by comparison with pure acetic acid, which also appears at 134.6 ppm in ^{31}P NMR, Supplementary Figure S7).

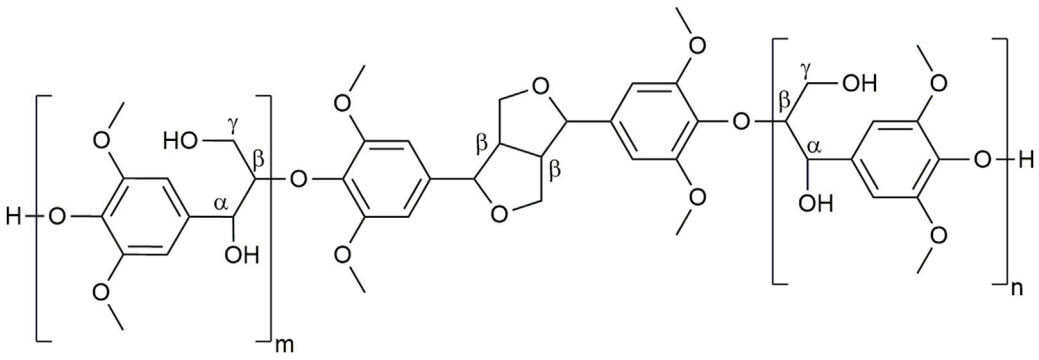

FIGURE 4
Putative structure of S dehydrogenative polymers (S-DHPs) used as model substrate.

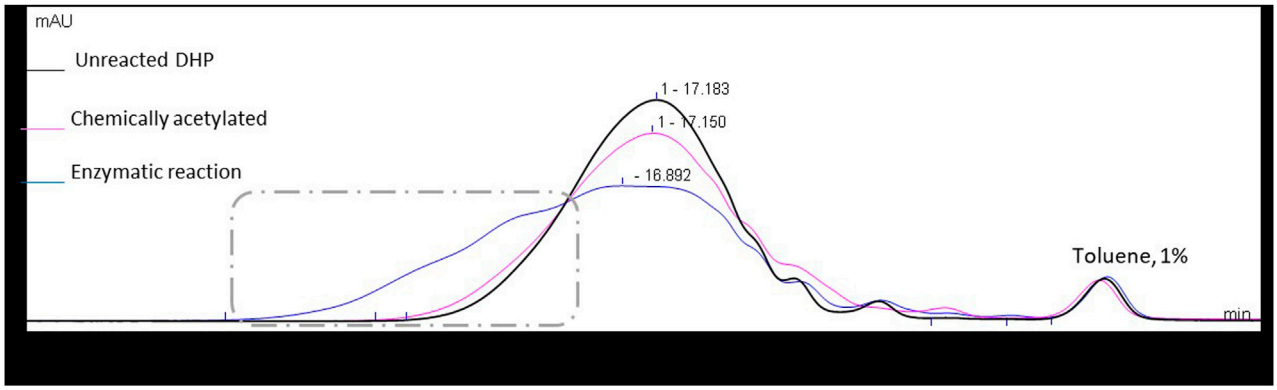

FIGURE 5
Size exclusion chromatograms in THF of the starting material and the enzymatic and chemically acetylated DHPs, using UV detection at 280 nm. Signals normalized to the toluene peak eluted at 21.1 min.

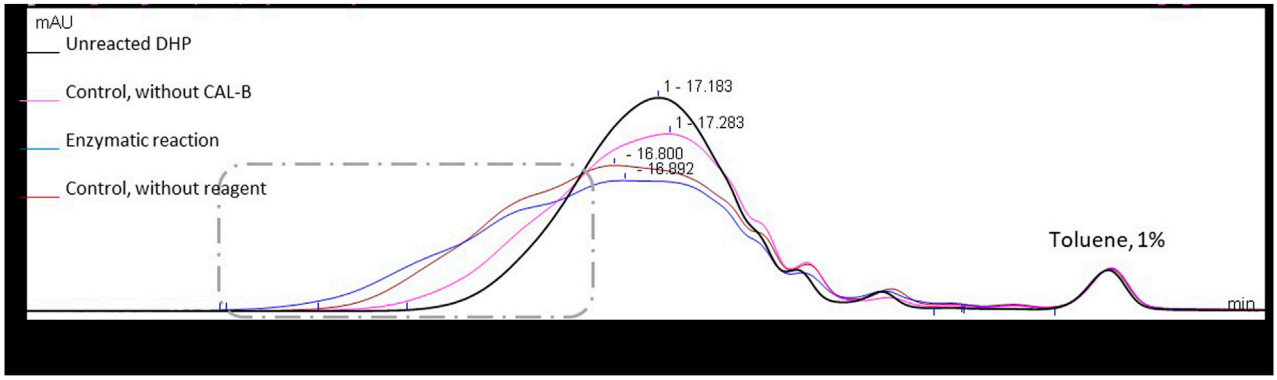

FIGURE 6
Size exclusion chromatograms in THF for DHPs in different reaction systems (48 h in MEK (10 g/L)), using UV detection at 280 nm. Signals normalized to the toluene peak eluted at 21.1 min.

TABLE 1 Characteristics of the substrate DHPs (Entry 1), enzymatically acetylated DHPs (Entry 2), and appropriate controls (Entries 3, 4) kept for 48 h under reflux in MEK (10 g/L); molar mass distributions determined [a]by SEC. Aliphatic and phenolic hydroxyl contents determined [b]by ^{31}P NMR.

Entry	Enzyme (% wt)	Acyl donor	M_n[a] (g/mol)	M_w[a] (g/mol)	PDI[a]	[Aliphatic OH][b] (mmol/g)	[Phenolic OH][b] (mmol/g)
1	—	—	1511	2731	1.81	3.32 ± 0.1	1.48 ± 0.05
2	10	Ethyl acetate	1046	3522	3.37	1.98 ± 0.1	1.55 ± 0.07
3	10	—	1101	2733	2.48	2.65 ± 0.05	1.64 ± 0.01
4	0	Ethyl acetate	1109	2676	2.41	2.76 ± 0.02	1.64 ± 0.02
5	10	Ethyl hexanoate	1906	4,658	2.79	2.91 ± 0.04	1.85 ± 0.01

The molar mass distribution of the samples was also determined through size exclusion chromatography (SEC), assuming that the acetylation could induce an increase in apparent molar mass. Chemically acetylated DHPs showed a slight increase in molar mass distribution when compared to the starting material (Figure 5). Surprisingly, this increase in apparent molar mass was even more significant in the case of enzymatic acetylation, while it should have a lower molar mass gain since its acetylation was partial. Such an observation suggests that side reactions, such as intermolecular cross-coupling reactions, may occur in these reaction conditions in the case of DHPs.

10.3389/fchem.2023.1239479

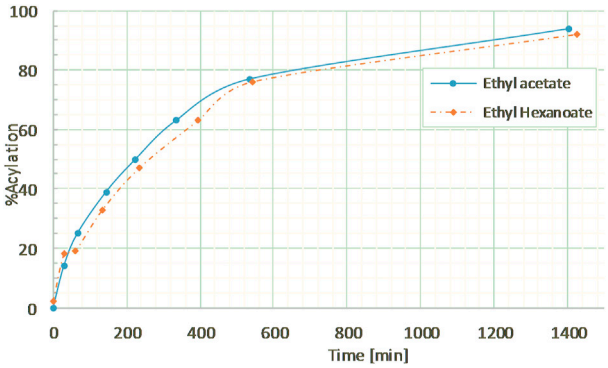

FIGURE 7
Kinetics of guaiacylglycerol-β-guaiacyl ether acylation by ethyl acetate or ethyl hexanoate, in MEK (10 g/L) under reflux, followed by ^{1}H NMR in $CDCl_3$.

Therefore, to better understand this unexpected result, two control reactions were run: one in the absence of any acyl donor and another in the absence of the catalyst CAL-B. In the two cases where CAL-B is present (control without acyl donor and enzymatic reaction), a significant increase in molar mass is observed, considering that lipase treatment is able to induce cross-coupling reactions between DHPs residues. In the absence of CAL-B, a similar molar mass increase is observed, but is far less important and probably also due to chemical modifications of the DHP structure upon thermal treatment (Figure 6). The hydroxyl group content of the different samples was then assessed through ^{31}P NMR after phosphorylation, a method commonly used for the quantification of the different types of lignin hydroxyls (Table 1) (Meng et al., 2019).

In the case of enzymatic acetylation, the aliphatic hydroxyl content significantly decreased (−40%, Entry 2), suggesting efficient acetylation, as observed by the appearance of an ester spot in ^{1}H-^{13}C HMBC NMR. Nevertheless, even if lower, this phenomenon was also observed in controls (−20% and −17%, Entries 3 and 4), where no acetate was observed through ^{1}H-^{13}C HMBC NMR, thus suggesting that this decrease in aliphatic hydroxyls can also be due to spontaneous side reactions. Moreover, this hypothesis is reinforced by an increase in the free phenol content, probably due to the cleavage of some β-*O*-4 bonds inside the oligomers. From such global observations it can be assumed once more that DHPs (and probably also lignin fractions) may undergo dramatic structural changes in these reaction conditions (temperature, solvent), including for instance β-*O*-4 bond cleavage and recondensation reactions. The balance between these two pathways, going from control reactions to the real reaction may be to some extent due to the generation of acetic acid in the medium containing the ethyl acetate and CAL-B, but also to the specific activity of CAL-B on lignin oligomers in the absence of any acyl donor.

Although confirming the occurrence of side reactions impacting the hydroxyl content in all cases, ^{31}P NMR appeared to be nevertheless unsuitable for precise quantification of the acylation yield for DHPs (and probably for lignin fractions), contrary to our expectations. Indeed, the acetylation yield, when estimated on the basis of ^{31}P NMR data, seemed largely overestimated (approximately 50% mol of the putative primary hydroxy groups). We thus concluded that another analytical method was needed to quantify the acylation yield. We envisaged the use of an indirect method based on either saponification or transesterification methods, allowing the reformation of acids or esters from the acylated lignins, which can be further quantified by GC-MS. However, such a process is incompatible with acetylated compounds since

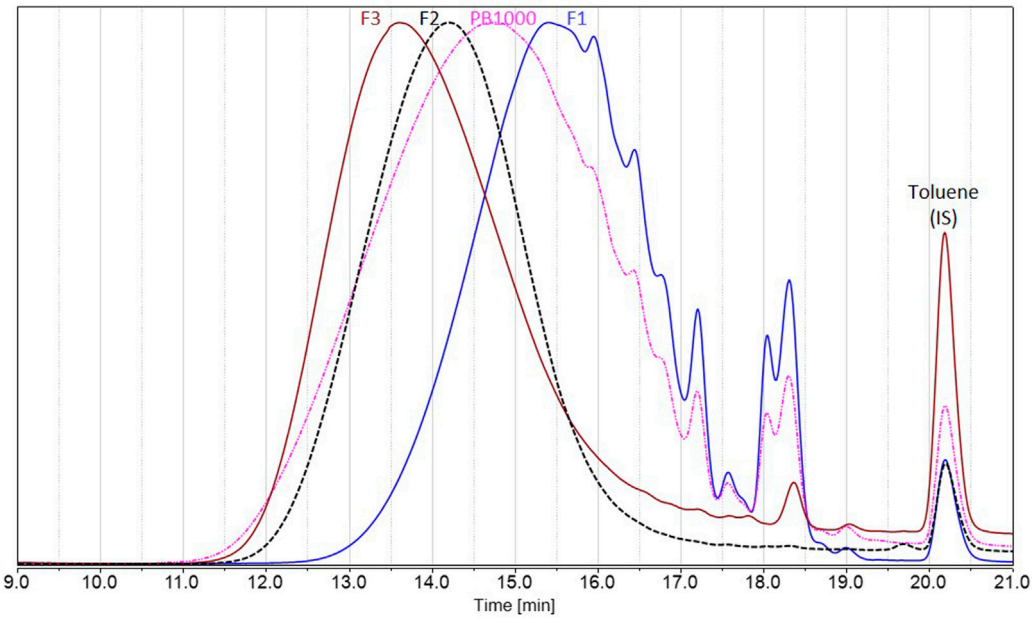

FIGURE 8
Size exclusion chromatography in THF of Protobind 1000 technical lignins (pink) and the resulting fractions F1 (blue), F2 (black), and F3 (brown), using UV detection at 280 nm. Signals normalized to the maximum height; toluene used as internal standard, eluted at 20.2 min.

TABLE 2 Characteristics of the different fractions (ethyl acetate F1, MEK F2, and insoluble F3 fractions) obtained from Protobind 1000 (PB1000) determined [a]by gravimetry, [b]by SEC, and [c]by ^{31}P NMR (spectra available in Supplementary Materials).

	%wt[a]	M_n[b] (g/mol)	M_w[b] (g/mol)	PDI[b]	[Aliphatic OH][c] (mmol/g)	[Phenolic OH][c] (mmol/g)	[COOH][c] (mmol/g)
PB1000	100	573	1744	3.04	1.94 ± 0.02	4.43 ± 0.05	1.17 ± 0.03
F1	36	385	813	2.11	1.16 ± 0.04	5.24 ± 0.09	1.27 ± 0.01
F2	27	1240	2188	1.76	1.41 ± 0.01	4.13 ± 0.01	1.02 ± 0.02
F3	37	1266	2695	2.13	2.50 ± 0.07	3.34 ± 0.12	0.96 ± 0.05

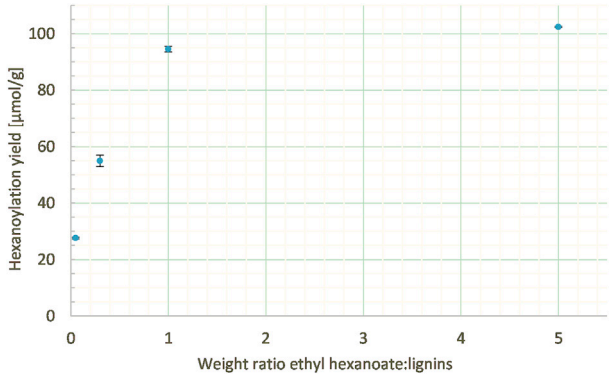

FIGURE 9
Hexanoylation yield obtained for different ethyl hexanoate: lignins weight ratios at a constant enzyme load (20% wt), lignins concentration in MEK (10 g/L), and reaction time (24 h); yield estimated by transmethylation followed by GC-MS.

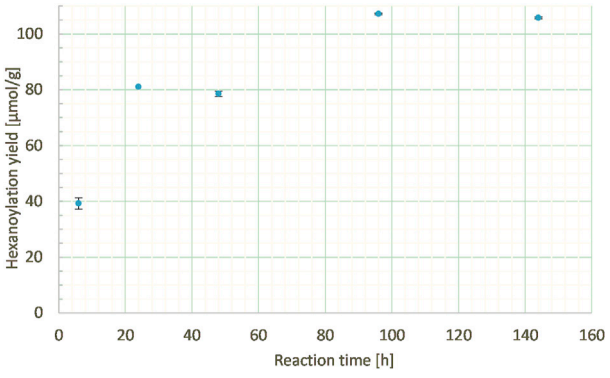

FIGURE 10
Hexanoylation yield obtained for different reaction times at a constant ethyl hexanoate:lignins weight ratio (1:1), enzyme load (10% wt), and lignins concentration in MEK (10 g/L); yield estimated by transmethylation followed by GC-MS.

it generates either acetic acid or methyl acetate, which are difficult to quantify by GC-MS. Another longer acyl donor was therefore chosen, ethyl hexanoate, as its excess can still be easily removed by either evaporation or hexane washing, and since its corresponding acid or methyl ester are easily quantifiable by GC-MS.

3.1.3 Hexanoylation of the dimer model compound

The hexanoylation process was first tested on the commercial dimer in order to assess the efficiency of this approach with a longer chain and a more apolar acyl donor. Guaiacylglycerol-β-guaiacyl ether dimer was thus reacted with ethyl hexanoate in a ratio of 5: 1 mol to ensure an excess of acyl donor at the same conditions (10% wt CAL-B, MEK, 10 g/L, reflux). The kinetics of hexanoylation was monitored by ^{1}H NMR (Supplementary Figure S8) and HPLC and was found to be very similar as the acetylation (Figure 7), with a hexanoylation yield of 76% after 9 h, thereby proving the versatility of the method in terms of acyl donor. Similar control experiment ran without CAL-B induced no structural changes of guaiacylglycerol-β-guaiacyl ether dimer (results not shown), thus confirming that hexanoylation was indeed only catalyzed by CAL-B.

3.1.4 Hexanoylation of DHPs and quantification of the acylation yield by a transmethylation/GC-MS procedure

DHPs were then reacted with an excess of ethyl hexanoate (5: 1 wt) in MEK (10 g/L) under reflux. After the biocatalyzed hexanoylation reaction and the removal of the supported CAL-B by filtration, the reaction medium was concentrated under reduced pressure and first cleaned from residual unreacted acyl donor through precipitation in hexane, and submitted to extended drying under vacuum. ^{1}H-^{13}C HMBC NMR proved the formation of an ester bond (Supplementary Figure S9) as well as the absence of residual acyl donor (no ethyl spots visible), which was confirmed by GC-MS analysis of the hexane supernatant. Saponification of the hexanoylated compounds was first tested but led to very tedious workup procedures and unsatisfying errors in the quantification of the resulting hexanoic acid. We thus turned to a transmethylation process, well-known in the field of triglyceride chemistry. Transmethylation aims to cleave the ester bonds and thus release the hexanoate moieties as methyl esters (Supplementary Figure S10). Thereafter, transmethylation followed by GC quantification established that 184 µmol of methyl hexanoate was released per Gram of reacted DHPs. This value, compared to the aliphatic hydroxyl content of the starting material determined by ^{31}P NMR (3.32 mmol/g, Table 1 Entry 5), indicates a hexanoylation yield of 5.5% mol of the aliphatic hydroxy groups; nevertheless, such a calculation underestimates the yield as it does not take into account the occurrence of side reactions decreasing the amount of available targeted aliphatic hydroxy groups and does not discriminate primary from secondary hydroxyl content, which may be equivalent according to the putative DHPs structure. Structural modification of DHPs was not investigated further as it was not the aim of this work;

10.3389/fchem.2023.1239479

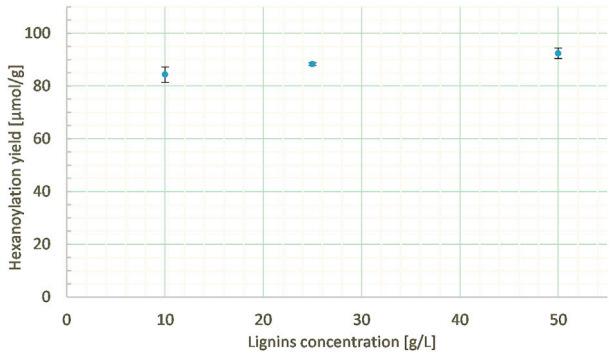

FIGURE 11
Hexanoylation yield obtained for different reaction concentrations at a constant ethyl hexanoate:lignins weight ratio (5:1), enzyme load (10% wt), solvent nature (MEK), and reaction time (24 h); yield estimated by transmethylation followed by GC-MS.

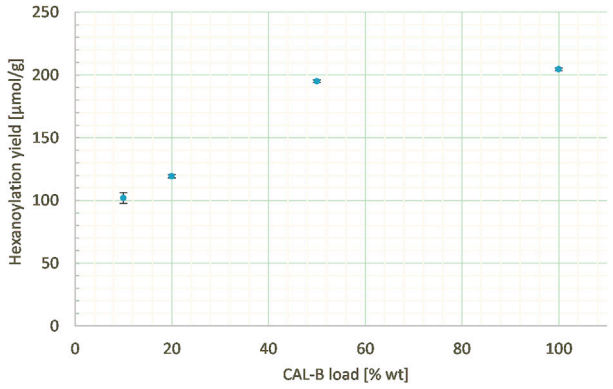

FIGURE 12
Hexanoylation yield obtained for different CAL-B loads at a constant ethyl hexanoate:lignins weight ratio (1:1), lignins concentration in MEK (25 g/L), and reaction time (24 h); yield estimated by transmethylation followed by GC-MS.

however, it appears more reliable to quantify acylation through transmethylation rather than structural analysis (^{31}P NMR or SEC), as we expected initially. For these reasons, the hexanoylation yield will be estimated by transmethylation and expressed in µmol/g. In initial attempts, we compared the quantification through peak area measurement inserted in the equation [molar concentration] = f ([peak area]) determined by injection of **CS** at different concentrations. Nevertheless, the use of an internal standard of close structure (methyl heptanoate, **MQS**) led to higher repeatability and was preferred in the remainder of our study, as described in the material and methods section.

This method is indirect and it can be applied to any acylated substrate of complex structure, as far as the residual unreacted acyl donor is quantified or, when possible, carefully eliminated. Therefore, this method was retained for hexanoylation yield estimation in the remainder of the study, aiming to transfer this biocatalyzed selective hexanoylation process to technical lignins and derived fractions.

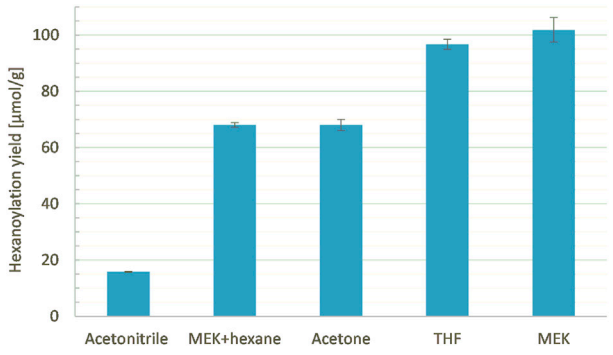

FIGURE 13
Hexanoylation yield obtained for different solvents as reaction media at a constant ethyl hexanoate:lignins weight ratio (1:1), enzyme load (10% wt), lignins concentration (25 g/L), and reaction time (24 h); yield estimated by transmethylation followed by GC-MS.

3.2 Transposition of the enzymatic hexanoylation to lignins

3.2.1 Fractionation of the technical lignins

To deal with less heterogeneous samples than the complex technical lignins Protobind 1000, sequential solvent fractionation was applied in order to obtain more defined lignin fractions (Lu et al., 2021; Jin et al., 2022). The first step involved ethyl acetate in order to eliminate lower molar mass compounds **F1** and to focus on polymeric chains, as they encounter more difficulties in accessing enzyme active sites. The second step involved MEK in order to extract a substrate soluble **F2** in the reaction media (MEK), as well as in analytical solvents, by eliminating the insoluble residue **F3**. These three fractions showed lower polydispersities than Protobind 1000 and exhibited increasing molar masses as follows: M_w (**F1**) < M_w (Protobind 1000) < M_w (**F2**) < M_w (**F3**), while the phenol content decreased in the opposite manner (Figure 8; Table 2).

3.2.2 Hexanoylation of lignins fraction F2

The hexanoylation of soda lignins fraction **F2** (lignins fraction soluble in MEK but insoluble in ethyl acetate) was thus conducted in MEK with ethyl hexanoate. The first attempt was conducted based on previous experimental parameters: 5 mass equivalent of ethyl hexanoate and 10% wt CAL-B regarding lignins were used in MEK (10 g/L) under reflux for 24 h, which led to a hexanoylation yield of 85 µmol/g. The same experiment conducted in absence of CAL-B showed no hexanoylation; this control informed us that CAL-B activity was responsible for the reaction and confirmed the accuracy of hexanoylation yield quantification through transmethylation followed by GC-MS, inducing no overestimation. In order better understand the reactivity of this new system, different key parameters have been studied to optimize enzymatic hexanoylation: 1) ethyl hexanoate:lignins weight ratio, 2) reaction time, 3) lignins concentration, 4) enzyme load, and 5) the solvent used as the reaction medium. In all following sections, different assays were

TABLE 3 Characteristics of the tested solvents and the resulting recovery (after precipitation in hexane) and acylation yields.

Solvent	Hildebrand parameter ($MPa^{1/2}$)	Boiling point (°C)	Recovery yield (%)	Acylation yield (μmol/g)
Acetone	**19.9**	**56**	**90**	**68**
Acetonitrile	**24.3**	**82**	**65**	**16**
MEK	**19.3**	**80**	**89**	**102**
MEK/Hexane (50/50)	**nd**	65	**72**	**68**
THF	**18.6**	**66**	**90**	**97**

compared based on their resulting hexanoylation yields determined through transmethylation followed by GC-MS. Some of the following studies were conducted in parallel; therefore, the fixed parameters are not necessarily optimized, aiming to detect tendencies rather than defining an optimized process.

3.2.2.1 Ethyl hexanoate:lignins weight ratio

The work on model DHPs was conducted with 5 mass equivalent of ethyl hexanoate in order to ensure a sufficient excess. However, such an excess led to tedious removal of residual unreacted acyl donor at the end of the process. Thus, various ethyl hexanoate:lignins weight ratios (from 0.05 to 5 mass equivalents) were studied at a constant enzyme load (20% wt), lignins concentration in MEK (10 g/L), and reaction time (24 h). Lowering the weight ratio of ethyl hexanoate: lignins from 5:1 to 1:1 gave similar results (102 and 94 μmol/g, respectively), while too low a ratio led to a drop in the hexanoylation yield (25 μmol/g with 0.05:1, Figure 9).

Thus, a 1:1 weight ratio was preferred as it makes the post-reaction workup easier and the process cheaper and greener by generating less side-products without significantly decreasing the hexanoylation yield.

3.2.2.2 Reaction time

Another key parameter can be the reaction time; thus, it was studied from 6 h to 6 days at a constant ethyl hexanoate:lignins weight ratio (1:1), enzyme load (10% wt), and lignins concentration in MEK (10 g/L). 6 h reaction time led to only half of the hexanoylation yield (39 μmol/g) compared to 24 h (81 μmol/g), indicating an incomplete process. Further extension of the reaction time led to a slight increase in the hexanoylation yield (Figure 10). Thus, time can be a parameter of interest but should be balanced according to the energetic cost and lignins side reactions.

3.2.2.3 Lignins concentration in MEK

The lignin concentration in MEK was varied from 10 to 50 mg/mL at a constant ethyl hexanoate:lignins weight ratio (5:1), percentage of enzyme (10% wt), and reaction duration (24 h). Similar hexanoylation yields (from 85 to 92 μmol/g) were obtained in the three cases (Figure 11), demonstrating the low impact of concentration on the studied range, thus allowing us to reduce the amount of solvent employed.

3.2.2.4 CAL-B load

In order to assess the impact of catalyst load on the reactivity, the percentage of supported enzyme was also varied from 10% to 100% wt according to lignins at a constant ethyl hexanoate:lignins weight ratio (1:1), lignins concentration in MEK (25 g/L), and reaction time (24 h). Indeed, the hexanoylation yield increased along with the CAL-B load (Figure 12), even if the phenomenon is far from being linear: increasing the load by 10 times doubled the yield (250 μmol/g). Thus, the CAL-B load is a real lever for increasing the hexanoylation yield; nevertheless, due to its high cost, a balance should be struck between cost and efficiency.

3.2.2.5 Solvent variation

It is known that CAL-B activity and stability are impacted by the polarity and temperature of the medium (Kitamoto et al., 2015; Banik et al., 2016). In our case, both are governed by the solvent chosen, which also impacts substrate solubilization. Thus, solvents of different polarities and different boiling points (acetonitrile, acetone, MEK, THF, or a mixture MEK/hexane (50/50), Table 3) were tested at a constant ethyl hexanoate:lignins weight ratio (1:1), enzyme load (10% wt), lignins concentration (25 g/L), and reaction time (24 h, Figure 13). Acetone, which shows a polarity similar to MEK (Hidebrand parameters of 19.9 and 19.3 $MPa^{1/2}$, respectively) but a lower boiling point (56°C and 80°C, respectively), led to a lower hexanoylation yield (68 μmol/g instead of 102 μmol/g). This lower reactivity might be related to the lower temperature, which decreases the CAL-B activity and/or impeaches ethanol removal. Acetonitrile, known to be compatible with CAL-B (Arcens et al., 2020) and suitable as a dimer acetylation medium, exhibits a boiling point (82°C) similar to MEK, but a higher Hildebrand parameter (24.3 $MPa^{1/2}$); the significantly lower hexanoylation yield (16 μmol/g) when compared to MEK might be due to the low solubility of lignins **F2** in acetonitrile, where only 65% was recovered (generally 90% is recovered). THF shows a similar Hildebrand parameter (18.6 $MPa^{1/2}$) but a lower boiling point than MEK (66 °C), leading to a similar hexanoylation yield of 97 μmol/g. THF appears therefore to be a choice for substrates of lower solubility. Finally, a mixture of MEK and hexane (50/50) was attempted in order to improve ethanol removal. The resulting hexanoylation yield was only 68 μmol/g, most likely due to the lower solubility of the substrate **F2** in this system (only 72% recovered). These overall observations tend to indicate that MEK is a good solvent of choice in our system. When one wants to change for another solvent, attention should be paid to both its boiling point (60°C–100°C) and its polarity (19–20 $MPa^{1/2}$) in order to preserve a certain reactivity.

4 Conclusion

This study demonstrates the feasibility of the enzymatic selective acylation of primary hydroxy groups of lignin fractions, using, first,

well controlled model compounds (commercial guaiacylglycerol-β-guaiacyl ether and sinapyl alcohol dehydrogenative polymers) in order to design and ensure reproducible efficiency of the analytical protocols to be used for the estimation of the acylation yield, as well as the selectivity of the process strictly inactive toward phenols. The whole process, applied to fractions of commercial wheat straw soda lignins Protobind 1000, led to relatively moderate hexanoylation yields (approximately 100 μmol/g), much lower than those obtained with model compounds. This drastic yield decrease is not only a result of the more complex structure of lignin fractions compared to DHPs, but also the process used for the preparation of the starting lignins (remaining salts and low pH of the resulting lignin fraction solutions, which may favor critical changes in the structure of the lignins). From a methodological point of view, we have also demonstrated that the transmethylation method is a versatile method for the determination of the acylation yield, more so than the direct chromatographic (SEC) and spectroscopic (^{31}P NMR) methods, the former not allowing direct quantification and the latter leading to a large overestimation of the acylation yield due to side-reactions, as demonstrated with DHPs. Moreover, this analytical approach involving transmethylation can be applied to any substrate, regardless of its structural complexity or solubility. Different hexanoylation conditions can be considered (in terms of solvent type, concentration, duration, and CAL-B load); thus, they can be adapted regarding 1) substrate specificities if required and/or 2) cost/efficiency balance target. Different experimental conditions have been tested with modified parameters and how they impact the acylation yield, allowing the design of a large panel of procedures that can be used according to the nature of the substrate (solubility and complexity) and the target efficiency. In future, we will diversify the acyl donor as well as the substrates in order to investigate the influence of biomass botanical origin and the impact of the lignin recovery procedure on the reactivity, assuming that the yield of this acylation reaction may be one of the possible quality criteria for technical lignins for further possible valorization routes. It is important to note that our preliminary results concerning the use of these modified lignins as either antioxidant additives for polymer compounding or as stabilizers for cosmetic emulsions are quite promising and demonstrate the significant advantage of modified lignins compared to starting lignins. These different studies are underway and will be reported in due time.

Data availability statement

The original contributions presented in the study are included in the article/Supplementary Materials, further inquiries can be directed to the corresponding author.

Author contributions

FP and P-HD contributed to conception, design, and funding of the study. AS and CH realized the experimental work of fractionation and hexanoylation. AS and FP developed the analytical methodology by GC-MS. AM synthesized, characterized, and provided model DHPs. AS wrote the first draft of the manuscript. CH, FP, and PD wrote sections of the manuscript. All authors contributed to the article and approved the submitted version.

Funding

AS's PhD fellowship was funded by the ABIES doctoral school. CH's PhD fellowship was funded by Lucas Meyer Cosmetics. The IJPB benefits from the support of Saclay Plant Sciences-SPS (ANR-17-EUR-0007).

Acknowledgments

The authors wish to acknowledge Laurent Cezard (IJPB) for his precious support regarding GC-MS developments.

Conflict of interest

The authors declare that the research was conducted in the absence of any commercial or financial relationships that could be construed as a potential conflict of interest.

Publisher's note

Supplementary material

The Supplementary Material for this article can be found online at: https://www.frontiersin.org/articles/10.3389/fchem.2023.1239479/full#supplementary-material

References

Allais, F., Ducrot, P.-H., Broussard, O., Petit, M., and Silioc, C. (2016). "Liant pour fibres minérales à base de lignosulfonate et d'un composé carbonyle, et mats obtenus,". WO2016120575A1 (France: France patent application).

Alzagameem, A., Klein, S. E., Bergs, M., Do, X. T., Korte, I., Dohlen, S., et al. (2019). Antimicrobial activity of lignin and lignin-derived cellulose and chitosan composites against selected pathogenic and spoilage microorganisms. *Polymers* 11, 670 doi:10.3390/polym11040670

Arca, H. C., Mosquera-Giraldo, L. I., Bi, V., Xu, D. Q., Taylor, L. S., and Edgar, K. J. (2018). Pharmaceutical applications of cellulose ethers and cellulose ether esters. *Biomacromolecules* 19, 2351–2376. doi:10.1021/acs.biomac.8b00517

Arcens, D., Grau, E., Grelier, S., Cramail, H., and Peruch, F. (2020). Impact of fatty acid structure on calb-catalyzed esterification of glucose. *Eur. J. Lipid Sci. Technol.* 122, 1900294. doi:10.1002/ejlt.201900294

Banik, S. D., Nordblad, M., Woodley, J. M., and Peters, G. H. (2016). A correlation between the activity of candida Antarctica lipase b and differences in binding free energies of organic solvent and substrate. *Acs Catal.* 6, 6350–6361. doi:10.1021/acscatal.6b02073

Benna-Zayani, M., Kbir-Ariguib, N., Trabelsi-Ayadi, M., and Grossiord, J. L. (2008). Stabilisation of w/o/w double emulsion by polysaccharides as weak gels. *Colloids Surfaces a-Physicochemical Eng. Aspects* 316, 46–54. doi:10.1016/j.colsurfa.2007.08.019

Bezerra, T. L., and Ragauskas, A. J. (2016). A review of sugarcane bagasse for second-generation bioethanol and biopower production. *Biofuels Bioprod. Biorefining-Biofpr* 10, 634–647. doi:10.1002/bbb.1662

Bouyer, E., Mekhloufi, G., Rosilio, V., Grossiord, J. L., and Agnely, F. (2012). Proteins, polysaccharides, and their complexes used as stabilizers for emulsions: Alternatives to synthetic surfactants in the pharmaceutical field. *Int. J. Pharm.* 436, 359–378. doi:10.1016/j.ijpharm.2012.06.052

Cassani, J., Luna, H., Navarro, A., and Castillo, E. (2007). Comparative esterification of phenylpropanoids versus hydrophenylpropanoids acids catalyzed by lipase in organic solvent media. *Electron. J. Biotechnol.* 10, 0–513. doi:10.2225/vol10-issue4-fulltext-3

Chakar, F. S., and Ragauskas, A. J. (2004). Review of current and future softwood kraft lignin process chemistry. *Industrial Crops Prod.* 20, 131–141. doi:10.1016/j.indcrop.2004.04.016

Chen, H. Y., Liu, J. B., Chang, X., Chen, D. M., Xue, Y., Liu, P., et al. (2017). A review on the pretreatment of lignocellulose for high-value chemicals. *Fuel Process. Technol.* 160, 196–206. doi:10.1016/j.fuproc.2016.12.007

Cresnar, K. P., Zamboulis, A., Bikiaris, D. N., Aulova, A., and Zemljic, L. F. (2022). Kraft lignin/tannin as a potential accelerator of antioxidant and antibacterial properties in an active thermoplastic polyester-based multifunctional material. *Polymers* 14, 1532. doi:10.3390/polym14081532

Czaikoski, A., Gomes, A., Kaufmann, K. C., Liszbinski, R. B., de Jesus, M. B., and da Cunha, R. L. (2020). Lignin derivatives stabilizing oil-in-water emulsions: Technological aspects, interfacial rheology and cytotoxicity. *Industrial Crops Prod.* 154, 112762. doi:10.1016/j.indcrop.2020.112762

de la Torre, M. J., Moral, A., Hernandez, M. D., Cabeza, E., and Tijero, A. (2013). Organosolv lignin for biofuel. *Industrial Crops Prod.* 45, 58–63. doi:10.1016/j.indcrop.2012.12.002

Dias, O. A. T., Sain, M., Cesarino, I., and Leao, A. L. (2019). Development of high bio-content polypropylene composites with different industrial lignins. *Polym. Adv. Technol.* 30, 70–78. doi:10.1002/pat.4444

Dutta Banik, S., Nordblad, M., Woodley, J. M., and Peters, G. H. (2016). A correlation between the activity of candida Antarctica lipase b and differences in binding free energies of organic solvent and substrate. *ACS Catal.* 6, 6350–6361. doi:10.1021/acscatal.6b02073

Duval, A., Molina-Boisseau, S., and Chirat, C. (2013). Comparison of kraft lignin and lignosulfonates addition to wheat gluten-based materials: Mechanical and thermal properties. *Industrial Crops Prod.* 49, 66–74. doi:10.1016/j.indcrop.2013.04.027

Gellerstedt, G. (2015). Softwood kraft lignin: Raw material for the future. *Industrial Crops Prod.* 77, 845–854. doi:10.1016/j.indcrop.2015.09.040

Graber, M., Bousquet-Dubouch, M. P., Lamare, S., and Legoy, M. D. (2003). Alcoholysis catalyzed by candida Antarctica lipase b in a gas/solid system: Effects of water on kinetic parameters. *Biochimica Biophysica Acta-Proteins Proteomics* 1648, 24–32. doi:10.1016/s1570-9639(03)00027-x

Gravitis, J., Abolins, J., Tupciauskas, R., and Veveris, A. (2010). Lignin from steam-exploded wood as binder in wood composites. *J. Environ. Eng. Landsc. Manag.* 18, 75–84. doi:10.3846/jeelm.2010.09

Hulin, L., Husson, E., Bonnet, J. P., Stevanovic, T., and Sarazin, C. (2015). Enzymatic transesterification of kraft lignin with long acyl chains in ionic liquids. *Molecules* 20, 16334–16353. doi:10.3390/molecules200916334

Jaufurally, A. S., Teixeira, A. R. S., Hollande, L., Allais, F., and Ducrot, P.-H. (2016). Optimization of the laccase-catalyzed synthesis of (±)-syringaresinol and study of its thermal and antiradical activities. *ChemistrySelect* 1, 5165–5171. doi:10.1002/slct.201600543

Jin, H. Q., Shi, H. Q., Jia, W. C., Sun, Y. N., Sheng, X. R., Guo, Y. Z., et al. (2022). Green solvents-based molecular weight controllable fractionation process for industrial alkali lignin at room temperature. *Int. J. Biol. Macromol.* 207, 531–540. doi:10.1016/j.ijbiomac.2022.03.049

Kitamoto, Y., Kuruma, Y., Suzuki, K., and Hattori, T. (2015). Effect of solvent polarity on enantioselectivity in candida Antarctica lipase b catalyzed kinetic resolution of primary and secondary alcohols. *J. Org. Chem.* 80, 521–527. doi:10.1021/jo502521e

Lahive, C. W., Kamer, P. C. J., Lancefield, C. S., and Deuss, P. J. (2020). An introduction to model compounds of lignin linking motifs; synthesis and selection considerations for reactivity studies. *Chemsuschem* 13, 4238–4265. doi:10.1002/cssc.202000989

Liu, Q. Q., Luo, L., and Zheng, L. Q. (2018). Lignins: Biosynthesis and biological functions in plants. *Int. J. Mol. Sci.* 19, 335. doi:10.3390/ijms19020335

Lora, J. H., and Glasser, W. G. (2002). Recent industrial applications of lignin: A sustainable alternative to nonrenewable materials. *J. Polym. Environ.* 10, 39–48. doi:10.1023/a:1021070006895

Lu, Y. D., Joosten, L., Donkers, J., Andriulo, F., Slaghek, T. M., Phillips-Jones, M. K., et al. (2021). Characterisation of mass distributions of solvent-fractionated lignins using analytical ultracentrifugation and size exclusion chromatography methods. *Sci. Rep.* 11, 13937. doi:10.1038/s41598-021-93424-0

Lucia, A., van Herwijnen, H. W. G., and Rosenau, T. (2020). Wood-based resins and other bio-based binders for the production of mineral wool. *Holzforschung* 74, 539–550. doi:10.1515/hf-2019-0280

Majira, A., Godon, B., Foulon, L., van der Putten, J. C., Cezard, L., Thierry, M., et al. (2019). Enhancing the antioxidant activity of technical lignins by combining solvent fractionation and ionic-liquid treatment. *Chemsuschem* 12, 4799–4809. doi:10.1002/cssc.201901916

Maldhure, A. V., and Ekhe, J. D. (2017). Effect of modifications of lignin on thermal, structural, and mechanical properties of polypropylene/modified lignin blends. *J. Thermoplast. Compos. Mater.* 30, 625–645. doi:10.1177/0892705715610402

Martinez-Garcia, M., Gracia-Vitoria, J., Vanbroekhoven, K., Dejonghe, W., and Satyawali, Y. (2023). Selective enzymatic esterification of lignin-derived phenolics for the synthesis of lipophilic antioxidants. *Antioxidants* 12, 657. doi:10.3390/antiox12030657

Meng, X. Z., Crestini, C., Ben, H. X., Hao, N. J., Pu, Y. Q., Ragauskas, A. J., et al. (2019). Determination of hydroxyl groups in biorefinery resources via quantitative 31P NMR spectroscopy. *Nat. Protoc.* 14, 2627–2647. doi:10.1038/s41596-019-0191-1

Miles-Barrett, D. M., Montgomery, J. R. D., Lancefield, C. S., Cordes, D. B., Slawin, A. M. Z., Lebl, T., et al. (2017). Use of bisulfite processing to generate high-beta-o-4 content water soluble lignosulfonates. *Acs Sustain. Chem. Eng.* 5, 1831–1839. doi:10.1021/acssuschemeng.6b02566

Miletic, N., Abetz, V., Ebert, K., and Loos, K. (2010). Immobilization of candida Antarctica lipase b on polystyrene nanoparticles. *Macromol. Rapid Commun.* 31, 71–74. doi:10.1002/marc.200900497

Mustranta, A., Forssell, P., and Poutanen, K. (1993). Applications of immobilized lipases to transesterification and esterification reactions in nonaqueous systems. *Enzyme Microb. Technol.* 15, 133–139. doi:10.1016/0141-0229(93)90037-3

Pion, F., Reano, A. F., Ducrot, P.-H., and Allais, F. (2013). Chemo-enzymatic preparation of new bio-based bis- and trisphenols: New versatile building blocks for polymer chemistry. *RSC Adv.* 3, 8988–8997. doi:10.1039/C3RA41247D

Ponomarenko, J., Lauberts, M., Dizhbite, T., Lauberte, L., Jurkjane, V., and Telysheva, G. (2015). Antioxidant activity of various lignins and-ligninrelated phenylpropanoid units with high and low molecular weight. *Holzforschung* 69, 795–805. doi:10.1515/hf-2014-0280

Pouteau, C., Dole, P., Cathala, B., Averous, L., and Boquillon, N. (2003). Antioxidant properties of lignin in polypropylene. *Polym. Degrad. Stab.* 81, 9–18. doi:10.1016/s0141-3910(03)00057-0

Ralph, J., Lundquist, K., Brunow, G., Lu, F., Kim, H., Schatz, P., et al. (2004). Lignins: Natural polymers from oxidative coupling of 4-hydroxyphenyl- propanoids. *Phytochem. Rev.* 3, 29–60. doi:10.1023/B:PHYT.0000047809.65444.a4

Reano, A. F., Pion, F., Domenek, S., Ducrot, P. H., and Allais, F. (2016). Chemo-enzymatic preparation and characterization of renewable oligomers with bisguaiacol moieties: Promising sustainable antiradical/antioxidant additives. *Green Chem.* 18, 3334–3345. doi:10.1039/c6gc00117c

Robertson, G. P., Hamilton, S. K., Barham, B. L., Dale, B. E., Izaurralde, R. C., Jackson, R. D., et al. (2017). Cellulosic biofuel contributions to a sustainable energy future: Choices and outcomes. *Science* 356, eaal2324. doi:10.1126/science.aal2324

Romhányi, V., Kun, D., and Pukánszky, B. (2018). Correlations among miscibility, structure, and properties in thermoplastic polymer/lignin blends. *ACS Sustain. Chem. Eng.* 6, 14323–14331. doi:10.1021/acssuschemeng.8b02989

Roy, R., Rahman, M. S., Amit, T. A., and Jadhav, B. (2022). Recent advances in lignin depolymerization techniques: A comparative overview of traditional and greener approaches. *Biomass* 2, 130–154. doi:10.3390/biomass2030009

Sharma, S., Sharma, A., Mulla, S. I., Pant, D., Sharma, T., and Kumar, A. (2020). "Lignin as potent industrial biopolymer: An introduction," in *Lignin: Biosynthesis and transformation for industrial applications*. Editors S. Sharma and A. Kumar (Cham: Springer International Publishing).

Sternberg, J., Sequerth, O., and Pilla, S. (2021). Green chemistry design in polymers derived from lignin: Review and perspective. *Prog. Polym. Sci.* 113, 101344. doi:10.1016/j.progpolymsci.2020.101344

Takada, M., Chandra, R., Wu, J., and Saddler, J. N. (2020). The influence of lignin on the effectiveness of using a chemithermomechanical pulping based process to pretreat softwood chips and pellets prior to enzymatic hydrolysis. *Bioresour. Technol.* 302, 122895. doi:10.1016/j.biortech.2020.122895

Thierry, M., Majira, A., Pegot, B., Cezard, L., Bourdreux, F., Clement, G., et al. (2018). Imidazolium-based ionic liquids as efficient reagents for the c-o bond cleavage of lignin. *Chemsuschem* 11, 439–448. doi:10.1002/cssc.201701668

Uppenberg, J., Ohrner, N., Norin, M., Hult, K., Kleywegt, G. J., Patkar, S., et al. (1995). Crystallographic and molecular-modeling studies of lipase b from candida Antarctica reveal a stereospecificity pocket for secondary alcohols. *Biochemistry* 34, 16838–16851.

doi:10.1021/bi00051a035

Vaishnav, P., and Demain, A. L. (2011). Unexpected applications of secondary metabolites. *Biotechnol. Adv.* 29, 223–229. doi:10.1016/j.biotechadv.2010.11.006

Vinardell, M. P., Ugartondo, V., and Mitjans, M. (2008). Potential applications of antioxidant lignins from different sources. *Industrial Crops Prod.* 27, 220–223. doi:10.1016/j.indcrop.2007.07.011

Weissbach, U., Dabral, S., Konnert, L., Bolm, C., and Hernandez, J. G. (2017). Selective enzymatic esterification of lignin model compounds in the ball mill. *Beilstein J. Org. Chem.* 13, 1788–1795. doi:10.3762/bjoc.13.173

Wen, J. L., Sun, S. L., Xue, B. L., and Sun, R. C. (2013). Recent advances in characterization of lignin polymer by solution-state nuclear magnetic resonance (nmr) methodology. *Mater. (Basel)* 6, 359–391. doi:10.3390/ma6010359

Weng, C. H., Peng, X. W., and Han, Y. J. (2021). Depolymerization and conversion of lignin to value-added bioproducts by microbial and enzymatic catalysis. *Biotechnol. Biofuels* 14, 84. doi:10.1186/s13068-021-01934-w

Wu, J. T., Liu, Q., Wang, C. H., Wu, W. J., and Han, W. P. (2021). Investigation of lignin as an alternative extender of bitumen for asphalt pavements. *J. Clean. Prod.* 283, 124663. doi:10.1016/j.jclepro.2020.124663

Wurzer, G. K., Bacher, M., Hettegger, H., Sumerskii, I., Musl, O., Fackler, K., et al. (2021). A general solvent system for the analysis of lignosulfonates by 31p nmr. *Anal. Methods* 13, 5502–5508. doi:10.1039/D1AY01241J

Yao, L., Yang, H. T., Meng, X. Z., and Ragauskas, A. J. (2022). Toward a fundamental understanding of the role of lignin in the biorefinery process. *Front. Energy Res.* 9. doi:10.3389/fenrg.2021.804086

Yu, Y., Shen, M. Y., Song, Q. Q., and Xie, J. H. (2018). Biological activities and pharmaceutical applications of polysaccharide from natural resources: A review. *Carbohydr. Polym.* 183, 91–101. doi:10.1016/j.carbpol.2017.12.009

Zakzeski, J., Bruijnincx, P. C., Jongerius, A. L., and Weckhuysen, B. M. (2010). The catalytic valorization of lignin for the production of renewable chemicals. *Chem. Rev.* 110, 3552–3599. doi:10.1021/cr900354u

Zhang, C. Q., Wu, H. C., and Kessler, M. R. (2015). High bio-content polyurethane composites with urethane modified lignin as filler. *Polymer* 69, 52–57. doi:10.1016/j.polymer.2015.05.046

Zhang, Y., Di, X. H., Wang, W., Song, M. J., Yu, Q., Wang, Z. M., et al. (2020). Kinetic study of lipase-catalyzed esterification of furoic acid to methyl-2-furoate. *Biochem. Eng. J.* 161, 107587. doi:10.1016/j.bej.2020.107587

Zhao, X. H., Zhang, Y. J., Wei, L. P., Hu, H. Y., Huang, Z. Q., Yang, M., et al. (2017). Esterification mechanism of lignin with different catalysts based on lignin model compounds by mechanical activation-assisted solid-phase synthesis. *Rsc Adv.* 7, 52382–52390. doi:10.1039/c7ra10482k

Zhou, N. N., Thilakarathna, W., He, Q. S., and Rupasinghe, H. P. V. (2022). A review: Depolymerization of lignin to generate high-value bio-products: Opportunities, challenges, and prospects. *Front. Energy Res.* 9. doi:10.3389/fenrg.2021.758744

frontiers | Frontiers in Chemistry

TYPE Original Research
PUBLISHED 19 October 2023
DOI 10.3389/fchem.2023.1270730

OPEN ACCESS

EDITED BY
Tamer S. Saleh,
National Research Centre, Egypt

REVIEWED BY
Mehdi Bahrami,
Fasa University, Iran
Amin Mohammadpour,
Shiraz University of Medical Sciences, Iran
Khalid Z. Elwakeel,
Jeddah University, Saudi Arabia

*CORRESPONDENCE
Ran Yu,
yuran@seu.edu.cn
Xin Zhu,
zhuxin@nies.org

RECEIVED 01 August 2023
ACCEPTED 09 October 2023
PUBLISHED 19 October 2023

CITATION
Luo M, Zhang X, Long T, Chen S, Zhan M, Zhu X and Yu R (2023), Modeling and optimization study on degradation of organic contaminants using nZVI activated persulfate based on response surface methodology and artificial neural network: a case study of benzene as the model pollutant.
Front. Chem. 11:1270730.
doi: 10.3389/fchem.2023.1270730

Modeling and optimization study on degradation of organic contaminants using nZVI activated persulfate based on response surface methodology and artificial neural network: a case study of benzene as the model pollutant

Moye Luo[1,2], Xiaodong Zhang[2], Tao Long[2], Sheng Chen[3], Manjun Zhan[4], Xin Zhu[2]* and Ran Yu[1]*

[1]Department of Environmental Science and Engineering, School of Energy and Environment, Southeast University, Nanjing, China, [2]State Environmental Protection Key Laboratory of Soil Environmental Management and Pollution Control, Nanjing Institute of Environmental Sciences, Ministry of Ecology and Environment, Nanjing, China, [3]Geo-engineering Investigation Institute of Jiangsu Province, Nanjing, China, [4]Nanjing Research Institute of Environmental Protection, Nanjing Environmental Protection Bureau, Nanjing, China

Due to the complicated transport and reactive behavior of organic contamination in groundwater, the development of mathematical models to aid field remediation planning and implementation attracts increasing attentions. In this study, the approach coupling response surface methodology (RSM), artificial neural networks (ANN), and kinetic models was implemented to model the degradation effects of nano-zero-valent iron (nZVI) activated persulfate (PS) systems on benzene, a common organic pollutant in groundwater. The proposed model was applied to optimize the process parameters in order to help predict the effects of multiple factors on benzene degradation rate. Meanwhile, the chemical oxidation kinetics was developed based on batch experiments under the optimized reaction conditions to predict the temporal degradation of benzene. The results indicated that benzene (0.25 mmol) would be theoretically completely oxidized in 1.45 mM PS with the PS/nZVI molar ratio of 4: 1 at pH 3.9˚C and 21.9 C. The RSM model predicted well the effects of the four factors on benzene degradation rate (R^2 = 0.948), and the ANN with a hidden layer structure of [8-8] performed better compared to the RSM (R^2 = 0.980). In addition, the involved benzene degradation systems fit well with the Type-2 and Type-3 pseudo-second order (PSO) kinetic models with R^2 > 0.999. It suggested that the proposed statistical and kinetic-based modeling approach is promising support for predicting the chemical oxidation performance of organic contaminants in groundwater under the influence of multiple factors.

KEYWORDS

benzene, activated persulfate, response surface methodology, artificial neural network, kinetics

1 Introduction

The widespread use of organics in industrial production and the lack of management of organic wastewater leakage and discharge have led to an increasing threat of organic contaminants to the public safety of subsurface ecosystems (Padhi and Gokhale, 2017). Benzene, as an important aromatic compound existing in pesticide intermediates and petroleum products, is widely used as an organic solvent in the industry (Liu et al., 2010; Zhao et al., 2020). Benzene has the potential to readily infiltrate the subsurface milieu during various stages of its lifecycle, encompassing production, storage, and transportation. Its inclusion in the U.S. EPA's National Priorities List is attributed to its well-documented carcinogenic, teratogenic, and mutagenic properties, which are observed in both its liquid and gaseous states (Xu Q. et al., 2021; Agency, 2023). Subsurface environmental exposure to benzene has become a global environmental problem (Singh and Fulekar, 2010; Padhi and Gokhale, 2014). Therefore, the rapid and precise remediation of benzene-contaminated groundwater to reduce public risk has become a widespread concern.

Among the many remediation strategies for organic compound contaminated groundwater, *in situ* chemical oxidation (ISCO) has attracted much attention for its advantages of economy and high efficiency (Matzek and Carter, 2016). At present, the sulfate radical-based advanced oxidation processes ($SO_4^{\cdot-}$ – AOPs) have been widely used in the remediation of organic contamination in groundwater. Persulfate (PS) is considered to be a promising oxidant, which degrades organic contaminants by producing sulfate free radicals. PS is often used in conjunction with activators to form highly active species during ISCO (Liang et al., 2008). Nano-zero-valent iron (nZVI) is an activator with strong reactivity, high catalytic activity, and reducing ability (Lominchar et al., 2018; Cabrera-Reina et al., 2020). The successful applications of nZVI in the remediation of organic compound contaminated groundwater have been reported. Zhu et al. (Zhu et al., 2016) found that PS/nZVI system effectively alleviated the $SO_4^{\cdot-}$ quenched by Fe^{2+} in the traditional ISCO process. Song et al. (Song et al., 2019) indicated that PS/nZVI oxidized up to 80% of benzene-based contamination in a pilot scale field study. Nevertheless, the prevailing researches on PS/nZVI oxidation technology revolved in the refinement and optimization of individual parameters such as oxidant dose, activator dose, pH and temperature (Srivastava et al., 2021b). Owing to the heterogeneity and the complexity of subsurface surroundings, the outcomes attained were not universally generalizable. Consequently, it is necessary to develop a predictive approach that holistically incorporates the impacts of multiple process parameters and environmental factors on the oxidation effectiveness in a simpler and more flexible way to support the determination of the optimal process parameter combination for a specific scenario.

The traditional one-factor-at-a-time (OFAT) approach for process parameter optimization necessitates an excessive amount of time and runs to ensure precision in effect estimation, and its ability to determine the interaction between input variables and the optimal levels of various factors is limited (Sachaniya et al., 2020). The process-centered, statistics-based response surface methodology (RSM) overcomes these disadvantages. RSM is a statistical modeling method that uses multiple quadratic regression equations to fit the global functional relationship between the factors and the response values through reasonable experimental design (Amiri et al., 2019; Bahrami et al., 2019). By analyzing the response surface contour plot, the interactions among the process parameters and contaminant degradation rate in the PS/nZVI oxidation system of organic contamination in groundwater would be determined, and the optimal factor value could be predicted by regression equation (Kasiri et al., 2008). The commonly used RSM design methods include Box-Benkhen design (BBD) and Center Composite Design (CCD). It is generally believed that CCD was suitable for situations with multi-factor and continuous variables, and when the number of variables is small (three to seven variables), and BBD could reveal the interaction of multiple factors affecting the remediation effect by using fewer experimental groups than CCD (Ray et al., 2009).

However, the quadratic regression modeling, frequently employed in RSM, may prove inadequate for capturing the intricate relationships between these factors and the responses. Integrating Artificial neural network (ANN) as a modeling tool alongside RSM may further enrich our understanding of the intricate connections between inputs (characteristic factors) and outputs (degradation rate). ANN has garnered extensive utilization in diverse scientific and engineering domains for simulation and prediction purposes (Aycan DÜMencİ et al., 2021). Its ability to adapt, learn, identify, verify, and reproduce associations enables ANN to effectively interpret the interaction of highly complex factors in the remediation process of contaminated groundwater, and to simulate and predict degradation data through the analysis of characteristic parameters (Zafar et al., 2012). Currently, ANN has demonstrated its efficacy in tackling numerous challenging issues within the realm of environmental remediation, such as the prediction of the elimination of hazardous compounds from industrial wastewater and the precise management of diverse degradation processes associated with organic contaminants (Lenzi et al., 2016; Srivastava et al., 2021a).

Chemical degradation kinetic models play a vital role in providing insight into transient degradation rates and comprehending the chemical oxidation process, thereby furnishing crucial information for simulating site-specific contaminant degradation on a larger scale (Lominchar et al., 2018). At present, the pseudo-first-order kinetic model (PFO), pseudo-second-order kinetic model (PSO), and intraparticle diffusion kinetic model (IPD, W-M equation) have been demonstrated as the simplified mathematical models for simulating advanced oxidation process (Zulfiqar et al., 2019). Therefore, combining the chemical degradation kinetic model with the RSM-ANN approach may provide a deeper insight into the transient degradation processes within the system, thus furnishing a more realistic framework to guide practical applications. Currently, the RSM-ANN-kinetic approach has been successfully applied in the areas such as optimizing wastewater treatment processes (Nayak and Pal, 2020; Igwegbe et al., 2023) and evaluating catalyst performance (Fattahi et al., 2014; Kassahun et al., 2021).

Many studies have been carried out in modeling and optimizing the degradation of organic contaminants through activated PS oxidation techniques using kinetic models based on OFAT (Cabrera-Reina et al., 2020; Heidari et al., 2022; Conte et al.,

TABLE 1 Variables and levels used in factorial design.

Levels	Variables	Low level (−1)	Medium level (0)	High level (+1)
1	Oxidizer dose (X_1) (mM)	0.25	0.75	1.25
2	Activator dose (X_2)	2	4	6
3	pH (X_3)	5	7	9
4	Temperature (X_4) (°C)	15	20	25

2023). Other studies focused on modeling and optimizing the pollutant degradation process via activated PS using the combined approach of RSM and ANN (Zhang et al., 2018; Asgari et al., 2020; Qiu et al., 2021). However, few studies have systematically explored the effectiveness of the coupled RSM-ANN-kinetic approach in predicting the oxidation of organic contaminants in groundwater by activated PS.

In this study, the modeling approach coupling two optimization systems namely, RSM-BDD and ANN with kinetic model was innovatively implemented to optimize the benzene degradation process parameters and predict the effect of PS/nZVI oxidation system with benzene. The RSM models of four independent parameters, including PS dosage, nZVI dosage, pH, and temperature were established based on batch experiments. The simulation accuracy of the RSM models was optimized using ANN to enhance the prediction accuracy of the advanced oxidation degradation models based on statistical data. In addition, the kinetic models suitable for predicting the degradation process of benzene-contaminated groundwater by the PS/nZVI oxidation system were developed.

2 Materials and methods

2.1 Field sample

The soil and groundwater samples used in this study were collected from an abandoned pesticide factory in Jiangsu Province, China. Benzene, toluene, ethylbenzene, and xylene (BTEX) was found to contaminate the core area of the site. The soils used in this work were taken from the non-polluted area at the edge of the site, and the uncontaminated groundwater was obtained from the upstream of the contaminated site. The soil samples were dried (for a week) in a greenhouse before being screened, and collected with a particle size of less than 2 mm for later use.

2.2 Microcosm experiment setup

Benzene was added to the collected uncontaminated groundwater to a final concentration of 0.25 mM (equivalent to 20 mg/L). The groundwater was then aliquoted to the standard 40 mL threaded vials filled with the pre-prepared soil and capped with a Teflon/silicone gasket to prevent the volatilization of contaminants. PS (purity >98%, Sinopharm Chemical Reagent Co., Ltd., China) and nZVI (Sinopharm Chemical Reagent Co., Ltd., China) were added to the above vials according to experimentally designed concentrations of RSM-BBD and sodium hydroxide solution (0.1 M) and hydrochloric acid solution (0.1 M) were used for pH adjustment. All the microcosmic vials were kept for 12 h at the design temperature after uniform oscillation. Then the sample were filtered through a 0.45 μm membranes before analysis. The residual benzene concentration analysis was conducted using a gas chromatography-mass spectrometrometry system (GC-MS, 7890A/5975C, Agilent, United States) equipped with a capillary column (J&W Scientific DB-624 60 m × 0.25 mm × 1.4 μm, Agilent) after a purge and trap concentrator (Eclipse 4,552and4,660, OI Analytical, United States). Three parallel experiments were set in each group to eliminate experimental errors and determine the reproducibility of the results, and one blank control group was set without degradant to eliminate interference caused by adsorption. The removal rate of benzene was calculated by the following formula:

$$\text{Benzene removal efficiency} = \frac{C_0 - C}{C_0} \times 100\% \quad (1)$$

C_0 and C were the concentrations of benzene in the system at the beginning and the end of the reaction.

2.3 Experimental designs with RSM method

Design Expert software (DES, Version 11.0) was used to analyze the influence of different environmental parameters on the degradation rate of benzene (response) in contaminated groundwater. A four-variable with three-level BBD experiments with three central points were designed to investigate the degradation trend of benzene in contaminated groundwater in the PS/nZVI oxidation system. Four independent variables were selected, including 1) oxidant (PS) dose, 2) activator (nZVI) dose, 3) pH, and 4) temperature, with three levels designed for each independent variable (coded values + 1, 0, and −1, see Table 1). The BBD-RSM method was used to design 29 sets of experiments under different process conditions (Table 2). These 4 independent factors were presented as X_1, X_2, X_3, and X_4, respectively for statistical computations. A quadratic model was established to fit the experimental results and show the relationship between all involved environmental variables. The quadratic model is as follows:

$$Y = b_0 + b_1X_1 + b_2X_2 + b_3X_3 + b_4X_4 + b_{12}X_1X_2 + b_{13}X_1X_3 + b_{14}X_1X_4 + b_{23}X_2X_3 + b_{24}X_2X_4 + b_{34}X_3X_4 + b_{11}X_1^2 + b_{22}X_2^2 + b_{33}X_3^2 + b_{44}X_4^2 + \varepsilon \quad (2)$$

In the formula, Y is the response factor predicting the degradation efficiency of benzene, b_0 is the fixed response value at the design centre point, b_i (i = 1, 2, 3, 4) represents the linear coefficient, b_{ii} (ii = 1, 2, 3, 4) is the quadratic coefficient, b_{ij} (i = 1, 2, 3,

TABLE 2 BBD matrix for experimental variables and response at four factor levels.

Std	Factors								Response	
	Oxidizer dose (X_1) (mM)		Activator dose (X_2)		pH (X_3)		Temperature (X_4) (°C)		Benzene degradation (%)	
	Actual	Coded	Actual	Coded	Actual	Coded	Actual	Coded	Actual	Predicted
1	0.25	−1	2	−1	7	0	20	0	57.40	58.06
2	1.25	+1	2	−1	7	0	20	0	90.13	90.67
3	0.25	−1	6	+1	7	0	20	0	72.11	70.61
4	1.25	+1	6	+1	7	0	20	0	96.25	89.66
5	0.75	0	4	0	5	−1	15	−1	83.05	83.69
6	0.75	0	4	0	9	+1	15	−1	58.82	59.75
7	0.75	0	4	0	5	−1	25	+1	84.27	85.70
8	0.75	0	4	0	9	+1	25	+1	68.26	64.13
9	0.25	−1	4	0	7	0	15	−1	70.59	69.26
10	1.25	+1	4	0	7	0	15	−1	92.18	97.18
11	0.25	−1	4	0	7	0	25	+1	69.04	63.74
12	1.25	+1	4	0	7	0	25	+1	94.68	96.53
13	0.75	0	2	−1	5	−1	20	0	78.40	79.77
14	0.75	0	6	+1	5	−1	20	0	87.36	88.74
15	0.75	0	2	−1	9	+1	20	0	63.45	67.70
16	0.75	0	6	+1	9	+1	20	0	77.06	74.66
17	0.25	−1	4	0	5	−1	20	0	69.02	70.31
18	1.25	+1	4	0	5	−1	20	0	98.29	96.92
19	0.25	−1	4	0	9	+1	20	0	53.52	54.26
20	1.25	+1	4	0	9	+1	20	0	80.17	83.82
21	0.75	0	2	−1	7	0	15	−1	66.18	66.36
22	0.75	0	6	+1	7	0	15	−1	72.65	67.62
23	0.75	0	2	−1	7	0	25	+1	77.56	81.52
24	0.75	0	6	+1	7	0	25	+1	85.43	83.58
25	0.75	0	4	0	7	0	20	0	81.84	80.92
26	0.75	0	4	0	7	0	20	0	81.93	78.93
27	0.75	0	4	0	7	0	20	0	81.48	78.80
28	0.75	0	4	0	7	0	20	0	83.08	84.25
29	0.75	0	4	0	7	0	20	0	83.69	85.75

4, j = 2, 3, 4) represents the effective coefficient of interactive regression, X_i, X_j represent independent variables, X_{ij} represents the effect of interaction between independent variables, X_i^2 and X_j^2 represent the secondary effects of each independent variable, ε is the statistical error. Analysis of variance (ANOVA) was used to analyse the established model. The significance of each coefficient in the equation was determined by the F test and *p*-value, and the prediction ability of the model was evaluated through graphical analysis and numerical analysis.

2.4 ANN design

The learning network used in this research was a hierarchical feedforward neural network with a back-propagation method, also known as an improved BP learning algorithm. Levenberg-Marquardt (LM) algorithm was selected for supervised learning functions to train the network because of its advantages of fast convergence and high computational accuracy (Srivastava et al., 2021a). The four variables determined by the response surface

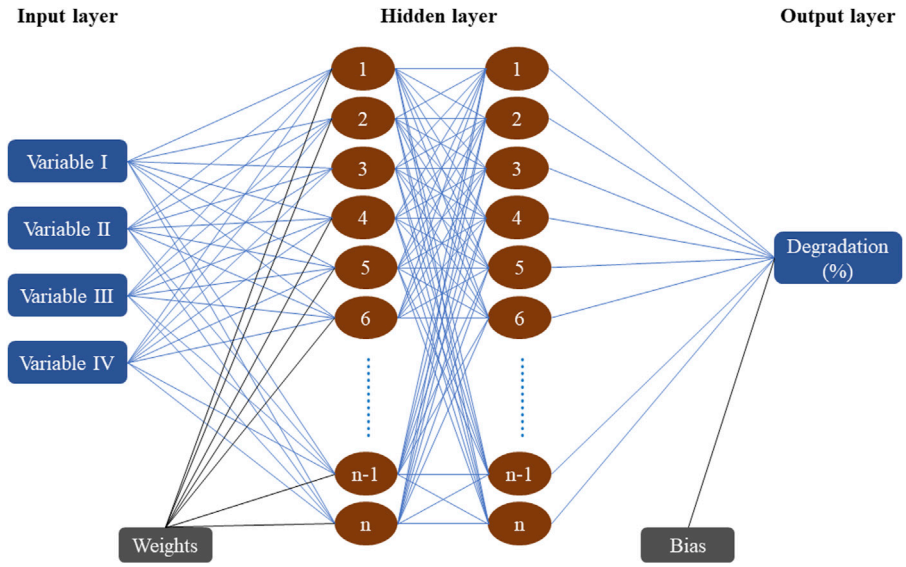

FIGURE 1
Schematic representation of neural network architecture with dual hidden layers.

TABLE 3 ANN model parameters.

Parameters	Value
Input layer neuron	04 (Oxidizer, Activator, pH, Temperature)
Output layer neuron	01 (Degradation rate)
Hidden layers	2
Transfer Function	TANSIG
Number of learning cycles	500 epochs
Performance function	MSE
Data division	70%–15% - 15% (Training -Test -Validation)
Learning function	Levenberg-Marquardt (LM)

method were used as input layer neurons (04), and output layer neuron (01) was set as the response of benzene degradation rate. This research adopted the double-layer structure network with better generalization ability than the single-hidden layer structure which optimized the network structure of the hidden layer (Figure 1). Estimation of the number of hidden layers and the number of neurons in each layer was the main difficulties in optimizing the structure of the neural network, this problem was solved by applying the thumb rule (Gazzaz et al., 2012). In all sample datasets, 70% were used for training the network learning, 15% were used for forming the verification set, and the other 15% were used for forming the network test set (Taqvi et al., 2017), to cross-validate the ANN model for benzene degradation by the PS/nZVI oxidation system. The specific model parameters in the ANN were shown in Table 3. The scenario settings used to optimize the hidden layer structure of the ANN model were shown in Table 4. The development of the ANN model was completed by MATLAB 9.8.0.1323502 (R2020A).

The prediction performance of the models was evaluated via error functions that include the coefficient of determination (R^2), root mean square error (RMSE), mean absolute deviation (MAD), and mean absolute percentage error (MAPE), expressed as:

$$R^2 = 1 - \frac{\sum_{I=1}^{N} (A_t - F_t)^2}{\sum_{I=1}^{N} (A_m - F_t)^2} \quad (3)$$

$$MAD = \frac{\sum_{i=1}^{n} |A_t - F_t|}{n} \quad (4)$$

$$RMSE = \sqrt{\frac{\sum_{i=1}^{n} (A_t - F_t)^2}{n}} \quad (5)$$

$$MAPE = \frac{\sum_{i=1}^{n} \left|\frac{A_t - F_t}{A_t}\right|}{n} \times 100 \quad (6)$$

Where A_t is the predicted value obtained by ANN or RSM, F_t is the experimental/observed value, A_m is the average of the predicted value, and n is the number of samples.

2.5 Kinetic model study

Under the optimum conditions given by RSM and ANN, the degradation kinetics of benzene with different concentrations (0.0625–1.25 mM) by the PS/nZVI oxidation system was studied. Degradation experiments were carried out on benzene solutions of specified concentrations based on optimized process parameters, and samples were collected at 20-min intervals to measure the residual benzene concentration in the system. The degradation results of benzene in the optimized experiment were modeled using the Pseudo-first order (PFO) and Pseudo-second order (PSO) kinetic models, which were widely used in the analysis of the degradation mechanism (Chowdhury et al., 2016). The diffusion mechanism of the degradation system

TABLE 4 Performance of ANN models with different structure of hidden layer (Bold values represent the optimal hidden layer structure).

Model id	Structure of hidden layer	R^2	MSE	RMSE	MAD	MAPE
BP1	1,1	0.8887	80.1415	8.9522	12.4607	0.3697
BP2	1,4	0.9221	76.6661	8.7559	13.464	0.3802
BP3	4,4	0.914	29.655	5.4456	13.3865	0.2768
BP4	4,8	0.9202	9.655	3.1072	8.6489	0.1712
BP5	**8,8**	**0.9801**	**0.8243**	**0.9079**	**3.0614**	**0.1564**
BP6	8,16	0.9172	4.0153	2.003	6.958	0.1748
BP7	16,16	0.9093	18.8257	4.3388	4.081	0.2582
BP8	16,32	0.8542	60.3357	7.7676	5.8504	0.1701
BP9	32,32	0.8341	92.1841	9.6012	13.7703	0.2858

was studied by the intraparticle diffusion (IPD) kinetic model (Zulfiqar et al., 2019).

i. PFO kinetic model

PFO kinetic model is an extensively adopted model to simulate the degradation process, which could be represented as follows:

$$\log(q_e - q) = \log(q_e) - K_1 t/2.303 \quad (7)$$

In the formula, K_1 (L/min) represents the degradation rate constant, q_e (mg/g) represents the degradation amount of benzene when the system reaches equilibrium, q (mg/g) represents the degradation amount of benzene at any time point in the reaction process, and t represents the time (min). The Curve Fitting Tool of MATLAB 9.8.0.1323502 (R2020A) was used to obtain the parameter values.

ii. PSO kinetic model

Five different forms of PSO kinetic models were used to fit the degradation rate results of benzene, namely,: Type-1 PSO, Type-2 PSO, Type-3 PSO, Type-4 PSO and Type-5 PSO. These Lagergren equations are extensively used for the degradation of liquid-solid phase based on solid capacity, and these PSO kinetic formulas could be expressed as following equations (Zulfiqar et al., 2018):

$$\frac{t}{q} = \frac{1}{K_2 q_e^2} + \frac{1}{q_e} t \quad \text{Type} - 1\ \text{PSO} \quad (8)$$

$$\frac{1}{q} = \left(\frac{1}{K_2 q_e^2}\right) \frac{1}{t} + \frac{1}{q_e} \quad \text{Type} - 2\ \text{PSO} \quad (9)$$

$$\frac{1}{t} = \frac{K_2 q_e^2}{q} - \frac{K_2 q_e^2}{q_e} \quad \text{Type} - 3\ \text{PSO} \quad (10)$$

$$\frac{q}{t} = K_2 q_e^2 - \frac{K_2 q_e^2 q}{q_e} \quad \text{Type} - 4\ \text{PSO} \quad (11)$$

$$\frac{1}{q_e - q} = \left(\frac{1}{q_e}\right) + K_2 t \quad \text{Type} - 5\ \text{PSO} \quad (12)$$

Where q_e (mg/g) and q (mg/g) respectively represent the amount of benzene removed by the oxidant per unit weight under equilibrium and at any time in the reaction process. K_2 (g/mg min) represents the PSO chemical degradation rate constants. Using Type-1 PSO, the graph against t *versus* t/q was plotted. The slope and intercept were used to achieve the values of constant factors. In term of Type-2 PSO kinetic model, the slope and intercept were used to receive the values of constant factors after plotting the graph against 1/t *versus* 1/q. In the case of Type-3 PSO kinetic equation, the graph between 1/q *versus* 1/t was plotted and obtained the constant values using slope and intercept. By using a Type-4 kinetic model, the graph plotted against q/t *versus* q for obtaining the values of constant factors from slope and intercept. Similarly, by employing the Type-5 PSO kinetic equation, the graph was plotted against t *versus* $1/(q_e\text{-}q)$ and calculate the values of K_2 and q_e by using the slope and intercept.

iii. IPD kinetic model

Another kinetic theory considered the controlling factor of the reaction rate of the PS/nZVI oxidation system from the perspective of solid-liquid mass transfer. The degradation process of the benzene molecules in the system could be summarized into three steps: 1) the mass transfer of the pollutant through the outer boundary layer at the solid-liquid interface; 2) the diffusion of the liquid through the solid-phase particle channels; and 3) the oxidative degradation of the $SO_4^{\cdot-}$ on the surface of the activator (Ocampo-Perez et al., 2011). The mass transfer rate or particle diffusion rate, or the coupling effect of the two mechanisms affected the overall degradation rate of nZVI-activated PS. The IPD kinetic model obtained the prediction of the reaction process through the correlation between $t^{0.5}$ and q_t, which was given by the following equation:

$$q_t = K_{id} t^{0.5} + C_i \quad (13)$$

Where K_{id} (mg/g $\text{min}^{0.5}$) and C_i refer to the rate constant of IPD and the boundary layer thickness of solid particles in the system, respectively.

3 Results and discussion

3.1 Statistical analysis for BBD-RSM

The BBD-RSM successfully simulated and predicted the PS/nZVI oxidation of benzene in synthetic contaminated groundwater at each design level of the four factors. The benzene degradation rate

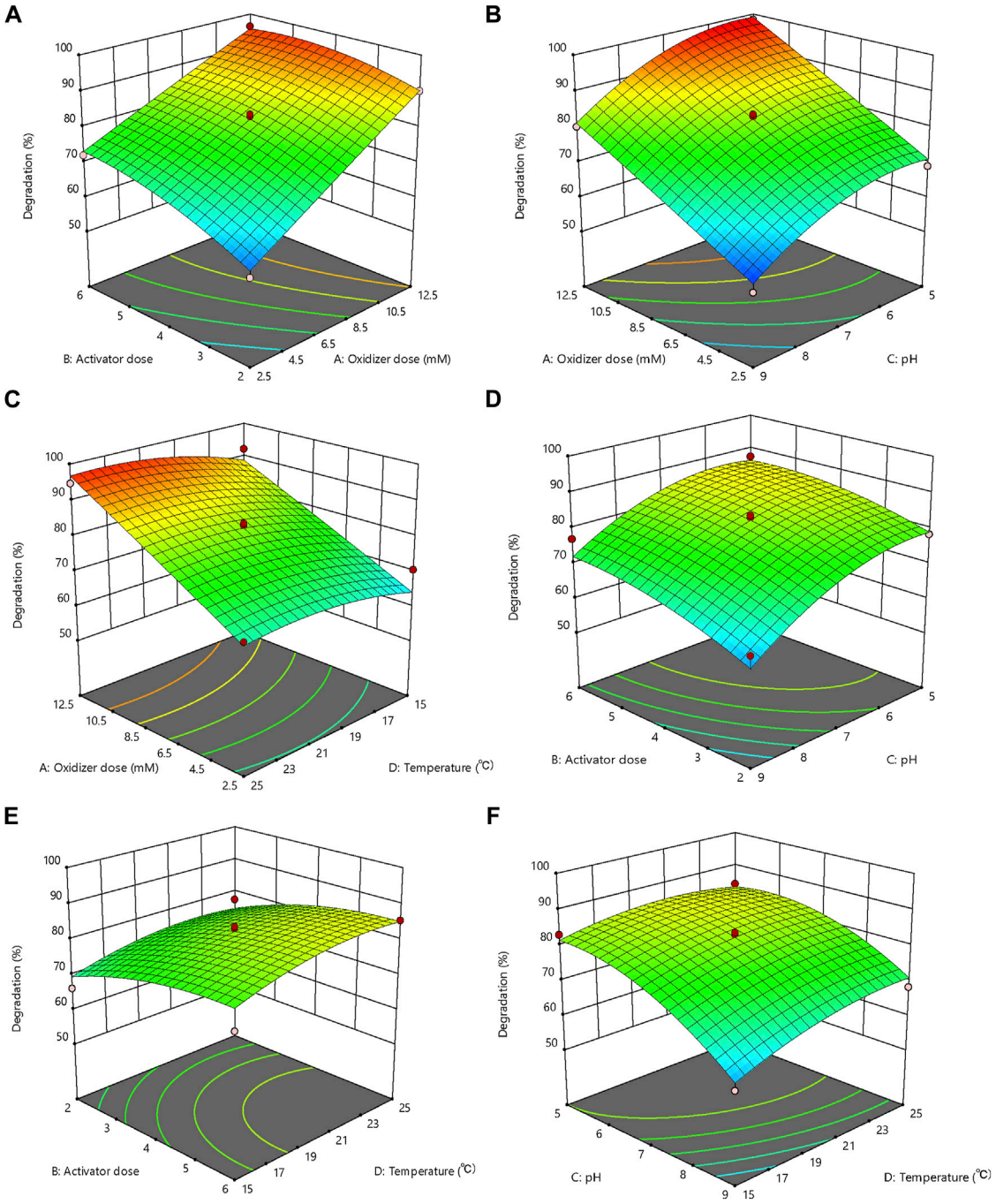

FIGURE 2
The response surface plot of benzene degradation as the function of **(A)** oxidizer and activator dosage, **(B)** pH and oxidizer dosage, **(C)** oxidizer dosage and temperature, **(D)** activator dosage and pH, **(E)** activator dosage and temperature, and **(F)** temperature and pH.

was between 53.52% and 98.29% in the batch experiments (Table 2). The ANOVA of BBD-RSM for benzene degradation with the PS/nZVI technology showed that the predicted degradation rate of the quadratic model was highly consistent ($p < 0.0001$) with the actual degradation rate (Supplementary Table S1).

The value of determination coefficient R^2 (0.948) indicated that the suggested quadratic equation was useful for predicting the benzene degradation rate in the PS/nZVI oxidation system within the range of experimental conditions. The R^2-adj value (0.895) of the RSM model was close enough to the R^2 value (0.948), indicating that the precision of the suggested response model was only slightly affected by the insignificant model terms. In general, R^2 values would increase by adding an item which has insignificant effects (p-value>0.05) to the proposed model, but the adjusted R^2 (R^2-adj) representing significant effects would not increase (Salarian et al., 2016). In addition, the predicted R^2 (0.792) also has favorable anastomose with the R^2-adj (0.895) (a difference of less than 0.2 was considered acceptable), further

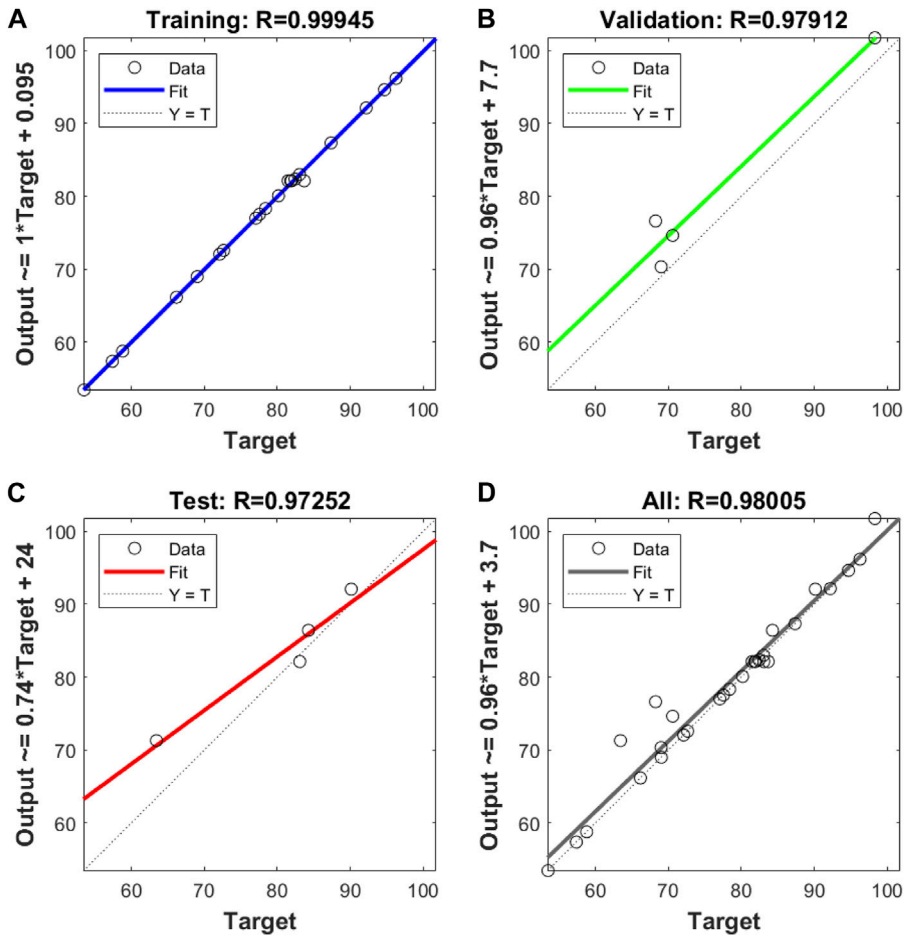

FIGURE 3
R^2 values of **(A)** training, **(B)** validation **(C)** testing, and **(D)** all data sets of ANN for benzene degradation (%) by PS/nZVI process.

indicating that the constructed BBD-RSM model had acceptable reproducibility.

According to the screening principle of the significance of RSM model variables (p-value <0.05 and F value >5), independent variables X_1, X_2, X_3, X_4, and X_3^2 were believed to have the most significant contributions to the accuracy of the suggested model and played the most important role in the simulation results. X_1 had the largest F value (146.20), indicating that its influence on the model was dominant compared with other factors. The measured results were fitted using a quadratic model, to achieve the following regression equations:

$$Y = 9.08 + 0.758X_1 + 0.280X_2 - 0.481X_3 + 0.174X_4 - 0.150X_1X_2 + 0.008X_1X_3 + 0.056X_1X_4 + 0.080X_2X_3 - 0.012X_2X_4 + 0.132X_3X_4 - 0.041X_1^2 - 0.152X_2^2 - 0.322X_3^2 - 0.158X_4^2 \quad (14)$$

The prediction accuracy of the proposed model for the degradation of benzene by the PS/nZVI oxidation system was verified using four different evaluation methods. The measured value and predicted value of the degradation rate of benzene showed a high degree of consistency (Supplementary Figure S1A), which provided the most direct evidence for the great performance of the prediction model. The externally studentized residual analysis showed that the error values were normally distributed along a mathematical expectation value μ) close to zero and a constant variance (σ^2), which confirmed the adequacy of the proposed model (Supplementary Figure S1B). In addition, the residuals of the experimental values and predicted values were uniformly distributed within a rectangular region centered at zero, indicating that the random error distribution of the proposed model was uniform and reasonable, which indirectly proved the stability of the RSM model (Supplementary Figure S1C,D).

The factor interaction analysis of the response surface methodology showed that the interaction between the PS and nZVI dosages exerted the dominant effects on the benzene degradation in synthetic contaminated groundwater (Figure 2A). In the response surface of the interaction between PS and nZVI dosages, the degradation rate of benzene showed a drastic increase with the dosage of PS increasing from 0.25 mM to 1.25 mM (53.52%–98.29%), while the effect of the activator on the reaction result was more moderate. However, when the amount of activator alone was controlled to increase from a 2:1 M ratio to 6:1, a 15% increase in benzene degradation rate was also observed (Figure 2A). This may owe to the $SO_4^{\cdot-}$ played a major role in benzene degradation, and the interaction between oxidants and activators directly determined the

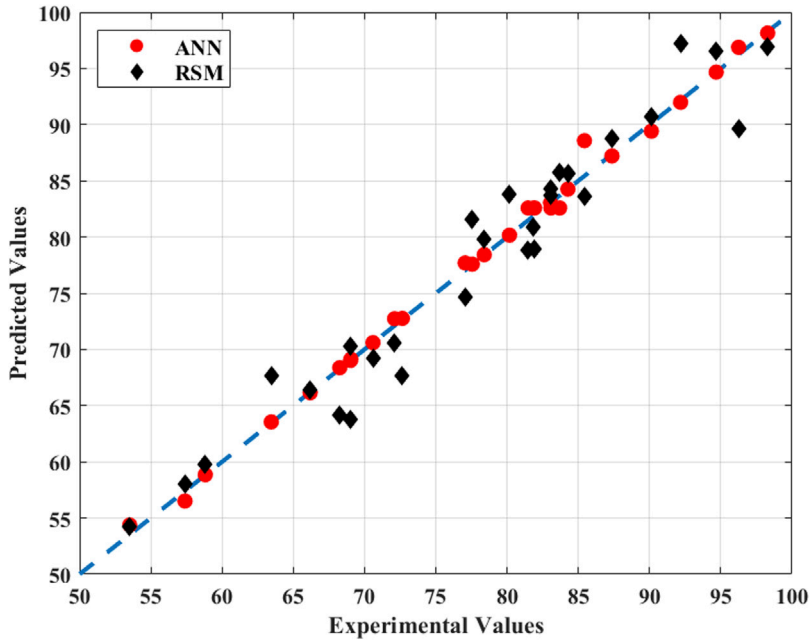

FIGURE 4
Comparison of experimental results with ANN/RSM predicted results.

rate of the $SO_4^{\cdot-}$ generation (Lominchar et al., 2018). Whereas, the effect of the activator on benzene degradation was much weaker, probably due to the activation potential not fully released at the set ratio with the oxidizer (Xu Z. et al., 2021). In conclusion, the PS and nZVI dosages were positively correlated with the benzene degradation rate, although PS dosage showed the more crucial role.

The response surface of the interaction between the PS dosage and pH showed that the degradation rate of benzene decreased with the transition from the acidic to the alkaline solution at a constant PS dosage (Figure 2B). Although both H^+ and OH^- have an activating effect on PS, alkaline conditions inhibited the transformation of nZVI to the activating Fe^{2+}, which suppressed the activation capacity of nZVI in the system. In addition, OH^- in the system would coordinate with Fe^{2+} and Fe^{3+} to form compounds with no activation efficiency, and reduce the activation ability (Rodriguez et al., 2014). Therefore, under acidic conditions and high PS dosage, the PS/nZVI oxidation system was more efficient for the benzene degradation. The response surface under the interaction between the PS dosage and temperature (Figure 2C), nZVI dosage and pH (Figure 2D), nZVI dosage and temperature (Figure 2E), and temperature and pH (Figure 2F) were relatively flat or behaved as the waterfall, which indicated that the interaction of these dependent variables had no significant effect, or was mainly caused by a single factor on the benzene degradation rate in synthetic contaminated groundwater.

3.2 Development of ANN model

The optimization results of the topological structure of the ANN model showed that when both hidden layers contain eight neurons, the evaluation function MSE, RMSE, MAD, and MAPE have the smallest values (Table 4, Scenario BP5), which represents a perfect match between the predicted value and the actual value. However, if the number of neurons in any hidden layer exceeds 8, the error of the ANN model increased instead. It was speculated that too many neurons in the hidden layer may lead to overfitting, increase the error of the test set and further increase the overall error function (Mutasa et al., 2020). Therefore, the optimal topology structure of the ANN model for the PS/nZVI oxidation of benzene was [4-8-8-1], in which case the lowest performance evaluation functions value and the highest R^2 value (0.9801) were obtained.

The simulation of benzene degradation rates using the ANN model structured in scenario BP5 showed high goodness of fit for training, validation, and test subset (Figures 3A–C), with the R^2 values of 0.9995, 0.9791, and 0.9725, respectively. In the overall model, the ANN model fits well with the "perfect fit line" (Figure 3D), and the R^2 value (0.9801) was slightly improved compared with that of the RSM model (0.948). Therefore, the developed cascade forward ANN model can be successfully used to simulate and predict the PS/nZVI oxidation of benzene in contaminated groundwater.

3.3 Comprehensive evaluation comparison between RSM and ANN models

The empirical modeling tool ANN displayed better prediction ability than RSM in the simulation and prediction of the PS/nZVI oxidation process of benzene in contaminated groundwater (Figure 4). We compared the observed values with the predicted values of the quadratic model obtained by RSM and the trained ANN model, respectively. Their predicted performance parameters were analyzed and the deviation of the calculated values from the

TABLE 5 PFO, Type-1 PSO, Type-2 PSO, Type-3 PSO, Type-4 PSO, Type-5 PSO, and IPD kinetic parameters for benzene in groundwater degradation onto PS/nZVI process.

Kinetic models	Parameters	Benzene concentrations				
		5 mg/L	10 mg/L	20 mg/L	50 mg/L	100 mg/L
PFO	K_1 (min^{-1})	0.07630	0.06455	0.05910	0.04733	0.4525
	q_e (mg/g)	2.665	1.975	1.195	1.355	0.9437
	R^2	0.7632	0.9084	0.995	0.9286	0.9759
Type-1 PSO	K_2 (min^{-1})	5.08E-05	1.27E-05	4.56E-04	5.13E-04	1.13E-04
	q_e (mg/g)	3.4321	6.2069	21.3873	40.3136	74.6969
	R^2	0.8385	0.5034	0.9827	0.9895	0.9699
Type-2 PSO	K_2 (min^{-1})	7.43E-05	3.95E-06	3.31E-04	4.00E-04	6.53E-04
	q_e (mg/g)	25.3872	150.3307	35.1989	64.4745	175.5618
	R^2	0.9995	0.9978	0.9964	0.9927	0.9886
Type-3 PSO	K_2 (min^{-1})	7.35E-05	4.69E-08	3.26E-04	3.93E-04	6.19E-04
	q_e (mg/g)	25.5277	137.0321	35.4286	64.8468	179.1892
	R^2	0.9995	0.9978	0.9964	0.9927	0.9886
Type-4 PSO	K_2 (min^{-1})	4.94E-05	9.92E-06	3.76E-04	4.05E-04	8.12E-04
	q_e (mg/g)	30.8333	97.2306	33.5975	64.272	161.9772
	R^2	0.821	0.398	0.9441	0.9489	0.8721
Type-5 PSO	K_2 (min^{-1})	2.33E-05	5.55E-05	0.000267	0.000478	0.000124
	q_e (mg/g)	44.03	43.48	52.69	61.56	141.2
	R^2	0.9965	0.9975	0.9436	0.9777	0.9796
IPD	K_{id} (mg/g $min^{0.5}$)	0.6002	1.242	1.995	3.851	9.334
	C_i	−1.937	−3.97	−1.389	7.607	−3.024
	R^2	0.9866	0.9979	0.9632	0.9085	0.9373

actual values of the two models was plotted. Compared with the RSM, the predicted value distribution of ANN was closer to the actual value. The evaluation function values for ANN were lower, and the values of the R^2 were closer to 1, which were signs of a well-fitted model (Supplementary Table S2). The highly predictive performance of the ANN was due to its ability to extract the basic interaction between dependent variables and independent variables with high accuracy without considering the degree of nonlinearity between variables, whereas the RSM only allowed fitting data based on mathematical equations (Lopez et al., 2017). It is generally accepted that RSM is usually used for the whole process of industrial system design starting from the experimental design. Its advantage reflects in putting forward more credible suggestions on the optimization of process parameters (Jiang et al., 2020). By contrast, ANN may be more suitable for processing massive experimental data, and focus on providing and establishing more detailed interrelationships between independent variables and dependent variables (Kasiri et al., 2008). Therefore, ANN may be a more powerful and flexible empirical modelling tool for remediation simulations of groundwater contaminated by organic compounds.

3.4 External validation of the model

Three groups of process parameters recommended by the proposed models that should completely degrade benzene in synthetic contaminated groundwater were selected and the predictive ability of the proposed models was externally validated by replicated experiments (Supplementary Table S3). The results showed that under the condition of complete degradation of benzene predicted by the RSM model, the measured degradation rates of the three experimental groups were 100%, 99.87%, and 98.79%, respectively, and the predicted benzene degradation rates by the trained ANN (BP5, which with the best predictive performance) were 99.86%, 99.98%, and 99.10%, respectively. The agreement between the experimental and predicted values indicated that it was feasible to use the proposed model to simulate the actual degradation situation. The MSE between the predicted and measured values of the two models were 0.4937 (RSM) and 0.0426 (ANN), respectively, which indicated that the simulation errors of both models were acceptable in the external validation phase, but ANN still outperformed RSM.

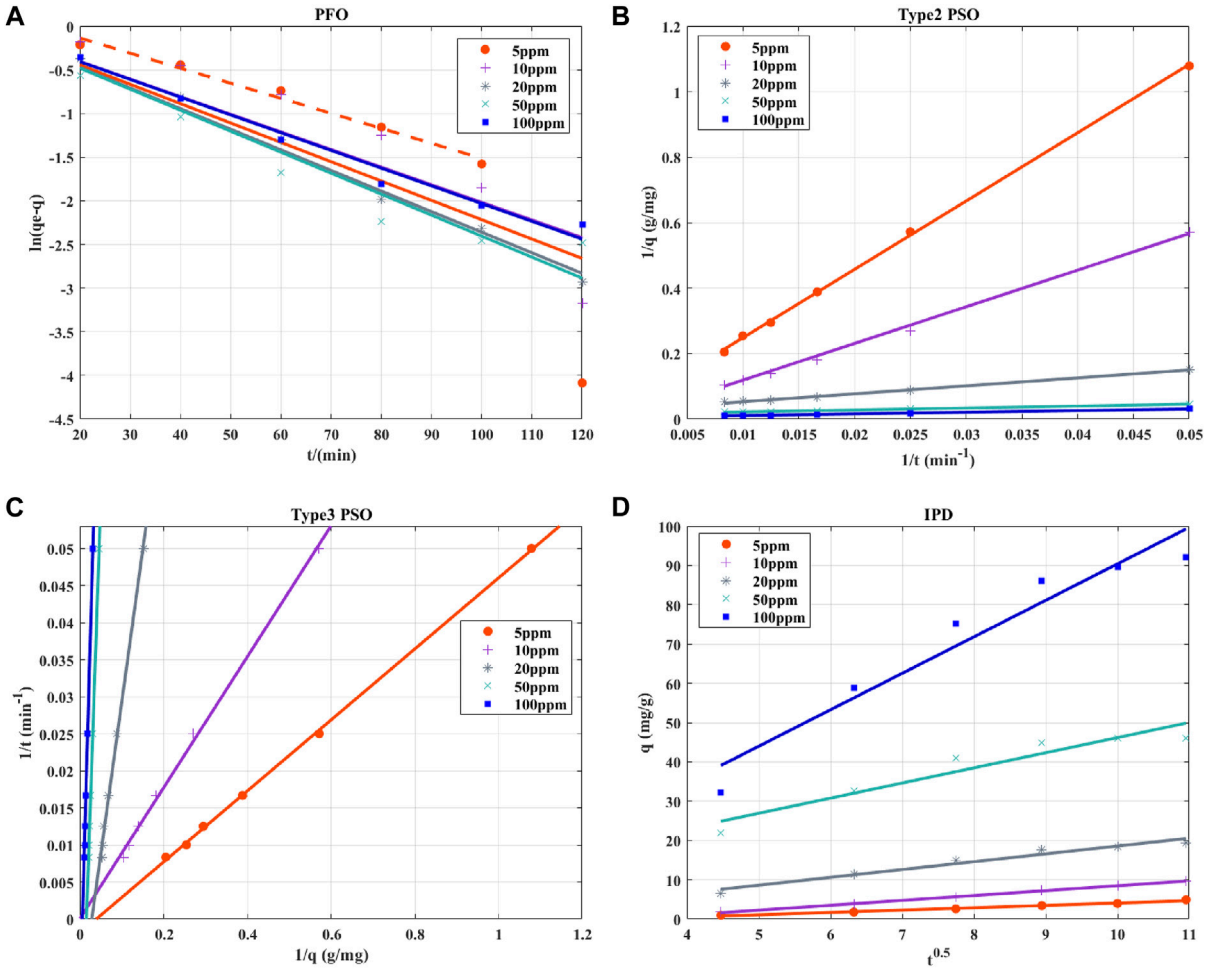

FIGURE 5
(A) PFO, **(B)** Type-2 PSO, **(C)** Type-3 PSO and **(4)** IPD kinetic models for benzene removal at optimized conditions given by suggested model.

3.5 Reaction kinetic studies

The kinetic parameters (q_e, K_1 and K_2) and correlation coefficients (R^2) of benzene degradation in synthetic contaminated groundwater by the PS/nZVI oxidation system were determined by linear regression method (Table 5). The R^2 values of different types of kinetic models were distributed between 0.3982 and 0.9995, and all types of kinetic models fit the experimental data well except for very few scenarios (e.g., Type-1 and Type-4 PSO at 10 mg/L benzene). The linear fitting diagram of the kinetic model showed that the fitting curve of the PFO deviated significantly from the experimental results (Figure 5A), and the parameter values of the PFO model also showed no significant regularity during the increase of benzene concentration from 0.0625 mM to 1.25 mM (Table 5), indicating that the PFO kinetic model may not be a reasonable model to explain the benzene degradation process. Type-2 and Type-3 PSO kinetic models showed the best fitting with the observed data of benzene degradation within the focused benzene concentration range of 0.0625–1.25 mM (Figures 5B,C), with R^2 values exceeding 0.99. The relationship between benzene degradation concentration *versus* time was more appropriately explained using these two types of PSO kinetic models, and they were fitted using 1/t *versus* 1/q or 1/q *versus* 1/t as the independent and dependent variables, respectively. Meanwhile, the instantaneous reaction rate models for different benzene initial concentrations can be selected from the Type-2 and Type-3 PSO kinetic models in Table 5. In addition, the results showed that the equilibrium benzene degradation amount (q_e) in PSO kinetic models were positively correlated with benzene concentration, and the rate constant K showed a trend of gradual increase with the pollutant concentration. The trend of the K value was opposite to the phenomenon observed by Zulfiqar et al. (Zulfiqar et al., 2019). This may be attributed to the increase in benzene concentration, which leads to higher collision probability between free radical particles and benzene molecules in the system, resulting in improved reaction rate (Shuchi et al., 2021).

In the IPD kinetic model, as the initial benzene concentration increased from 0.0625 mM, the value of diffusivity constant K_{id} increased from 0.6002 to 9.334 mg/g $min^{0.5}$ (Table 5). This may be due to the stronger reaction driving force induced by the higher benzene concentration and thus affected the mass transfer rate in the reaction process (Cheung et al., 2007). However, it has been reported that the linear curves of negative boundary layer thickness (C_i) and the linear curve of q_t *versus* $t^{0.5}$ would not exceed zero at all concentrations (Abdelwahab and Amin, 2013). The IPD model was considered to be unable to reasonably explain the mechanism of the PS/nZVI oxidation technology due to abnormality in

the fitted C_i values (Figure 5D). Therefore, type II and type III PSO maybe the reasonable models to explain the benzene degradation process by the PS/nZVI oxidation system.

4 Conclusion

In this work, the modeling approach coupling BBD-RSM and modified ANN with kinetic model was implemented to optimize the benzene degradation process parameters and predict the effect of PS/nZVI oxidation system. The results indicated that the modeled optimum levels of variables were 1.45 mM PS with a Na^+/nZVI molar ratio of 4:1 at pH 3.9°C and 21.9°C, under which 0.25 mM of benzene would theoretically be completely removed. The ANN model had better prediction performance compared with RSM, due to its strong nonlinear fitting ability. The structure of the hidden layer and the number of neurons contained in each layer significantly affected the predictive performance of the ANN. By employing the thumb rule during the test, we found that when the structure of hidden layers was [8-8], the evaluation indices of the ANN reached the optimal level. Furthermore, the developed degradation reaction kinetics showed that Type-2 and Type-3 PSO kinetic models were more suitable to explain the benzene degradation process by the PS/nZVI oxidation system. Our study is expected to provide a new approach for modeling and optimization of chemical oxidative remediation of organic contamination in groundwater.

Data availability statement

The original contributions presented in the study are included in the article/Supplementary Material, further inquiries can be directed to the corresponding authors.

Author contributions

ML: Conceptualization, Methodology, Resources, Writing–original draft. XZ: Methodology, Writing–review and editing. TL: Funding acquisition, Writing–review and editing. SC: Methodology, Writing–review and editing. MZ: Validation, Writing–review and editing. XZ: Conceptualization, Funding acquisition, Methodology, Writing–review and editing. RY: Funding acquisition, Writing–review and editing.

Funding

The author(s) declare financial support was received for the research, authorship, and/or publication of this article. This work was supported by the National Key R&D Program of China (grant number 2018YFC1803100), the National Natural Science Foundation of China (grant number 52270119), and Foundation Program of Jiangsu Geological Engineering Survey Institute [grant number KY-202205]. Program of Nanjing Institute of Environmental Sciences, Ministry of Ecology and Environment: Integration of Ecological and Environmental Protection in Yangtze River Delta [grant number ZX2022QT047].

Conflict of interest

The authors declare that the research was conducted in the absence of any commercial or financial relationships that could be construed as a potential conflict of interest.

Publisher's note

Supplementary material

The Supplementary Material for this article can be found online at: https://www.frontiersin.org/articles/10.3389/fchem.2023.1270730/full#supplementary-material

References

Abdelwahab, O., and Amin, N. K. (2013). Adsorption of phenol from aqueous solutions by Luffa cylindrica fibers: kinetics, isotherm and thermodynamic studies. *Egypt. J. Aquatic Res.* 39 (4), 215–223. doi:10.1016/j.ejar.2013.12.011

Agency, U. S. E. P. (2023). *Superfund: national Priorities list (NPL)*. EPA.

Amiri, M. J., Bahrami, M., and Dehkhodaie, F. (2019). Optimization of Hg(II) adsorption on bio-apatite based materials using CCD-RSM design: characterization and mechanism studies. *J. Water Health* 17 (4), 556–567. doi:10.2166/wh.2019.039

Asgari, G., Shabanloo, A., Salari, M., and Eslami, F. (2020). Sonophotocatalytic treatment of AB113 dye and real textile wastewater using ZnO/persulfate: modeling by response surface methodology and artificial neural network. *Environ. Res.* 184, 109367. doi:10.1016/j.envres.2020.109367

Aycan Dümencİ, N., Cagcag Yolcu, O., Aydin Temel, F., and Turan, N. G. (2021). Identifying the maturity of co-compost of olive mill waste and natural mineral materials: modelling via ANN and multi-objective optimization. *Bioresour. Technol.* 338, 125516. doi:10.1016/j.biortech.2021.125516

Bahrami, M., Amiri, M. J., and Bagheri, F. (2019). Optimization of the lead removal from aqueous solution using two starch based adsorbents: design of experiments using response surface methodology (RSM). *J. Environ. Chem. Eng.* 7 (1), 102793. doi:10.1016/j.jece.2018.11.038

Cabrera-Reina, A., Miralles-Cuevas, S., Oller, I., Sánchez-Pérez, J. A., and Malato, S. (2020). Modeling persulfate activation by iron and heat for the removal of contaminants of emerging concern using carbamazepine as model pollutant. *Chem. Eng. J.* 389, 124445. doi:10.1016/j.cej.2020.124445

Cheung, W. H., Szeto, Y. S., and McKay, G. (2007). Intraparticle diffusion processes during acid dye adsorption onto chitosan. *Bioresour. Technol.* 98 (15), 2897–2904. doi:10.1016/j.biortech.2006.09.045

Chowdhury, S., Mandal, P. C., Zulfiqar, M., and Subbarao, D. (2016). "Development of ionothermal synthesis of titania nanomaterial for waste-water treatment," in *Advanced materials research* (Transactions Technical Publication), 537–541.

Conte, L. O., Legnettino, G., Lorenzo, D., Cotillas, S., Prisciandaro, M., and Santos, A. (2023). Degradation of Lindane by persulfate/ferrioxalate/solar light process: influential

operating parameters, kinetic model and by-products. *Appl. Catal. B-Environmental* 324, 122288. doi:10.1016/j.apcatb.2022.122288

Fattahi, M., Kazemeini, M., Khorasheh, F., and Rashidi, A. (2014). Kinetic modeling of oxidative dehydrogenation of propane (ODHP) over a vanadium-graphene catalyst: application of the DOE and ANN methodologies. *J. Industrial Eng. Chem.* 20 (4), 2236–2247. doi:10.1016/j.jiec.2013.09.056

Gazzaz, N. M., Yusoff, M. K., Aris, A. Z., Juahir, H., and Ramli, M. F. (2012). Artificial neural network modeling of the water quality index for Kinta River (Malaysia) using water quality variables as predictors. *Mar. Pollut. Bull.* 64 (11), 2409–2420. doi:10.1016/j.marpolbul.2012.08.005

Heidari, M., Sadeghi, M., Arbabi, M., Mardani, G., Sedehi, M., and Emadi, Z. (2022). Combination of nonionic surfactants with thermal-activated persulfate for simultaneous removal of phenanthrene and pyrene from alluvial soil: a kinetic study. *Soil and Sediment Contam.* 31 (4), 468–482. doi:10.1080/15320383.2021.1963668

Igwegbe, C. A., Obi, C. C., Ohale, P. E., Ahmadi, S., Onukwuli, O. D., Nwabanne, J. T., et al. (2023). Modelling and optimisation of electrocoagulation/flocculation recovery of effluent from land-based aquaculture by artificial intelligence (AI) approaches. *Environ. Sci. Pollut. Res.* 30 (27), 70897–70917. doi:10.1007/s11356-023-27387-2

Jiang, N., Zhao, Y., Shang, K., Lu, N., Li, J., and Wu, Y. (2020). Degradation of toluene by pulse-modulated multistage DBD plasma: Key parameters optimization through response surface methodology (RSM) and degradation pathway analysis. *J. Hazard. Mater.* 393, 122365. doi:10.1016/j.jhazmat.2020.122365

Kasiri, M. B., Aleboyeh, H., and Aleboyeh, A. (2008). Modeling and optimization of heterogeneous photo-fenton process with response surface methodology and artificial neural networks. *Environ. Sci. Technol.* 42 (21), 7970–7975. doi:10.1021/es801372q

Kassahun, S. K., Kiflie, Z., Kim, H., and Baye, A. F. (2021). Process optimization and kinetics analysis for photocatalytic degradation of emerging contaminant using N-doped TiO2-SiO2 nanoparticle: artificial Neural Network and Surface Response Methodology approach. *Environ. Technol. Innovation* 23, 101761. doi:10.1016/j.eti.2021.101761

Lenzi, G. G., Evangelista, R. F., Duarte, E. R., Colpini, L. M. S., Fornari, A. C., Menechini Neto, R., et al. (2016). Photocatalytic degradation of textile reactive dye using artificial neural network modeling approach. *Desalination Water Treat.* 57 (30), 14132–14144. doi:10.1080/19443994.2015.1064035

Liang, C., Huang, C. F., and Chen, Y. J. (2008). Potential for activated persulfate degradation of BTEX contamination. *Water Res.* 42 (15), 4091–4100. doi:10.1016/j.watres.2008.06.022

Liu, J.-H., Maity, J. P., Jean, J.-S., Chen, C.-Y., Chen, C.-C., and Ho, S.-Y. (2010). Biodegradation of benzene by pure and mixed cultures of Bacillus spp. *World J. Microbiol. Biotechnol.* 26 (9), 1557–1567. doi:10.1007/s11274-010-0331-9

Lominchar, M. A., Rodriguez, S., Lorenzo, D., Santos, N., Romero, A., and Santos, A. (2018). Phenol abatement using persulfate activated by nZVI, H2O2 and NaOH and development of a kinetic model for alkaline activation. *Environ. Technol.* 39 (1), 35–43. doi:10.1080/09593330.2017.1294203

Lopez, M. E., Rene, E. R., Boger, Z., Veiga, M. C., and Kennes, C. (2017). Modelling the removal of volatile pollutants under transient conditions in a two-stage bioreactor using artificial neural networks. *J. Hazard Mater* 324, 100–109. doi:10.1016/j.jhazmat.2016.03.018

Matzek, L. W., and Carter, K. E. (2016). Activated persulfate for organic chemical degradation: a review. *Chemosphere* 151, 178–188. doi:10.1016/j.chemosphere.2016.02.055

Mutasa, S., Sun, S., and Ha, R. (2020). Understanding artificial intelligence based radiology studies: what is overfitting? *Clin. Imaging* 65, 96–99. doi:10.1016/j.clinimag.2020.04.025

Nayak, A. K., and Pal, A. (2020). Statistical modeling and performance evaluation of biosorptive removal of Nile blue A by lignocellulosic agricultural waste under the application of high-strength dye concentrations. *J. Environ. Chem. Eng.* 8 (2), 103677. doi:10.1016/j.jece.2020.103677

Ocampo-Perez, R., Leyva-Ramos, R., Mendoza-Barron, J., and Guerrero-Coronado, R. M. (2011). Adsorption rate of phenol from aqueous solution onto organobentonite: surface diffusion and kinetic models. *J. Colloid Interface Sci.* 364 (1), 195–204. doi:10.1016/j.jcis.2011.08.032

Padhi, S. K., and Gokhale, S. (2017). Benzene biodegradation by indigenous mixed microbial culture: kinetic modeling and process optimization. *Int. Biodeterior. Biodegrad.* 119, 511–519. doi:10.1016/j.ibiod.2016.10.011

Padhi, S. K., and Gokhale, S. (2014). Biological oxidation of gaseous VOCs – rotating biological contactor a promising and eco-friendly technique. *J. Environ. Chem. Eng.* 2 (4), 2085–2102. doi:10.1016/j.jece.2014.09.005

Qiu, Y., Zhang, Q., Wang, Z. H., Gao, B., Fan, Z. X., Li, M., et al. (2021). Degradation of anthraquinone dye reactive blue 19 using persulfate activated with Fe/Mn modified biochar: radical/non-radical mechanisms and fixed-bed reactor study. *Sci. Total Environ.* 758, 143584. doi:10.1016/j.scitotenv.2020.143584

Ray, S., Lalman, J. A., and Biswas, N. (2009). Using the Box-Benkhen technique to statistically model phenol photocatalytic degradation by titanium dioxide nanoparticles. *Chem. Eng. J.* 150 (1), 15–24. doi:10.1016/j.cej.2008.11.039

Rodriguez, S., Vasquez, L., Costa, D., Romero, A., and Santos, A. (2014). Oxidation of Orange G by persulfate activated by Fe(II), Fe(III) and zero valent iron (ZVI). *Chemosphere* 101, 86–92. doi:10.1016/j.chemosphere.2013.12.037

Sachaniya, B. K., Gosai, H. B., Panseriya, H. Z., and Dave, B. P. (2020). Bioengineering for multiple PAHs degradation for contaminated sediments: response surface methodology (RSM) and artificial neural network (ANN). *Chemom. Intelligent Laboratory Syst.* 202, 104033. doi:10.1016/j.chemolab.2020.104033

Salarian, A.-A., Hami, Z., Mirzaei, N., Mohseni, S. M., Asadi, A., Bahrami, H., et al. (2016). N-doped TiO2 nanosheets for photocatalytic degradation and mineralization of diazinon under simulated solar irradiation: optimization and modeling using a response surface methodology. *J. Mol. Liq.* 220, 183–191. doi:10.1016/j.molliq.2016.04.060

Shuchi, S. B., Suhan, M. B. K., Humayun, S. B., Haque, M. E., and Islam, M. S. (2021). Heat-activated potassium persulfate treatment of Sudan Black B dye: degradation kinetic and thermodynamic studies. *J. Water Process Eng.* 39, 101690. doi:10.1016/j.jwpe.2020.101690

Singh, D., and Fulekar, M. H. (2010). Benzene bioremediation using cow dung microflora in two phase partitioning bioreactor. *J. Hazard. Mater.* 175 (1), 336–343. doi:10.1016/j.jhazmat.2009.10.008

Song, Y., Fang, G., Zhu, C., Zhu, F., Wu, S., Chen, N., et al. (2019). Zero-valent iron activated persulfate remediation of polycyclic aromatic hydrocarbon-contaminated soils: an *in situ* pilot-scale study. *Chem. Eng. J.* 355, 65–75. doi:10.1016/j.cej.2018.08.126

Srivastava, A., Aghilesh, K., Nair, A., Ram, S., Agarwal, S., Ali, J., et al. (2021a). Response surface methodology and artificial neural network modelling for the performance evaluation of pilot-scale hybrid nanofiltration (NF) and reverse osmosis (RO) membrane system for the treatment of brackish ground water. *J. Environ. Manag.* 278, 111497. doi:10.1016/j.jenvman.2020.111497

Srivastava, A., Aghilesh, K., Nair, A., Ram, S., Agarwal, S., Ali, J., et al. (2021b). Response surface methodology and artificial neural network modelling for the performance evaluation of pilot-scale hybrid nanofiltration (NF) and reverse osmosis (RO) membrane system for the treatment of brackish ground water. *J. Environ. Manag.* 278, 111497. doi:10.1016/j.jenvman.2020.111497

Taqvi, S. A., Tufa, L. D., Zabiri, H., Mahadzir, S., Shah Maulud, A., and Uddin, F. (2017). "Artificial neural network for anomalies detection in distillation column," in *Modeling, design and simulation of systems*. Editors M. S. Mohamed Ali, H. Wahid, N. A. Mohd Subha, S. Sahlan, M. A.Md. Yunus, and A. R. Wahap (Singapore: Springer), 302–311.

Xu, Q., Shi, F., You, H., and Wang, S. (2021a). Integrated remediation for organic-contaminated site by forcing running-water to modify alkali-heat/persulfate via oxidation process transfer. *Chemosphere* 262, 128352. doi:10.1016/j.chemosphere.2020.128352

Xu, Z., Huang, J., Fu, R., Zhou, Z., Ali, M., Shan, A., et al. (2021b). Enhanced trichloroethylene degradation in the presence of surfactant: pivotal role of Fe(II)/nZVI catalytic synergy in persulfate system. *Sep. Purif. Technol.* 272, 118885. doi:10.1016/j.seppur.2021.118885

Zafar, M., Kumar, S., Kumar, S., and Dhiman, A. K. (2012). Optimization of polyhydroxybutyrate (PHB) production by Azohydromonas lata MTCC 2311 by using genetic algorithm based on artificial neural network and response surface methodology. *Biocatal. Agric. Biotechnol.* 1 (1), 70–79. doi:10.1016/j.bcab.2011.08.012

Zhang, L. L., Ding, W., Qiu, J. T., Jin, H., Ma, H. K., Li, Z. F., et al. (2018). Modeling and optimization study on sulfamethoxazole degradation by electrochemically activated persulfate process. *J. Clean. Prod.* 197, 297–305. doi:10.1016/j.jclepro.2018.05.267

Zhao, B., Huang, F., Zhang, C., Huang, G., Xue, Q., and Liu, F. (2020). Pollution characteristics of aromatic hydrocarbons in the groundwater of China. *J. Contam. Hydrology* 233, 103676. doi:10.1016/j.jconhyd.2020.103676

Zhu, C., Fang, G., Dionysiou, D. D., Liu, C., Gao, J., Qin, W., et al. (2016). Efficient transformation of DDTs with persulfate activation by zero-valent iron nanoparticles: a mechanistic study. *J. Hazard. Mater.* 316, 232–241. doi:10.1016/j.jhazmat.2016.05.040

Zulfiqar, M., Chowdhury, S., Sufian, S., and Omar, A. A. (2018). Enhanced photocatalytic activity of Orange II in aqueous solution using solvent-based TiO2 nanotubes: kinetic, equilibrium and thermodynamic studies. *J. Clean. Prod.* 203, 848–859. doi:10.1016/j.jclepro.2018.08.324

Zulfiqar, M., Samsudin, M. F. R., and Sufian, S. (2019). Modelling and optimization of photocatalytic degradation of phenol via TiO2 nanoparticles: an insight into response surface methodology and artificial neural network. *J. Photochem. Photobiol. A Chem.* 384, 112039. doi:10.1016/j.jphotochem.2019.112039

frontiers | Frontiers in Chemistry

TYPE Original Research
PUBLISHED 02 November 2023
DOI 10.3389/fchem.2023.1252996

OPEN ACCESS

EDITED BY
Florent Allais,
AgroParisTech—Institut des Sciences et Industries du Vivant et de L'environnement, France

REVIEWED BY
Marco Rabuffetti,
University of Milan, Italy
Teodora Bavaro,
University of Pavia, Italy

*CORRESPONDENCE
Alessio Romerio,
alessio.romerio@unimib.it

RECEIVED 04 July 2023
ACCEPTED 26 September 2023
PUBLISHED 02 November 2023

CITATION
Romerio A and Peri F (2023), Cleaner synthesis of preclinically validated vaccine adjuvants.
Front. Chem. 11:1252996.
doi: 10.3389/fchem.2023.1252996

Cleaner synthesis of preclinically validated vaccine adjuvants

Alessio Romerio* and Francesco Peri

Department of Biotechnology and Biosciences, Università degli Studi di Milano-Bicocca, Milano, Italy

We developed synthetic glycophospholipids based on a glucosamine core (FP compounds) with potent and selective activity in stimulating Toll-Like Receptor 4 (TLR4) as agonists. These compounds have activity and toxicity profiles similar to the clinically approved adjuvant monophosphoryl lipid A (MPLA), included in several vaccine formulations, and are now in the preclinical phase of development as vaccine adjuvants in collaboration with Croda International PLC. FP compound synthesis is shorter and less expensive than MPLA preparation but presents challenges due to the use of toxic solvents and hazardous intermediates. In this paper we describe the optimization of FP compound synthesis. The use of regio- and chemoselective reactions allowed us to reduce the number of synthesis steps and improve process scalability, overall yield, safety, and Process Mass Intensity (PMI), thus paving the way to the industrial scale-up of the process.

KEYWORDS

optimization, green chemistry, TLR4, glycolipid, medicinal chemistry

1 Introduction

Vaccine introduction in 1798 rapidly decreased the morbidity and mortality of several deadly diseases, and their widespread use has been the reason for the eradication or attenuation of several pandemic diseases, including smallpox and the recent COVID-19 (Hilleman, 2000; Stewart and Devlin, 2006; Kayser and Ramzan, 2021; Zheng et al., 2022).

Many modern vaccines, the so-called subunit vaccines, only include parts of the pathogen, normally protein antigens, instead of the entire pathogen. They are therefore safer but less immunogenic than the vaccines containing the whole attenuated pathogen, thus requiring the addition of adjuvants (Delany et al., 2014).

Molecular adjuvants are chemical entities able to induce a strong, but controlled, immune response, thus increasing the efficacy of the vaccine in terms of the quality, intensity, and duration of immune response (Shah et al., 2017; O'Hagan et al., 2020).

The use of adjuvants contributes to the reduction of the amount of antigen required in a vaccine formulation. As normally the antigen is the most expensive component, adjuvants also have the potential to decrease the cost of vaccines, making them more accessible in developing countries (Delany et al., 2014; O'Hagan et al., 2020).

There is high industrial interest in this field: the market size of vaccine adjuvants has been valued at 895 million USD in 2021. This value is expected to double by 2027, with a forecast compound growth rate of 10.6% year-on-year, due to the involvement of companies such as GlaxoSmithKline PLC, Merck KGaA, and Croda International PLC (Industry Research, 2022).

However, the rate of innovation in the field of vaccine adjuvants has been extremely low in the last 20 years, and a formulation of aluminium salts (Alum) has been the only clinically approved adjuvant for years and even today very few compounds have been approved for human use (Li et al., 2008; Lambrecht et al., 2009; Shah et al., 2017).

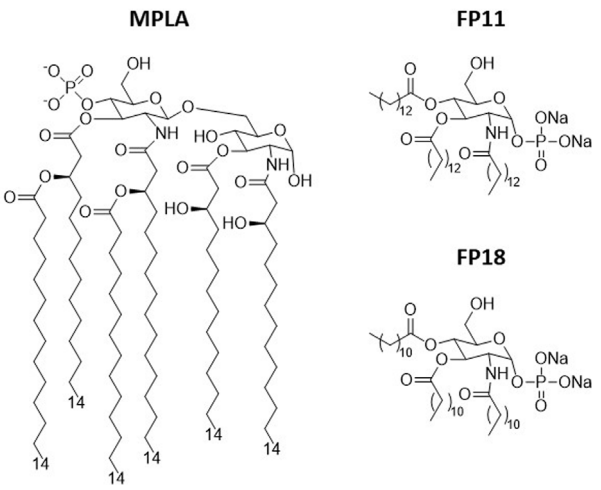

FIGURE 1
MPLA and FP compounds.

A clinically approved vaccine adjuvant is monophosphoryl Lipid A (MPLA, Figure 1), (Mata-Haro et al., 2007; Casella and Mitchell, 2008) a well-characterized Toll-like Receptor 4 (TLR4) agonist, included in several vaccine formulations (Cervarix®, Fendrix®, Shingrix®, Mosquirix®, Pollinex-Quattro®) (O'Hagan et al., 2020).

Synthetic MPLA (Avanti Lipids, United States) is a complex molecule, with a disaccharide core and linear and branched fatty acid chains with a stereogenic center at C-3, whose synthesis is long (>25 steps) with elevated production costs (the present cost of MPLA is ~230 USD/mg in the American market). Furthermore, MPLA synthesis (699800P Avanti MPLA (PHAD®); Reed and Carter, 2014) is based on a massive use of "red" or environmentally undesirable solvents such as Pyridine or DMF (Alfonsi et al., 2008; Byrne et al., 2016; Joshi and Adhikari, 2019).

We recently synthesized **FP11** and **FP18** compounds (Figure 1), that showed to have similar activity to MPLA in inducing innate immune response in animal models of vaccination (Facchini et al., 2021). Their mechanism of action has been studied and it is based on the selective stimulation of the Toll-Like Receptor 4 (TLR4), one of the most important molecular switches of innate immunity (Peri and Minotti, 2019; Facchini et al., 2021). FP compounds possess however a simpler molecular formula and a shorter synthesis than MPLA. FPs retain most of the proinflammatory properties of MPLA when tested *in vitro* as well as the adjuvancy *in vivo* (Facchini et al., 2021). Due to their potential as cheaper substitutes for MPLA, we are developing FPs in collaboration with Croda International PLC as efficient substitutes for MPLA as vaccine adjuvants.

Albeit definitively more convenient than MPLA, FP compound synthesis (Scheme 1) still presents some hurdles that may prevent industrial scalability and cause a significant environmental impact, having a Process Mass Intensity (PMI) of 3.0×10^4 (Facchini et al., 2021). Furthermore, it employs a large amount of undesirable solvents (e.g., Pyridine, DMF, DCM), as defined by the Pfizer solvent bundle book, a widely accepted guideline for medicinal chemistry (Alfonsi et al., 2008; Byrne et al., 2016; Joshi and Adhikari, 2019). Here, we report a new, improved synthesis for FP designed with industrial scalability and environmental indications as guidelines. While the new synthesis still requires limited amounts of hazardous solvents, it is significantly shorter than the original one, translating in higher overall yields and lower PMI, a very important result due to the forecasted launch on the market of FP.

2 Results and discussion

We aimed to optimize the synthetic pathway of **FP11** and **FP18** (Scheme 1) in terms of the number of synthesis steps, safety, and environmental impact.

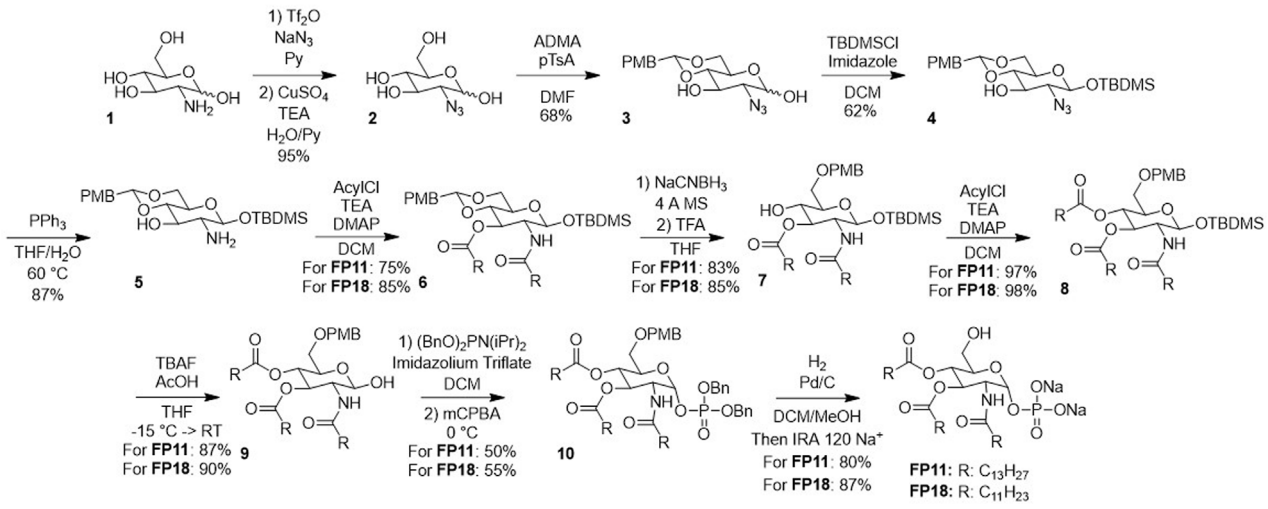

SCHEME 1
Previous synthesis of FP compounds.

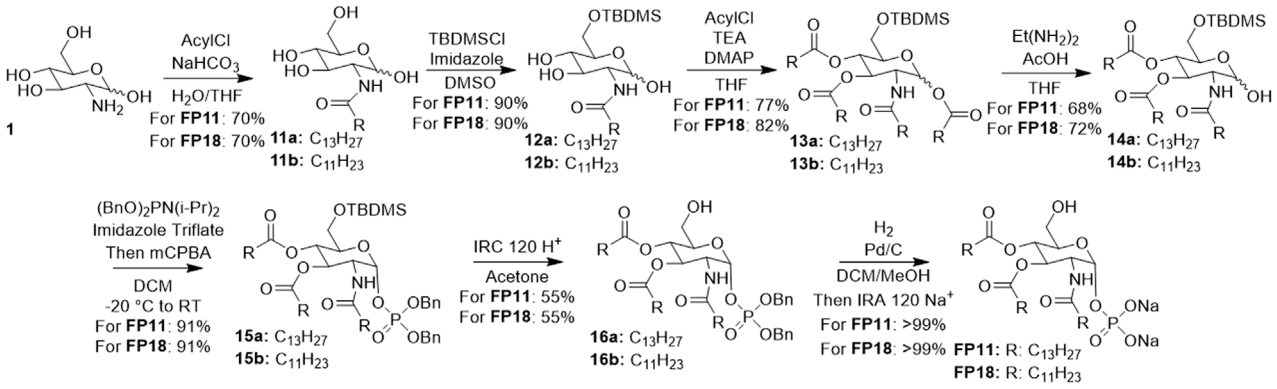

SCHEME 2
Cleaner synthesis for FP compounds, charcaterized by a reduced number of reactions, a limited use of red solvent, reduced PMI and increased yield.

TABLE 1 Solvent screening for the silylation reaction.

Solvent	Concentration (M)	Imidazole (Eq.)	Temperature (°C)	Yield (%)
Py	0.1	-	70	50
Py	0,1	-	20	60
DMF	0.1	2.5	20	N/D
MeCN	0.1	2.5	20	N/D
DMSO	0.1	2.5	20	25
DMSO	0.05	2.5	65	20
tBuOH	0.05	1.5	85	N/D
DMSO	0.05	1.5	20	90

The published synthesis requires 10 steps with an overall yield of 7%. A chromatographic purification is required for 8 reaction steps out of 10, directly impacting the PMI of the process, calculated to 3.0×10^4 (Peri and Minotti, 2019; Facchini et al., 2021).

Some synthetic steps have high safety and environmental hazards. For example, the first reaction requires the formation of a potentially explosive low molecular weight azide using the highly toxic pyridine as co-solvent; and high amounts of toxic and pollutant solvents such as DMF and DCM are abundantly used throughout the process.

Finally, the absence of chemical orthogonality between the protective groups does not allow for an easy selective deprotection, in the perspective of selectively functionalizing the C-6 hydroxyl group.

A new, versatile synthesis has been designed (Scheme 2) with a reduced number of synthetic steps (7) and purifications and less toxic solvents involved. The overall yield is 18% and a PMI of 9.8×10^3. This synthesis can be applied for both **FP11** and **FP18** by employing the correct lipid chain: reaction yields are very similar with a very narrow error range.

The first step is the acylation of the glucosamine on the 2-NH, exploiting its higher reactivity, so that it is not necessary to protect it anymore.

The second reaction is a silylation on the 6-OH of compound **11**, the only protection step in the synthesis: it is possible to regioselectively protect the more reactive primary alcohol over the other hydroxyls. However, the protecting group has to be carefully selected: a small one (e.g., TMS, TES) would not be selective enough; and a larger one (e.g., TBDPS, Trt) would prevent phosphorylation for sterical reasons. An additional challenge in this reaction was the choice of the solvent (Table 1), due to the poor solubility of the substrate both in aqueous and organic solvents. Initially, diluted pyridine was used, with a yield of 50%, but its extreme toxicity prompted us to search for a better medium. Several solvents were screened (i.e., MeCN, tBuOH, DMF) to no result, as the substrate failed to dissolve and the product was obtained only in traces. Finally, we managed to dissolve the substrate in DMSO at a low concentration (0.05 M) and to perform the reaction with a yield of 90%: therefore, we managed both to avoid pyridine and to reduce the PMI.

The third step of the pathway is the acylation of **12** on C-3 and C-4 hydroxyls. The reaction was first carried out in pyridine, which was eventually replaced with THF maintaining the high yield (80%) and reducing the hazards. The reaction stereochemistry at the anomeric carbon is dependent on the reaction conditions: short reaction time, high temperature and catalyst loading favor the formation of the thermodynamic α anomer, while longer reaction time, low temperature, and catalyst loading favor the formation of the kinetic β product (Romerio et al., 2023). As we have to remove

the anomeric lipid chain (*v. infra*), the anomeric configuration is not relevant and it is possible to choose the protocol most suitable to one's needs.

The fourth step is a regioselective deacylation of **13** with cleavage of the lipid chain in the anomeric position using a mixture of acetic acid and ethylenediamine. Interestingly, the anomeric acyl group acted as a leaving group in the presence of acids, and configuration seems to be retained (Zhang and Kováč, 1999).

Subsequent phosphorylation of **14** was performed using the phosphite to phosphate strategy, in which the compound undergoes a phosphitylation followed by one-pot oxidation to phosphate, similar to the previously published synthesis. This reaction is highly stereoselective: it always results in pure α configuration, independently from the starting configuration, as shown in several previous publications (Cighetti et al., 2014; Facchini et al., 2018; 2021; Peri and Minotti, 2019).

The 6-OH of **15** was then deprotected in mild conditions to avoid phosphate cleavage. Optimal cleavage conditions without concomitant reaction of protected phosphate consisted of the use of IRC 120 H^+ resin in acetone. The reaction proceeded with 55% yield, but recycling of unreacted **15** allowed to further enhance yield.

Benzyl groups on the phosphates of compound **16** were removed by catalytic hydrogenation, as in the original synthesis (Peri and Minotti, 2019; Facchini et al., 2021).

The new synthesis is scalable for industrial production, with higher overall yield, lower PMI, and minimum use of "undesirable" or "red" solvents (Alfonsi et al., 2008; Byrne et al., 2016; Joshi and Adhikari, 2019).

3 Conclusion

Here we reported a new synthesis for FP compounds: a class of chemically simplified analogues of the known vaccine adjuvant MPLA, whose synthesis is significantly long and expensive. Regio- and chemoselective reactions allowed a drastic reduction in the use of protecting groups. Consequently, we managed to reduce the number of steps needed for the synthesis, which increased the overall yield (from 7% to 18%) and reduced the PMI (from 3.0×10^4 to 9.8×10^3) of the process. Furthermore, we eliminated the first hazardous intermediate and greatly decreased the use of red solvents replacing them with green or yellow solvents (Acetone, DMSO, or THF).

The described optimized synthesis will be further adapted to safety requirements and employed for industrial upscaling and production of the new immunostimulating agents **FP11** and **FP18**.

4 Materials and methods

All reagents and solvents were purchased from commercial sources and used without further purifications, unless stated otherwise. Reactions were monitored by thin-layer chromatography (TLC) performed over Silica Gel 60 F254 plates (Merck®). Flash chromatography purifications were performed on silica gel 60 60–75 μm from a commercial source. Solvent removal by rotavapor was carried out at 40 °C for most solvents and 55 °C for toluene and water, unless otherwise stated. ^{1}H, ^{13}C, and ^{31}P NMR spectra were recorded with Bruker Advance 400 with TopSpin® software, or with NMR Varian 400 with Vnmrj software. Chemical shifts are expressed in ppm with respect to Me_4Si; coupling constants are expressed in Hz. The multiplicity in the ^{13}C spectra was deducted by APT experiments. Exact masses were recorded with Agilent 6500 Series Q-TOF LC/MS System. The purity of the final compounds was about 95% as assessed by quantitative NMR analysis. Optical rotation values were acquired with Anton Paar MCP 100 polarimeter with a Type II cell (l = 100 mm; Ø = 5 mm) operating at 20 °C.

4.1 Compound 11a

2-tetracanamido-2-deoxy-α,β-D-glucopyranose.

Glucosamine hydrochloride **1** (10 g, 46 mmol, 1 eq.) and $NaHCO_3$ (10.54 g, 124.2 mmol, 2.7 eq.) were dissolved in water (100 mL). Then, previously dissolved miristoyl chloride (12.5 g, 51.2 mmol, 1.1 eq.) in THF (100 mL) was added dropwise to the solution at 0 °C. A white solid started precipitating in the reaction flask. After 6 h stirring, the solution was filtered and a white solid was obtained, which was washed with 4 °C water. The solid was resuspended in 50 mL of HCl 0.5 M and stirred for 30 min. Afterward, the suspension was filtered again and the white solid was resuspended in 50 mL of THF. The white solid was again recovered by filtration. Excess water was then coevaporated with toluene under reduced pressure, to obtain the desired product **11a** as a white powder in 70% yield (12.50 g) as an anomeric mixture. The compound was used without further purification.

^{1}H NMR (400 MHz, DMSO-d6) δ 7.64 (d, $J_{NH\beta,\ H\text{-}2\beta}$ = *8.3 Hz*, 1H, NHβ), 7.50 (d, $J_{NH\alpha,\ H\text{-}2\alpha}$ = *8.0 Hz*, 4H, NHα), 6.46 (d, $J_{1\text{-}OH\beta,\ H\text{-}1\beta}$ = *6.3 Hz*, 1H, 1-OHβ), 6.41 – 6.36 (m, 3H, 1-OHα), 4.94 – 4.86 (m, 8H, H-1α+6-OHβ, 4-OHα), 4.78 (d, $J_{4\text{-}OH\beta,\ H\text{-}4\beta}$ = *5.2 Hz*, 1H, 4-OHβ), 4.57 (d, $J_{3\text{-}OH\alpha,\ H\text{-}3\alpha}$ = *5.1 Hz*, 3H, 3-OHα), 4.53 (t, $J_{3\text{-}OH\beta,\ H\text{-}3\beta}$ = *5.8 Hz*, 1H, 3-OHβ), 4.42 (dt, $J_{6\text{-}OH\alpha,\ H\text{-}6\alpha}$ = *11.5*, $J_{H\text{-}1\beta,\ 1\text{-}OH\beta}$ *5.5 Hz*, 5H, H-1β+6-OHα), 3.71 – 3.38 (m, 22H, H-3β, H-2α, H-2β, H-3α, H-4α, H-4β, H-5α, H-5β), 3.30 – 3.22 (m, 1H), 3.15 – 3.01 (m, 6H, H-6α, H-6β), 2.08 (dt, $J_{CH2\alpha,\ CH2\beta}$ = *10.9*, *7.4 Hz*, 10H, CH_2α chains), 1.47 (q, $J_{CH2\beta,\ CH2\alpha}$ = *7.0 Hz*, 11H, CH_2β chains), 1.24 (s, 80H, chains bulk), 0.90 – 0.82 (m, 15H, CH_3 chains).

^{13}C NMR (101 MHz, DMSO-d6) δ 173.3, 172.8, 96.1, 91.1, 77.2, 74.8, 72.5, 71.6, 71.4, 70.9, 61.6, 57.6, 54.7, 40.6, 40.4, 40.2, 40.0, 39.8, 39.6, 39.4, 36.2, 35.8, 31.8, 29.5, 29.5, 29.4, 29.4, 29.2, 29.2, 29.1, 25.8, 22.6, 14.4.

HRMS (ESI-Q-TOF): m/z [M + Na^+] calculated for $C_{20}H_{39}NNaO_6^+$: 412.2670. Found: 412.2674.

α_D = +19.45

4.2 Compound 11b

2-dodecanamido-2-deoxy-α,β-D-glucopyranose.

Glucosamine hydrochloride **1** (5 g, 23.2 mmol, 1 eq.) and $NaHCO_3$ (5.27 g, 63 mmol, 2.7 eq.) were dissolved in water (50 mL). Then, previously dissolved lauroyl chloride (5.60 g, 25.6 mmol, 1.1 eq.) in THF (50 mL) was added dropwise to the solution at 0 °C. A white solid started precipitating in the reaction

flask. After 6 h stirring, the solution was filtered and a white solid was obtained, which was washed with 4 °C water. The solid was resuspended in 30 mL of HCl 0.5 M and stirred for 30 min. Afterwards, the suspension was filtered again and the white solid was resuspended in 30 mL of THF. The white solid was again recovered by filtration. Excess water was then coevaporated with toluene under reduced pressure, to obtain the desired product **11b** as a white powder in 70% yield (6.00 g) as an anomeric mixture. The compound was used without further purification.

^{1}H NMR (400 MHz, DMSO-d6) δ 7.66 (d, $J_{NH\beta,\ H\text{-}2\beta}$ = *8.0 Hz*, 1H, NHβ), 7.49 (d, $J_{NH\alpha,\ H\text{-}2\alpha}$ = *7.7 Hz*, 4H, NHα), 6.44 (d, $J_{1\text{-}OH\beta,\ H\text{-}1\beta}$ = *6.2 Hz*, 1H, 1-OHβ), 6.39 – 6.33 (m, 4H, 1-OHα), 4.95 – 4.91 (m, 5H, H-1α+6-OHβ), 4.89 (d, $J_{4\text{-}OH\alpha,\ H\text{-}4\alpha}$ = *5.2 Hz*, 4H, 4-OHα), 4.79 (d, $J_{4\text{-}OH\beta,\ H\text{-}4\beta}$ = *4.8 Hz*, 1H, 4-OHβ), 4.59 (d, $J_{3\text{-}OH\alpha,\ H\text{-}3\alpha}$ = *5.1 Hz*, 4H, 3-OHα), 4.51 (t, $J_{3\text{-}OH\beta,\ H\text{-}3\beta}$ = *5.8 Hz*, 1H, 3-OHβ), 4.42 (dt, $J_{6\text{-}OH\alpha,\ H\text{-}6\alpha}$ = *11.5*, $J_{H\text{-}1\beta,\ 1\text{-}OH\beta}$ *5.5 Hz*, 5H, H-1β+6-OHα), 3.67 (dd, $J_{H\text{-}3\beta,\ H\text{-}2\beta}$ = *11.8*, $J_{H\text{-}3\beta,\ 3\text{-}OH\beta}$ = *4.6 Hz*, 1H, H-3β), 3.61 – 3.40 (m, 14H, H-2α, H-2β, H-3α, H-4α, H-4β, H-5α, H-5β), 3.11 (ddd, $J_{H\text{-}6\alpha a,\ H\text{-}6\alpha b}$ = *9.7*, $J_{H\text{-}6\alpha b,\ H\text{-}6\alpha a}$ = *8.2*, $J_{H\text{-}6\alpha a,\ H\text{-}5\alpha}$ = *5.1 Hz*, 4H, H-6α), 3.08 – 3.03 (m, 2H, H-6β), 2.08 (dt, $J_{CH2\alpha,\ CH2\beta}$ = *10.9*, *7.4 Hz*, 10H, CH_2α chains), 1.47 (q, $J_{CH2\beta,\ CH2\alpha}$ = *7.0 Hz*, 11H, CH_2β chains), 1.24 (s, 80H, chains bulk), 0.90 – 0.82 (m, 15H, CH_3 chains).

^{13}C NMR (101 MHz, DMSO-d6) δ 173.3, 172.8, 96.1, 91.0, 77.2, 74.7, 72.4, 71.5, 71.3, 70.8, 61.5, 57.5, 54.7, 40.5, 40.3, 40.1, 39.9, 39.7, 39.5, 39.3, 36.1, 35.7, 31.7, 29.5, 29.5, 29.4, 29.4, 29.2, 29.2, 29.1, 25.8, 22.6, 14.4.

HRMS (ESI-Q-TOF): m/z [M + Na^+] calculated for $C_{18}H_{35}NNaO_6^+$: 384.2361. Found: 384.2364.

α_D = +47.63

4.3 Compound 12a

2-tetradecanamido-2-deoxy-6-O-tert-butyldimethylsilyl-α,β-D-glucopyranose.

To a solution of **11a** (3.0 g, 7.7 mmol, 1 eq.) and imidazole (785 mg, 11.5 mmol, 1.5 eq.) in dimethylsulfoxide (154 mL, 0.05 M) a solution of TBDMSCl (1.28 g, 8.5 mmol, 1.1 eq.) in DCM (13 mL) was added dropwise under an inert atmosphere in an ice bath. Subsequently, the solution was allowed to return to room temperature and stirred overnight. Reaction, monitored by TLC (DCM/MeOH 9:1; Rf product: 0.50), was then stopped and the solution was concentrated under reduced pressure. Then it was diluted with EtOAc and washed three times with NH_4Cl. The organic phase thus obtained was dried with Na_2SO_4 and the solvent was removed by rotavapor. The crude product thus obtained (3.65 g) was resuspended in heptanes at 0 °C for 30 min. Then, the suspension was filtered under vacuum and the desired compound was recovered as a white solid. After filtration, 3.50 g of compound **12a** as a whiteish solid was obtained, in 90% yield.

^{1}H NMR (400 MHz, MeOD) δ 5.12 (d, $J_{H\text{-}1\alpha,\ H\text{-}2}$ = *4.2 Hz*, 0H; H-1α), 4.58 (d, $J_{H\text{-}1\beta,\ H\text{-}2}$ = *8.1 Hz*, 1H; H-1β), 4.03 – 3.92 (m, 1H; H-3), 3.83 (dd, $J_{H\text{-}4,\ H\text{-}3}$ = 11.2, $J_{H\text{-}4,\ H\text{-}5}$ = 5.3 Hz, 1H; H-4), 3.60 (t, J = 9.2 Hz, 1H; H-2), 3.49 – 3.22 (m, 5H; H-5, H-6), 2.25 (t, $J_{CH2\alpha,\ CH2\beta}$ = Hz, 2H, CH_2α chains), 1.64 (q, $J_{CH2\beta,\ CH2\alpha}$ = *7.3 Hz*, 2H, CH_2β chains), 1.33 (d, *J = 14.4 Hz*, 21H, Chains bulk), 1.03 – 0.80 (m, 14H; 3x CH_3 chains + 9x tBu-Si), 0.21 – 0.04 (m, 7H; Me-Si).

^{13}C NMR (101 MHz, MeOD) δ 175.9, 95.7, 76.8, 74.8, 70.7, 62.9, 57.3, 48.2, 48.0, 47.8, 47.6, 47.4, 47.2, 47.0, 36.1, 31.7, 29.4, 29.4, 29.2, 29.1, 29.1, 28.9, 25.6, 25.1, 24.8, 22.3, 17.9, 13.0, −6.5, −6.5.

HRMS (ESI-Q-TOF): m/z [M + Na^+] calculated for $C_{26}H_{53}NNaO_6Si^+$: 526.3534. Found: 526.3542.

α_D = −72.2

4.4 Compound 12b

2-dodecanamido-2-deoxy-6-O-tert-butyldimethylsilyl-α,β-D-glucopyranose.

To a solution of **11b** (3 g, 8.3 mmol, 1 eq.) and imidazole (850 mg, 12.4 mmol, 1.5 eq.) in dimethylsulfoxide (166 mL, 0.05 M) a solution of TBDMSCl (1.4 g, 9.1 mmol, 1.1 eq.) in DCM (14 mL) was added dropwise under an inert atmosphere in an ice bath. Subsequently, the solution was allowed to return to room temperature and stirred overnight. Reaction, monitored by TLC (DCM/MeOH 9:1; Rf product: 0.50), was then stopped and the solution was concentrated under reduced pressure. Then it was diluted with EtOAc and washed three times with NH_4Cl. The organic phase thus obtained was dried with Na_2SO_4 and the solvent was removed by rotavapor. The crude product thus obtained (3.85 g) was resuspended in heptanes at 0 °C for 30 min. Then, the suspension was filtered under vacuum and the desired compound was recovered as a white solid. After filtration, 3.71 g of compound **12b** as a whiteish solid was obtained, in 90% yield.

^{1}H NMR (400 MHz, DMSO-d6) δ 7.62 (d, $J_{NH,\ H\text{-}2}$ = *7.9 Hz*, 1H; NH), 6.43 (d, $J_{1\text{-}OH,\ H\text{-}1}$ = *6.4 Hz*, 1H; 1-OH), 4.90 (d, $J_{4\text{-}OH,\ H\text{-}4}$ = *6.5 Hz*, 1H; 4-OH), 4.77 (d, $J_{3\text{-}OH,\ H\text{-}3}$ = *9.1 Hz*, 1H; 3-OH), 4.42 (t, $J_{H\text{-}1,\ H\text{-}2}$ = *7.0 Hz*, 1H; H-1), 3.86 (d, $J_{H\text{-}6a,\ H\text{-}6b}$ = *10.8 Hz*, 1H; H-6a), 3.66 (dd, $J_{H\text{-}6b,\ H\text{-}6a}$ = *11.0*, $J_{H\text{-}6b,\ H\text{-}5}$ *4.6 Hz*, 1H; H-6b), 3.30 (d, $J_{H\text{-}2,\ NH}$ = *7.9 Hz*, 2H; H-2 + H-3), 3.14 – 2.98 (m, 2H; H-4 + H-5), 2.06 (t, $J_{CH2\alpha,\ CH2\beta}$ = *7.4 Hz*, 2H CH_2α chain), 1.48 (s, 2H; CH_2β chains), 1.24 (s, 20H; chain bulk), 0.94 – 0.74 (m, 12H 3x CH_3 chains + 9x tBu-Si), 0.05 (d, *J = 3.0 Hz*, 6H; Me-Si).

^{13}C NMR (101 MHz, DMSO-d6) δ 173.2, 95.9, 77.1, 74.8, 70.8, 63.6, 57.5, 40.6, 40.4, 40.2, 40.0, 39.8, 39.6, 39.4, 36.2, 31.8, 29.5, 29.5, 29.4, 29.4, 29.2, 29.1, 26.4, 25.8, 22.6, 18.6, 14.4, −4.7, −4.7.

HRMS (ESI-Q-TOF): m/z [M + Na^+] calculated for $C_{24}H_{49}NNaO_6Si^+$: 498.3226. Found: 498.3223.

α_D = +50.4

4.5 Compound 13a

1,3,4-tri-O-tetradecanoyl-2-tetradecanamido-2-deoxy-6-O-tert-butyldimethylsilyl-β-D-glucopyranose.

Compound **12a** (1.0 g, 2.0 mmol, 1 eq.) was dissolved in anhydrous THF (40 mL, 0.05 M) under Ar atmosphere at −20 °C. Triethylamine (1.1 mL, 8.0 mmol, 4.0 eq.) and miristoyl chloride (1.7 mL, 6.4 mmol, 3.2 eq.) were added dropwise to the solution, then also 4-dimethylaminopyridine (24 mg, 0.2 mmol, 0.1 eq.) was

added. The reaction was stirred over 2 h, then controlled by TLC (DCM/MeOH 95:5; Rf product: 0.98). Subsequently, the solution was diluted in EtOAc and washed with 1 M HCl. The organic phase thus obtained was dried with Na_2SO_4 and the solvent was removed by rotavapor. The crude product thus obtained (4 g) was purified by flash chromatography (Hep/EtOAc 93:7; Rf Product: 0.35). After purification, 1.80 g of compound **13a** was obtained, in 77% yield.

^{1}H NMR (400 MHz, $CDCl_3$) δ 5.72 (d, $J_{H\text{-}1,\ H\text{-}2}$ = *9.3 Hz*, 1H, H-1), 5.30 (m, 2H, NH, H-3), 5.08 (t, $J_{H\text{-}4,\ H\text{-}3}$ = *9.8 Hz*, 1H, H-4), 4.31 – 4.21 (m, 1H, H-2), 4.02 (dd, $J_{H\text{-}5,\ H\text{-}4}$ = *9.8*, $J_{H\text{-}5,\ H\text{-}6a}$ = *4.4 Hz*, 1H, H-5), 3.66 (d, $J_{H\text{-}6,\ H\text{-}5}$ = *3.8 Hz*, 2H, H-6), 2.28 – 2.20 (m, 4H; CH_2α chains), 2.12 (m, 2H; CH_2α chains), 1.56 (s, 14H; CH_2β chains), 1.24 (d, J = 2.9 Hz, 74H; chains bulk), 0.94 – 0.76 (m, 21H; 12x CH_3 chains + 9x tBu-Si), 0.04 (m, 6H; Me-Si).

^{13}C NMR (101 MHz, $CDCl_3$) δ 174.3, 173.0, 172.0, 91.7, 77.3, 77.0, 76.7, 70.7, 70.7, 68.3, 62.6, 52.2, 36.8, 34.2, 34.2, 31.9, 29.7, 29.7, 29.7, 29.6, 29.6, 29.5, 29.5, 29.5, 29.4, 29.3, 29.3, 29.2, 29.2, 25.9, 25.9, 25.6, 25.0, 24.9, 22.7, 18.4, 14.1, −5.3.

HRMS (ESI-Q-TOF): m/z [M + Na^+] calculated for $C_{68}H_{131}NNaO_9Si^+$: 1156.9485. Found: 1156.9478.

α_D = +32.2

4.6 Compound 13b

1,3,4-tri-O-dodecanoyl-2-dodecanamido-2-deoxy-6-O-tert-butyldimethylsilyl-α-D-glucopyranose.

Compound **12b** (2.0 g, 4.2 mmol, 1 eq.) was dissolved in anhydrous THF (84 mL, 0.05 M) under Ar atmosphere. Triethylamine (2.3 mL, 16.8 mmol, 4.0 eq.) and lauroyl chloride (3.2 mL, 13.4 mmol, 3.2 eq.) were added dropwise to the solution, then also 4-dimethylaminopyridine (1.63 g, 13.4 mmol, 3.2 eq.) was added. The reaction was stirred over 2 h, then controlled by TLC (DCM/MeOH 95:5; Rf product: 0.98). Subsequently, the solution was diluted in EtOAc and washed with 1 M HCl. The organic phase thus obtained was dried with Na_2SO_4 and the solvent was removed by rotavapor. The crude product thus obtained (4 g) was purified by flash chromatography (Hep/EtOAc 93:7; Rf Product: 0.31). After purification, 3.43 g of compound **13b** were obtained, in 82% yield.

^{1}H NMR (400 MHz, $CDCl_3$) δ 6.19 (d, $J_{H\text{-}1,\ H\text{-}2}$ = *3.7 Hz*, 1H; H-1), 5.51 (d, $J_{NH,\ H\text{-}2}$ = *8.8 Hz*, 1H; NH), 5.27 – 5.20 (m, 1H; H-3), 5.18 (m, 1H; H-4), 4.40 (ddd, $J_{H\text{-}2,\ H\text{-}3}$ = *10.6*, $J_{H\text{-}2,\ NH}$ = *8.9*, $J_{H\text{-}2,\ H\text{-}1}$ = *3.7 Hz*, 1H; H-2), 3.80 (ddd, $J_{H\text{-}5,\ H\text{-}4}$ = *9.6*, $J_{H\text{-}5,\ H\text{-}6a}$ = *4.5*, $J_{H\text{-}5,\ H\text{-}6b}$ = *2.7 Hz*, 1H; H-5), 3.68 – 3.61 (m, 2H; H-6), 2.38 (t, $J_{CH2\alpha,\ CH2\beta}$ = *7.5 Hz*, 2H; CH_2α chain), 2.28 – 2.22 (m, 4H; CH_2α chain), 2.07 (dt, $J_{CH2\alpha,\ CH2\beta}$ = *11.5*, *3.5 Hz*, 2H; CH_2α chain), 1.70 – 1.60 (m, 3H; CH_2β chains), 1.55 (ddd, $J_{CH2\beta,\ CH2\alpha}$ = *10.9*, *9.6*, *3.1 Hz*, 7H; CH_2β chains), 1.37 – 1.20 (m, 94H; chains bulk), 0.90 – 0.84 (m, 25H; 12x CH_3 chains + 9x tBu-Si), 0.04 – −0.01 (m, 7H; Me-Si).

^{13}C NMR (101 MHz, $CDCl_3$) δ 174.8, 172.9, 171.7, 171.5, 90.5, 77.3, 77.0, 76.7, 72.7, 70.8, 67.6, 62.0, 51.3, 36.6, 34.2, 34.2, 34.1, 33.8, 31.9, 29.6, 29.6, 29.5, 29.4, 29.4, 29.3, 29.3, 29.2, 29.2, 29.1, 29.1, 29.1, 25.8, 25.5, 24.9, 24.9, 24.9, 24.7, 22.7, 18.2, 14.1, −5.4.

HRMS (ESI-Q-TOF): m/z [M + Na^+] calculated for $C_{60}H_{115}NNaO_9Si^+$: 1044.8233. Found: 1044.8239.

α_D = +10.5

4.7 Compound 14a

2-tetradecanamido-2-deoxy-3,4-di-O-tetradecanoyl-6-O-tert-butyldimethylsilyl-β-D-glucopyranose.

Compound **13a** (1.8 g, 1.6 mmol, 1 eq.) was dissolved in anhydrous THF (40 mL, 0.04 M) with 1% v/v of water. Acetic acid (460 µL, 8.0 mmol, 5.0 eq.) and ethylenediamine (1.6 mL, 24.0 mmol, 15.0 eq.) were added to the solution at 0 °C. The reaction was allowed to return to room temperature (20 °C) and stirred for 4 h, then controlled by TLC (Hep/EtOAc 9:1; Rf starting material: 0.00). Subsequently, the solution was diluted in EtOAc and washed three times with 1 M HCl and three times with $NaHCO_3$. A white precipitate forms during the washings, which is removed by filtration and discarded (amide between lauric acid and ethylenediamine). The organic liquid phase thus obtained was dried with Na_2SO_4 and the solvent was removed by rotavapor. The crude product thus obtained (1.7 g) was purified by flash chromatography (Tol/EtOAc 85:15; Rf product: 0.21). After purification, 1.0 g of compound **14a** was obtained, in 68% yield.

^{1}H NMR (400 MHz, $CDCl_3$) δ 5.73 (d, $J_{NH,\ H\text{-}2}$ = *9.3 Hz*, 1H; NH), 5.34 – 5.22 (m, 2H; H-3 + H-1), 5.08 (m, 1H; H-4), 4.33 – 4.17 (m, 1H; H-2), 4.03 (ddd, $J_{H\text{-}5,\ H\text{-}4}$ = *10.1*, $J_{H\text{-}5,\ H\text{-}6a}$ = *4.5*, $J_{H\text{-}5,\ H\text{-}6b}$ = *3.2 Hz*, 1H; H-5), 3.69 – 3.62 (m, 2H; H-6), 2.26 – 2.20 (m, 4H; CH_2α chain), 2.12 (td, $J_{CH2\alpha,\ CH2\beta}$ = *7.5*, *5.5 Hz*, 2H; CH_2α chain), 1.64 – 1.50 (m, 7H; CH_2β chains), 1.37 – 1.19 (m, 74H; chains bulk), 0.97 – 0.82 (m, 22H; 9x CH_3 chains + 9x tBu-Si), 0.05 (t, *J* = *3.9 Hz*, 7H; Me-Si).

^{13}C NMR (101 MHz, $CDCl_3$) δ 174.3, 173.0, 172.0, 91.7, 77.3, 77.0, 76.7, 70.8, 70.6, 68.4, 62.6, 52.2, 36.8, 34.2, 34.2, 34.1, 31.9, 29.7, 29.6, 29.6, 29.6, 29.5, 29.5, 29.4, 29.4, 29.3, 29.3, 29.3, 29.3, 29.2, 29.2, 25.9, 25.9, 25.6, 24.9, 24.9, 24.9, 22.7, 18.4, 14.1, −5.3, −5.4.

HRMS (ESI-Q-TOF): m/z [M^+] calculated for $C_{54}H_{105}NO_8Si^+$: 946.7502. Found: 946.7494.

α_D = +10.83

4.8 Compound 14b

2-dodecanamido-2-deoxy-3,4-di-O-dodecanoyl-6-O-tert-butyldimethylsilyl-α-D-glucopyranose.

Compound **13b** (1.5 g, 1.5 mmol, 1 eq.) was dissolved in anhydrous THF (38 mL, 0.04 M) with 1% v/v of water. Acetic acid (428 µL, 7.5 mmol, 5.0 eq.) and ethylenediamine (1.5 mL, 22.5 mmol, 15.0 eq.) were added to the solution at 0 °C. The reaction was allowed to return to room temperature (20 °C) and stirred for 4 h, then controlled by TLC (Hep/EtOAc 9:1; Rf starting material: 0.00). Subsequently, the solution was diluted in EtOAc and washed three times with 1 M HCl and three times with $NaHCO_3$. A white precipitate forms during the washings, which is removed by filtration and discarded (amide between lauric acid and ethylenediamine). The organic liquid phase thus obtained was dried with Na_2SO_4 and the solvent was removed by rotavapor. The crude product thus obtained (1.4 g) was purified by flash chromatography (Tol/EtOAc 85:15; Rf product: 0.21). After purification, 882 mg of compound **14b** were obtained, in 72% yield.

^{1}H NMR (400 MHz, $CDCl_3$) δ 5.73 (d, $J_{NH,\ H\text{-}2}$ = *9.3 Hz*, 1H; NH), 5.34 – 5.22 (m, 2H; H-3 + H-1), 5.08 (m, 1H; H-4), 4.33 – 4.17 (m, 1H; H-2), 4.03 (ddd, $J_{H\text{-}5,\ H\text{-}4}$ = *10.1*, $J_{H\text{-}5,\ H\text{-}6a}$ = *4.5*, $J_{H\text{-}5,\ H\text{-}6b}$ = *3.2 Hz*, 1H; H-5), 3.69 – 3.62 (m, 2H; H-6), 2.26 – 2.20 (m, 4H; CH_2α chain), 2.12 (td, $J_{CH2\alpha,\ CH2\beta}$ = *7.5*, *5.5 Hz*, 2H; CH_2α chain), 1.64 – 1.50 (m, 7H; CH_2β chains), 1.37 – 1.19 (m, 58H; chains bulk), 0.97 – 0.82 (m, 22H; 9x CH_3 chains + 9x tBu-Si), 0.05 (t, *J* = *3.9 Hz*, 7H; Me-Si).

^{13}C NMR (101 MHz, $CDCl_3$) δ 174.3, 173.0, 172.0, 91.7, 77.3, 77.0, 76.7, 70.8, 70.6, 68.4, 62.6, 52.2, 36.8, 34.2, 34.2, 34.1, 31.9, 29.7, 29.6, 29.6, 29.6, 29.5, 29.5, 29.4, 29.4, 29.3, 29.3, 29.3, 29.3, 29.2, 29.2, 25.9, 25.9, 25.6, 24.9, 24.9, 24.9, 22.7, 18.4, 14.1, −5.3, −5.4.

HRMS (ESI-Q-TOF): m/z [M^+] calculated for $C_{48}H_{93}NO_8Si^+$: 839.6670. Found: 839.6667.

α_D = −16.5

4.9 Compound 15a

1-(dibenzyl)phosphor-2-tetradecanamido-2-deoxy-3,4-di-O-tetradecanoyl-6-O-tert-butyldimethylsilyl-α-D-glucopyranose.

Compound **14a** (690 mg, 0.75 mmol, 1 eq.) and imidazole triflate (436 mg, 1.7 mmol, 2.25 eq.) were dissolved in DCM (37.5 mL, 0.02 M) under inert atmosphere. Dibenzyl N,N-diisopropylphosphoramidite (570 mg, 1.65 mmol, 2.2 eq) was added to the solution at 0 °C. The reaction was monitored by TLC (Hep/EtOAc 8:2, Rf product: 0.15); after 30 min, substrate depletion was detected. The solution was then cooled at −20 °C and a solution of meta-chloroperbenzoic acid (516 mg, 3.0 mmol, 4 eq.) in 5 mL of DCM was added dropwise. After 30 min the reaction was allowed to return to RT (20 °C) and left stirring overnight. After TLC analysis (Hep/EtOAc 8:2; Rf product: 0.29), the reaction was quenched with 15 mL of a saturated $NaHCO_3$ solution and concentrated by rotavapor. The mixture was then diluted in EtOAc and washed 3 times with a saturated $NaHCO_3$ solution and three times with a 1 M HCl solution. The organic phase was recovered, dried with Na_2SO_4, and the solvent was removed by rotavapor. The crude thus obtained was purified by flash column chromatography (Hep/EtOAc 8:2; Rf product: 0.29). In total, 810 mg of pure compound **15a** were obtained as a yellow oil in a 91% yield.

^{1}H NMR (400 MHz, $CDCl_3$) δ 7.42 – 7.29 (m, 11H; aromatics), 5.70 (dd, $J_{H\text{-}1,\ P\text{-}1}$ = *6.0*, $J_{H\text{-}1,\ H,2}$ = *3.2 Hz*, 1H; H-1), 5.62 (d, $J_{NH,\ H\text{-}2}$ = *9.1 Hz*, 1H; N-H), 5.25 – 5.15 (m, 2H; H-4 + H-3), 5.13 – 4.95 (m, 4H; CH_2Ph), 4.33 (ddt, $J_{H\text{-}2,\ H\text{-}3}$ = *10.6*, $J_{H\text{-}2,\ NH}$ = *9.0*, $J_{H\text{-}2,\ H\text{-}1}$ = *3.2 Hz*, 1H; H-2), 3.90 (dt, $J_{H\text{-}5,\ H\text{-}4}$ = *8.2*, $J_{H\text{-}5,\ H\text{-}6}$ = *3.8 Hz*, 1H; H-5), 3.61 – 3.51 (m, 2H; H-6), 2.28 – 2.17 (m, 4H; CH_2α chain), 1.85 (hept, $J_{CH2\alpha,\ CH2\beta}$ = *7.48*, *7.48*, *7.48*, *7.48*, *7.31*, *7.31 Hz*, 2H; CH_2α chain), 1.61 – 1.47 (m, 5H; CH_2β chains), 1.47 – 1.37 (m, 2H; CH_2β chains), 1.33 – 1.10 (m, 70H; chains bulk), 0.91 – 0.82 (m, 18, 9x CH_3 chains + 9x tBu-Si), −0.02 (d, *J* = *5.9 Hz*, 6H; Me-Si).

^{13}C NMR (101 MHz, $CDCl_3$) δ 174.2, 173.1, 171.6, 135.5, 135.4, 135.4, 135.3, 128.8, 128.7, 128.7, 128.4, 128.2, 128.0, 127.8, 96.8, 96.7, 77.3, 77.0, 76.7, 72.4, 70.2, 69.8, 69.7, 69.7, 69.7, 67.1, 61.4, 51.9, 51.8, 36.3, 34.2, 34.1, 31.9, 29.7, 29.7, 29.7, 29.6, 29.5, 29.5, 29.4, 29.3, 29.2, 29.2, 29.1, 25.8, 25.8, 25.4, 24.9, 24.9, 22.7, 18.3, 14.1, −5.5, −5.5.

^{31}P NMR (162 MHz, $CDCl_3$) δ −2.49 (s, 1P, P-1).

HRMS (ESI-Q-TOF): m/z [M + Na^+] calculated for $C_{68}H_{118}NNaO_{11}PSi^+$: 1206.8104. Found: 1206.8113.

α_D = +3.0

4.10 Compound 15b

1-(dibenzyl)phosphor-2-dodecanamido-2-deoxy-3,4-di-O-dodecanoyl-6-O-tert-butyldimethylsilyl-α-D-glucopyranose.

Compound **14b** (2.12 g, 2.4 mmol, 1 eq.) and imidazole triflate (1.4 g, 5.4 mmol, 2.25 eq.) were dissolved in DCM (121 mL, 0.02 M) under inert atmosphere. Dibenzyl N,N-diisopropylphosphoramidite (1.83 g, 5.3 mmol, 2.2 eq) was added to the solution at 0 °C. The reaction was monitored by TLC (Hep/EtOAc 8:2); after 30 min, substrate depletion was detected. The solution was then cooled at −20 °C and a solution of meta-chloroperbenzoic acid (1.66 g, 9.7 mmol, 4 eq.) in 17 mL of DCM was added dropwise. After 30 min the reaction was allowed to return to RT (20 °C) and left stirring overnight. After TLC analysis, the reaction was quenched with 15 mL of a saturated $NaHCO_3$ solution and concentrated by rotavapor. The mixture was then diluted in EtOAc and washed 3 times with a saturated $NaHCO_3$ solution and three times with a 1 M HCl solution. The organic phase was recovered, dried with Na_2SO_4, and the solvent was removed by rotavapor. The crude thus obtained was purified by flash column chromatography (Hep/EtOAc 8:2; Rf product: 0.29). In total, 2.41 g of pure compound **15a** was obtained as a yellow oil in a 91% yield.

^{1}H NMR (400 MHz, $CDCl_3$) δ 7.45 – 7.29 (m, 10H; aromatics), 5.70 (dd, $J_{H\text{-}1,\ P\text{-}1}$ = *5.9*, $J_{H\text{-}1,\ H,2}$ = *3.2 Hz*, 1H; H-1), 5.60 (d, $J_{NH,\ H\text{-}2}$ = *9.1 Hz*, 1H; N-H), 5.25 – 5.13 (m, 2H; H-4 + H-3), 5.13 – 4.97 (m, 4H; CH_2Ph), 4.33 (ddt, $J_{H\text{-}2,\ H\text{-}3}$ = *10.6*, $J_{H\text{-}2,\ NH}$ = *9.0*, $J_{H\text{-}2,\ H\text{-}1}$ = *3.1 Hz*, 1H; H-2), 3.90 (dt, $J_{H\text{-}5,\ H\text{-}4}$ = *10.8*, $J_{H\text{-}5,\ H\text{-}6}$ = *3.1 Hz*, 1H; H-5), 3.56 (dd, $J_{H\text{-}6,\ H\text{-}5}$ = *3.1*, ^2J = *1.8 Hz*, 2H; H-6), 2.28 – 2.17 (m, 4H; CH_2α chain), 1.85 (hept, $J_{CH2\alpha,\ CH2\beta}$ = *7.48*, *7.48*, *7.48*, *7.48*, *7.31*, *7.31 Hz*, 2H; CH_2α chain), 1.61 – 1.46 (m, 5H; CH_2β chains), 1.46 – 1.36 (m, 2H; CH_2β chains), 1.33 – 1.10 (m, 50H; chains bulk), 0.92 – 0.82 (m, 18, 9x CH_3 chains + 9x tBu-Si), −0.02 (d, *J* = *5.9 Hz*, 6H; Me-Si).

^{13}C NMR (101 MHz, $CDCl_3$) δ 174.2, 173.1, 171.6, 135.5, 135.4, 135.3, 129.0, 128.9, 128.8, 128.7, 128.7, 128.2, 128.0, 125.3, 96.8, 96.7, 77.3, 77.0, 76.7, 72.4, 70.2, 69.8, 69.7, 69.7, 69.6, 67.1, 61.5, 51.9, 51.8, 36.3, 34.2, 34.1, 31.9, 29.6, 29.6, 29.6, 29.5, 29.4, 29.3, 29.3, 29.3, 29.2, 29.2, 29.1, 25.8, 25.4, 24.9, 24.9, 22.7, 18.3, 14.1, −5.5, −5.5.

^{31}P NMR (162 MHz, $CDCl_3$) δ −2.51 (s, 1P, P-1).

HRMS (ESI-Q-TOF): m/z [M + Na^+] calculated for $C_{62}H_{106}NNaO_{11}PSi^+$: 1122.7165. Found: 1122.7152.

α_D = +29.8

4.11 Compound 16a

1-(dibenzyl)phosphor-2-tetradecanamido-2-deoxy-3,4-di-O-tetradecanoyl-α-D-glucopyranose.

Compound **15a** (500 mg, 0.42 mmol, 1 eq.) was dissolved in acetone (8.4 mL, 0.05 M) and IRC 120 H^+ (3.75 g, 750% m/m) was added at RT (20 °C). The solution was left stirring for 48 h and monitored by TLC (Hep/Acetone 8:2; Rf product: 0.35). After reaction completion, the solution was filtered to remove the resin. The organic phase thus obtained was evaporated by rotavapor. The crude product thus obtained was purified by flash column chromatography (Hep/Acetone 85:15; Rf Product: 0.31). After purification, 247 mg of compound **16b** was obtained as a white solid in a 55% yield.

^{1}H NMR (400 MHz, $CDCl_3$) δ 7.42 – 7.29 (m, 9H; aromatics), 5.70 (dd, $J_{H\text{-}1,\ P\text{-}1}$ = *5.6*, $J_{H\text{-}1,\ H\text{-}2}$ = *3.3 Hz*, 1H; H-1), 5.59 (d, $J_{NH,\ H\text{-}2}$ = *9.1 Hz*, 1H; NH), 5.24 (dd, $J_{H\text{-}3,\ H\text{-}2}$ = *10.9*, $J_{H\text{-}3,\ H\text{-}4}$ = *9.6 Hz* 1H; H-3), 5.14 – 4.99 (m, 5H; CH_2Ph + H-4), 4.40 – 4.30 (m, 1H; H-2), 3.81 (dt, $J_{H\text{-}5,\ H\text{-}4}$ = *10.3 Hz*, $J_{H\text{-}5,\ H\text{-}6a}$ = *4.1*, $J_{H\text{-}5,\ H\text{-}6b}$ = *2.2*, 1H; H-5), 3.53 (dd, $J_{H\text{-}6a,\ H\text{-}6b}$ = *13.0*, $J_{H\text{-}6a,\ H\text{-}5}$ = *2.2 Hz*, 1H; H-6b), 3.44 (dd, $J_{H\text{-}6b,\ H\text{-}6a}$ = *13.0*, $J_{H\text{-}6b,\ H\text{-}5}$ = *4.1 Hz*, 1H; H-6a), 2.33 – 2.19 (m, 4H; CH_2α chain), 1.98 – 1.81 (m, 2H; CH_2α chain), 1.62 – 1.38 (m, 7H; CH_2β chains), 1.47 – 1.39 (m, 2H; CH_2β chains), 1.32 – 1.17 (m, 61H; chains bulk), 0.92 – 0.84 (m, 9H; CH_3 chains).

^{13}C NMR (101 MHz, $CDCl_3$) δ 128.5, 128.4, 127.8, 77.3, 77.0, 76.7, 69.2, 69.1, 48.9, 36.7, 34.2, 34.2, 31.9, 29.7, 29.6, 29.5, 29.4, 29.3, 29.2, 29.1, 25.6, 24.9, 24.7, 22.7, 14.1.

^{31}P NMR (162 MHz, $CDCl_3$) δ −2.32 (s, 1P, P-1).

HRMS (ESI-Q-TOF): m/z [M + Na^+] calculated for $C_{62}H_{104}NNaO_{11}P^+$: 1092.7239. Found: 1092.7228.

α_D = +40.2

4.12 Compound 16b

1-(dibenzyl)phosphor-2-dodecanamido-2-deoxy-3,4-di-O-dodecanoyl-α-D-glucopyranose.

Compound **15a** (500 mg, 0.45 mmol, 1 eq.) was dissolved in acetone (9.0 mL, 0.05 M) and IRC 120 H^+ (3.75 g, 750% m/m) was added at RT (20 °C). Solution was left stirring for 48 h and monitored by TLC (Hep/Acetone 8:2; Rf product: 0.35). After reaction completion, the solution was filtered to remove the resin. Organic phase thus obtained was evaporated by rotavapor. Crude product thus obtained was purified by flash column chromatography (Hep/Acetone 85:15; Rf Product: 0.31). After purification, 244 mg of compound **16b** was obtained as a white solid in a 55% yield.

^{1}H NMR (400 MHz, $CDCl_3$) δ 7.42 – 7.29 (m, 10H; aromatics), 5.70 (dd, $J_{H\text{-}1,\ P\text{-}1}$ = *5.4*, $J_{H\text{-}1,\ H\text{-}2}$ = *3.4 Hz*, 1H; H-1), 5.61 (d, $J_{NH,\ H\text{-}2}$ = *9.0 Hz*, 1H; NH), 5.27 – 5.20 (dd, $J_{H\text{-}3,\ H\text{-}2}$ = *10.9*, $J_{H\text{-}3,\ H\text{-}4}$ = *9.5 Hz* 1H; H-3), 5.13 – 5.00 (m, 5H; benzylics + H-4), 4.39 – 4.31 (m, 1H; H-2), 3.81 (dt, $J_{H\text{-}5,\ H\text{-}4}$ = *10.2 Hz*, 1H; H-5), 3.53 (dd, $J_{H\text{-}6a,\ H\text{-}6b}$ = *12.9*, $J_{H\text{-}6a,\ H\text{-}5}$ = *1.7 Hz*, 1H; H-6a), 3.44 (dd, $J_{H\text{-}6b,\ H\text{-}6a}$ = *13.0*, $J_{H\text{-}6b,\ H\text{-}5}$ = *4.0 Hz*, 1H; H-6b), 2.26 (ddd, $J_{CH2\alpha,\ CH2\beta}$ = *17.3*, *11.4*, *4.6 Hz*, 5H; CH_2α chain), 1.97 – 1.81 (m, 2H; CH_2α chain), 1.62 – 1.49 (m, 5H; CH_2β chains), 1.47 – 1.39 (m, 2H; CH_2β chains), 1.32 – 1.17 (m, 55H; chains bulk), 0.88 (t, *J* = *6.7 Hz*, 10H; CH_3 chains).

^{13}C NMR (101 MHz, $CDCl_3$) δ 174.0, 173.1, 135.4, 135.3, 135.2, 128.9, 128.8, 128.7, 128.1, 128.0, 96.5, 96.4, 77.3, 77.0, 76.7, 72.0, 70.0, 69.9, 69.9, 69.8, 69.5, 67.6, 60.7, 51.9, 51.8, 40.8, 36.3, 34.1, 34.1, 31.9, 29.7, 29.6, 29.6, 29.6, 29.5, 29.4, 29.3, 29.3, 29.2, 29.1, 29.1, 28.4, 25.4, 24.9, 23.8, 22.7, 20.8, 17.5, 17.3, 14.6, 14.1.

^{31}P NMR (162 MHz, $CDCl_3$) δ −2.32 (s, 1P, P-1).

HRMS (ESI-Q-TOF): m/z [M + Na^+] calculated for $C_{56}H_{92}NNaO_{11}P^+$: 1008.6300. Found: 1008.6306.

α_D = +23.2

4.13 Compound FP11

1-phospho-2-tetradecanamido-2-deoxy-3,4-di-O-tetradecanoyl-α-D-glucopyranose (sodium salt).

Compound **16** (50 mg, 0.05 mmol, 1 eq.) dissolved in a 1:1 mixture of MeOH and DCM (5 mL, 0.01 M) was put under inert atmosphere. Palladium on carbon (10 mg, 20% m/m) was added to the solution. The reaction environment was put under vacuum, then H_2 atmosphere was added. The solution was stirred for 2 h, H_2 was removed and the reaction was monitored by TLC (EtPet/acetone 8:2; Rf product: 0.00). TEA (100 µL, 2% v/v) was added to the mixture, and the reaction was stirred for 15 min. The solution was filtered on syringe filters PALL 4549T Acrodisc 25 mm with GF/0.45 µm Nylon to remove the catalyst and solvents were evaporated by rotavapor. The crude was resuspended in a 1:1 DCM/MeOH solution and IRC 120 H^+ was added. After 30 min stirring, IRC 120 H^+ was removed by filtration, and the solution was evaporated. The crude was again dissolved in 1:1 DCM/MeOH solution and IRC 120 Na^+ was added. After 30 min stirring, IRC 120 Na^+ was filtered and solvents were removed by rotavapor. The crude product was purified through reverse chromatography employing a C4 functionalized column (PUREZZA-Sphera Plus Standard Flash Cartridge C4 - 25um - Size 25 g) in the Biotage® Isolera LS System (gradient: H_2O/THF 70:30 to 15:85 over 10 CV with 1% of an aqueous solution of Et_3NHCO_3 at pH 7.5; Retention time: 12–14 min). In total, 45 mg of **FP11** was obtained as a white powder in a quantitative yield.

^{1}H NMR (400 MHz, MeOD) δ 5.58 (dd, $J_{H\text{-}1,\ P\text{-}1}$ = *6.6*, $J_{H\text{-}1,\ H\text{-}2}$ = *3.4 Hz*, 1H; H-1), 5.34 (dd, $J_{H\text{-}3,\ H\text{-}2}$ = *10.9* $J_{H\text{-}3,\ H\text{-}4}$ = *9.4 Hz*, 1H; H-3), 5.15 (dd, $J_{H\text{-}4,\ H\text{-}5}$ = *10.3* $J_{H\text{-}4,\ H\text{-}3}$ = *9.4 Hz*, 1H; H-4), 4.35 (dt, $J_{H\text{-}2,\ H\text{-}3}$ = *10.9*, $J_{H\text{-}2,\ H\text{-}1}$ = *3.2 Hz*, 1H; H-2), 4.08 (ddd, $J_{H\text{-}5,\ H\text{-}4}$ = *10.3*, $J_{H\text{-}5,\ H\text{-}6b}$ = *4.7*, $J_{H\text{-}5,\ H\text{-}6a}$ = *2.4 Hz*, 1H; H-5), 3.68 (dd, $J_{H\text{-}6a,\ H\text{-}6b}$ = *12.4*, $J_{H\text{-}6a,\ H\text{-}6b}$ = *2.3 Hz*, 1H; H-6a), 3.57 (dd, $J_{H\text{-}6b,\ H\text{-}6a}$ = *12.3*, $J_{H\text{-}6b,\ H\text{-}5}$ = *4.7 Hz*, 1H; H-6b), 2.40 – 2.15 (m, 6H; CH_2α chain), 1.65 – 1.51 (m, 6H; CH_2β chains), 1.30 (s, 64H; chains bulk), 0.94 – 0.87 (m, 9H; CH_3 chains).

^{13}C NMR (101 MHz, MeOD) δ 175.1, 173.1, 172.5, 94.6, 71.2, 70.6, 68.5, 60.3, 51.7, 51.6, 48.2, 48.0, 47.8, 47.6, 47.4, 47.2, 47.0, 35.6, 33.7, 33.6, 31.7, 31.7, 29.4, 29.4, 29.4, 29.3, 29.3, 29.2, 29.2, 29.2, 29.1, 29.1, 29.1, 29.0, 29.0, 28.9, 28.8, 25.6, 25.5, 24.5, 24.5, 22.3, 13.0.

^{31}P NMR (162 MHz, MeOD) δ −1.93 (s, 1P, P-1).

HRMS ESI-MS: $[M\text{-}H]^-$ calculated for $C_{48}H_{91}NO_{11}P^-$ m/z = 888.6335; found: m/z = 888.6328.

α_D = +56.5

4.14 Compound FP18

1-phospho-2-dodecanamido-2-deoxy-3,4-di-O-dodecanoyl-α-D-glucopyranose (sodium salt).

Compound **16** (50 mg, 0.05 mmol, 1 eq.) dissolved in a 1: 1 mixture of MeOH and DCM (5 mL, 0.01 M) was put under inert atmosphere. Palladium on carbon (10 mg, 20% m/m) was added to the solution. The reaction environment was put under vacuum, then H_2 atmosphere was added. The solution was stirred for 2 h, H_2 was removed and the reaction was monitored by TLC (EtPet/acetone 8:2; Rf product: 0.00). TEA (100 µL, 2% v/v) was added to the mixture, and the reaction was stirred for 15 min. The solution was filtered on syringe filters PALL 4549T Acrodisc 25 mm with GF/0.45 µm Nylon to remove the catalyst and solvents were evaporated by rotavapor. The crude was resuspended in a 1:1 DCM/MeOH solution and IRC 120 H^+ was added. After 30 min stirring, IRC 120 H^+ was removed by filtration and the solution was evaporated. The crude was again dissolved in 1:1 DCM/MeOH solution and IRC 120 Na^+ was added. After 30 min stirring, IRC 120 Na^+ was filtered and solvents were removed by rotavapor. The crude product was purified through reverse chromatography employing a C4 functionalized column (PUREZZA-Sphera Plus Standard Flash Cartridge C4 - 25um - Size 25 g) in the Biotage® Isolera LS System (gradient: H_2O/THF 70:30 to 15: 85 over 10 CV with 1% of an aqueous solution of Et_3NHCO_3 at pH 7.5; Retention time: 12–14 min). In total, 45 mg of **FP18** was obtained as a white powder in a quantitative yield.

^{1}H NMR (400 MHz, MeOD) δ 5.57 (dd, $J_{H\text{-}1,\ P\text{-}1}$ = *6.6*, $J_{H\text{-}1,\ H\text{-}2}$ = *3.4 Hz*, 1H; H-1), 5.35 (dd, $J_{H\text{-}3,\ H\text{-}2}$ = *10.8*, $J_{H\text{-}3,\ H\text{-}4}$ = *9.3 Hz*, 1H; H-3), 5.15 (dd, $J_{H\text{-}4,\ H\text{-}5}$ = *10.1* $J_{H\text{-}4,\ H\text{-}3}$ = *9.5 Hz*, 1H; H-4), 4.34 (dt, $J_{H\text{-}2,\ H\text{-}3}$ = *10.9*, $J_{H\text{-}2,\ H\text{-}1}$ = *2.9 Hz*, 1H; H-2), 4.10 (ddd, $J_{H\text{-}5,\ H\text{-}4}$ = *10.4*, $J_{H\text{-}5,\ H\text{-}6b}$ = *4.6*, $J_{H\text{-}5,\ H\text{-}6a}$ = *2.3 Hz*, 1H; H-5), 3.68 (dd, $J_{H\text{-}6a,\ H\text{-}6b}$ = *12.5*, $J_{H\text{-}6a,\ H\text{-}6b}$ = *2.4 Hz*, 1H; H-6a), 3.57 (dd, $J_{H\text{-}6b,\ H\text{-}6a}$ = *12.3*, $J_{H\text{-}6b,\ H\text{-}5}$ = *4.7 Hz*, 1H; H-6b), 2.40 – 2.12 (m, 7H; CH_2α chain), 1.65 – 1.51 (m, 7H; CH_2β chains), 1.32 (s, 55H; chains bulk), 1.00 – 0.82 (m, 10H; CH_3 chains).

^{13}C NMR (101 MHz, MeOD) δ 175.1, 173.1, 172.5, 94.6, 71.2, 70.6, 68.5, 60.3, 51.7, 51.6, 48.2, 48.0, 47.8, 47.6, 47.4, 47.2, 47.0, 35.6, 33.7, 33.6, 31.7, 31.7, 29.4, 29.4, 29.4, 29.3, 29.3, 29.2, 29.2, 29.2, 29.1, 29.1, 29.1, 29.0, 29.0, 28.9, 28.8, 25.6, 25.5, 24.5, 24.5, 22.3, 13.0.

^{31}P NMR (162 MHz, MeOD) δ −1.88 (s, 1P, P-1).

HRMS ESI-MS: $[M\text{-}H]^-$ calculated for $C_{42}H_{79}NO_{11}P^-$ m/z = 804.5396; found: m/z = 804.5401.

α_D = +24.2

Data availability statement

The datasets presented in this study can be found in online repositories. The names of the repository/repositories and accession number(s) can be found in the article/Supplementary Material.

Author contributions

All authors listed have made a substantial, direct, and intellectual contribution to the work and approved it for publication.

Funding

European Union's Horizon 2020 research and innovation program under the Marie Skłodowska-Curie, project BactiVax (www.bactivax.eu) grant agreement No. 860325; the Italian consortium CINMPIS.

Conflict of interest

The authors declare that the research was conducted in the absence of any commercial or financial relationships that could be construed as a potential conflict of interest.

Publisher's note

All claims expressed in this article are solely those of the authors and do not necessarily represent those of their affiliated organizations, or those of the publisher, the editors and the reviewers. Any product that may be evaluated in this article, or claim that may be made by its manufacturer, is not guaranteed or endorsed by the publisher.

Supplementary material

The Supplementary Material for this article can be found online at: https://www.frontiersin.org/articles/10.3389/fchem.2023.1252996/full#supplementary-material

References

699800P Avanti MPLA (PHAD®) 699800P Avanti MPLA (PHAD®) 699800P Avanti MPLA (PHAD®). Available at: https://www.sigmaaldrich.com/IT/it/product/avanti/699800p.

Alfonsi, K., Colberg, J., Dunn, P. J., Fevig, T., Jennings, S., Johnson, T. A., et al. (2008). 'Green chemistry tools to influence a medicinal chemistry and research chemistry based organisation'. *Green Chem.* 10 (1), 31–36. doi:10.1039/b711717e

Byrne, F. P., Jin, S., Paggiola, G., Petchey, T. H. M., Clark, J. H., Farmer, T. J., et al. (2016). Tools and techniques for solvent selection: green solvent selection guides. *Sustain. Chem. Process.* 4, 7. doi:10.1186/s40508-016-0051-z

Casella, C. R., and Mitchell, T. C. (2008). 'Putting endotoxin to work for us: monophosphoryl lipid a as a safe and effective vaccine adjuvant'. *Cell. Mol. Life Sci.* 65 (20), 3231–3240. doi:10.1007/s00018-008-8228-6

Cighetti, R., Ciaramelli, C., Sestito, S. E., Zanoni, I., Kubik, Ł., Ardá-Freire, A., et al. (2014). 'Modulation of CD14 and TLR4×MD-2 activities by a synthetic lipid A mimetic'. *ChemBioChem* 15 (2), 250–258. doi:10.1002/cbic.201300588

Delany, I., Rappuoli, R., and De Gregorio, E. (2014). Vaccines for the 21st century. *Embo Mol. Med.* 6 (6), 708–720. doi:10.1002/emmm.201403876

Facchini, F. A., Zaffaroni, L., Minotti, A., Rapisarda, S., Calabrese, V., Forcella, M., et al. (2018). 'Structure-activity relationship in monosaccharide-based toll-like receptor 4 (TLR4) antagonists'. *J. Med. Chem.* 61 (7), 2895–2909. doi:10.1021/acs.jmedchem.7b01803

Facchini, F. A., Minotti, A., Luraghi, A., Romerio, A., Gotri, N., Matamoros-Recio, A., et al. (2021). 'Synthetic glycolipids as molecular vaccine adjuvants: mechanism of action in human cells and *in vivo* activity'. *J. Med. Chem.* 64, 12261–12272. doi:10.1021/acs.jmedchem.1c00896

Hilleman, M. R. (2000). 'Vaccines in historic evolution and perspective: a narrative of vaccine discoveries'. *J. Hum. Virology* 3 (2), 1436–1447. doi:10.1016/s0264-410x(99)00434-x

Industry Research (2022) 'GLOBAL VACCINE ADJUVANTS INDUSTRY RESEARCH REPORT, COMPETITIVE LANDSCAPE, MARKET SIZE, REGIONAL STATUS AND PROSPECT', p. 107.

Joshi, D. R., and Adhikari, N. (2019). 'An overview on common organic solvents and their toxicity'. *J. Pharm. Res. Int.* 28 (3), 1–18. doi:10.9734/jpri/2019/v28i330203

Kayser, V., and Ramzan, I. (2021). Vaccines and vaccination: history and emerging issues. *Hum. Vaccines Immunother.* 17 (12), 5255–5268. Taylor and Francis. doi:10.1080/21645515.2021.1977057

Lambrecht, B. N., Kool, M., Willart, M. A., and Hammad, H. (2009). 'Mechanism of action of clinically approved adjuvants'. *Curr. Opin. Immunol.* 21 (1), 23–29. doi:10.1016/j.coi.2009.01.004

Li, H., Willingham, S. B., Ting, J. P. Y., and Re, F. (2008). 'Cutting edge: inflammasome activation by alum and alum's adjuvant effect are mediated by NLRP3'. *J. Immunol.* 181 (1), 17–21. doi:10.4049/jimmunol.181.1.17

Mata-Haro, V., Cekic, C., Martin, M., Chilton, P. M., Casella, C. R., and Mitchell, T. C. (2007). 'The vaccine adjuvant monophosphoryl lipid A as a TRIF-biased agonist of TLR4'. *Science* 316, 1628–1632. doi:10.1126/science.1138963

O'Hagan, D. T., Lodaya, R. N., and Lofano, G. (2020). The continued advance of vaccine adjuvants – "we can work it out". *Seminars Immunol.* 50, 101426. doi:10.1016/j.smim.2020.101426

Peri, F., and Minotti, A. (2019). *New synthetic agonists of TLR4 receptor*.

Reed, S. G., and Carter, D. (2014). *Synthetic glucopyranosyl lipid aduvants adjuvants*.

Romerio, A., Gotri, N., Franco, A. R., Artusa, V., Shaik, M. M., Pasco, S. T., et al. (2023). New glucosamine-based TLR4 agonists: design, synthesis, mechanism of action, and *in vivo* activity as vaccine adjuvants. *J. Med. Chem.* 66, 3010–3029. doi:10.1021/acs.jmedchem.2c01998

Shah, R. R., Hassett, K. J., and Brito, L. A. (2017). "Overview of vaccine adjuvants: introduction, history, and current status," in *Vaccine adjuvants*, 1–13. doi:10.1007/978-1-4939-6445-1_1

Stewart, A. J., and Devlin, P. M. (2006). 'The history of the smallpox vaccine'. *J. Infect.* 52 (5), 329–334. doi:10.1016/j.jinf.2005.07.021

Zhang, J., and Kováč, P. (1999). 'An alternative method for regioselective, anomeric deacylation of fully acylated carbohydrates'. *J. Carbohydr. Chem.* 18 (4), 461–469. doi:10.1080/07328309908544010

Zheng, C., Shao, W., Chen, X., Zhang, B., Wang, G., and Zhang, W. (2022). Real-world effectiveness of COVID-19 vaccines: a literature review and meta-analysis. *Int. J. Infect. Dis.* 114, 252–260. doi:10.1016/j.ijid.2021.11.009

frontiers | Frontiers in Chemistry

TYPE Original Research
PUBLISHED 07 November 2023
DOI 10.3389/fchem.2023.1269845

OPEN ACCESS

EDITED BY
Josef Maroušek,
Biology Centre of the Academy of Sciences of the Czech Republic, Czechia

REVIEWED BY
Eda Weiss,
University of Bristol, United Kingdom
Fumitaka Hayashi,
Shinshu University, Japan
Derya Özgür,
Gazi University, Türkiye
Daphiny Pottmaier,
Nottingham Trent University, United Kingdom

*CORRESPONDENCE
Theppawut Ayudhya,
ayudhya_t@utpb.edu

RECEIVED 31 July 2023
ACCEPTED 24 October 2023
PUBLISHED 07 November 2023

CITATION
Dingra N, Witty M, Celis M, Boppana N and Ayudhya T (2023), Transformation of struvite from wastewater to a hydrogen fuel storage compound ammonia borane.
Front. Chem. 11:1269845.
doi: 10.3389/fchem.2023.1269845

Transformation of struvite from wastewater to a hydrogen fuel storage compound ammonia borane

Nin Dingra[1], Michael Witty[2], Marie Celis[1], Narendra Boppana[3] and Theppawut Ayudhya[1]*

[1]Department of Chemistry, University of Texas Permian Basin, Odessa, TX, United States, [2]School of Pure and Applied Sciences, Florida SouthWestern State College, Fort Myers, FL, United States, [3]Department of Chemical Engineering, University of Texas Permian Basin, Odessa, TX, United States

Ammonia borane (NH_3BH_3) is a carrier of hydrogen gas that is known as a carbon-free renewable energy source. A high hydrogen content of ammonia borane and its stability in air at ambient temperatures make it a valuable molecule for its potential use as a hydrogen storage compound. In this study, we investigate a new approach for synthesizing ammonia borane using wastewater-derived ammonia source. Wastewater recycling has always been a global interest towards sustainability. In addition to reclaiming the water, recycling nutrients in wastewater is a topic of interest. Nutrients such as nitrogen, magnesium, and phosphorous are readily recovered from wastewater as struvite ($NH_4MgPO_4{\cdot}6H_2O$). This new process involves converting urine into struvite, and then reacting struvite with alkali borohydrides to produce a high-purity ammonia borane. The use of mild reaction conditions without extensive purification process, together with high purity ammonia borane product make this process a desirable course of action for recycling the nitrogen waste. In the course of moving towards a sustainable environment, the energy and wastewater industries will benefit from this combined process of nitrogen removal from wastewater to generate a renewable carbon-free energy molecule.

KEYWORDS

ammonia borane, hydrogen storage, struvite, sustainable energy, urine, wastewater

1 Introduction

Nutrient recovery from wastewater, specifically human excreta, has been a major focus of ecological sanitation, an approach that allows safe recycling of nutrients rather than discarding them into the freshwater bodies (Esrey, 2001; Simha and Ganesapillai, 2007). The chemical composition of human excreta contains various important nutrients including nitrogen (N), potassium (K), and phosphorous (P). Although human urine accounts for less than 1% of total wastewater volume, more than 80% of total-N, more than 50% of total-K and total-P are found in urine (Kirchmann and Pettersson, 1994). Therefore, source-separation systems are optimal for recovering N and P in maximum amounts compared to the conventional wastewater treatment systems (Malila et al., 2019). These nutrients are often recovered in the form of struvite, a white crystalline substance consisting of equal molar amounts of ammonium, magnesium, and phosphate with the formula of $NH_4MgPO_4{\cdot}6H_2O$. In solutions that contain magnesium, ammonium, and phosphate,

struvite forms crystals under the optimal pH values (Doyle and Parsons, 2002). Struvite crystals have several possible shapes including a distinctive form with triangular faces known as the Coffin Lid form which we will refer to later (Witty, 2016b). Struvite forms spontaneously in wastewater and is often found in the pipes of sewerage treatment plants causing blockages and reducing water flow. Due to this, many have developed methods for effective, frequent, and fast removal of struvite. A pilot-scale and long-term treatment of source separated urine to recover phosphorus and nitrogen as struvite has also been reported (Zamora et al., 2017) making struvite readily accessible to be used as nitrogen and phosphorus source in the agricultural industry as fertilizer. Although many excellent technologies exist for harvesting these nutrients (Maroušek et al., 2020) there is still great interest in struvite technology which is growing exponentially.

The recycled nutrients from wastewater can also be directed towards other purposes such as making energy storage molecules in the energy industry. An increase in energy demand and consumption, along with a desire to reduce fossil fuel utilization, creates a demand for finding ways to transition to more carbon free and renewable energy sources (Veziroglu, 2007; Maaß and Möckel, 2019). The new sources should be eco-friendly and must also be sustainable, abundant, and have high energy density. Although wind and solar energy are abundant, the main obstacle for capturing energy from these sources is energy storage and intermittent availability. Hydrogen fuel appears to fit the desired qualities needed for a clean energy solution (Acar and Dincer, 2020). However, the challenges for storage and transport of gaseous H_2 involving high pressure (up to 80 MPa) and liquefaction (−253°C) remain major obstacles in the use of hydrogen gas as fuel (Durbin and Malardier-Jugroot, 2013). These shortcomings led researchers to discover safer and more effective ways of storing hydrogen fuel. A solution to resolve this problem is to use solid hydrides or solid absorbent materials for hydrogen storage (Stephens et al., 2007).

The study of complex solid hydrides, such as sodium borohydride ($NaBH_4$), lithium borohydride ($LiBH_4$), sodium aluminum hydride ($NaAlH_4$), magnesium borohydride [$Mg(BH_4)_2$], and lastly ammonia borane (NH_3BH_3) as potential sources of hydrogen gas and the development of ways to release it from the solids is a rapidly developing field of research (Puszkiel et al., 2017; Akbayrak and Özkar, 2018). Ammonia borane (AB), NH_3BH_3, is of particular interest since it has a very high hydrogen content (19.6 wt%) and is highly stable in the air at ambient temperatures (Komova et al., 2013). The release of hydrogen from AB starts immediately upon its melting, around 100°C, leaving polymeric structures that can release more hydrogen at 130°C (Hamilton et al., 2009). Hydrogen liberation from AB is significantly improved by using transition metal catalyst such as TiO_2 with water adsorbed, which allowed for the hydrogen release at 80°C (Komova et al., 2013; Zhang et al., 2017). Overall, ammonia borane represents an optimal hydrogen source in terms of the stability of its crystal form, transport, and hydrogen release process. Despite its potential in the field of hydrogen energy, the availability of highly pure ammonia borane still remains a challenge.

Various methods for the synthesis of ammonia borane have been reported in the literature (Li et al., 2014; Hirscher et al., 2020). Early reports on preparation of AB accounted the decomposition of the diammoniate of diborane in ether or polyether solutions (Shore et al., 1958; Shore and Parry, 1958). Another approach for AB synthesis uses displacement reactions where borane is transferred from a weak base such as THF or DMS to a strong base, NH_3 (Beres et al., 1971; Jaska et al., 2003). The yield and purity of AB obtained from these methods are less attractive due to the formation of unstable intermediates such as ammonia diborane, diammonia diborane, and other ionic by-products (Chen et al., 2013). The most prevalent method for preparation of AB is metathesis reaction that use borohydrides and ammonium salts (Ramachandran and Gagare, 2007; Heldebrant et al., 2008). These reactions are carried out in the anhydrous ether solvents and under inert atmosphere. Of all the methods discussed, metathesis reactions appear to give highest yield and purity. In this study, development of a new approach for AB synthesis using struvite as a starting material is explored. This new synthetic route allows for recycling struvite, an otherwise wasteful product, to generate AB–a molecule with great potential for use as a stable hydrogen source.

2 Materials and methods

2.1 Reagents and equipment

Sodium borohydride (99%, Acros Organics), tetrahydrofuran (99.8%, Thermo Scientific), struvite (98%, Alfa Aesar), magnesium sulfate anhydrous (99.5%, Fisher Chemical), magnesium sulfate heptahydrate (98%, Thermo Scientific), sodium hydroxide (97%, Fisher Chemical), denatured ethanol (90% ethanol, 5% isopropanol, 5% methanol, Research Products International), and deuterium oxide (99.9% D, Cambridge Isotope Laboratories) were purchased from Fisher Scientific. Struvite from wastewater was prepared as described below. The NMR (^1H and ^{11}B) spectra were recorded using Bruker 400 MHz Avance III spectrometer. Perkin Elmer SpectrumOne IR spectrometer was used for FT-IR analyses. Thermogravimetric analysis and differential scanning calorimetry analysis were obtained using Mettler Toledo DSC3+ apparatus. Scanning electron microscope with energy dispersive spectrometry were recorded using ThermoScientific Prisma E scanning electron microscope.

2.2 Preparation of struvite from wastewater

Struvite crystals were prepared as previously reported (Witty et al., 2020). Briefly, one gallon (3.785 L) of human urine was gathered over several days and stored at 4°C. Then 10.501 g $MgSO_4{\cdot}7H_2O$ and 2.836 g NaOH was added and storage at 4°C was continued for 16 h. Crystals of struvite formed during this time were separated from the remainder of liquid waste by decanting and washing with water five times. The crystals were dried at 50°C to a freely flowing fine off-white powder. A small sample was resuspended in pure water and viewed using optical microscopy at ×40 magnification.

2.3 Preparation of ammonia borane from sodium borohydride and struvite

Struvite from two sources were used–the one prepared from wastewater and commercially available struvite purchased from

Fisher Scientific. Different molar ratios of sodium borohydride ($NaBH_4$) and struvite ($NH_4MgPO_4{\cdot}6H_2O$) were heated to the desired temperatures and stirred for 16–96 h. Briefly, sodium borohydride ($NaBH_4$, 568 mg, 15 mmol) and struvite ($NH_4MgPO_4{\cdot}6H_2O$, 3.681 g, 15 mmol) were suspended in tetrahydrofuran (THF, 60 mL) as a slurry mixture in a 200 mL round bottom flask fitted with a reflux condenser and a magnetic stir bar. The reaction mixture was heated to 45°C and stirred for 72 h. Reaction completion was confirmed by ^{11}B NMR when H_2 production stops. After cooling to room temperature, the remaining solid (excess struvite and other by-products) was removed by filtration. The filtrate was then dried over anhydrous $MgSO_4$ and filtered again. Finally, THF solvent was removed by rotary evaporation to obtain the white solid AB product (96 mg, 21%, >99% purity) without further purification. For the experiments that were halted before the completion of the reaction, crude product was purified using ethanol as follows. Crude AB was dissolved in ethanol and stirred for 10 min. After removing the solids by filtration, ethanol was removed by rotary evaporator to get purified AB product.

2.4 Scanning electron microscopy (SEM) and energy-dispersive X-ray spectroscopy (EDX)

Struvite crystals were analyzed by using ThermoScientific Prisma E scanning electron microscope in a charge-up reduction mode which required no sample coating. SEM image measurements were made with FEI xT software and EDX analyses were done by using Pathfinder X-ray microanalysis software.

2.5 Thermogravimetric (TG) and differential scanning calorimetry (DSC) analyses

Weight change (TGA) and differential heat flow (DSC) were simultaneous measured on dry samples using Mettler Toledo DSC3+ device. All measurement were performed under N_2 atmosphere with a purge flow of 50 mL min^{-1}. Approximately 10 mg of struvite was added to an open alumina crucible, heated from 30.0°C to 300.0°C at a rate of 20°C min^{-1} and then held at 300.0°C for another 1.5 min. AB samples were analyzed in open alumina crucibles under similar conditions using approximately 2 mg samples at a heating rate of 5°C min^{-1} until it reaches to 210°C.

2.6 FTIR and NMR analyses

Solid AB samples were analyzed directly on IR spectrometer equipped with diamond-ATR probe for identifying the product (Supplementary Figures S3–S8). For NMR, samples were dissolved in D_2O solvent and analyzed by using Bruker 400 MHz Avance III spectrometer at room temperature. MNOVA software was used for spectral analysis. Ammonia borane signals: ^1H NMR in D_2O δ = 1.26 (q, 3H, BH_3); ^{11}B NMR in D_2O δ = −24.11 (q, BH_3).

3 Results and discussion

3.1 Physical and chemical compositions of struvite from wastewater

Struvite crystals from crude human urine were easily obtained. They were pitted as usual from formation in this complex mixture. However, they clearly showed the typical Coffin Lid form in some cases, as seen from the regular triangular crystal faces shown in Figure 1. Many other crystals were in the Chromosome form of struvite. This variability is caused by inconstant growth rates for the various crystal faces. Using inexpensive salts like $MgSO_4.7H_2O$ or ash for base (Witty, 2016a) improve economic viability tremendously. Unlike many methods recommended for struvite production, no special energy input beyond labor is needed. Our methods also use optimal crystal growth for sedimentation and air drying.

SEM image presented in Figure 2A shows both the Coffin Lid and Chromosome crystal forms with the average crystal length about 200 µm. Larger crystal size can be obtained by having fairly basic condition (pH 8–9) and allowing longer time for crystal growth. EDX result (Figure 2B) confirms the presence of struvite showing the abundant elements–N, Mg, P, and O. Struvite formula ($NH_4MgPO_4{\cdot}6H_2O$) has the N:P ratio of 1 to 1 but EDX result suggests this ratio to be 1 to 1.5. In addition to the typical elements from struvite, EDX also displays the presence of potassium (K). This likely comes from K-struvite ($KMgPO_4{\cdot}6H_2O$) which is favored to form in higher pH values (Rodrigues et al., 2019) and may explain the discrepancy of the N:P ratio.

Differential scanning calorimetry (DSC) and thermogravimetric (TGA) analyses of commercially available struvite and struvite from wastewater treatment are shown in Figures 3A, B, respectively. Differential scanning calorimetry (DSC) data were simultaneously obtained along with respective thermograms shown. Previous studies suggested that decomposition of struvite depends on heating rate (Iqbal et al., 2008). In this study, struvite samples were heated at a rate of 20°C per minute. Both struvite samples starts decomposing at 60°C and the decomposition rates increased at 80°C with a major mass loss of approximately 43% between 110°C and 200°C. The total mass loss for both samples at 300°C was 51% (Figure 3B). This is consistent with the theoretical mass loss of 51.4% for losing 1 mol of ammonia and 6 mol of water leaving solid Mg-pyrophosphate (Bianchi et al., 2020). A single, broad endothermic peak in both samples (Figure 3A) corresponds to the major mass loss which occurs when water and ammonia are lost simultaneously from struvite. Almost identical thermograms and the amount of heat absorbed (Supplementary Figures S1, S2) for the mass losses from the two sources suggests that these two samples are essentially the same.

3.2 Synthesis of ammonia borane from struvite

Synthesis of ammonia borane has been widely reported using various different methods including liquid ammonia and ammonium salts as the sources of ammonia. Metathesis reaction of ammonium salts with metal borohydrides is usually performed under mild reaction conditions to give reasonable yields and purity

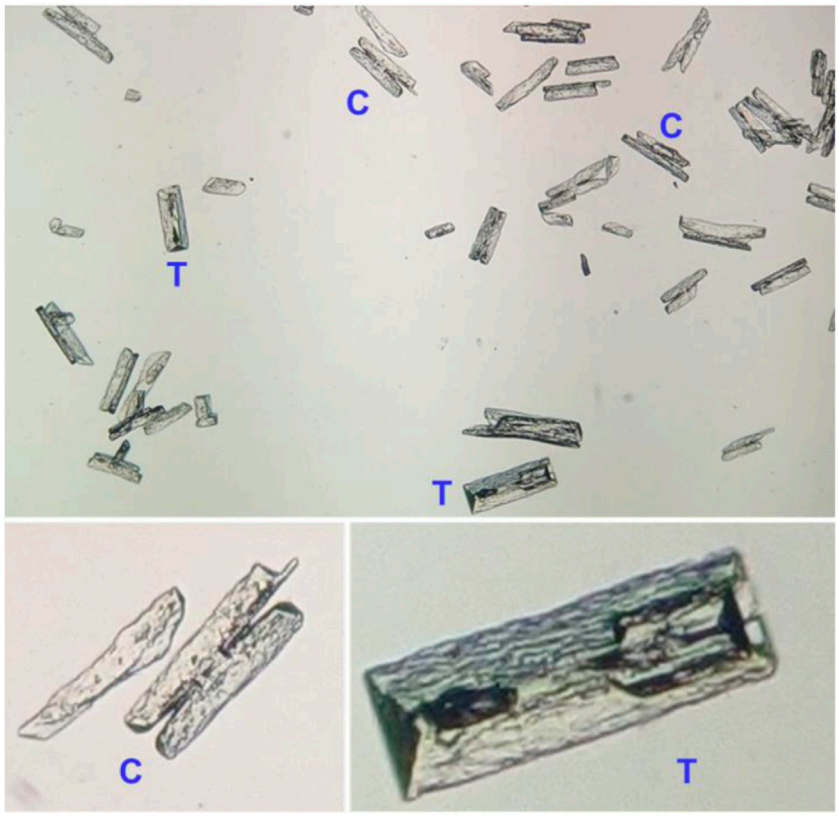

FIGURE 1
Optical microscopy of struvite crystals from human urine at 40x magnification. Triangular crystal faces (T) for Coffin Lid crystal forms are seen. Many other crystals have the Chromosome crystal form (C), some with crystal arms broken.

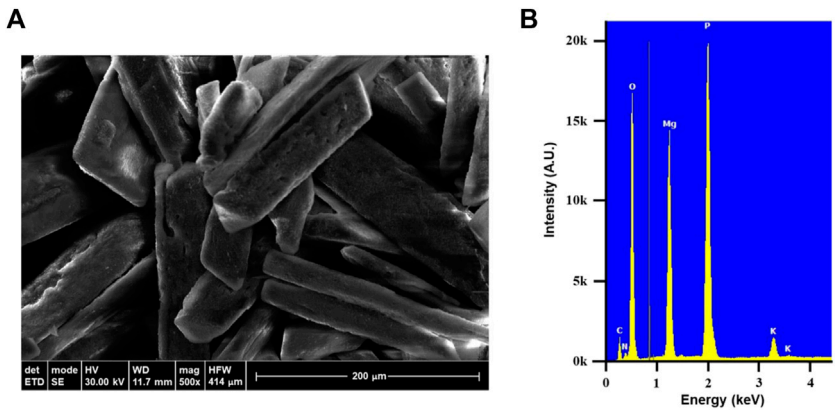

FIGURE 2
(A) SEM image of wastewater-derived struvite crystals. **(B)** EDX result of the struvite showing the presence of nitrogen, magnesium, phosphorous, oxygen, and potassium.

(Ramachandran and Gagare, 2007; Heldebrant et al., 2008). Since the recycled struvite contains ammonia that can be liberated fairly easily, it is used as a source of ammonia in this metathesis reaction as shown in Eq. 1. The conditions and yields of AB synthesis experiments are summarized in Table 1. The influence on the yield by several factors were tested–the ratio of the two reactants, the variations in the amount of solvent and the temperature, and the reaction time.

$$NH_4MgPO_4 \cdot 6H_2O + NaBH_4 \rightarrow NH_3BH_3 + NaMgPO_4 + H_2 + 6H_2O \quad (1)$$

Different ratios of sodium borohydride to struvite were examined first. Entry number 1 contains 1:1 ratio of the two reactants in 30 mL of

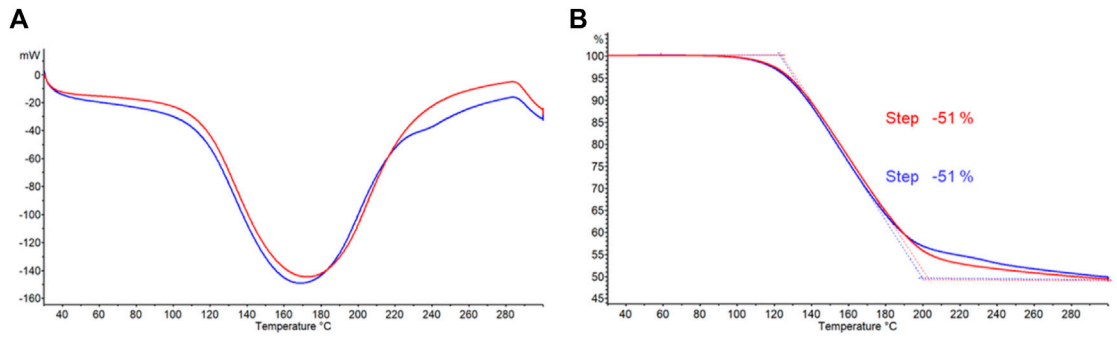

FIGURE 3
(A) Differential scanning calorimetry (DSC) and **(B)** thermogravimetric analysis (TGA) curves for struvite samples from different sources. Commercially available struvite is shown in blue and struvite from wastewater treatment is shown in red.

TABLE 1 Varied conditions of ammonia borane synthesis from struvite and sodium borohydride. Commercially available struvite was used for most trials. Entry number 3, marked with *, is the struvite obtained from wastewater. ** crude yield with impurities.

Entry number	$NaBH_4$ (mmol)	Struvite (mmol)	THF (mL)	Temperature (°C)	Time (hours)	Percent yield
1	15	15	30	45	72	19
2	15	15	60	45	72	21
3*	15	15	30	45	72	21
4	15	23	30	45	72	14
5	23	15	30	45	72	24
6	45	18	60	45	72	42
7	45	18	60	45	96	39
8	15	15	60	55	48	12
9	15	15	75	55	48	14
10	15	15	30	45	16	19/32**

THF solvent. Entry 2 uses the same ratio but doubling the volume of the solvent. Both were reacted at 45°C for 72 h and yielded similar amounts of product at 19%–21%. Using struvite obtained from wastewater (entry 3) produced results no different to that from commercial struvite (entry 1). Results from entry 1 and 3 confirm the DSC and TGA analyses from Figure 3 that the quality of the two starting materials is essentially the same. Observing gas evolution is a good way to monitor completion of the reaction as the hydrogen gas cease to form when $NaBH_4$ is completely consumed. In order to see if the reaction time can be reduced, reaction temperature was increased to 55°C as seen in entry 8 and 9. At this temperature, the reaction was completed in 48 h. However, raising the temperature reduced the yield to 12%–14% which indicates that AB product decomposition was also taking place as it was being made. AB is known to be stable in the solid state but undergoes slow decomposition in solvents such as THF and the decomposition of AB is expedited at temperatures beyond 50°C (Wang and Geanangel, 1988). In addition, $NaBH_4$ breaksdown at a faster rate at higher temperatures (Schlesinger et al., 1953) making it less available to react with struvite.

The $NaBH_4$ to struvite ratio was then changed to 1:1.5 and 1.5:1 in entry 4 and 5 respectively. When struvite was in excess, we observed a drop in the yield to only 14%. On the other hand, the yield increases to 24% when extra $NaBH_4$ was added in the reaction. This could be rationalized by the fact that struvite crystal contains 6 mol of water per 1 mol of ammonium, and water also reacts with borohydride producing hydrogen gas. In fact, these 6 mol of water will consume 1.5 mol of $NaBH_4$. This suggests that instead of 1 mol of borohydride for 1 mol of struvite, 2.5 mol of borohydride is consumed. To confirm this assumption, a 2.5 to 1 mol ratio of borohydride and struvite was tested in trials 6 and 7. Increasing $NaBH_4$ yielded higher amounts of products at a 39%–42% range. Because $NaBH_4$ readily reacts with water from struvite, having excess of it will ensure that the reaction moves forward to form ammonia borane. Metathesis reactions using borohydride and ammonium salts are generally carried out under mild temperatures and at low reagent concentrations. In fact, the product yield and purity depend on the reaction condition kept at low concentrations (Ramachandran and Gagare, 2007). We also tried different concentrations in our experiments increasing the solvent amount used for the reactions but there are negligible differences in the yield or the purity.

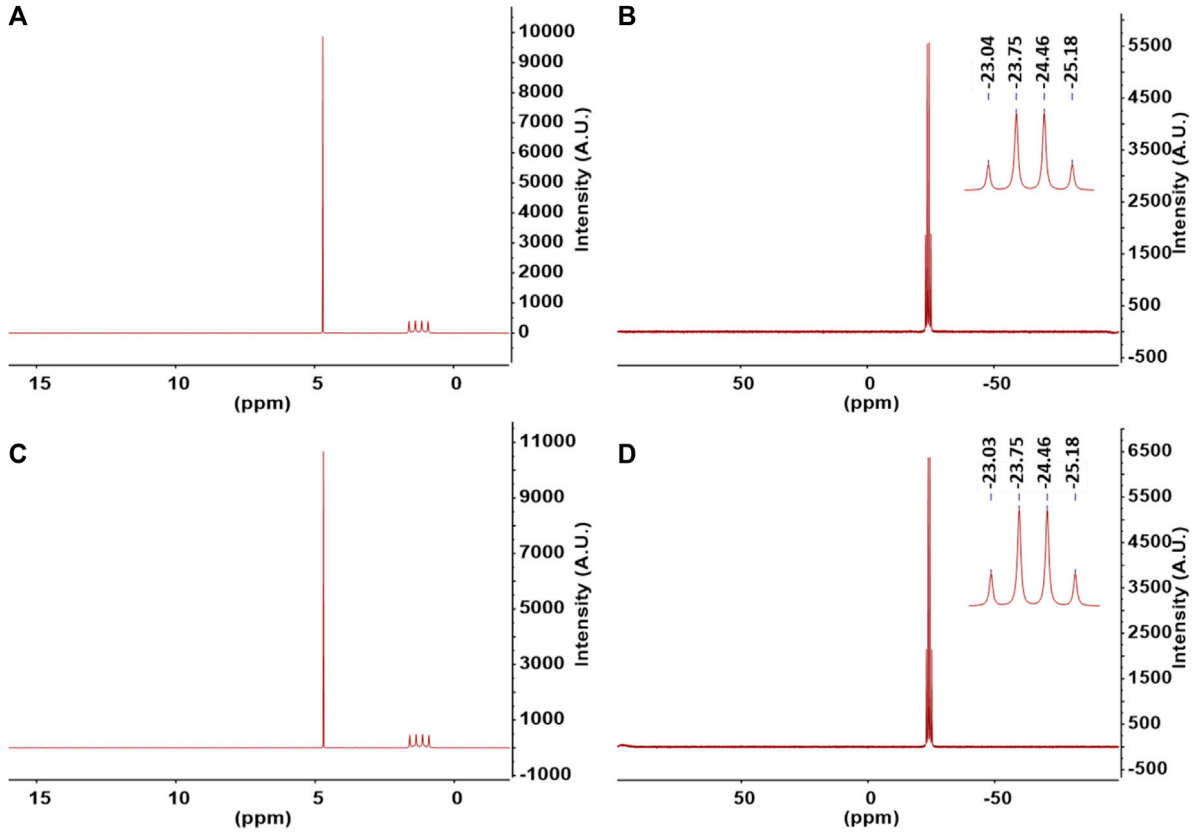

FIGURE 4
(A) ^{1}H NMR and **(B)** ^{11}B NMR of ammonia borane synthesized using commercially available struvite. **(C)** ^{1}H NMR and **(D)** ^{11}B NMR of ammonia borane synthesized using reclaimed struvite from wastewater. Samples were dissolved in D_2O and spectra acquired at room temperature.

Examination of the mole ratio variability suggests that higher yields can be achieved with excess $NaBH_4$. The best result which gives roughly 42% yield is obtained from $NaBH_4$ to struvite ratio of 3:1 at low temperature. In practical applications, the wastewater product, struvite, should be the one present in excess amount. Nevertheless, even with the stoichiometric ratio of the reactants, 20% yield is obtained at a high purity. The THF solvent from this reaction can be reclaimed from the rotary evaporator minimizing the waste. Further improvement on the yield in the future can be made by incorporationg anhydrous reagents in the reaction mixture to absorb water from struvite crystals.

3.3 Analysis of ammonia borane product for purity

In order to analyze the purity of ammonia borane product, nuclear magnetic resonance (NMR) spectroscopy was employed. The samples were dissolved in D_2O solvent for the analysis. This solvent was chosen since the primary impurities such as boric acid and borates dissolve in water but do not dissolve in standard NMR solvents including DMSO-d_6, THF-d_4, or CH_3CN-d_3. Therefore, we expect any impurities present in the sample to appear on the spectra when dissolved in D_2O. ^{1}H and ^{11}B NMR of ammonia borane synthesized from commercially available struvite and struvite from wastewater are shown in Figures 4A–D, respectively. ^{1}H NMR spectra of AB products in Figures 4A, C exhibit a quartet of BH_3 at δ1.26 ppm (J = 92.0 Hz) as a result of ^{11}B nucleus splitting the proton signal. A quartet peak at δ-24.11 ppm in the ^{11}B NMR spectrum (Figures 4B, D) indicates the presence of a boron atom with three hydrogens as in -BH_3. Both ^{11}B and ^{1}H NMR spectra in D_2O show only the peaks attributed to AB product and HDO solvent residue (^{1}H NMR δ4.70 ppm) from proton exchange with NH_3. The major concern when using borohydrides with even a trace amount of water in the reaction is the reactivity of boron towards water producing undesired side products such as boric acid and tetrahydroxyborate [$B(OH)_4^-$] species (Schlesinger et al., 1953). There are no traces of the reactant $NaBH_4$ or other boron species on ^{11}B NMR as well as other hydrogen-containing compounds in the ^{1}H NMR spectra. Once the reaction is allowed to continue until completion, ammonia borane produced from this process, without further purification, is of very high purity at >99% as determined by ^{1}H and ^{11}B NMR spectroscopy.

In cases where the reaction is stopped before completion, the product contains high amounts of impurities. Example sample (Table 1 entry 10) was prepared to test if simple purification method can eliminate impurities and give a pure AB product. The

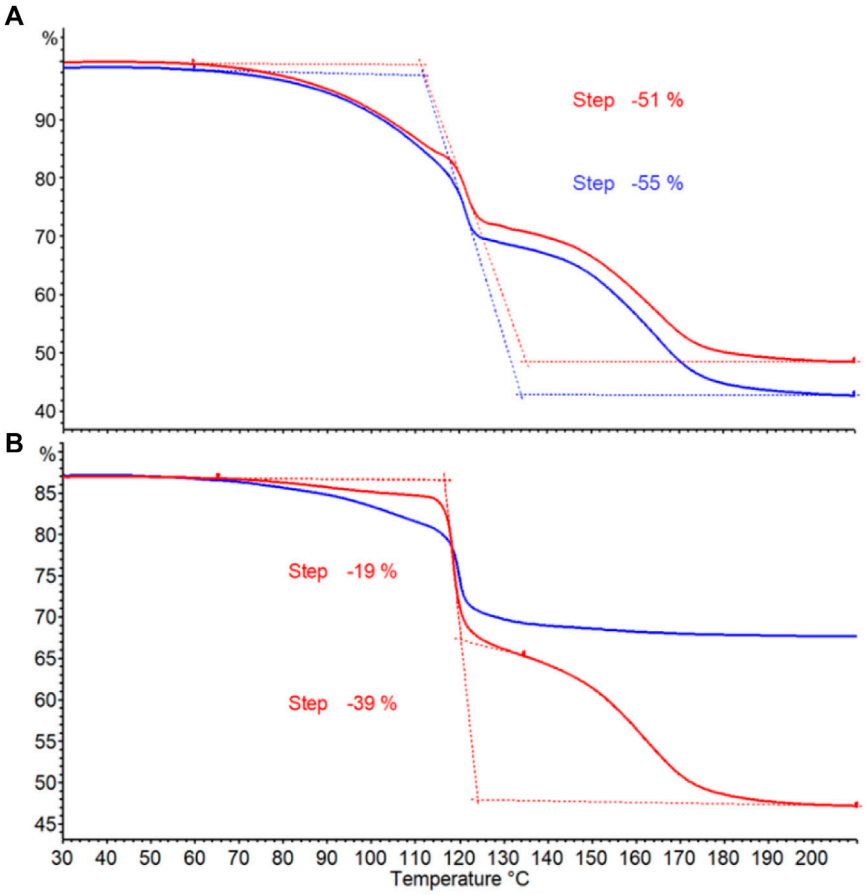

FIGURE 5
Thermogravimetric curves for determining thermal decomposition of AB. **(A)** Pure AB products from wastewater struvite (blue) and commercial struvite (red). **(B)** AB sample obtained from stopping the reaction at 16 h (Table 1 entry 10). Crude AB (blue) and purified AB (red) obtained from ethanol purification.

majority of impurities present appears to be borate (12%) and unreacted borohydride (4%) (Supplementary Figure S9E). After dissolving crude product in ethanol, filtering the impurities, and evaporating the solvent, purified product was achieved. This simple purification step provides pure AB product as confirmed by spectroscopic analyses (Supplementary Figures S6, S9C, D). The yield after purification is 19% which is essentially the same as the yield obtained when the reaction is allowed to continue until completion at 72 h. It is reasonable to assume that the ongoing decomposition of the AB product as it is being made limits the amount of product we can recover. Synthetic routes that provide impure AB product present major challenges for purification as AB must be of high purity for it to be useful as a hydrogen fuel. One of the methods used to improve the purity of AB involves dissolving the crude AB in the organic solvents such as ether and extracting the impurities with highly basic aqueous sodium hydroxide solution (Drost, 2014). Our method uses ethanol which is a common, inexpensive solvent and does not require extraction using caustic solutions. Borohydride in crude product is easily removed by reaction with ethanol. The resulting product, a form of borate, is insoluble in ethanol. By filtering out the insoluble impurities, we achieve a pure AB at >99% purity.

3.4 Thermolytic properties of ammonia borane by thermogravimetric analysis

Thermogravimetric (TG) analysis is routinely used for screening hydrogen storage materials including ammonia borane. Thermal decomposition of ammonia borane occurs in two stages. The first stage involves AB decomposition into hydrogen gas and aminoborane (NH_2BH_2). At a higher temperature, AB decomposes in the second stage to hydrogen gas as well as ammonia (NH_3), diborane (B_2H_6), and borazine ($B_3N_3H_6$) (Frueh et al., 2011; Demirci, 2021). TG curves obtained from AB products prepared are shown in Figure 5. The onset temperature of the first main decomposition is found consistently around 65°C for all the samples. These onset temperatures are comparable to those of AB doped with metal chlorides and of AB in mesoporous materials (Nakagawa et al., 2016; Sullivan et al., 2017). The onset temperature for the second stage decomposition is 135°C for all pure samples. Crude AB with impurities does not show second stage decomposition (Figure 5B blue line). Percent weight losses for pure AB products from wastewater struvite and commercial struvite are 55% and 51% respectively (Figure 5A). Purified AB also shows 39% weight loss while impure AB only loses 19% (Figure 5B). The hydrogen content in AB is only 19.6 wt%, yet the extra weight loss come from losing decomposition by-products

such as NH_2BH_2, NH_3, B_2H_6, and $B_3N_3H_6$. This higher weight loss is due to the use of open crucible which allows the gases to escape easily therefore preventing the reaction of by-products towards the formation of polymeric solid residues (Petit and Demirci, 2019). Likewise, another synthesis stopped at 24 h and subjected to ethanol purification also show similar TGA analyses for crude and purified AB (Supplementary Figure S14). We observe that while the weight losses and the curves for pure AB products from one-step synthesis that requires no purification are similar (Figure 5A), they are slightly different from those of ethanol-purified AB. The curve at the first stage of decomposition is sharper (Figure 5B) and the weight loss is less for purified AB. Varying degree of crystallinity in AB products obtained from different solvents may be responsible for the differences in the TG profiles observed.

4 Conclusion

Hydrated crystal struvite ($NH_4MgPO_4{\cdot}6H_2O$) from wastewater is used in this research for the synthesis of ammonia borane (NH_3BH_3). The chemical nature of ammonia borane as a source of hydrogen makes it valuable for potential use in applications where a compact and safe hydrogen storage is required. Future direction includes scaling up the process and mitigating the challenges that come from safely handling the hydrogen gas byproduct. Human urine contains many chemical entities, proteins and even human and bacterial cells. It is remarkable to have such a simple process that starts with a high degree of chemical and biological complexity and ends up with such a high degree of purity for ammonia borane that is used as a renewable energy source. This process is extremely valuable for wastewater and energy industries as something that is considered a waste product is converted into a valuable material.

Data availability statement

The original contributions presented in the study are included in the article/Supplementary Material, further inquiries can be directed to the corresponding author.

Author contributions

ND: Conceptualization, Writing–original draft, Writing–review and editing. MW: Formal Analysis, Investigation, Writing–review and editing. MC: Investigation, Writing–original draft. NB: Investigation, Writing–original draft. TA: Conceptualization, Investigation, Supervision, Writing–review and editing, Writing–original draft.

Funding

The authors declare financial support was received for the research, authorship, and/or publication of this article. We thank the support by UT System STARs Program and FSW Academic Research Council for funding this research.

Conflict of interest

The authors declare that the research was conducted in the absence of any commercial or financial relationships that could be construed as a potential conflict of interest.

Publisher's note

Supplementary material

The Supplementary Material for this article can be found online at: https://www.frontiersin.org/articles/10.3389/fchem.2023.1269845/full#supplementary-material

References

Acar, C., and Dincer, I. (2020). The potential role of hydrogen as a sustainable transportation fuel to combat global warming. *Int. J. Hydrogen Energy* 45 (5), 3396–3406. doi:10.1016/j.ijhydene.2018.10.149

Akbayrak, S., and Özkar, S. (2018). Ammonia borane as hydrogen storage materials. *Int. J. Hydrogen Energy* 43 (40), 18592–18606. doi:10.1016/j.ijhydene.2018.02.190

Beres, J., Dodds, A., Morabito, A. J., and Adams, R. M. (1971). Dimethyl sulfide-borane as a borane carrier. *Inorg. Chem.* 10 (9), 2072–2074. doi:10.1021/ic50103a049

Bianchi, L., Kirwan, K., Alibardi, L., Pidou, M., and Coles, S. R. (2020). Recovery of ammonia from wastewater through chemical precipitation: investigating the kinetic mechanism and reactions pathway of struvite decomposition. *J. Therm. Anal. Calorim.* 142, 1303–1314. doi:10.1007/s10973-019-09108-5

Chen, X., Zhao, J. C., and Shore, S. G. (2013). The roles of dihydrogen bonds in amine borane Chemistry. *Acc. Chem. Res.* 46 (11), 2666–2675. doi:10.1021/ar400099g

Demirci, U. B. (2021). Mechanistic insights into the thermal decomposition of ammonia borane, a material studied for chemical hydrogen storage. *Inorg. Chem. Front.* 8, 1900–1930. doi:10.1039/D0QI01366H

Doyle, J. D., and Parsons, S. A. (2002). Struvite formation, control and recovery. *Water Res.* 36 (16), 3925–3940. doi:10.1016/s0043-1354(02)00126-4

Drost, K. J. (2014). *Ammonia borane purification method. US Patent No. US9604850B2.* Washington DC: US Patent and Trademark Office.

Durbin, D. J., and Malardier-Jugroot, C. (2013). Review of hydrogen storage techniques for on board vehicle applications. *Int. J. Hydrogen Energy* 38 (34), 14595–14617. doi:10.1016/j.ijhydene.2013.07.058

Esrey, S. A. (2001). Towards a recycling society: ecological sanitation--closing the loop to food security. *Water Sci. Technol.* 43 (4), 177–187. doi:10.2166/wst.2001.0215

Frueh, S., Kellett, R., Mallery, C., Molter, T., Willis, W. S., King'ondu, C., et al. (2011). Pyrolytic decomposition of ammonia borane to boron nitride. *Inorg. Chem.* 50 (3), 783–792. doi:10.1021/ic101020k

Hamilton, C. W., Baker, R. T., Staubitzc, A., and Manners, I. (2009). B–N compounds for chemical hydrogen storage. *Chem. Soc. Rev.* 38 (1), 279–293. doi:10.1039/b800312m

Heldebrant, D. J., Karkamkar, A., Linehana, J. C., and Autrey, T. (2008). Synthesis of ammonia borane for hydrogen storage applications. *Energy Environ. Sci.* 1, 156–160. doi:10.1039/B808865A

Hirscher, M., Yartys, V. A., Baricco, M., Bellosta Von Colbe, J., Blanchard, D., Bowman, R. C., et al. (2020). Materials for hydrogen-based energy storage – past, recent

progress and future outlook. *J. Alloys Compd.* 827, 153548. doi:10.1016/j.jallcom.2019.153548

Iqbal, M., Bhuiyan, H., Mavinic, D. S., and Koch, F. A. (2008). Thermal decomposition of struvite and its phase transition. *Chemosphere* 70 (8), 1347–1356. doi:10.1016/j.chemosphere.2007.09.056

Jaska, C. A., Temple, K., Lough, A. J., and Manners, I. (2003). Transition metal-catalyzed formation of boron-nitrogen bonds: catalytic dehydrocoupling of amine-borane adducts to form aminoboranes and borazines. *J. Am. Chem. Soc.* 125 (31), 9424–9434. doi:10.1021/ja030160l

Kirchmann, H., and Pettersson, S. (1994). Human urine - chemical composition and fertilizer use efficiency. *Fertilizer Res.* 40, 149–154. doi:10.1007/BF00750100

Komova, O. V., Simagina, V. I., Kayl, N. L., Odegova, G. V., Netskina, O. V., Chesalov, Y. A., et al. (2013). Improved low-temperature hydrogen generation from NH3BH3 and TiO2 composites pretreated with water. *Int. J. Hydrogen Energy* 38 (15), 6442–6449. doi:10.1016/j.ijhydene.2013.03.074

Li, H., Yang, Q., Chen, X., and Shore, S. G. (2014). Ammonia borane, past as prolog. *J. Organomet. Chem.* 751 (1), 60–66. doi:10.1016/j.jorganchem.2013.08.044

Maaß, H. J., and Möckel, H. O. (2019). Combined decarbonization of electrical energy generation and production of synthetic fuels by renewable energies and fossil fuels. *Chem. Eng. Technol.* 43 (1), 111–118. doi:10.1002/ceat.201900384

Malila, R., Lehtoranta, S., and Viskari, E.-L. (2019). The role of source separation in nutrient recovery – comparison of alternative wastewater treatment systems. *J. Clean. Prod.* 219, 350–358. doi:10.1016/j.jclepro.2019.02.024

Maroušek, J., Kolář, L., Strunecký, O., Kopecký, M., Bartoš, P., Marouškova, A., et al. (2020). Modified biochars present an economic challenge to phosphate management in wastewater treatment plants. *J. Clean. Prod.* 272 (1), 123015. doi:10.1016/j.jclepro.2020.123015

Nakagawa, Y., Zhang, T., Kitamura, M., Isobe, S., Hino, S., Hashimoto, N., et al. (2016). A systematic study of the effects of metal chloride additives on H2 desorption properties of ammonia borane. *J. Chem. Eng. Data* 61 (5), 1924–1929. doi:10.1021/acs.jced.6b00143

Petit, J.-F., and Demirci, U. B. (2019). Discrepancy in the thermal decomposition/dehydrogenation of ammonia borane screened by thermogravimetric analysis. *Int. J. Hydrogen Energy* 44 (27), 14201–14206. doi:10.1016/j.ijhydene.2018.10.148

Puszkiel, J., Garroni, S., Milanese, C., Gennari, F., Klassen, T., Dornheim, M., et al. (2017). Tetrahydroborates: development and potential as hydrogen storage medium. *Inorganics* 5, 74. doi:10.3390/inorganics5040074

Ramachandran, P. V., and Gagare, P. D. (2007). Preparation of ammonia borane in high yield and purity, methanolysis, and regeneration. *Inorg. Chem.* 46 (19), 7810–7817. doi:10.1021/ic700772a

Rodrigues, D. M., Do Amaral Fragoso, R., Carvalho, A. P., Hein, T., and Guerreiro De Brito, A. (2019). Recovery of phosphates as struvite from urine-diverting toilets: optimization of pH, Mg:PO4 ratio and contact time to improve precipitation yield and crystal morphology. *Water Sci. Technol.* 80 (7), 1276–1286. doi:10.2166/wst.2019.371

Schlesinger, H. I., Brown, H. C., Finholt, A. E., Gilbreath, J. R., Hoekstra, H. R., and Hyde, E. K. (1953). Sodium borohydride, its hydrolysis and its use as a reducing agent and in the generation of hydrogen. *J. Am. Chem. Soc.* 75 (1), 215–219. doi:10.1021/ja01097a057

Shore, S. G., Girardot, P. R., and Parry, R. W. (1958). Chemical evidence for the structure of the "diammoniate of diborane." V. A tracer study of the reaction between sodium and the "diammoniate of diborane". *J. Am. Chem. Soc.* 80 (1), 20–24. doi:10.1021/ja01534a006

Shore, S. G., and Parry, R. W. (1958). Chemical evidence for the structure of the "diammoniate of diborane." II. The preparation of ammonia-borane. *J. Am. Chem. Soc.* 80 (1), 8–12. doi:10.1021/ja01534a003

Simha, P., and Ganesapillai, M. (2007). Ecological Sanitation and nutrient recovery from human urine: how far have we come? A review. *Sustain. Environ. Res.* 27 (3), 107–116. doi:10.1016/j.serj.2016.12.001

Stephens, F. H., Pons, V., and Baker, R. T. (2007). Ammonia–borane: the hydrogen source par excellence? *Dalton Trans.* 25, 2613–2626. doi:10.1039/b703053c

Sullivan, J. A., Herron, R., and Phillips, A. D. (2017). Towards an understanding of the beneficial effect of mesoporous materials on the dehydrogenation characteristics of NH3BH3. *Appl. Catal. B Environ.* 201, 182–188. doi:10.1016/j.apcatb.2016.08.040

Veziroglu, T. N. (2007). "21st century's energy: hydrogen energy system," in *Assessment of hydrogen energy for sustainable development. NATO science for peace and security series C: environmental security*. Editors J. W. Sheffield and Ç. Sheffield (Dordrecht: Springer).

Wang, J. S., and Geanangel, R. A. (1988). 11B NMR studies of the thermal decomposition of ammonia borane in solution. *Inorg. Chim. Acta* 148 (2), 185–190. doi:10.1016/S0020-1693(00)87499-X

Witty, M. (2016a). Ancient Roman urine Chemistry. *Acta Archaeol.* 87 (1), 179–191. doi:10.1111/j.1600-0390.2016.12170.x

Witty, M. (2016b). Hooke's gravel was struvite. *Notes Queries* 63 (4), gjw218–570. doi:10.1093/notesj/gjw218

Witty, M., Al-Bahou, R., Copley, S., Dingra, N. N., and Ayudhya, T. I. (2020). Facile and simultaneous separation of nitrogen, phosphorus and bacteria from urine by using ash depth filters which harvest ammonium and phosphate as Struvite Enriched Ash. *J. Water Sanit. Hyg. Dev.* 10 (2), 374–377. doi:10.2166/washdev.2020.013

Zamora, P., Georgieva, T., Salcedo, I., Elzinga, N., Kuntke, P., and Buisman, C. J. N. (2017). Long-term operation of a pilot-scale reactor for phosphorus recovery as struvite from source-separated urine. *J. Chem. Technol. Biotechnol.* 92 (5), 1035–1045. doi:10.1002/jctb.5079

Zhang, X., Kam, L., Trerise, R., and Williams, T. J. (2017). Ruthenium-Catalyzed ammonia borane dehydrogenation: mechanism and utility. *Acc. Chem. Res.* 50 (1), 86–95. doi:10.1021/acs.accounts.6b00482

frontiers | Frontiers in Chemistry

TYPE Review
PUBLISHED 27 November 2023
DOI 10.3389/fchem.2023.1306182

OPEN ACCESS

EDITED BY
Daily Rodriguez-Padron,
Ca' Foscari University of Venice, Italy

REVIEWED BY
Antonio Pineda,
University of Cordoba, Spain
Peter Joseph Deuss,
University of Groningen, Netherlands

*CORRESPONDENCE
Christophe Len,
christophe.len@chimieparistech.psl.eu

RECEIVED 03 October 2023
ACCEPTED 14 November 2023
PUBLISHED 27 November 2023

CITATION
Len C, Duhan V, Ouyang W, Nguyen R and Lochab B (2023), Mechanochemistry and oleochemistry: a green combination for the production of high-value small chemicals.
Front. Chem. 11:1306182.
doi: 10.3389/fchem.2023.1306182

Mechanochemistry and oleochemistry: a green combination for the production of high-value small chemicals

Christophe Len[1,2]*, Vaishaly Duhan[3], Weiyi Ouyang[1], Remi Nguyen[2] and Bimlesh Lochab[3]

[1]School of Chemistry, Xi'an Jiaotong University, Xi'an, China, [2]Institute of Chemistry for Life and Health Sciences, Chimie ParisTech, PSL Research University, Paris, France, [3]Materials Chemistry Laboratory, Department of Chemistry, School of Natural Sciences, Shiv Nadar Institution of Eminence, Gautam Buddha Nagar, Greater Noida, India

Mechanochemistry and oleochemistry and their combination have been known for centuries. Nevertheless, bioeconomy and circular economy concepts is much more recent and has motivated a regain of interest of dedicated research to improve alternative technologies for the valorization of biomass feedstocks. Accordingly, this review paper aims essentially at outlining recent breakthroughs obtained in the field of mechanochemistry and oleochemicals such as triglycerides, fatty acids, and glycerol derivatives. The review discusses advances obtained in the production of small chemicals derived from oils with a brief overview of vegetable oils, mechanochemistry and the use of mechanochemistry for the synthesis of biodiesel, lipidyl-cyclodextrine, dimeric and labelled fatty acids, calcium diglyceroxide, acylglycerols, benzoxazine and solketal. The paper also briefly overviews advances and limits for an industrial application.

KEYWORDS

mechanochemistry, vegetable oil, glycerol, batch reactor, continuous flow reactor

1 Introduction

For several decades now, society has been confronting significant challenges directly linked to our way of life. The world's population continues to grow, leading to an ever-increasing demand for energy. At the same time, concerns arise due to the scarcity of resources, including food and water, and the depletion of fossil fuel reserves. These issues are of utmost importance for the wellbeing of future generations. To address these challenges, scientists, governments, politicians, and citizens are actively engaged in creating and promoting new practices to establish a more sustainable society for the future. However, achieving this societal transformation is no simple task and demands substantial, multidisciplinary collaborative efforts to develop greener technologies and environmentally friendly methodologies such as mechanochemistry (Mateti et al., 2021; Michalchuk et al., 2021; Bolt et al., 2022; Cuccu et al., 2022), microwave chemistry (da Costa et al., 2023; Kumar et al., 2023; Nguyen et al., 2021; Zhao et al., 2020; Rodriguez-Padron et al., 2020), sonochemistry (Maddikeri et al., 2012; Martinez et al., 2021; Kargar et al., 2022) and others. Mechanochemistry, a cutting-edge branch of chemistry, aligns seamlessly with the principles of "green chemistry." Green chemistry aims to design and develop chemical processes that are more environmentally friendly, sustainable, and less hazardous.

Mechanochemistry contributes to these goals by promoting efficient, solvent-free, and energy-saving reactions. It eliminates or minimizes the use of toxic or harmful reagents and reduces waste generation. Additionally, mechanochemical processes often require lower temperatures, lowering energy consumption and greenhouse gas emissions. The technique also enhances reaction selectivity, leading to fewer byproducts and less need for purification steps. This synergy between mechanochemistry and green chemistry fosters innovation in the development of cleaner, more sustainable chemical processes. It opens the door to more eco-friendly manufacturing, benefiting both the environment and the chemical industry, making it a crucial component of sustainable chemistry practices. Among the promising alternatives to tackle future challenges are renewable resources such as vegetable oil (Xia and Larock, 2010; Yara-Varon et al., 2017), lignocellulose (Vu et al., 2020; Lobato-Peralta et al., 2021; Ning et al., 2021), and others and the concept of biorefinery (Botero Gutierrez et al., 2017; Calvo-Flores and Martin-Martinez, 2022). Oleochemistry, the chemistry of oil plays a pivotal role in harnessing renewable resources for various applications. Derived from natural fats and oils, oleochemicals serve as a sustainable alternative to traditional petrochemicals. This branch of chemistry is centered around utilizing triglycerides and fatty acids from plant and animal sources, making it inherently renewable. One of the key advantages of oleochemistry is its reliance on bio-based feedstocks, which are replenishable through agriculture and farming practices. This reduces our dependence on finite fossil resources, contributing to a more sustainable and eco-friendly chemical industry. Oleochemicals can be transformed into a wide range of valuable products, including biodiesel, soaps, surfactants, lubricants, and more. Furthermore, oleochemistry aligns with the principles of green chemistry, emphasizing the use of environmentally benign processes and reduced waste generation. It offers a viable pathway to reduce greenhouse gas emissions and mitigate environmental impacts associated with traditional petrochemical production. As the world seeks more sustainable alternatives, oleochemistry stands as a promising and renewable resource with a bright future in various industries. By adopting processes similar to or even more sustainable than those used in petrochemicals, we can effectively recover biomass and biomass waste (da Costa et al., 2022; Khodadadi et al., 2020), enabling the production of valuable chemicals, materials, fuels, and energy (Nayak and Bhushan, 2019; Chen et al., 2020; Nasrollahzadeh et al., 2020). Despite the advantages, the use of biomass also presents certain challenges. One such issue is the competition between food/feed production and non-food chemistry, as the demand for biomass increases. Additionally, the expanded use of biomass has implications for land use and water availability, necessitating careful consideration and sustainable management practices.

Nevertheless, the chemical industry has a growing need to replace petro-sourced small molecules with bio-sourced molecules and, also to create new biobased molecules with identical or different properties using green innovative technology. This review aims to present and comment on the latest advancements in the valorization of oils such as triglycerides, fatty acids, fatty esters, and glycerol (oleochemistry) through mechanochemistry as an innovative technique for the production of high-value small molecules.

2 Vegetable oils: production, chemical modification to small chemicals

According to the US Department of Agriculture (USDA), the world's vegetable oil production for the year 2023/24 is projected to reach 222.8 million tonnes, showing a 2.7% increase compared to the previous year (2022/2023) (Vegetable oil production in 2023/24 expected to be up on previous year, 2023). In 2022, the Global Vegetable Oil Market was valued at USD 2.192 Billion, and it is expected to grow significantly with a projected value of USD 4.46 Billion by 2030. The industry is expected to register a Compound Annual Growth Rate (CAGR) of 9.3% during the forecast period of 2022–2028 (Vegetable oil market–Industry analysis, trends and forecast (2023-2029). The global vegetable oil market is segmented based on type, including soybean oil, rapeseed oil, sunflower oil, palm oil, olive oil, corn oil, peanut oil, coconut oil, and others. Furthermore, it is categorized by packaging applications, with food products accounting for 27%, followed by animal feed at 21%, cosmetics at 19%, pharmaceuticals at 13%, biodiesel at 10%, and others at 10%. The distribution channels include direct sales, supermarkets, convenience stores, specialty stores, e-commerce, and others. Key players in this market include Cargill, Wilmar International, Archer Daniels Midland Company, Avril group, and others (Vegetable oil market–Industry analysis, trends and forecast (2023-2029).

The main components of vegetable oils are triglycerides, which consist of a glycerol moiety and three fatty acid chains, either identical or different. Figure 1 illustrates the most common natural fatty acids that have been identified for the vegetable oils.

Most vegetable oils are utilized either directly or shortly after refinement, but some require chemical modification before they can be used. This modification process involves various chemical reactions targeting the carboxy groups, the methylene sites next to ester, the unsaturated bonds or the allylic carbon atom, tailored to meet specific industrial requirements (Figure 2). In the case of ricinolein, another possibility is to modify the hydroxyl group in position 12.

In industrial processing, vegetable oils are transformed into glycerol, fatty acids, methyl esters, and fatty alcohols (Biermann et al., 2011). To obtain specific chemicals of interest, subsequent chemical modification steps are often undertaken. These reactions primarily involve addressing the unsaturated bonds, such as epoxidation, hydroformylation, dimerization, thiol-ene coupling, oxidative cleavage (ozonolysis), olefin metathesis, pericyclic reactions, radical additions, as well as transition-metal catalyzed and Diels–Alder syntheses for aromatic compounds. The range of chemicals produced includes, but is not limited to, soaps, surfactants, emollients, fuel, pesticide formulations, and lubricants.

Among the compounds obtained from vegetable oil, glycerol (propane-1,2,3-triol) is both a side-product of biodiesel industry and a platform molecule of interest (Len et al., 2018; Varma and Len, 2019; Zhao et al., 2023). With a steady compound annual growth rate (CAGR) of 1.7% projected between 2022 and 2031, the sales of glycerol are expected to rise from $4.3 billion to $5.1 billion (Glycerol market to Garner $5.1 billion, globally by 2031 at 1.7% CAGR says allied market research, 2022). The increasing demand for glycerol is driven by its wide-ranging applications in various products, including personal care items, pharmaceuticals, and the food and beverage industry. As a result, the

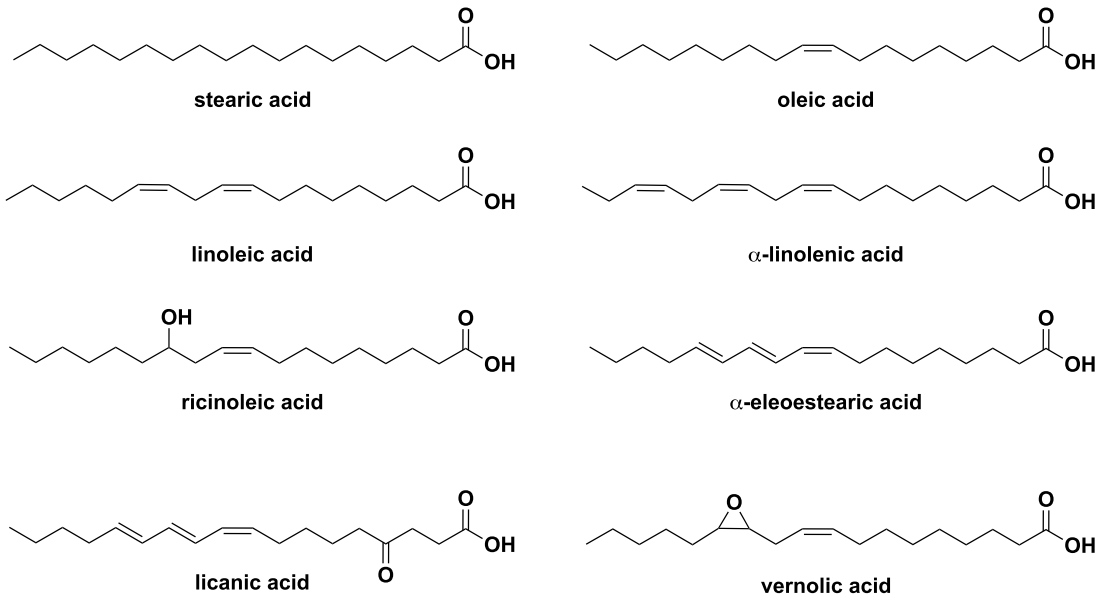

FIGURE 1
Main fatty acids present in the composition of vegetable oils.

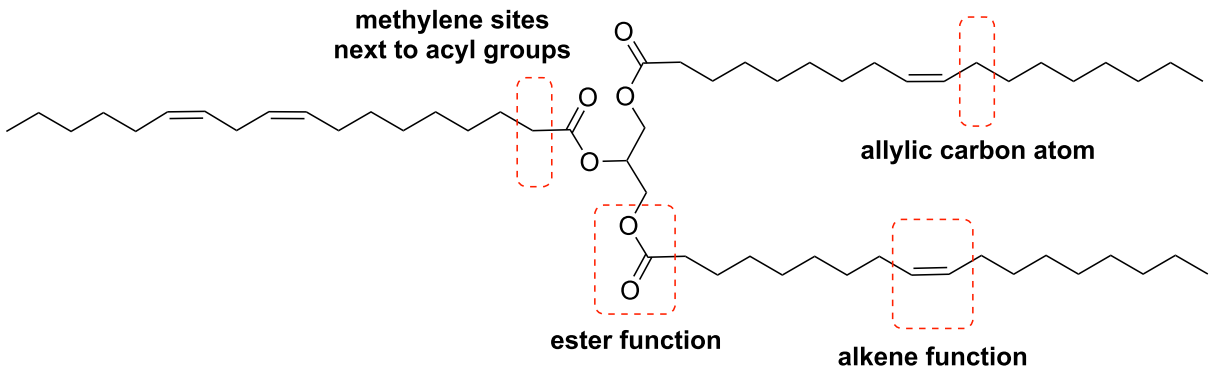

FIGURE 2
Main chemical reactive sites of unsaturated triglycerides.

demand for glycerol is anticipated to keep growing steadily. Moreover, glycerol is as a source of biobased C_3 carbon atoms capable of being converted into more than 2000 products. These products include acrolein, acrylic acid, ethylene glycol, oxalic acid, syngas, 1,2- and 1,3-propanediol, mono-, di- and triglycerides, epichlorohydrin, polyglycerols, ketals, acetals, and many others. These derivatives find specific applications in industries like polymers, agrochemicals, and pharmaceuticals (Figure 3).

3 Mechanochemistry: principle, equipement and mechanism

Mechanochemistry has garnered significant interest as a powerful, sustainable, time-saving, environmentally friendly, and cost-effective synthesis method for preparing new functional materials. This approach relies on chemical and physicochemical transformations driven by mechanical force through grinding and milling. The IUPAC defines the mechanochemical synthesis as: "a chemical reaction that is induced by the direct absorption of mechanical energy" (Horie et al., 2004; Balaz et al., 2013; Rightmire and Hanusa, 2016). Mechanochemistry enables chemical reactions to take place through the application of mechanical energy, which can be provided either by manual grinding or automated milling, often without the use of solvents. When necessary, the use of small quantities of solvent is necessary to enhance chemical reactivity and this is where the term "Liquid-Assisted Grinding" (or solvent-drop grinding) is employed (Ying et al., 2021). When liquid-assisted grinding is used, the solubility of the reactants in the solvent is not considered because the solvent acts

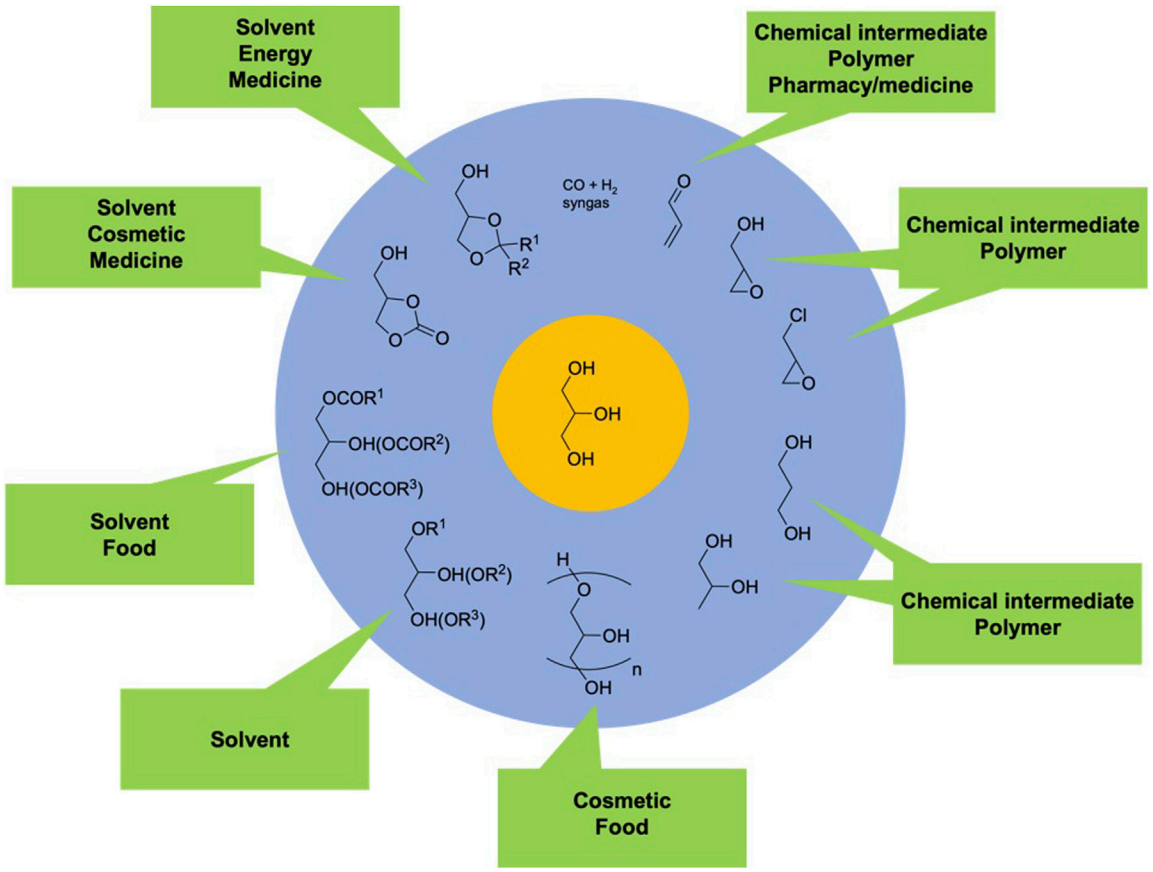

FIGURE 3
Roadmap to selected bio-based C_3 chemicals starting from glycerol and their applications (Varma and Len, 2019).

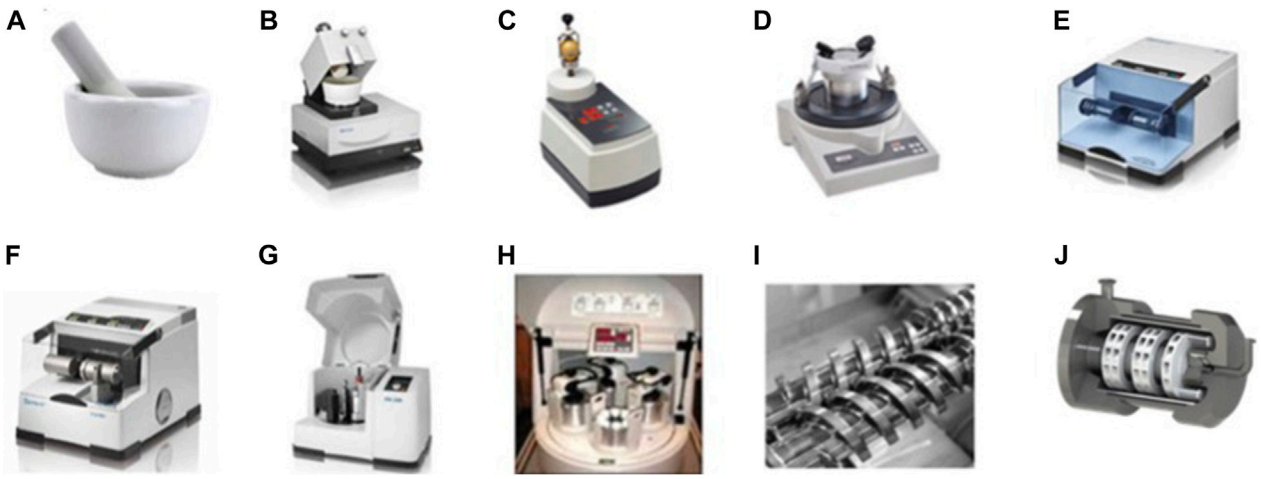

FIGURE 4
Most utilized types of grinding and milling equipment. **(A)** Mortar and pestle. **(B)** Automatic mortar. **(C)** Vertical vibrational mini-mill. **(D)** Vibratory micro-mill. **(E)** Vibrational ball mill. **(F)** Vibrational ball mill with temperature. **(G)** Planetary ball mill. **(H)** Multisample mill. **(I)** Twin screw for continuous mechanochemical synthesis. **(J)** Continuous flow heated mechanochemical reactor.

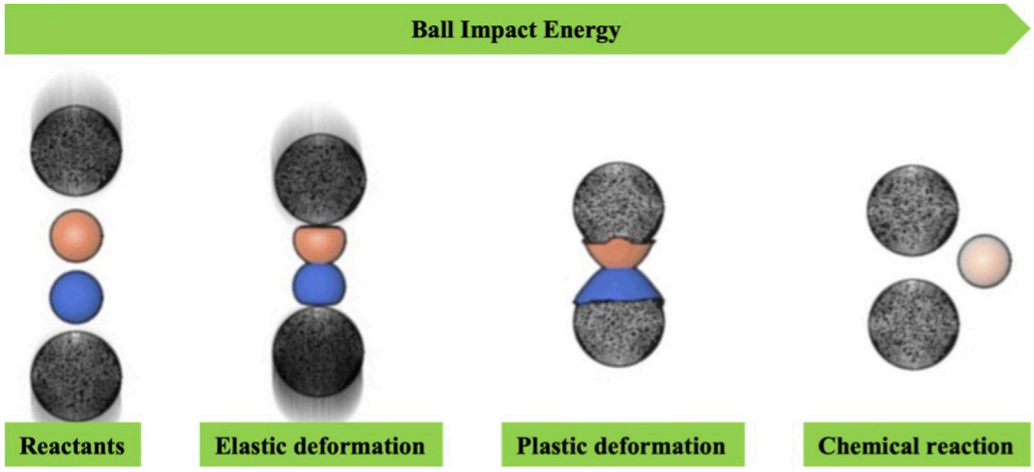

FIGURE 5
Basic concept for ball impact energy in mechanochemical synthesis (Wang et al., 2023).

more like a catalyst. In order to determine whether we are in the domain of liquid-assisted grinding, the scale η has been defined as the volume of solvent (μL) divided by the total mass of the reactants (mg). The scale ? varies from $0 < \eta < 1$ and is independent of the nature of the solvent such as polarity, basicity, and hydrogen bonding capacity as well as the relative molar masses of the solvent and reactants.

Manual grinding is commonly accomplished using a mortar and pestle. This equipment is simple to use and cost-effective, but it exposes the reagents to the environment, which can be hazardous. Alternatively, different automated milling devices are available for other grinding processes. For example, we can cite different batch reactors such as automatic mortars, vertical vibrational mini-mill, vibratory micro-mill, vibrational ball mill with or without temperature control, planetary ball mill, multisample mill (Figure 4). To date, only three types of continuous flow equipments exist: single and twin-screw for continuous mechanochemical synthesis and continuous flow heated mechanochemical reactor (Figure 4).

The mechanism of mechanochemistry is still being studied; however, it is evident that mechanically activated reactions do not obey a single mechanism. Mechanochemistry through mechanical action (impact, shear, or friction) allows the breaking of intramolecular bonds, thereby generating subsequent chemical reactions (Michalchuk et al., 2021; O'Neill and Boulatov, 2021; Pagola, 2023). Impact is typically achieved through processes such as a jet mill, a falling hammer and disintegrator, while shear occurs in a mortar and pestle as well as an extruder. The simultaneous application of impact and shear forces is accomplished in devices such as a vibrational mill, an attritor, and a planetary mill (Figure 5). Regardless of the specific mode of action, the disruption of weaker bonds and the generation of surface plasmas resulting from mechanical impacts give rise to radical species. These species also play a role in activating chemical synthesis. The mechanical energy generated during mechanochemical activation leads to an increase in temperature, mass transfer, diffusion of surface molecules, reduction in powder size, and an increase in surface area. Various other mechanisms of action, each somewhat distinct, have been reported in the literature for mechanochemical synthesis. Among them, the friction-induced magma-plasma generation (hot spot theory) and the liquefaction of reagents through an amorphous phase or the formation of eutectic blends have been reported (Rothenberg et al., 2001; James et al., 2012).

Mechanochemistry finds applications across a diverse range of chemical disciplines, exemplified by cocrystals, metal–organic frameworks, molecular rearrangement, materials chemistry, polymer chemistry, porous materials, organic chemistry, biochemistry, pharmaceuticals, active pharmaceutical ingredients (APIs), and energy storage materials (Tan and Garcia, 2019; Cuccu et al., 2022). In the upcoming chapter, we will exclusively delve into the synthesis of small organic molecules utilizing oil-derived products such as triglycerides, fatty acids, fatty esters, glycerol and derivatives.

4 Mechanochemical transformations of oleochemicals into high-value small chemicals

4.1 From vegetable oils to biodiesel

Biodiesel presents a compelling alternative to petrodiesel, gaining increasing traction owing to growing environmental concerns and the drive to promote renewable energy. This sustainable fuel is derived from the transesterification of various vegetable oils, including edible, inedible, and residual ones, often employing methanol or ethanol. The resulting biodiesel is a blend of monoalkyl esters derived from long-chain fatty acids, ranging from C_8 to C_{24} carbon atoms (Ma and Hanna, 1999). This mixture of fatty acid methyl esters boasts several environmental advantages, notably reducing emissions of CO, unburned hydrocarbons, particulates, and SO_2. While both homogeneous and heterogeneous catalysts have been proposed, homogeneous catalysis is the preferred method for achieving a high yield of methyl/ethyl esters (Kiss et al., 2010;

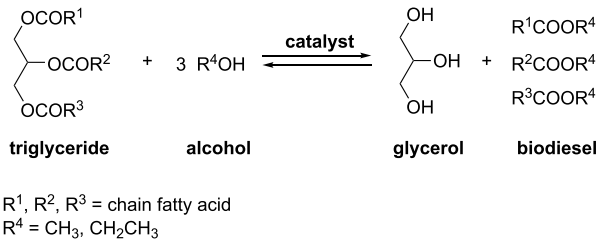

SCHEME 1
General chemical equation of the biodiesel formation.

Borges and Diaz, 2012; Rizwanul Fattah et al., 2020). Homogeneous catalysis allows for the use of base catalysts (such as NaOH, KOH, NaOMe, KOMe) and acid catalysts (like H_2SO_4, HCl). Among these, base-catalyzed transesterification stands out as a more rapid and commercially favored option due to its operation under moderate conditions (Scheme 1). Nevertheless, a common challenge in biodiesel production, regardless of the catalyst used, is the poor miscibility of vegetable oils and methanol, leading to reduced reaction rates, especially in continuous flow processs. To address this limitation, alternative processes employing mechanochemistry in semi-continuous flow have been reported (Malpartida et al., 2020b; Malpartida et al., 2020). These innovative approaches offer potential solutions to enhance the overall efficiency of biodiesel production.

CaO is a efficient base for the production of biodiesel (Alba-Rubio et al., 2010; Kouzu and Hidaka, 2012). According to some authors, CaO was the active phase only in the beginning of the reaction. Then, calcium diglyceroxide (CaDG) obtained from CaO and glycerol is the real catalyst of the trans-esterification (Kouzu and Hidaka, 2012; Kouzu et al., 2018). Using this concept, CaDG and triglyceride was studied for the formation of fatty acid methyl ester (FAME) *via* trans-esterification by employing a molar ratio of methanol to oil close to stoichiometry (4:1) and using 1.5% by weight of CaDG as the catalyst. With a continuous input flow between 4 and 45 L h^{-1} a semi-continuous mechanochemical reactor (volume of 0.5 L) containing yttrium-doped zirconia beads (diameter of 0.3–2.0 mm) occupying a 55%–70% volume was employed. Subsequent stirring for 4 h at 50°C or 24 h at room temperature completed the reaction and permitted to produce biodiesel with a yield of more than 90% (Scheme 2). This novel biodiesel production process is readily scalable and can be applied to the conversion of used cooking oils without any significant loss of yield (Malpartida et al., 2020b; Malpartida et al., 2020). A cost study was conducted, revealing the newfound approach to be more economical than the conventional batch stirred process. These results suggest that the methanol-oil molar ratio can be reduced from 12:1 to 4:1, and the catalyst weight can be decreased from 4% to 1.5% in a standard laboratory scale reactor, utilizing a more cost-effective process compared to the conventional batch stir method.

Mechanical energy, thermal energy, and pressure activation in continuous flow have proven highly advantageous in this biodiesel production process. The synergistic effect of achieving simultaneous activation has successfully addressed several drawbacks, leading to significant improvements, including: i) substantially shorter reaction times, ranging from hours to minutes; ii) lower operating temperatures attributed to the non-equilibrium conditions created by mechanical activation; iii) reduced mass transfer limitations due to an increased number of collisions; iv) minimized methanol usage; v) enabled real-scale production, transitioning from milliliters to liters; vi) increased yields and/or selectivity, owing to the simultaneous regeneration of the catalyst surface during the reaction.

The same research group investigated biodiesel production from both sunflower oil and used cooking oil, employing a slightly higher molar ratio of methanol to oil (5:1 compared to 4:1) and a lower flow rate (4 L h^{-1}) (Malpartida et al., 2020b; Malpartida et al., 2020). The findings indicated that similar catalytic activity was observed up to 120 min, yielding 80%. However, beyond 120 min, the ester yields from the oils decreased by 17%. The authors propose that this reduction may be attributed to the neutralization of the basic sites of the calcium diglycerate (CaDG) catalyst by the free fatty acids present in the waste oils.

4.2 From fatty acids methyl ester to lipidyl-cyclodextrins

Cyclodextrins (CDs) are macrocyclic malto-oligosaccharides produced from starch through enzymatic conversion. They

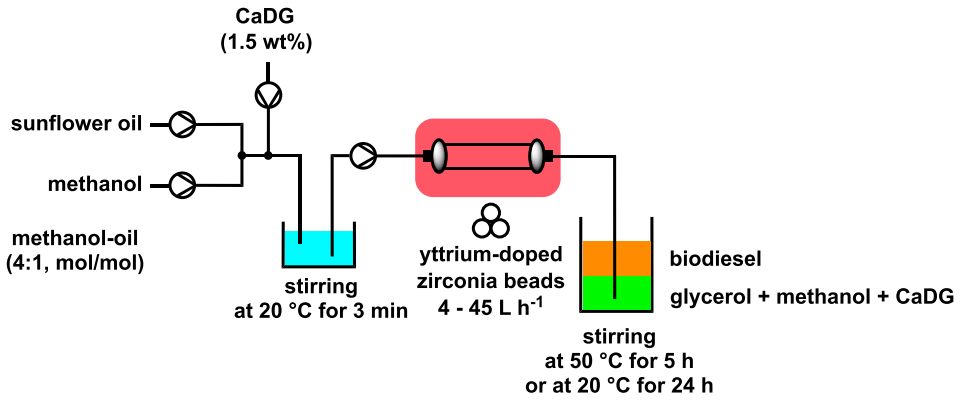

SCHEME 2
Semi-continuous biodiesel production catalyzed by CaDG using a high-throughput reactor filles with beads (Malpartida et al., 2020b; Malpartida et al., 2020).

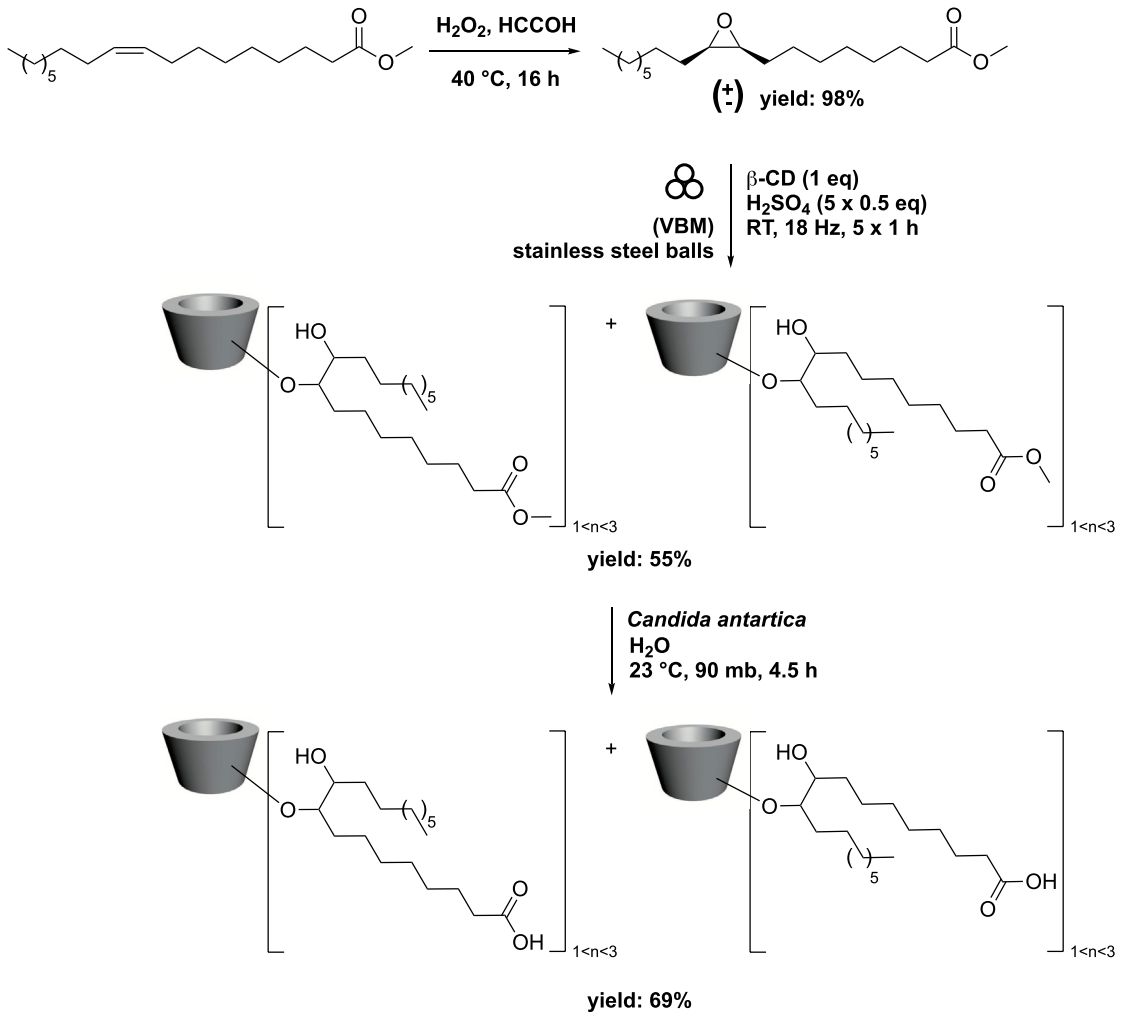

SCHEME 3
Synthesis of bicaternary lipidyl-cyclodextrins from oleic acid in 3 steps *via* ring-opening of methyl oleate epoxide by vibrating ball-milling in a mixer mill (Oliva et al., 2020).

consist of α-(1→4)-linked D-glucopyranose units in a $^4C_1$ chair conformation. Due to their unique 3D structure, unmodified CDs are hydrophilic with a conical cavity that is essentially hydrophobic. This characteristic enables CDs to form inclusion complexes with various lipophilic guest molecules, utilizing their hydrophobic cup-like structure (Szejtli, 1998). By introducing lipophilic groups, modified CDs gain self-assembly properties and the ability to form complexes with invited molecules, enhancing their vectorization capabilities. In this context, bicaternary lipidyl-cyclodextrins have been synthesized by combining methyl oleate epoxide with various CDs (Oliva et al., 2020). The process began with conventional epoxidation of methyl oleate using H_2O_2 in the presence of formic acid, yielding a racemic mixture of the corresponding methyl oleate epoxide. To prevent the formation of a sticky paste, which could hinder reactivity, the epoxide's ring opening was conducted in five steps. Successive additions of methyl oleate epoxide and H_2SO_4 were made to the β-CDs, and the reaction was carried out by vibrating ball-milling (VBM) in a mixer mill (volume of 65 mL) containing 12 stainless steel balls (3 balls with diameter of 12.7 mm, 5 balls with diameter of 6.4 mm, and 4 balls with diameter of 4.0 mm). For the balls, the use of different diameters and the ratio between them were not studied. The ball milling process was conducted for 1 h at a frequency of 18 Hz. The target compound was obtained in 55% yield, with 1, 2, or 3 fatty acid methyl ester grafts. Next, enzymatic hydrolysis of the terminal ester was performed in the presence of *Candida antarctica* in water at 90 mbar and 23 °C, resulting in the corresponding carboxylic acid in 69% yield (Scheme 3).

In order to have a structure activity relationship, the authors tried different CDs with or without hydroxypropyl groups (α-CD, β-CD, γ-CD, HP-α-CD, HP-β-CD, HP-γ-CD) permitting to obtain α-CD $(C_9)_2$OOMe, γ-CD $(C_9)_2$OOMe, HP-α-CD $(C_9)_2$OOMe, HP-β-CD $(C_9)_2$OOMe and HP-γ-CD $(C_9)_2$OOMe in 28%–44% yields.

4.3 From fatty acids to dimeric fatty acids

The oleochemical dicarboxylic acids make up approximately 0.5% of the total dicarboxylic acid market for monomers, with phthalic and terephthalic acids representing 87%. Due to their

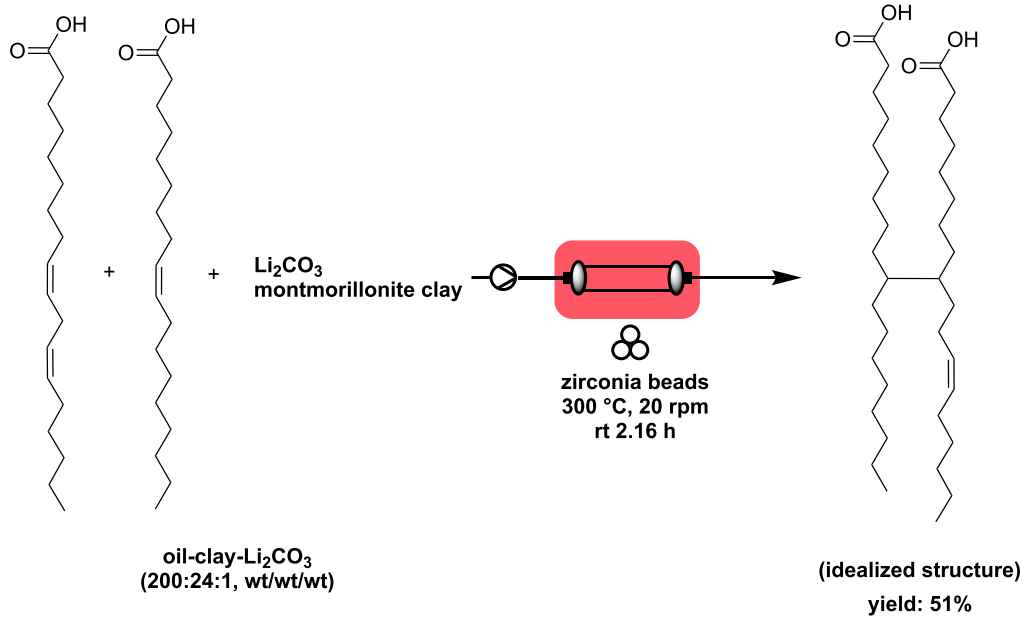

SCHEME 4
Continuous dimerization of soybean fatty acid using a horizontal ball-mill reactor (Lu et al., 2019).

unique chemical nature, these oleochemical-derived dicarboxylic acids tend to modify or alter condensation polymers, thus occupying a special niche market. Some desirable properties associated with oleochemical-derived dicarboxylic acids include elasticity, flexibility, high impact strength, hydrolytic stability, hydrophobicity, lower glass transition temperatures, and increased flexibility (Paraskar et al., 2023).

Researchers reported the continuous production of dimeric fatty acid from soybean fatty acid (oleic acid-linoleic acid weight ratio of 33: 65) in the presence of acidic montmorillonite clay and lithium carbonate (Lu et al., 2019). To facilitate the reaction, an innovative ball-mill reactor was designed and utilized for this study. The stainless reactor had 3 baffles to enhance radial turbulence and 10 clapboards to divide the reactor into 11 small reactors in series, making it akin to a plug-flow reactor. A solution of oil-clay-lithium carbonate with a weight ratio of 200:24:1 was injected using a peristaltic pump into the horizontal continuous ball mill reactor, which was filled with zirconia beads (bead-to-mass ratio = 12) and operated at 300°C. The residence time was 2.16 h, and the rotation speed was set at 20 rpm. The resulting dimeric fatty acid was obtained with a yield of 51% (Scheme 4). Interestingly, the authors found that using similar conditions in a stirred flask (500 mL) at 400 rpm allowed for the production of the diacid with a yield of 63%. However, the lower yield obtained in the continuous flow process was attributed to the dissolution of some metal ions, such as Fe^{3+} and Ni^{2+}, from the continuous ball mill reactor.

4.4 From natural fatty acids to labeled fatty acids

Fatty acids play a crucial role in biological systems and have wide-ranging applications in materials science, including drug formulation and surface-functionalization of nanoparticles (Magkos and Mittendorfer, 2009; Remize et al., 2020). To gain a deeper understanding of their biological mechanisms, researchers have reported the mechanochemical synthesis of isotopically labeled fatty acids, specifically with ^{17}O and ^{18}O labeling.

The target compounds were successfully produced through two mechanochemical steps: first, by activating the carboxylic function using 1,1′-carbonyldiimidazole (CDI), and then hydrolyzing the acyl imidazole intermediate with enriched H_2O^* (97% ^{18}O-enriched H_2O^* and 90% ^{17}O-enriched H_2O^*) (Spackova et al., 2020). The synthesis process involved milling a mixture of oleic acid and CDI (1.1 eq) at 25 Hz for 30 min using vibrating ball-milling (volume of 10 mL) in a mixer mill filled with two stainless steel beads (diameter of 10 mm). Subsequently, complete hydrolysis with H_2O^* (2 eq) was performed for 1 h using the same equipment. After standard work-up procedures, the target compound was obtained with an impressive 90% yield, with an average enrichment of 44% for the ^{18}O labeled molecules and 36% for the ^{17}O labeled molecules per carboxylic oxygen (Scheme 5).

When stearic acid was used instead of oleic acid, the addition of K_2CO_3 (at 1 eq) as a base was necessary to expedite the hydrolysis step (Scheme 6). The authors explained that the base promoted the formation of HO*- and subsequently facilitated the deamidation reaction. Interestingly, the appearance of the mixture varied when starting from oleic acid compared to stearic acid. The acyl imidazole intermediate derived from oleic acid had a pasty consistency, while that derived from stearic acid exhibited a more powdery texture (Spackova et al., 2020).

An extension of this process was reported by the same research group, which involved fatty acids with a carbon chain containing carbon atoms between C12 to C18 (Spackova et al., 2021). Additionally, the extension encompassed polyunsaturated fatty acids (PUFAs) containing up to four double bonds. The hydrolysis time varied depending on the acyl imidazole derivatives used, ranging from 1 to 3 h (Figure 6).

The researchers also developed a one-pot mechanochemical saponification method for other polyunsaturated fatty acids (PUFAs),

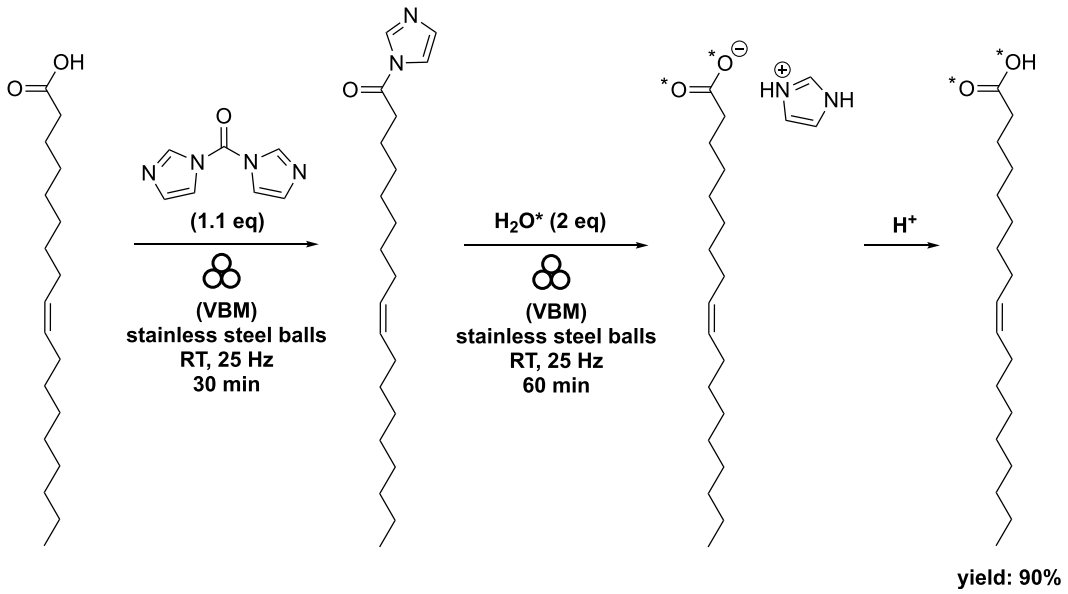

SCHEME 5
Synthesis of labeled oleic acid by vibrating ball-milling in a mixer mill (Spackova et al., 2020).

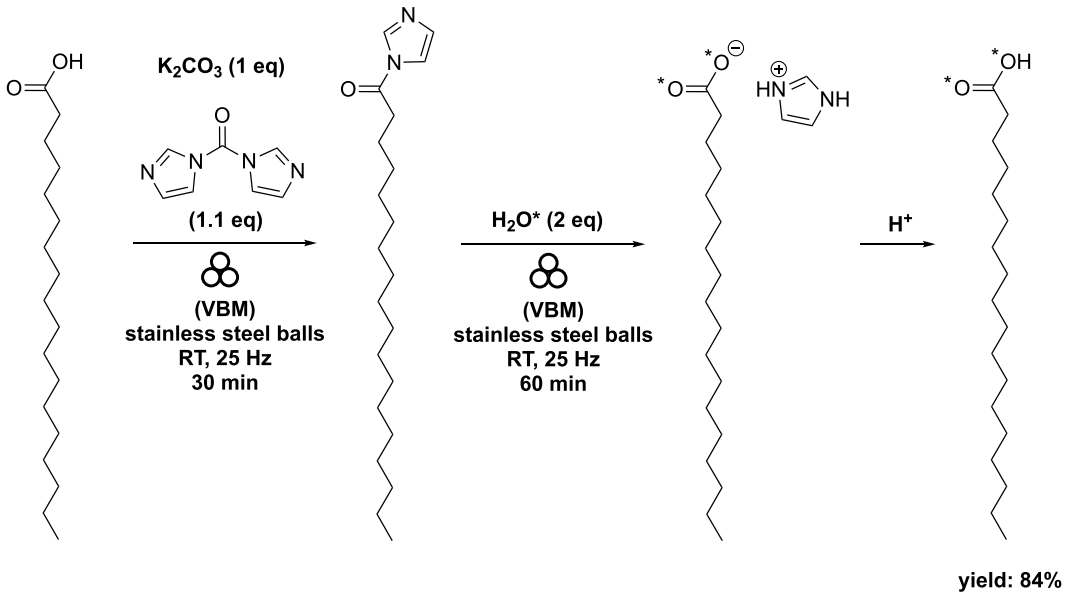

SCHEME 6
Synthesis of labeled stearic acid by vibrating ball-milling in a mixer mill (Spackova et al., 2020).

namely, ethyl α-linolenate, ethyl eicosapentaenoate, and ethyl docosahexaenoate (Spackova et al., 2021). In this process, a mixture of the ethyl ester of the respective PUFA, sodium ethoxide (at 1.5 equiv.), and H_2O^* (at 3 eq) was milled at 25 Hz for 30 min using vibrating ball-milling in a mixer mill. Employing conventional work-up techniques, the corresponding labeled PUFAs were obtained with yields exceeding 93% and showed high enrichment levels (Figure 7).

4.5 From glycerol to calcium diglyceroxide (CaDG)

As mentioned earlier for biodiesel production, CaDG serves as an active basic catalyst and is commonly synthesized through conventional methods (Kouzu and Hidaka, 2012; Kouzu et al., 2018; Malpartida et al., 2020b; Malpartida et al., 2020). Additionally, CaDG finds applications as a plasticizer and

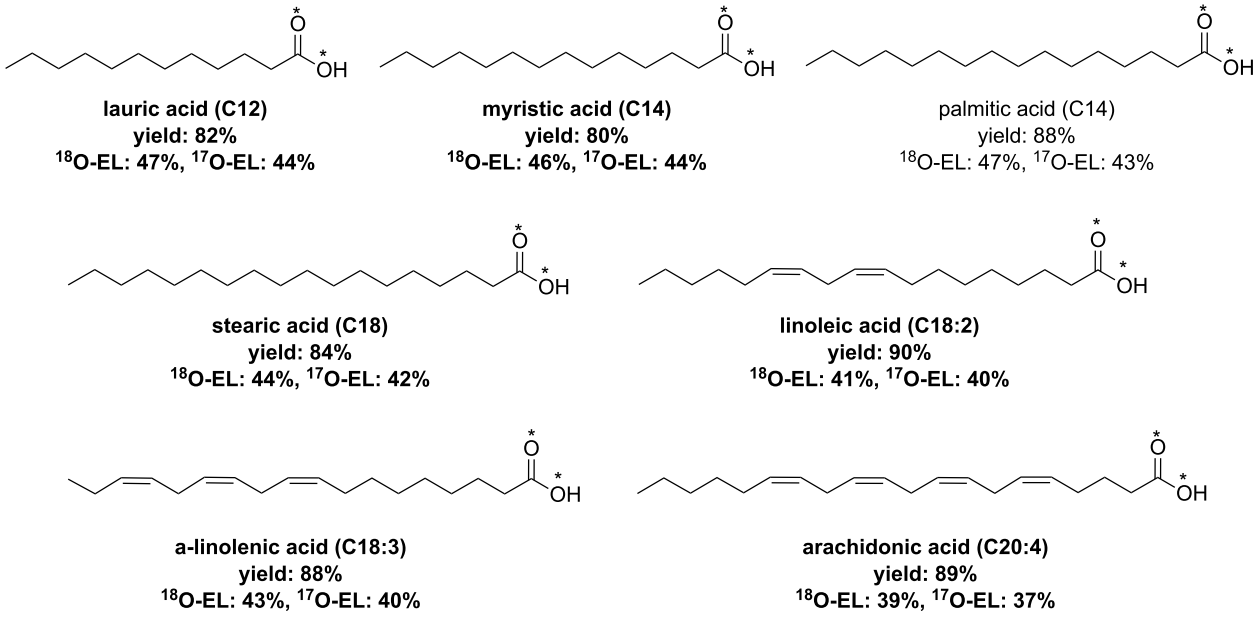

FIGURE 6
Synthesis of labeled fatty acids by vibrating ball-milling in a mixer mill (Spackova et al., 2021).

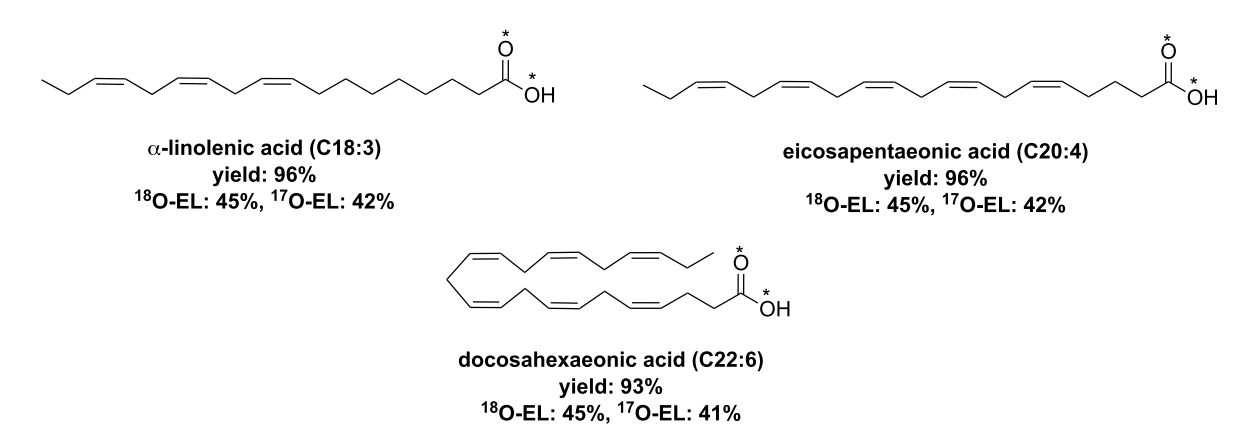

FIGURE 7
Labeled polyunsaturated fatty acids obtained by vibrating ball-milling in a mixer mill (Spackova et al., 2021).

thermal stabilizer for plastics. Seeking an alternative process for CaDG production, a mechanochemical approach involving a mixture of glycerol and CaO in a 1:5 M ratio was reported (Lukic et al., 2016). They did a planetary ball milling (PBM) operating in an air atmosphere at 270 rpm for 5 h. Afterward, methanol was added, and the resulting mixture was further milled for 15 min, followed by conventional work-up. This procedure allowed the synthesis of CaDG in high yield. The catalyst thus obtained was then utilized for the methanolysis of sunflower oil, resulting in the corresponding FAME (fatty acid methyl esters) with high efficiency.

Subsequently, the synthesis of CaDG using a continuous mechanochemical reactor (MCR), utilizing the same equipment employed for biodiesel production (Malpartida et al., 2020b; Malpartida et al., 2020). Glycerol and CaO were mixed in two different molar ratios, 3 and 5, in a mixer tank. The resulting mixture was pumped into the continuous mechanochemical reactor (volume of 0.5 L) at a flow rate of 4 and 150 L h^{-1}, respectively. The reactor was filled with yttrium-doped zirconia beads (diameter: 0.3–2.0 mm), occupying 55%–70% of the reactor volume. In this study, the quantification of crystalline CaDG formation was accomplished through the utilization of the Rietveld method. An X-ray diffraction (XRD) analysis was performed on all the samples, and the nominal composition derived from the structure identification step was refined using a Rietveld analysis. The most accurate refinement was achieved by considering factors such as sample displacement, background correction, peak profile parameters, and the scaling of each distinct phase. Using

TABLE 1 Influence of different experimental variables on the formation of CaDG using a continuous mechanochemical reactor (Malpartida et al., 2020b; Malpartida et al., 2020).[a]

Entry	Glycerol quality (wt% of H_2O)	rt (min)	Glycerol-CaO molar ratio	T (°C)	Yield of CaDG (XRD) (%)
1	0	5	3	25	15
2	0	5	3	50	18
3	0	5	5	25	18
4	0	5	5	50	84
5	0	30	3	25	91
6	0	30	3	50	>99
7	0	30	5	25	>99
8	0	30	5	50	55
9	10	30	5	50	>99

[a]Reaction conditions: a mixture of glycerol-CaO, molar ratio (3 or 5) was pumped into the continuous mechanochemical reactor filled with yttrium-doped zirconia beads (diameter of 0.5 mm), occupying 55%–70% of the reactor volume for a residence time (5 and 30 min).

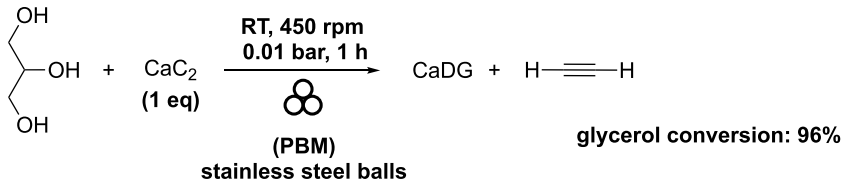

SCHEME 7
Synthesis of acetylene and CaDG starting from calcium carbide and glycerol in a planetary ball mill (Li et al., 2018).

yttrium-doped zirconia beads (diameter of 0.5 mm), CaDG was obtained with quantitative yield after a 30-min residence time (Table 1, lines 6–9). However, with a glycerol-CaO molar ratio of 3, the temperature needed to be increased to 50°C for optimal yield (Table 1, lines 5 and 6). At room temperature (25°C), a higher glycerol-to-CaO molar ratio 5) was necessary to achieve yields exceeding 99% (Table 1, lines 5 and 7). At 50 °C, the same conditions gave only CaDG in 55% yield. The researchers also tested the influence of water presence due to glycerol's hydrophilic nature. In the presence of 10 wt% water and a glycerol-CaO molar ratio of 5, CaDG was obtained in quantitative yield with a residence time of 30 min (Table 1, entry 9).

CaDG was obtained as a side-product during the mechanochemical production of acetylene by reacting calcium carbide (CaC_2) with glycerol (Li et al., 2018). The molar ratio of glycerol-CaC_2 used was 1, and the mixture was subjected to 1 hour of milling at 450 rpm at room temperature in a planetary ball mill (volume of 250 mL) filled with stainless steel balls. The stainless steel balls comprised 2 balls with a diameter of 15 mm, 4 balls with a diameter of 12 mm, 25 balls with a diameter of 10 mm, 43 balls with diameters of 08 mm, and 232 balls with a diameter of 3 mm. As previously reported, the choice to use of different diameters and different ratio between them were not described by the authors. To prevent air impurities, a vacuum of 0.01 bar was applied, which also minimized the risk of explosions due to the presence of oxygen. As a result, the desired acetylene was obtained in good yield, with 96% glycerol conversion (Scheme 7).

The authors highlighted that the mechanochemical reaction rate of CaC_2 with glycerol significantly increased with the rising rotating speed, and the efficiency of this reaction exceeded that of the corresponding thermal chemical reaction. In summary, the current process proves effective for the efficient production of high-purity acetylene and CaDG. The mechanochemical reaction of CaC_2 with glycerol demonstrates greater efficiency than the corresponding thermochemical reaction at high temperatures, with CaC_2 showing higher reactivity compared to CaO with glycerol. Importantly, when compared to conventional acetylene production methods, the authors did not detect any PH_3, AsH_3, and H_2S formed as side reactions involving Ca_3P_2, Ca_3As_2, and CaS, respectively. This absence is attributed to the higher reactivity of glycerol relative to water, which enhances the reaction's selectivity.

4.6 From glycidol to glycerol esters

Esterification of glycerol enables the production of various valuable chemicals, such as monoacylglycerol (MAG) and diacylglycerol (DAG). Among these chemicals, diacylglycerols (DAGs) play significant signaling roles in cells (DAG signaling), along with many other amphipathic or hydrophobic small molecules exhibiting lipid structures (Eichmann and Lass, 2015). DAGs are glycerolipids composed of two fatty acids esterified to glycerol. DAGs are produced through the enzymatic breakdown of glycerophospholipids and the lipolysis of TAGs (triacylglycerols).

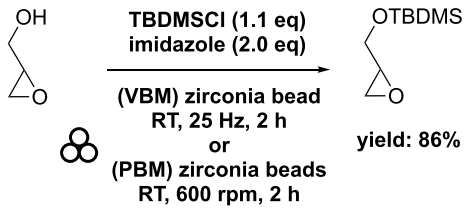

SCHEME 8
Silylation of glycidol with TBDMSCl by vibrating ball-milling in a mixer mill or in a planetary ball mill (Ardila-Fierro et al., 2019).

Extracting pure DAGs and TAGs from natural sources proves challenging due to the structural diversity of fatty acids in acylglycerols and their subtle differences in chain length, degree of unsaturation, double bond position, and stereochemistry. The chemical synthesis of protected DAGs from glycerol or glycidol requires several preparative steps involving organic solvents like CH_2Cl_2, THF, or Et_2O (Martin et al., 1994).

To achieve greener conditions and produce MAG and DAG derivatives, researchers have investigated solventless mechanochemical synthesis. In this process, a mixture of glycidol, tert-butylchlorodimethylsilane (1.1 eq), and imidazole (2.2 eq) was combined in a mixer mill (volume of 10 mL) filled with one zirconia ball (diameter of 10 mm) and subjected to 25 Hz for 2 h. The resulting tert-butyl-dimethylsilyl glycidyl ether was obtained with an 86% yield (Ardila-Fierro et al., 2019). Similarly, a comparable experiment using a planetary ball mill at 600 rpm yielded the target chemical in an 88% yield, demonstrating no significant difference between the two equipment setups (Scheme 8). Comparison with conventional process showed that the ball milling approach facilitated a solventless reaction and reduced the reaction time from overnight to just 2 h (Zaed and Sutherland, 2011; Winkler et al., 2013).

In order to have a good selectivity for the ring opening of the epoxide with fatty acid as nucleophile, the use of Jacobsen cobalt (II)-salen complex (*S*,*S*)-cat has been selected. A blend of stearic acid (1 eq) and chiral (*S*,*S*)-cat (2.5 mol%) was subjected to milling in a mixer mill (volume of 20 mL) containing a single zirconia ball (diameter of 10 mm) for 15 min at 25 Hz under an oxygen atmosphere. Subsequently, DIPEA (1 eq) was introduced, and the resulting mixture was milled for an additional 10 min. Lastly, glycidyl ether (1 eq) was added to the container, and the resulting mixture was milled at 25 Hz for 155 min. This process yielded two regioisomers: 1-stearoyl-3-(*tert*-butyldimethylsilyl)-sn-glycerol in 42% yield and 2-stearoyl-3-(*tert*-butyldimethylsilyl)-sn-glycerol in 12% yield (Ardila-Fierro et al., 2019) (Scheme 9). Compared to the solventless batch reaction, the ball milling process reduced the reaction time from 16 h to 3 h (Fodran and Minnaard, 2013). It is worth noting that the initial 16-h duration was not an optimized experimental condition.

Subsequently, starting with the major regioisomer 1-stearoyl-3-(*tert*-butyldimethylsilyl)-sn-glycerol, a secondary esterification was investigated using stearic acid (1.2 eq) along with DCC (1.2 eq) and DMAP (10 mol%) in a mixer mill (volume of 10 mL) containing a single zirconia ball (diameter of 10 mm) at 25 Hz for 2 h. This procedure afforded diester in a remarkable 97% yield (Scheme 10). Application of this method to oleic acid, linoleic acid, and arachidonic acid yielded the corresponding diesters in 90%, 91%, and 74% yields, respectively (Figure 8). While similar conditions were employed in conventional reactions conducted in heptane, the time required was substantially longer (16 h compared to 2 h), despite the absence of any optimizations (Fodran and Minnaard, 2013). The subsequent deprotection of the primary hydroxyl group to remove the silyl group was accomplished under acidic conditions, yielding the 1,2-distearoyl derivative in an 81% yield. In order to achieve higher yields and prevent acyl migration from the secondary to primary positions, the ball milling technique was not employed.

The diester 1,2-distearoyl-3-(*tert*-butyldimethylsilyl)-sn-glycerol was combined with 4-nitrophenyl chloroformate (1 eq) in the presence of NEt_3 (1.5 eq). Subsequently, the resulting mixture underwent milling using the same equipment, operating at a frequency of 25 Hz for 90 min. Without the need for additional purification steps, the reaction mixture was then introduced to 7-hydroxycoumarin (1 eq) and NEt_3 (1.5 eq). The combined mixture was stirred at 25 Hz for 3 h. This process yielded a complex mixture

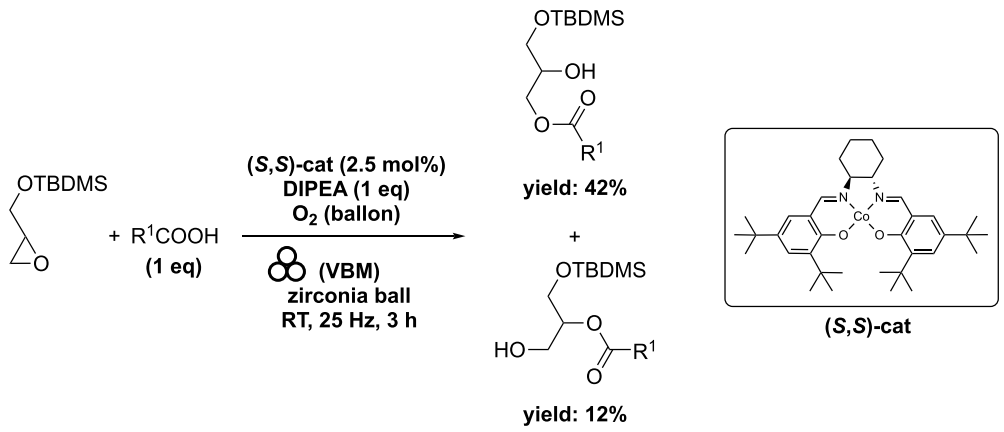

SCHEME 9
Cobalt-catalyzed ring-opening of epoxide by vibrating ball-milling in a mixer mill (Ardila-Fierro et al., 2019).

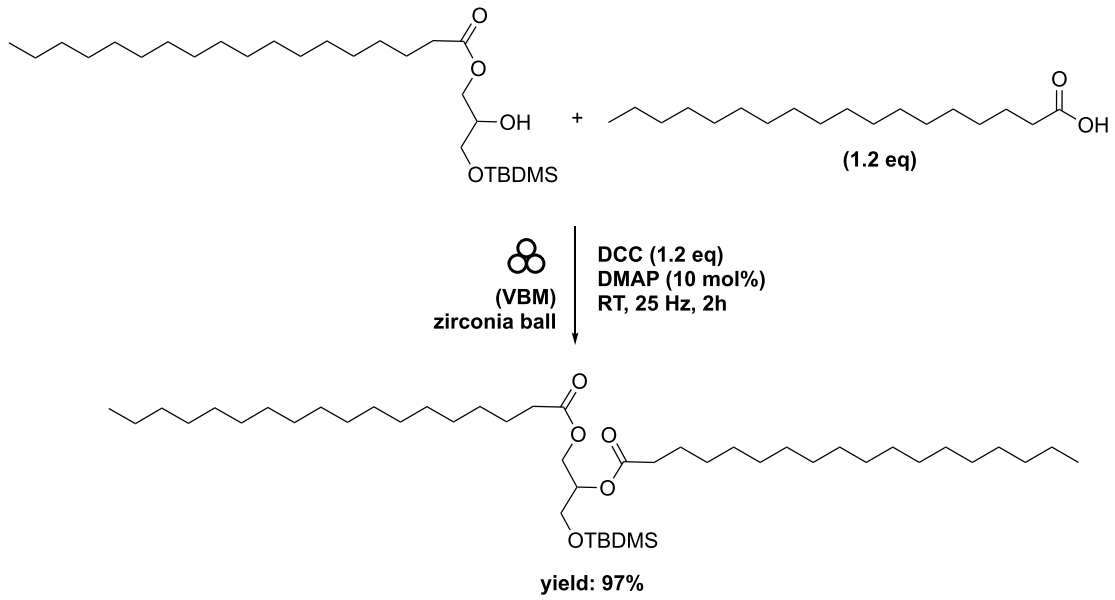

SCHEME 10
Mechanical synthesis of DAG obtained by vibrating ball-milling in a mixer mill (Ardila-Fierro et al., 2019).

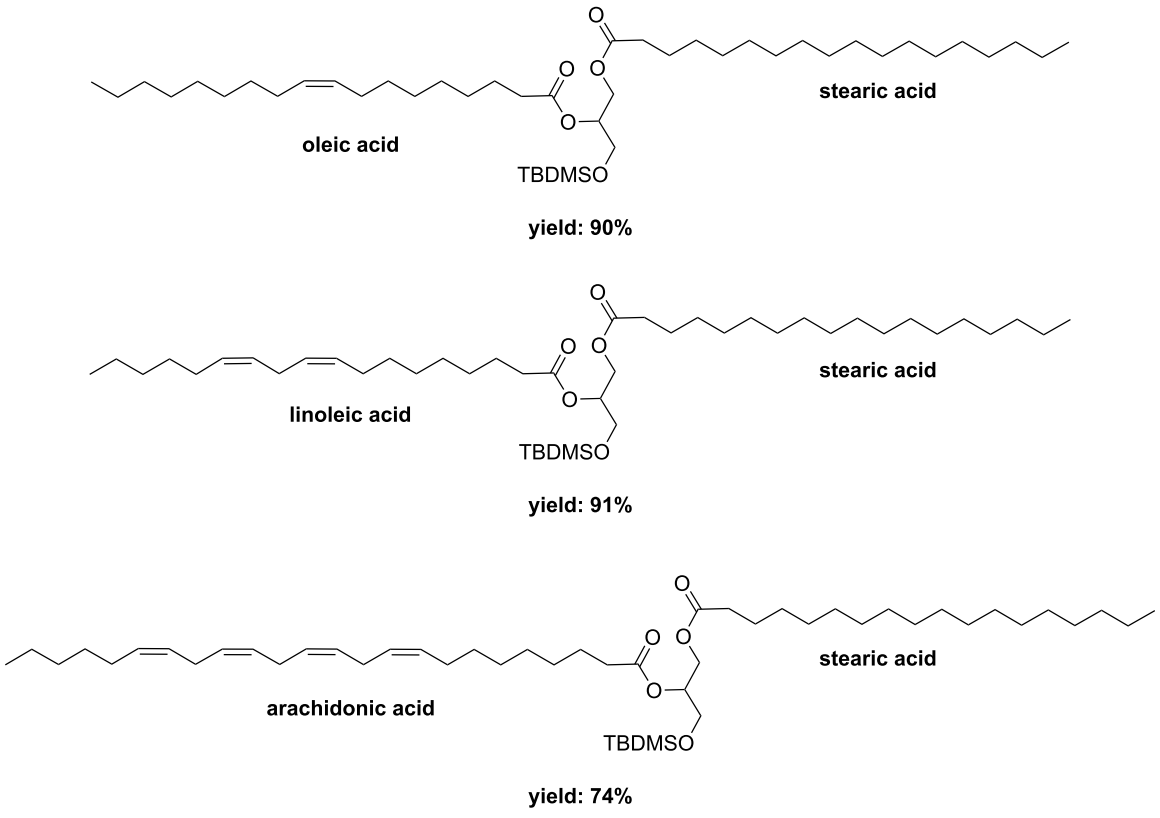

FIGURE 8
Different DAGs obtained by vibrating ball-milling in a mixer mill (Ardila-Fierro et al., 2019).

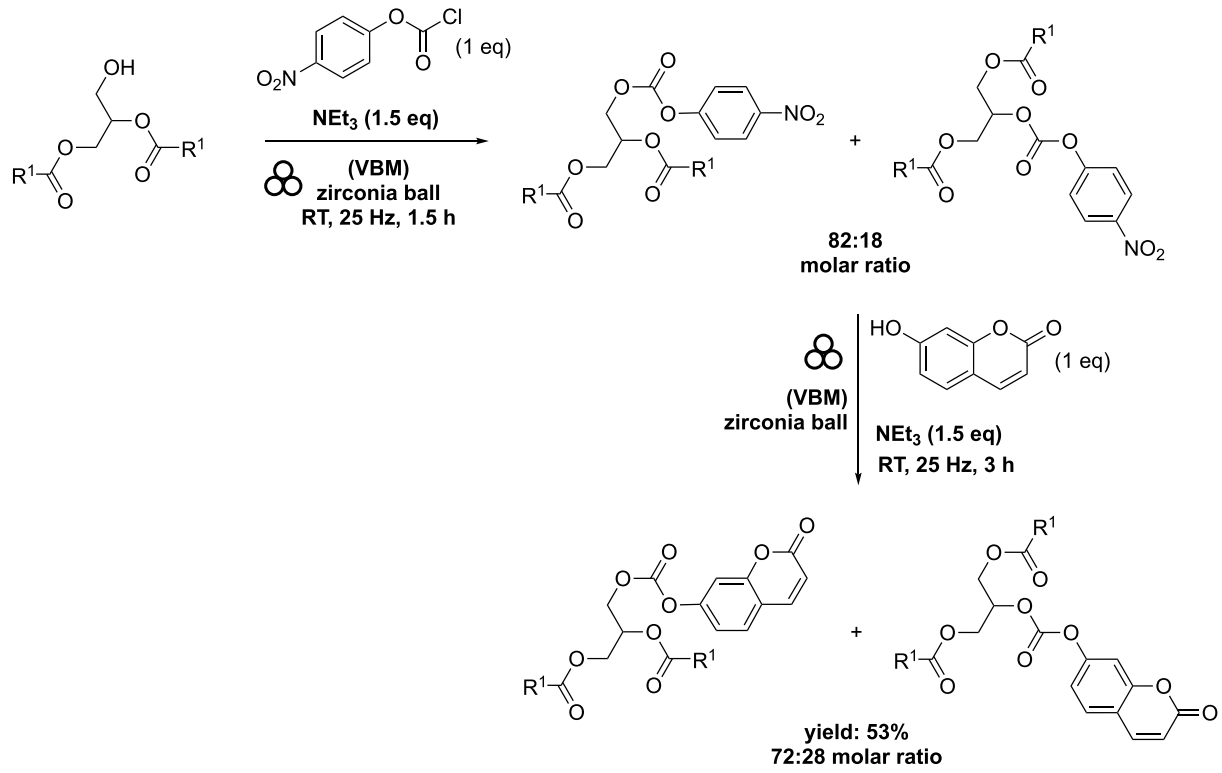

SCHEME 11
Conjugation of DAG with 7-hydroxycoumarin by vibrating ball-milling in a mixer mill (Ardila-Fierro et al., 2019).

of two compounds: 1,2-distearoyl-3-((((2-oxo-2H-chromen-7-yl)oxy)carbonyl)oxy)-sn-glycerol and 1,3-distearoyl-2-((((2-oxo-2H-chromen-7-yl)oxy)carbonyl)oxy)-sn-glycerol, in a molar ratio of 2.5:1. The overall yield achieved from this procedure was 53% (Scheme 11). A acyl migration occurred from the secondary hydroxyl group to the primary hydroxyl group as expected but this migration was limited.

4.7 From glycerol to benzoxazine

Benzoxazines are heterocyclic compounds with potent biological activities (Garg et al., 2013) as monomer and with unique properties after polymerization. Polybenzoxazine is a relatively new class of polymeric phenolic resins with various excellent characteristics, including outstanding stiffness, low dielectric constant, high heat resistance, low flammability, and minimal moisture absorption when exposed to moisture, chemicals, and other corrosive liquid, therefore, they are ideal polymers to use in special and extreme cases (Machado et al., 2021; Ding et al., 2022).

In order to produce a biobased benzoxazine, a mixture of glycerol (1–3 eq), diethyl carbonate (1.4 eq), and 2-aminophenol (1 eq) was combined with K_2CO_3 (0.1 eq). This mixture was then processed within a planetary ball mill (volume of 125 mL) filled with stainless steel balls (60 g with a diameter of 2 mm) for durations of 60 and 120 min operating at 350 rpm. The outcomes of these experiments underscore that mechanochemistry is not a miraculous technology. Attempts to use liquid-assisted grinding by introducing a small quantity of acetone were unsuccessful (Torres-Pastor et al., 2022). Additional tests were conducted to initiate the reaction utilizing microwaves as an alternative technology. These experiments yielded improved conversions (<25%) and selectivities (<35%), albeit still at a relatively low level.

Recent studies have shown promising advancements in certain reactions through a combination of successive milling and microwave techniques (Martinez et al., 2023). In one experiment, glycerol (1 eq), diethyl carbonate (1.4 eq), 2-aminophenol (1 eq), and K_2CO_3 (0.12 eq) were subjected to milling in a planetary ball mill reactor (volume 125 mL), containing stainless steel balls (60 g with a diameter of 2 mm), for 60 min at 350 rpm. Subsequently, a microwave-assisted organic reaction was conducted at 110°C (300 W) for 60 min. This process led to a 38% conversion of 2-aminophenol, with a remarkable 93% selectivity towards the benzoxazine derivative (Torres-Pastor et al., 2022) (Scheme 12). Increase the rpm from 350 to 1,000 to enhance the phenol conversion, while significantly reducing the selectivity from 93% to 7%. Notably, attempts at conventional heating in place of microwave activation resulted in a conversion of 2-aminophenol of less than 5%.

4.8 From glycerol to solketal

Solketal (1,3-di-*O*-isopropylidene-glycerol) holds significant promise across various domains, serving as a versatile molecule in pharmaceutical chemistry as a synthetic intermediate, an isopropylidene protective group in C3-based organic chemistry, a solvent and plasticizer in polymer chemistry, and even as a fuel

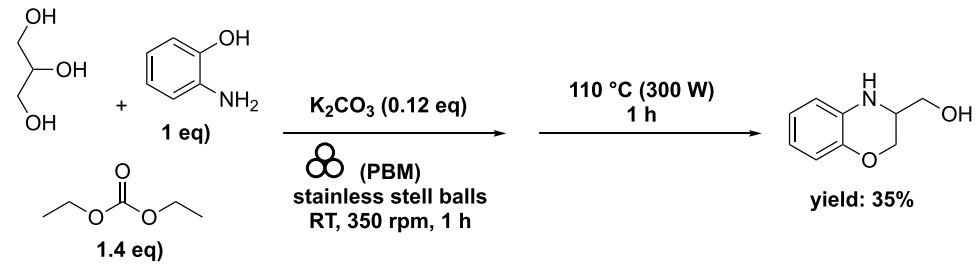

SCHEME 12
Synthesis of benzoxazine from glycerol using successive mechanochemistry in ball mill and microwave irradiation (Torres-Pastor et al., 2022).

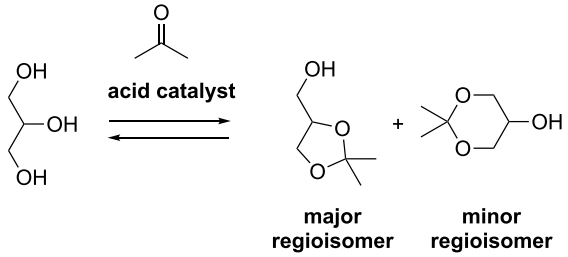

SCHEME 13
General ketalization of glycerol with acetone in acid conditions.

additive (Garcia et al., 2008; Mota et al., 2010; Silva et al., 2010; Nanda et al., 2016; Zahid et al., 2021; Yu et al., 2022). The synthesis of solketal involves an acetalization reaction between glycerol and acetone under acidic conditions (Zahid et al., 2021). This reaction exists in equilibrium, potentially yielding 1,3-di-*O*-isopropylidene-glycerol as a byproduct (Scheme 13). Typically, homogeneous acid catalysts such as H_2SO_4 or HCl are employed, although both homogeneous Lewis acids and heterogeneous acid catalysts can also find application (Kiakalaiehet et al., 2018; Zahid et al., 2020).

Given the industrial outlook, extensive efforts have been directed towards developing continuous flow processes for solketal synthesis (Khodadadi et al., 2021). However, certain limitations persist within these continuous flow methods. Challenges include the immiscibility of glycerol with acetone due to differing physicochemical parameters, necessitating the use of organic co-solvents. Additionally, homogeneous catalysis demands substantial quantities of catalysts, while heterogeneous catalysis suffers from low flow rates. The presence of water, a byproduct of the reaction, also leads to catalyst deactivation.

In addition to the transfer of mechanical energy and milling, bead mechanochemistry emerges as a highly efficient method for homogenization. Indeed, patented studies have demonstrated that this innovative technique effectively addresses the miscibility challenges encountered in solketal synthesis under homogeneous acid catalysis conditions (Len et al., 2021). This method has been employed for the continuous flow mechanochemical synthesis of solketal, using equipment and processes similar to those described above for CaDG and continuous flow biodiesel mechanochemistry (Malpartida et al., 2020b; Malpartida et al., 2020). Various conditions and homogeneous acid catalysts were examined, with the most favorable outcomes observed for $FeCl_3 \bullet 6H_2O$ as Lewis acid in both loop and continuous flow processes at 56°C. This led to a remarkable 99% solketal yield within residence times of less than 15 min. These investigations in presence of a solvent stand as pioneering examples showcasing the efficacy of continuous flow bead mechanochemistry in facilitating organic synthesis.

4.9 Advantages and limits

Mechanochemistry has become an attractive method for producing various materials, polymers and small chemicals. Most of these advantages can be associated with the twelve principles of green chemistry (Figure 9).

The main advantages of mechanochemistry encompass the promotion of solvent-free reactions, leading to a significant reduction in waste and pollution generation while simultaneously lowering economic costs. Additionally, mechanochemical processes often yield larger quantities of products when compared to analogous solution reactions. They also generally entail shorter reaction times, meticulous control over stoichiometry, and enhanced product selectivity. Another notable advantage of mechanochemistry, as opposed to traditional solution-based methods, is its capability to enable the utilization of reagents that are conventionally deemed inert or highly insoluble. However, it is crucial to acknowledge that mechanochemistry does not provide a universal solution to all synthetic challenges. Although mechanochemistry is an ancient technique, the understanding of the entire range of phenomena is still in its early stages, particularly concerning fundamental physicochemical knowledge. Indeed, to this day, the thermodynamic variables used to study and control chemical reactions, such as temperature and pressure, are not yet measured or controlled systematically. Other parameters and mechanisms are still unknown: the amounts of energy transferred or made available through the combination of temperature and applied mechanical treatment, mass transfers in heterogeneous phase reactions, increased selectivity, and more. In summary, mechanochemistry offers environmentally friendly and efficient reactions but is typically restricted to solid-state processes. In contrast, oleochemistry provides sustainable and

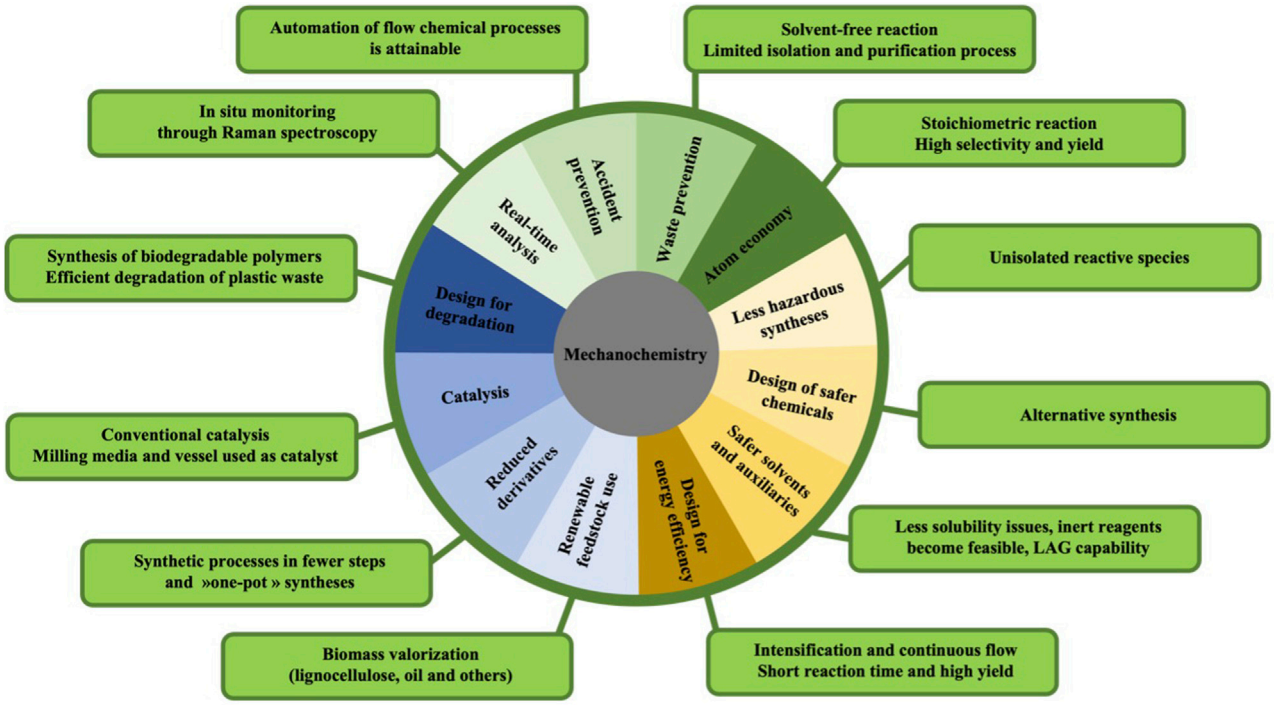

FIGURE 9
Twelve principles of green chemistry and mechanochemistry inputs.

biodegradable chemicals, both in liquid and solid forms. Both fields come with their distinct advantages and challenges, making them valuable in diverse applications within the chemical industry.

5 Conclusion

This comprehensive review explores the significant contributions of oleochemistry, emphasizing its vital role in providing non-fossil resources and invaluable molecules. It also delves into the growing interest in combining mechanochemistry with molecules derived from untreated or modified oils, guided by insights from relevant scientific studies. Oleochemistry, which includes vegetable oils and their derivatives, offers a wealth of platform molecules for producing high-value chemicals, presenting a promising alternative to petroleum resources. The diverse chemical components within oleochemicals, such as esters, C-C double bonds, and hydroxyl groups, make them versatile building blocks. Mechanochemical synthesis emerges as an environmentally conscious, potent, sustainable, time-efficient, cost-effective, and ecologically friendly method for creating novel functional materials. By manipulating various synthetic parameters, such as milling methods, materials, time, temperature, and process control agents, biobased molecules' synthesis can be significantly improved compared to traditional activation methods. Mechanochemistry has widespread applications across different research areas and industries, making it crucial for future investigations.

The review highlights key achievements in mechanochemistry and oleochemistry. Notably, a semi-continuous mechanochemical reactor equipped with beads achieved a biodiesel yield exceeding 90% from triglycerides, showcasing scalability and environmental benefits. Mechanochemical reactions starting from fatty acids and esters, including the use of methyl oleate epoxide and cyclodextrins, demonstrated the technique's merits. Continuous production of dimeric fatty acids in a ball-mill reactor and the synthesis of labeled fatty acids further illustrate its potential. Glycerol, another essential component in oleochemistry, was successfully utilized in various mechanochemical reactions. A continuous mechanochemical reactor with beads produced CaDG compounds with exceptional selectivity and high yields. The synergy of glycerol and CaC2 in a planetary ball mill resulted in acetylene production of superior quality. The review also covers the synthesis of various glycerol-based compounds, demonstrating the versatility of glycerol in mechanochemistry. The text acknowledges that, while comparisons between conventional and mechanochemical methods are sometimes made, these often involve variations in reagents and the presence of solvents, making it challenging to assess the distinct contributions of different milling technologies.

In summary, this review underscores the pivotal role of oleochemistry in providing sustainable and versatile molecules while showcasing the potential of mechanochemistry for the environmentally conscious and efficient synthesis of biobased compounds. The achievements in biodiesel production, fatty acid transformations, glycerol-

based reactions, and other applications exemplify the exciting possibilities in this interdisciplinary field.

Author contributions

CL: Investigation, Supervision, Writing–review and editing. VD: Writing–original draft. WO: Writing–original draft. RN: Writing–original draft. BL: Investigation, Supervision, Writing–review and editing.

Funding

The author(s) declare financial support was received for the research, authorship, and/or publication of this article. VD and BL would like to acknowledge the financial support from the Shiv Nadar Foundation and the SERB-Power Research Grant (Grant No. SPG/2021/002537).

Conflict of interest

The authors declare that the research was conducted in the absence of any commercial or financial relationships that could be construed as a potential conflict of interest.

The author(s) declared that they were an editorial board member of Frontiers, at the time of submission. This had no impact on the peer review process and the final decision.

Publisher's note

References

Alba-Rubio, A. C., Santamaria-Gonzales, J., Merida-Robles, J. M., Moreno-Tost, R., Martin-Alonso, D., Jmenez-Lopez, A., et al. (2010). Heterogeneous transesterification processes by using CaO supported on zinc oxide as basic catalysts. *Catal. Today* 149, 281–287. doi:10.1016/j.cattod.2009.06.024

Ardila-Fierro, K. J., Pich, A., Spehr, M., Hernandez, J. G., and Bolm, C. (2019). Synthesis of acylglycerol derivatives by mechanochemistry. *Beilstein J. Org. Chem.* 15, 811–817. doi:10.3762/bjoc.15.78

Balaz, P., Achimovicova, M., Balaz, M., Billik, P., Cherkezova-Zheleva, Z., Criado, J. M., et al. (2013). Hallmarks of mechanochemistry: from nanoparticles to technology. *Chem. Soc. Rev.* 42, 7571–7637. doi:10.1039/C3CS35468G

Biermann, U., Bornscheuer, U., Meier, M. A. R., Metzger, J. O., and Schafer, H. J. (2011). Oils and fats as renewable raw materials in chemistry. *Angew. Chem. Int. Ed.* 50, 3854–3871. doi:10.1002/anie.201002767

Bolt, R. R. A., Leitch, J. A., Jones, A. C., Nicholson, W. I., and Browne, D. L. (2022). Continuous flow mechanochemistry: reactive extrusion as an enabling technology in organic synthesis. *Chem. Soc. Rev.* 51, 4243–4260. doi:10.1039/d1cs00657f

Borges, M. E., and Diaz, L. (2012). Recent developments on heterogeneous catalysts for biodiesel production by oil esterification and transesterification reactions: a review. *Renew. Sustain. Energy Rev.* 16, 2839–2849. doi:10.1016/j.rser.2012.01.071

Botero Gutierre, C. D., Serna, D. L. R., and Alzate, C. A. C. (2017). A comprehensive review on the implementation of the biorefinery concept in biodiesel production plants. *Biofuel Res. J.* 15, 691–703. doi:10.18331/BRJ2017.4.3.6

Calvo-Flores, F. G., and Martin-Martinez, F. J. (2022). Biorefineries: achievements and challenges for a bio-based economy. *Front. Chem.* 10, 973417. doi:10.3389/fchem.2022.973417

Chen, S., Feng, H., Zheng, J., Ye, J., Song, Y., Yang, H., et al. (2020). Life cycle assessment and economic analysis of biomass energy technology in China: a brief review. *Processes* 8, 1112. doi:10.3390/pr8091112

Cuccu, F., De Luca, L., Delogu, F., Colacino, E., Solin, N., Mocci, R., et al. (2022). Mechanochemistry: new tools to navigate the uncharted territory of "impossible" reactions. *ChemSusChem* 15, e202200362. doi:10.1002/cssc.202200362

da Costa, A. A. F., de Oliveira, A. D. N., Esposito, R., Auvigne, A., Len, C., Luque, R., et al. (2023). Glycerol and microwave-assisted catalysis: recent progress in batch and flow devices. *Sustain. Energy Fuels* 7, 1768–1792. doi:10.1039/d2se01647h

da Costa, A. A. F., de Oliveira, A. D. N., Esposito, R., Len, C., Luque, R., Noronha, R. C. R., et al. (2022). Glycerol and catalysis by waste/low-cost materials a review. *Catalysts* 12, 570. doi:10.3390/catal12050570

Ding, H., Wang, X., Song, L., and Hu, Y. (2022). Recent advances in flame retardant bio-based benzoxazine resins. *J. Renew. Mat.* 10, 871–895. doi:10.32604/jrm.2022.018150

Eichmann, T. O., and Lass, A. (2015). DAG tales: the multiple faces of diacylglycerol – stereochemistry, metabolism, and signaling. *Cell. Mol. Life Sci.* 72, 3931–3952. doi:10.1007/s00018-015-1982-3

Fodran, P., and Minnaard, A. J. (2013). Catalytic synthesis of enantiopure mixed diacylglycerols – synthesis of a major *M. tuberculosis* phospholipid and platelet activating factor. *Org. Biomol. Chem.* 11, 6919. doi:10.1039/c3ob41483c

Garcia, E., Laca, M., Perez, E., Garrido, A., and Peinado, J. (2008). New class of acetal derived from glycerin as a biodiesel fuel component. *Energy fuels.* 22, 4274–4280. doi:10.1021/ef800477m

Garg, V., Kumar, A., Chaudhari, A., Agrawal, S., Tomar, P., and Sreenivasan, K. K. (2013). Synthesis, biological evaluation and molecular docking studies of 1,3-benzoxazine derivatives as potential anticancer agents. *Med. Chem. Res.* 22, 5256–5266. doi:10.1007/s00044-013-0534-3

Glycerol market to Garner $5.1 billion, globally by 2031 at 1.7% CAGR says allied market research (2022). Glycerol market to Garner $5.1 billion, globally by 2031 at 1.7% CAGR says allied market research. Available at: https://www.finanznachrichten.de/nachrichten-2022-06/56306365-glycerol-market-to-garner-dollar-5-1-billion-globally-by-2031-at-1-7-cagr-says-allied-market-research-008.htm (Accessed June 14, 2022).

Horie, K., Baron, M., Fox, R. B., He, J., Hess, M., Kahovec, J., et al. (2004). Definitions of terms relating to reactions of polymers and to functional polymeric materials (IUPAC Recommendations 2003). *Pure Appl. Chem.* 76, 889–906. doi:10.1351/pac200476040889

James, S. L., Adams, C. J., Bolm, C., Braga, D., Collier, P., Friscic, T., et al. (2012). Mechanochemistry: opportunities for new and cleaner synthesis. *Chem. Soc. Rev.* 41, 413–447. doi:10.1039/c1cs15171a

Kargar, P. G., Len, C., and Luque, R. (2022). Cu/cellulose-modified magnetite nanocomposites as a highly active and selective catalyst for ultrasound-promoted aqueous *O*-arylation Ullmann and sp-sp^2 Sonogashira cross-coupling reactions. *Sustain. Chem. Pharm.* 27, 100672. doi:10.1016/j.scp.2022.100672

Khodadadi, M. R., Malpartida, I., Tsang, C. W., Lin, C. S. K., and Len, C. (2020). Recent advances on the catalytic conversion of waste cooking oil. *Mol. Catal.* 494, 111128. doi:10.1016/j.mcat.2020.111128

Khodadadi, M. R., Thiel, J., Varma, R. S., and Len, C. (2021). Innovative continuous synthesis of solketal. *J. Flow. Chem.* 11, 725–735. doi:10.1007/s41981-021-00148-3

Kiakalaiehet, A. T., Amin, N. A. S., Najaafi, N., and Tarighi, S. (2018). A review on the catalytic acetalization of bio-renewable glycerol to fuel additives. *Front. Chem.* 6, 573. doi:10.3389/fchem.2018.00573

Kiss, F. E., Jovanovic, M., and Boskovic, G. C. (2010). Economic and ecological aspects of biodiesel production over homogeneous and heterogeneous catalysts. *Fuel Proc. Technol.* 91, 1316–1320. doi:10.1016/j.fuproc.2010.05.001

Kouzu, M., Fujimori, A., Fukakusa, R. T., Satoi, N., and Yahagi, S. (2018). Continuous production of biodiesel by the CaO-catalyzed transesterification operated with continuously stirred tank reactor. *Fuel Process. Technol.* 181, 311–317. doi:10.1016/j.fuproc.2018.10.008

Kouzu, M., and Hidaka, J. S. (2012). Transesterification of vegetable oil into biodiesel catalyzed by CaO: a review. *Fuel* 93, 1–12. doi:10.1016/j.fuel.2011.09.015

Kumar, S., Prince, P., Monika, M., Kumar, P., Len, C., and Singh, B. K. (2023). A unified, microwave-assisted, palladium-catalyzed regioselective ortho-monohalogenation of 1-alkyl/benzyl-3-phenylquinoxalin-2(1*H*)-ones. *ChemistrySelect* 8, e202204821. doi:10.1002/slct.202204821

Len, C., Delbecq, F., Corpas, C. C., and Ramos, E. R. (2018). Continuous flow conversion of glycerol into chemicals: an overview. *Synthesis* 50, 723–740. doi:10.1055/s-0036-1591857

Len, C., Khodadadi, M. R., Thiel, J., and Lacoste, F. (2021). *Procédé de fabrication du (2,2-dimethyl-1,3-dioxolan-4-yl)methanol*. WO2021110688A1.

Li, A., Song, H., Xu, X., Meng, H., Lu, Y., and Li, C. (2018). Greener production process of acetylene and calcium diglyceroxide via mechanochemical reaction of CaC2 and glycerol. *ACS Sustain. Chem. Eng.* 6, 9560–9565. doi:10.1021/acssuschemeng.8b01864

Lobato-Peralta, D. R., Duque-Brito, E., Villafan-Vidales, H. I., Longoria, A., Sebastian, P. J., Cuentas-Gallegos, A. K., et al. (2021). A review on trends in lignin extraction and valorization of lignocellulosic biomass for energy applications. *J. Clean. Prod.* 293, 126123. doi:10.1016/j.jclepro.2021.126123

Lu, X., Wang, Z., Hu, D., Liang, X., and Ji, J. (2019). Design of a horizontal ball-mill reactor and its application in dimerization of natural fatty acids. *Ind. Eng. Chem. Res.* 58, 10768–10775. doi:10.1021/acs.iecr.9b00943

Lukic, I., Kesic, Z., Zdujic, M., and Skala, D. (2016). Calcium diglyceroxide synthesized by mechanochemical treatment, its characterization and application as catalyst for fatty acid methyl esters production. *Fuel* 165, 159–165. doi:10.1016/j.fuel.2015.10.063

Ma, F., and Hanna, M. A. (1999). Biodiesel production: a review1Journal series #12109, agricultural research division, institute of agriculture and natural resources, university of Nebraska–Lincoln.1. *Bioressour. Technol.* 70, 1–15. doi:10.1016/s0960-8524(99)00025-5

Machado, I., Hsieh, I., Rachita, E., Salum, M. L., Iguchi, D., Pogharian, N., et al. (2021). A truly bio-based benzoxazine derived from these natural reactants obtained under environmentally friendly conditions and its polymer properties. *Green Chem.* 23, 5051. doi:10.1039/d1gc00951f

Maddikeri, G. L., Pandit, A. B., and Gogate, P. R. (2012). Intensification approaches for biodiesel synthesis from waste cooking oil: a review. *Ind. Eng. Chem. Res.* 51, 14610–14628. doi:10.1021/ie301675j

Magkos, F., and Mittendorfer, B. (2009). Stable isotope-labeled tracers for the investigation of fatty acid and triglyceride metabolism in humans *in vivo*. *Clin. Lipidol.* 4, 215–230. doi:10.2217/clp.09.9

Malpartida, I., Maireles-Torres, P., Lair, V., Halloumi, S., Thiel, J., and Lacoste, F. (2020). New high-throughput reactor for biomass valorization. *Chem. Proc.* 2, 31. doi:10.3390/ECCS2020-07583

Malpartida, I., Maireles-Torres, P., Vereda, C., Rodriguez-Maroto, J. M., Halloumi, S., Lair, V., et al. (2020). Semi-continuous mechanochemical process for biodiesel production under heterogeneous catalysis using calcium diglyceroxide. *Renew. Energy* 159, 117–126. doi:10.1016/j.renene.2020.05.020

Martin, S. F., Josey, J. A., Wong, Y. L., and Dean, D. W. (1994). General method for the synthesis of phospholipid derivatives of 1,2-O-Diacyl-sn-Glycerols. *J. Org. Chem.* 59, 4805–4820. doi:10.1021/jo00096a023

Martinez, F., Cravotto, G., and Cintas, P. (2021). Organic sonochemistry: a chemist's timely perspective on mechanisms and reactivity. *J. Org. Chem.* 86, 13833–13856. doi:10.1021/acs.joc.1c00805

Martinez, V., Stolar, T., Karadeniz, B., Brekalo, I., and Uzarevic, K. (2023). Advancing mechanochemical synthesis by combining milling with different energy sources. *Nat. Rev. Chem.* 7, 51–65. doi:10.1038/s41570-022-00442-1

Mateti, S., Mathesh, M., Liu, Z., Tao, T., Ramireddy, T., Glushenkov, A. M., et al. (2021). Mechanochemistry: a force in disguise and conditional effects towards chemical reactions. *Chem. Commun.* 57, 1080–1092. doi:10.1039/d0cc06581a

Michalchuk, A. A. L., Boldyreva, E. V., Belenguer, A. M., Emmerling, F., and Boldyrev, V. V. (2021). Tribochemistry, mechanical alloying, mechanochemistry: what is in a name? *Front. Chem.* 9, 685789. doi:10.3389/fchem.2021.685789

Mota, C. J. A., da Silva, C. X. A., Rosenbach, N., Costa, J., and da Silva, F. (2010). Glycerin derivatives as fuel additives: the addition of glycerol/acetone ketal (solketal) in gasolines. *Energy fuels*. 24, 2733–2736. doi:10.1021/ef9015735

Nanda, M. R., Zhang, Y., Yuan, Z., Qin, W., Ghaziaskar, H. S., and Xu, C. (2016). Catalytic conversion of glycerol for sustainable production of solketal as a fuel additive: a review. *Renew. Sust. Energy Rev.* 56, 1022–1031. doi:10.1016/j.rser.2015.12.008

Nasrollahzadeh, M., Shafiei, N., Nezafat, Z., and Bidgoli, N. S. S. (2020). Recent progresses in the application of lignin derived (nano)catalysts in oxidation reactions. *Mol. Catal.* 489, 110942. doi:10.1016/j.mcat.2020.110942

Nayak, S. N., and Bhushan, B. (2019). An overview of the recent trends on the waste valorization techniques for food wastes. *J. Environ. Manag.* 233, 352–370. doi:10.1016/j.jenvman.2018.12.041

Nguyen, R., Galy, N., Alamary, F. A., and Len, C. (2021). Microwave-assisted continuous flow for the selective oligomerization of glycerol. *Catalysts* 11, 166. doi:10.3390/catal11020166

Ning, P., Yang, G., Hu, L., Sun, J., Shi, L., Zhou, Y., et al. (2021). Recent advances in the valorization of plant biomass. *Biotechnol. Biofuels* 14, 102. doi:10.1186/s13068-021-01949-3

Oliva, E., Mathiron, D., Rigaud, S., Monflier, E., Sevin, E., Bricout, H., et al. (2020). New lipidyl-cyclodextrins obtained by ring opening of methyl oleate epoxide using ball milling. *Biomolecules* 10, 339. doi:10.3390/biom10020339

O'Neill, R. T., and Boulatov, R. (2021). The many flavours of mechanochemistry and its plausible conceptual underpinnings. *Nat. Rev. Chem.* 5, 148–167. doi:10.1038/s41570-020-00249-y

Pagola, S. (2023). Outstanding advantages, current drawbacks, and significant recent developments in mechanochemistry: a perspective view. *Crystals* 13, 124. doi:10.3390/cryst13010124

Paraskar, P. M., Major, I., Ladole, M. R., Doke, R. B., Patil, N. R., and Kulkarni, R. D. (2023). Dimer fatty acid – a renewable building block for high-performance polymeric materials. *Ind. Crops Prod.* 200, 116817. doi:10.1016/j.indcrop.2023.116817

Remize, M., Planchon, F., Loh, A. N., Le Grand, F., Bideau, A., Le Goic, N., et al. (2020). Study of synthesis pathways of the essential polyunsaturated fatty acid 20:5n-3 in the diatom *Chaetoceros Muelleri* using ^{13}C-isotope labeling. *Biomolecules* 10, 797. doi:10.3390/biom10050797

Rightmire, N. R., and Hanusa, T. P. (2016). Advances in organometallic synthesis with mechanochemical methods. *Dalton Trans.* 45, 2352–2362. doi:10.1039/C5DT03866A

Rizwanul Fattah, I. M., Ong, H. C., Mahlia, T. M. I., Mofir, M., Silitonga, A. S., Ashrafur Rahman, S. M., et al. (2020). State of the art of catalysts for biodiesel production. *Front. Energy Res.* 8, 101. doi:10.3389/fenrg.2020.00101

Rodriguez-Padron, D., Zhao, D., Garin Ortega, R. N., Len, C., Balu, A. M., Garcia, A., et al. (2020). Characterization and antioxidant activity of microwave-extracted phenolic compounds from biomass residues. *ACS Sustain. Chem. Eng.* 8, 1513–1519. doi:10.1021/acssuschemeng.9b06002

Rothenberg, G., Downie, A. P., Raston, C. L., and Scott, J. L. (2001). Understanding solid/solid organic reactions. *J. Am. Chem. Soc.* 123, 8701–8708. doi:10.1021/ja0034388

Silva, P. H. R., Gonçalves, V. L. C., and Mota, C. J. A. (2010). Glycerol acetals as anti-freezing additives for biodiesel. *Bioresour. Technol.* 101, 6225–6229. doi:10.1016/j.biortech.2010.02.101

Spackova, J., Fabra, C., Cazals, G., Hubert-Roux, M., Schmiz-Afonso, I., Goldberga, L., et al. (2021). Cost-efficient and user-friendly ^{17}O/^{18}O labeling procedures of fatty acids using mechanochemistry. *Chem. Commun.* 57, 6812–6815. doi:10.1039/d1cc02165f

Spackova, J., Fabra, C., Mittelette, S., Gaillard, E., Chen, C. H., Cazals, G., et al. (2020). Unveiling the structure and reactivity of fatty-acid based (nano)materials thanks to efficient and scalable 17O and 18O-isotopic labeling schemes. *J. Am. Chem. Soc.* 142, 21068–21081. doi:10.1021/jacs.0c09383

Szejtli, J. (1998). Introduction and general overview of cyclodextrin chemistry. *Chem. Rev.* 98, 1743–1754. doi:10.1021/cr970022c

Tan, D., and Garcia, F. (2019). Main group mechanochemistry: from curiosity to established protocols. *Chem. Soc. Rev.* 48, 2274–2292. doi:10.1039/c7cs00813a

Torres-Pastor, M. A., Espro, C., Selva, M., Perosa, A., Romero Reyes, A. A., Osman, S. M., et al. (2022). Glycerol valorization towards a benzoxazine derivative through a milling and microwave sequential strategy. *Molecules* 27, 632. doi:10.3390/molecules27030632

Varma, R. S., and Len, C. (2019). Glycerol valorization under continuous flow conditions – recent advances. *Curr. Opin. Green Sustain. Chem.* 15, 83–90. doi:10.1016/j.cogsc.2018.11.003

Vegetable oil market – Industry analysis, trends and forecast (2023-2029). *Vegetable oil market – industry analysis, trends and forecast*, 2023–2029. Accessed: 01 June 2023) Available at: https://www.maximizemarketresearch.com/market-report/global-vegetable-oil-market/108821/.

Vegetable oil production in 2023/24 expected to be up on previous year (2023). Vegetable oil production in 2023/24 expected to be up on previous year. Available at: https://www.ofimagazine.com/news/vegetable-oil-production-in-2023-24-expected-to-be-up-on-previous-year (Accessed July 10, 2023).

Vu, H. P., Nguyen, L. N., Vu, M. T., Johir, Md. A. H., McLaughlan, R., and Nghiem, L. D. (2020). A comprehensive review on the framework to valorise lignocellulosic biomass as biorefinery feedstocks. *Sci. Total Environ.* 743, 140630. doi:10.1016/j.scitotenv.2020.140630

Wang, W., Chai, M., Zulkifli, M. Y. B., Xu, K., Chen, Y., Wang, L., et al. (2023). Metal-organic framework composites from a mechanochemical process. *Mol. Syst. Des. Eng.* 8, 560–579. doi:10.1039/D2ME00211F

Winkler, J. W., Uddin, J., Serhan, C. N., and Petasis, N. A. (2013). Stereocontrolled total synthesis of the potent anti-inflammatory and pro-resolving lipid mediator resolving D3 and its aspirin-triggered 17*R*-epimer. *Org. Lett.* 15, 1424–1427. doi:10.1021/ol400484u

Xia, Y., and Larock, R. C. (2010). Vegetable oil-based polymeric materials: synthesis, properties, and applications. *Green Chem.* 12, 1893–1909. doi:10.1039/C0GC00264J

Yara-Varon, E., Li, Y., Balcells, M., Canela-Garayoa, R., Fabiano-Tixier, A. S., and Chemat, F. (2017). Vegetable oils as alternative solvents for green oleo-extraction, purification and formulation of food and natural products. *Molecules* 22, 1474. doi:10.3390/molecules22091474

Ying, P., Yu, J., and Su, W. (2021). Liquid-assisted grinding mechanochemistry in the synthesis of pharmaceuticals. *Adv. Synth. Catal.* 363, 1246–1271. doi:10.1002/adsc.202001245

Yu, B. Y., Tseng, T. Y., Yang, Z. Y., and Shen, S. J. (2022). Evaluation on the solketal production processes: rigorous design, optimization, environmental analysis, and control. *Process Saf. Environ. Prot.* 157, 140–155. doi:10.1016/j.psep.2021.11.011

Zaed, A. M., and Sutherland, A. (2011). Total synthesis of clavaminol A, C and H. *Org. Biomol. Chem.* 9, 8030. doi:10.1039/c1ob06060k

Zahid, I., Ayoub, M., Abdullah, B. B., Hamza Nazir, M., Ameen, M., Zulqarnain, M. Y. M. H., et al. (2020). Production of fuel additive solketal via catalytic conversion of biodiesel-derived glycerol. *Ind. Eng. Chem. Res.* 59 (48), 20961–20978. doi:10.1021/acs.iecr.0c04123

Zahid, I., Ayoub, M., Abdullah, B. B., Mukhtar, A., Saqib, S., Rafiq, S., et al. (2021). Glycerol conversion to solketal: catalyst and reactor design, and factors affecting the yield. *ChemBioEng* 8, 227–238. doi:10.1002/cben.202000015

Zhao, D., Rodriguez-Padron, D., Luque, R., and Len, C. (2020). Insights into selective oxidation of 5-hydroxymethylfurfural to 5-hydroxymethyl-2-furancarboxylic acid using silver oxide. *ACS Sustain. Chem. Eng.* 23, 8486–8495. doi:10.1021/acssuschemeng.9b07170

Zhao, M., Wang, Y., Zhou, W., Zhou, W., and Gong, Z. (2023). Co-valorization of crude glycerol and low-cost substrates via oleaginous yeasts to micro-biodiesel: status and outlook. *Renew. Sustain. Energy Rev.* 180, 113303. doi:10.1016/j.rser.2023.113303

frontiers | Frontiers in Chemistry

TYPE Original Research
PUBLISHED 25 September 2024
DOI 10.3389/fchem.2024.1457265

OPEN ACCESS

EDITED BY
Jianhua Zhang,
Victoria University, Australia

REVIEWED BY
Rachid Hsissou,
Chouaïb Doukkali University, Morocco
Celal Duran,
Karadeniz Technical University, Türkiye

*CORRESPONDENCE
Syed Muhammad Salman,
salman@icp.edu.pk
Asad Ali,
asad.ali@asssociated.ltu.se

RECEIVED 18 July 2024
ACCEPTED 30 August 2024
PUBLISHED 25 September 2024

CITATION
Nawaz S, Salman SM, Ali A, Ali B, Shah SN and Rahman LU (2024) Kinetics and thermodynamics investigations of efficient and eco-friendly removal of alizarin red S from water via acid-activated *Dalbergia sissoo* leaf powder and its magnetic iron oxide nanocomposite.
Front. Chem. 12:1457265.
doi: 10.3389/fchem.2024.1457265

Kinetics and thermodynamics investigations of efficient and eco-friendly removal of alizarin red S from water via acid-activated *Dalbergia sissoo* leaf powder and its magnetic iron oxide nanocomposite

Saleem Nawaz[1], Syed Muhammad Salman[1]*, Asad Ali[2]*, Basit Ali[1], Syed Nusrat Shah[1] and Latif Ur Rahman[3]

[1]Department of Chemistry, Islamia College Peshawar, Peshawar, Pakistan, [2]Energy Engineering, Division of Energy Science, Lulea University of Technology, Lulea, Sweden, [3]Institute of Chemical Sciences, University of Peshawar, Peshawar, Pakistan

The present work aimed to highlight an efficient, readily accessible, and cost-effective adsorbent derived from *Dalbergia sissoo* (DS) leaf powder for removing the environmentally hazardous dye "alizarin red S" (ARS) from hydrous medium. A variant of the adsorbent is activated via sulfuric acid and composited with magnetic iron oxide nanoparticles (DSMNC). Both adsorbents are thoroughly characterized using techniques such as Fourier transform infrared spectroscopy, point of zero charge, energy-dispersive X-ray spectroscopy, and scanning electron microscopy, which show that they have a porous structure rich in active sites. Different adsorption conditions are optimized with the maximum removal efficiency of 76.63% for DS and 97.89% for DSMNC. The study was highlighted via the application of various adsorption isotherms, including Freundlich, Langmuir, Temkin, and Dubinin–Radushkevich, to adsorption data. Pseudo-first-order, pseudo-second-order, and intra-particle diffusion models were utilized to investigate the kinetics and mechanism of adsorption. The Freundlich model and pseudo-second-order kinetics exhibited the best fit, suggesting a combination of physical interactions, as confirmed by the D–R and Temkin models. The dominant adsorbate–adsorbent interactive interactions responsible for ARS removal were hydrogen bonding, dispersion forces, and noncovalent aromatic ring adsorbent pi-interactions. Thermodynamic parameters extracted from adsorption data indicated that the removal of the mutagenic dye "ARS" was exothermic and spontaneous on both DS and DSMNC, with DSMNC exhibiting higher removal efficiency.

KEYWORDS

alizarin red S, adsorptive removal, *Dalbergia sissoo*, *Dalbergia sissoo*-magnetic iron oxide nanocomposite, adsorption isotherms, thermodynamics and kinetics

1 Introduction

The direct release of harmful waste from various origins into aquatic environments that lack adequate processing is the primary challenge to water quality. A significant source of water pollution stems from organic pollutant effluents via numerous industries, including leather manufacturing, paint production, textiles, and paper. Even in trace amounts, these substances can harm aquatic environments and pose risks to all living organisms (Lebkiri et al., 2023; Bensalah et al., 2023). For instance, the dye industry is ranked as the 10th most contaminating sector in terms of river water quality, contributing 17%–20% of industrial water degradation (Kadiri et al., 2021; Gul et al., 2021). Annually, between 5,000 and 10,000 tons of dyes are dumped into rivers owing to their widespread usage. Alizarin red S (ARS) is one of the most commonly used dyes. These dyes are classified as anionic dyes because their molecules dissociate in water with negative charges, posing a risk to the health of the marine habitat and the surrounding community when directly expelled into surface waters. They obstruct the sunlight that is vital for the process of photosynthesis in aquatic plants (Pirkarami and Olya, 2017; Yagub et al., 2014; Wong et al., 2020). Consequently, effective management of textile effluents is crucial to safeguard the ecosystem and the surrounding environment.

Alizarin red S (ARS), also known as 1,2-dihydroxy-9,10-anthraquinone sulfonic acid sodium salt, is a dye that has been used extensively since ancient times and has significant adverse impacts on the ecosystem (Hu et al., 2019). It is highly desired by industries such as textiles, food, and dyes due to its water solubility of 20 g/L (Fayazi et al., 2015). Acting as a color indicator, it has a pKa value ranging from 4.6 to 6.5 and is commonly found in the effluent of these sectors (Chin et al., 2015). Data from tests on rabbits indicate that ARS can sensitize the skin, cause minor irritation to the eyes, and is known to be hazardous and carcinogenic (Sowjanya et al., 2022). It has been shown to induce dermatitis in humans and has the potential to act as an allergen. Its LD_{50} value, when administered intravascularly, is 70 mg/kg (Gautam et al., 2020). Due to its potential to cause oxidative damage to organisms, it has been claimed to be mutagenic and carcinogenic (Delpiano et al., 2021).

Membrane percolation, photolytic decay, high-performance liquid chromatography, membrane electrophoresis, flocculation-coagulation, chemical and electrochemical oxidation, ion exchange processes, filtration followed by coagulation, ozonation followed by coagulation, and adsorption are common techniques for analyzing and treating pollutants (Jebli et al., 2023; Gautam et al., 2017; Kamarehie et al., 2019). However, the extensive use of costly chemicals, poor effectiveness, formation of secondary noxious waste, and high operating and upkeep charges limit their applicability (Detpisuttitham et al., 2020). Compared to other methods, adsorption is highly effective at removing colors from industrial effluents, resulting in clean, high-quality water by eliminating most contaminants found in wastewater.

When treating runoff from the dye industry using an adsorption technique, pure, high-quality water free of coloring material and other contaminants is produced. Despite extremely small concentrations, the presence of dyes can diminish the visual appeal of water. Due to the durability and complex aromatic ring structure of dyes, persistent dyes like ARS are challenging to treat in aqueous mediums using conventional methods. Adsorption, however, offers a simple, cost-effective method that has gained popularity due to its minimal waste disposal advantage (Zhou et al., 2019; Aragaw and Bogale, 2021; Nistor et al., 2021).

According to the literature that has evaluated diverse biosorbents, biosorption is among the most cost-effective and straightforward practices for removing color from industrial effluent (Adegoke and Bello, 2015; Kumar et al., 2021). This method utilizes readily available, reasonably priced, and efficiently treated or untreated materials as biosorbents. Biosorbents can be treated with different acids to enhance their capacity to absorb various colors on their fine, porous surfaces.

The quantity of dye that can be adsorbed depends on several factors, including pH, contact time, temperature, type and dosage of adsorbents, and original dye concentration. The optimal sorbent parameters for specific dye adsorption can vary significantly (Sultana et al., 2023), and optimizing each parameter is beneficial for both large-scale commercial applications and understanding the adsorption mechanism. Colors from industrial runoff can be effectively biosorbed through the utilization of plant biomasses, rice husks, algae, walnut shells, wood, coconut coir dust, and numerous other waste materials that have undergone chemical modification (Kainth et al., 2024).

Adsorptive removal of ARS using *Dilbergia sissoo* leaf powder and its magnetic nanocomposite has not been reported. According to the experimental results, 78.7% of alizarin red S was removed from water-based solutions under optimum environmental factors using polypyrrole-coated magnetic nanoparticles (Gholivand et al., 2015).

In the present study, powdered *Dilbergia sissoo* (DS) leaves underwent treatment with acid and were subsequently composited with magnetic iron oxide nanoparticles to create an adsorbent for the elimination of ARS from an aqueous medium.

2 Material and methods

2.1 Adsorbent preparation

Leaves of DS were cleansed repeatedly using distilled water to eliminate any grime present. Afterward, the DS sample was oven-dried at 80°C for 24 h and subsequently screened to acquire DS particles with size 125 μm. DS powder was soaked in 2M H_2SO_4 (Merck 98%) for 24 h for activation, cleansed with distilled water twice to remove the acid, and dehydrated in an oven at 80°C.

Magnetic iron oxide-nanocomposite was prepared by the co-precipitation method (Oroujizad et al., 2023). In this method, specified quantities (1:2 mole ratio) of $FeSO_4.7H_2O$ (Sigma Aldrich ≥99%) and $FeCl_3.6H_2O$ (Sigma Aldrich ≥99%) were dispersed in 100 mL of deionized water and continuously stirred at 70–80°C with the continuous dropwise addition of 10% ammonia (Sigma Aldrich 25%) until pH 10 is achieved. Then, the activated DS leaf powder (1g) was slowly added until a black precipitate was formed, indicating the formation of the nanocomposite. The hot mixture containing the precipitate was brought to ambient temperature, filtered, and cleaned with distilled water. The residue was dehydrated at 60°C in an oven and converted to a fine powder form.

2.2 Solution preparation

A 1,000 mg/L stock solution of ARS (Sigma Aldrich 97%) was prepared that was subsequently diluted to create desired dye working solutions. HCl (Sigma Aldrich 37%) and NaOH (Merck ≥ 97.0%) solutions having 0.1M concentrations were used to regulate the solution pH.

2.3 Characterization of DS and DSMNC

To comprehensively comprehend the adsorption mechanism, the prepared adsorbents underwent characterization both pre- and post-adsorption utilizing Fourier transform infrared spectroscopy (FTIR) (Agilent Technologies, United States), scanning electron microscopy (SEM), and energy-dispersive X-ray spectroscopy (EDS) (JEOL Japan). The adsorption efficiency was determined using a UV-visible spectrophotometer from Shimadzu (model 1900) in Japan.

2.4 Batch adsorption analysis

A batch sorption analysis was carried out using a 100 mL conical flask containing 50 mL of ARS solution (40–120 mg.L^{-1}) placed on a shaker operating at 200 rpm (15–150 min). After each adsorption experiment, the DS and DSMNC composite (0.05–0.6 g) were separated from the dye effluent through filtration, and the absorbance of each solution was measured at 423 nm (experimentally determined at pH_{PZC}) to determine its concentration after adsorption. The percentage of adsorptive removal (E%) and the maximum uptake capacity (q_e in mg/g) of ARS were determined using Equations 1,2. These equations utilized an ARS reference curve established with various working solutions of the dye.

$$q_e = \frac{(C_0 - C_a)V}{m}, \quad (1)$$

$$\%Removal = \frac{(C_0 - C_a)}{C_0} X\,100, \quad (2)$$

where C_o (mg/L) is the concentration of ARS before adsorption, C_a (mg/L) is the ARS concentration after adsorption, V(L) is the volume of solution in liters, and m (g) is the mass of the adsorbent.

Kinetics, isothermal, and thermodynamic models were applied to the adsorption data.

3 Result and discussion

3.1 Characterizations of adsorbents

The functional groups located on the surface of the adsorbents (DS and DSMNC) were assessed through Fourier transform infrared spectroscopy (FTIR) and are depicted in Figures 1A, B. FTIR spectra revealed the presence of numerous functional groups.

The appearance of a strong peak at 544 cm^{-1}, denoting stretching of the Fe-O bond, is confirmation of the formation of magnetic iron oxide nanocomposite (Salari, 2022; Mahmoodi et al., 2019). The occurrence of –OH and –NH functional groups was verified by the bands observed between 3,000 cm^{-1} and 4,000 cm^{-1} (Ali et al., 2019). The peak at 2,850–2,922 cm^{-1} accounts for C-H stretching (Pal et al., 2007). The appearance of the peak at 2,100–2,260 cm^{-1} corresponds to C≡C stretching. The pronounced peaks observed within the wave number range of 1,600–1,650 cm^{-1} indicate the presence of conjugated stretching associated with the carboxylic and carbonyl groups' C=O bonds (Malik et al., 2020). The peaks between 1,400 cm^{-1} and 1,450 cm^{-1} correspond to the aromatic ring present (Oyekanmi et al., 2021). The peaks between 1,200 cm^{-1} and 1,320 cm^{-1} correspond to a carboxylic acid group. The peaks between 1,020 cm^{-1} and 1,200 cm^{-1} indicate C-OH stretching (Dehkhoda et al., 2014). The peak appearing between 675 cm^{-1} and 895 cm^{-1} corresponds to C=C. Shifting of some of the peaks identified in the FTIR spectra of the dye-loaded samples suggests interactions between the dye molecules and the sorbent material. These groups actively participate in the interactions and hydrogen bonds and enhance the degree of adsorption (Jawad et al., 2020; Oyekanmi et al., 2021).

The surface morphology of the adsorbent is characterized by the SEM images of DS and DSMNC before and after adsorption depicted in Figures 2, 3. It is clear from the figure that the particle size decreases when the magnetic nanocomposite is formed with the biomass. An increase in surface area and an increased amount of adsorbed dye is expected on DSMNC compared to DS.

The EDS spectra of DS and DSMNC are visualized in Figures 4A–D, respectively. The appearance of strong Fe peaks in the EDS spectra of DSMNC confirms the formation of the magnetic nanocomposite. Additionally, a hyperchromic shift is observed in the peaks of C, S, and Na in the post-adsorption spectra of both DS and DSMNC. This shift indicates an increase in the elemental compositions of these elements present in ARS, supporting its adsorption onto both DS and DSMNC.

In the context of studying the sorption of colorant from aqueous media, the pH level at which adsorbent exhibits zero cumulative surface charge, known as the point of zero charge (pH_{PZC}), emerges as a critical parameter. The pH level of the dye solution significantly contributes to determining the amount of adsorbent that can be effectively adsorbed (Chowdhury et al., 2011; Murthy et al., 2020). This is because variations in pH facilitate the electrification of both the adsorbate particles and the functional moieties present upon the adsorbent interface; consequently, alterations in the pH of the medium alter the surface charges on the adsorbent, thereby influencing the rate of adsorption (Sen et al., 2011).

The pH_{PZC} values obtained from the plot are 5.2 for DS and 4.2 for DSMNC shown by Figure 5. pH values lower than the pH_{PZC} are ideal for the adsorption of ARS with anionic groups. This is because protonation causes the adsorbent surface to become cationic, facilitating the adsorption process.

3.2 Optimization of adsorption factors

Figure 6 represents fine-tuning of adsorption conditions for the removal of ARS using DS and DSMNC. A batch adsorption experiment was performed to examine the impact of the adsorbent dose on the removal of ARS onto the surface of DS

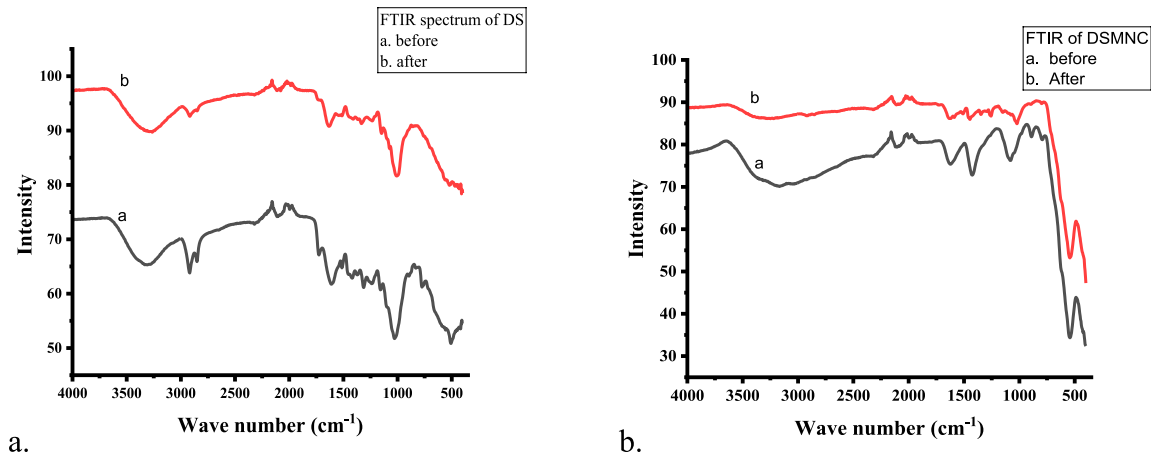

FIGURE 1
FTIR spectra of **(A)** DS and **(B)** DSMNC before and after adsorption.

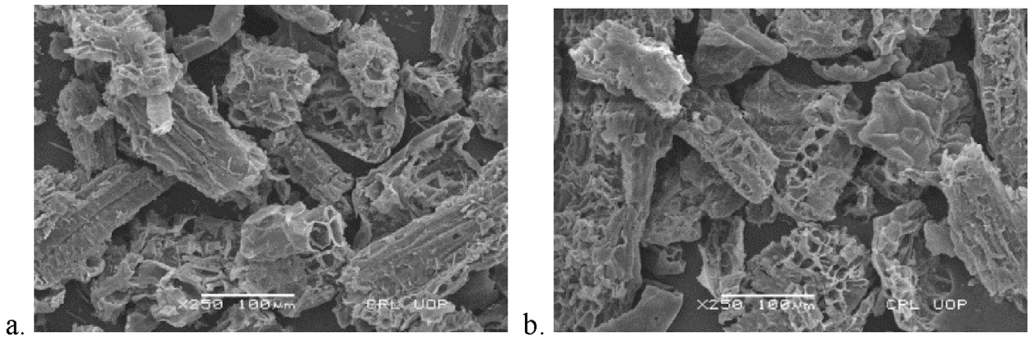

FIGURE 2
SEM analysis of DS **(A)** before and **(B)** after adsorption.

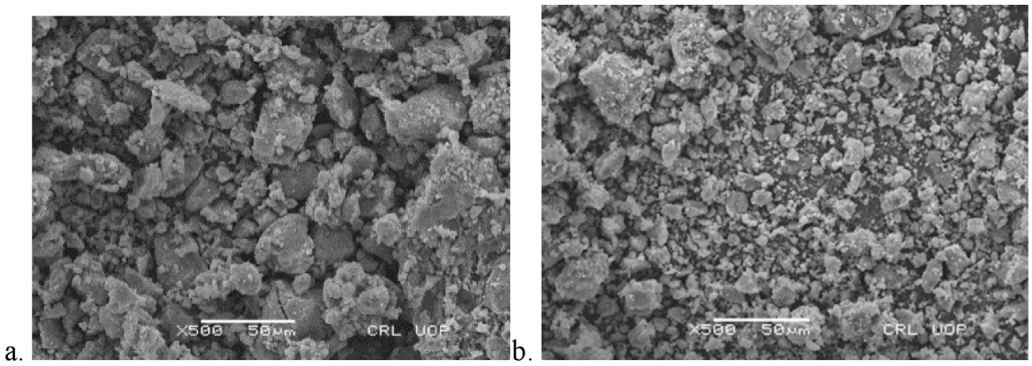

FIGURE 3
SEM analysis of DSMNC **(A)** before and **(B)** after adsorption.

and DSMNC. The adsorbents (0.05–0.6 g) were added to 50 mL of 100 mg/L of ARS, taken in 250 mL flasks, and shaken for 60 min at 200 rpm. The remaining dye content in the solutions was subsequently determined via spectrophotometry. Similar experimental approaches were employed to scrutinize the influence of the preliminary dye concentration (40 mg/L–120 mg/L), shaking time (15–150 min), pH (1.5–13.5) ionic strength, and temperature (20°C–80°C) on the adsorption process.

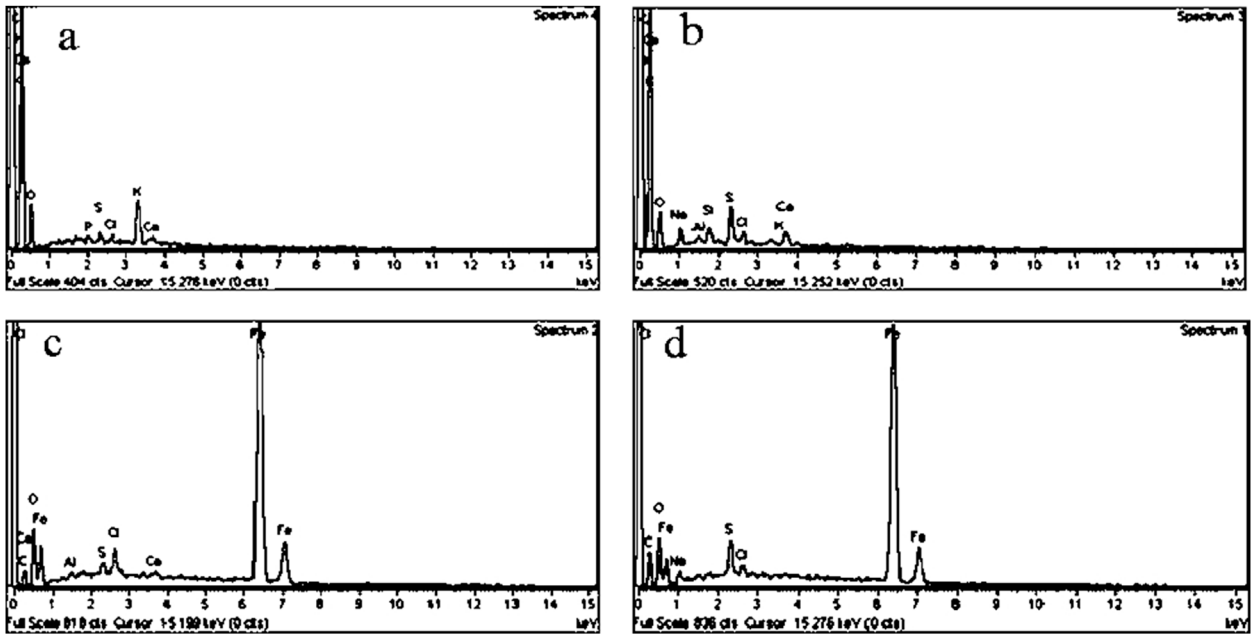

FIGURE 4
EDS spectra of DS **(A)** before and **(B)** after adsorption and of DSMNC **(C)** before and **(D)** after adsorption.

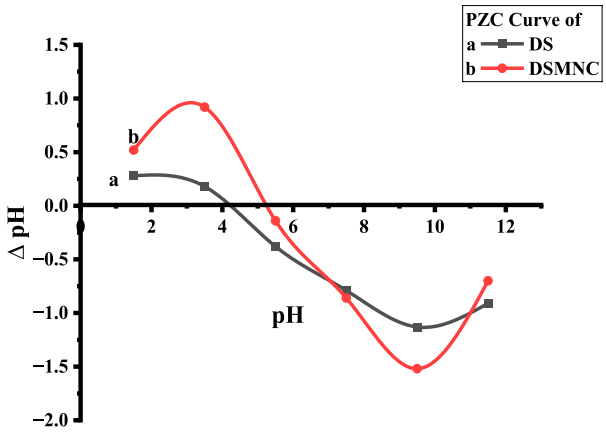

FIGURE 5
pH_{pzc} of DS and DSMNC.

The effect of pH is shown in Figure 6A by plotting the percentage removal vs. pH. As shown by the figure, the percentage removal of ARS increases with the increase of pH, reaches the optimum value near pH_{PZC}, and decreases afterward at a constant amount of adsorbent dose, concentration, temperature, and shaking time. The removal efficiency is higher when DSMNC (88.25%) is used than when DS (70.2%) is used as an adsorbent. The values of q_e remain almost constant till pH_{PZC} and are followed by a decrease above this pH. The surplus positive charges will additionally impact the surface charge of the adsorbent. Consequently, the intricately structured aromatic compounds of ARS will progressively adhere to the highly porous surface of the adsorbent, thereby stabilizing the dispersion status (Zare et al., 2015).

The influence of the initial dye concentration on the percentage removal of ARS onto DS and DSMNC is expressed in Figure 6B by plotting percentage removal vs. concentration. As portrayed in the figure, the percentage removal of ARS increases with increases in the initial dye concentration and reaches an optimum value (66.7% for DS and 97.89% for DSMNC) when the other parameters are kept constant. Furthermore, increasing the amount of dye beyond the optimum concentration led to saturation of the adsorption surfaces. This resulted in lowering the adsorption percentage. As the concentration of dye increases, more free dye particles are available to interact with the adsorbent, resulting in the formation of dye particle–adsorbent particle interactions, thereby enhancing the efficiency of dye removal. However, there comes a point where the dye removal efficiency may decrease or stabilize as the dye concentration reaches saturation (Ibrahim et al., 2019). There is an increase in the value of q_e in the pre-optimum value in a relatively steep manner, while after it reaches the optimum concentration, the curve flattens. The increase in the amount of dye creates a driving force for mass transfer, so the adsorbed dye amount per gram of adsorbent (q_e, mg/g) increases.

The adsorbent dose and the percentage removal are directly related to the adsorption process (Elzahar and Bassyouni, 2023). Figure 6C illustrates the impact of the dose on the adsorption of ARS. With the rise in the quantity of the adsorbent, the percentage removal of dye also increases, reaching a maximum value of 76.6% for DS at 0.4 grams and 93.82% for DSMNC at 0.2 grams, after which it stabilizes. This trend can be credited to the expanded accessibility of adsorption sites with the higher adsorbent dosage, leading to enhanced dye–adsorbent interactions (Saha et al., 2011). There is a decrease in the q_e value with the increase in the adsorbent amount. This may be due to the fact that at the lower adsorbent amount, most of the adsorption sites are occupied by ARS

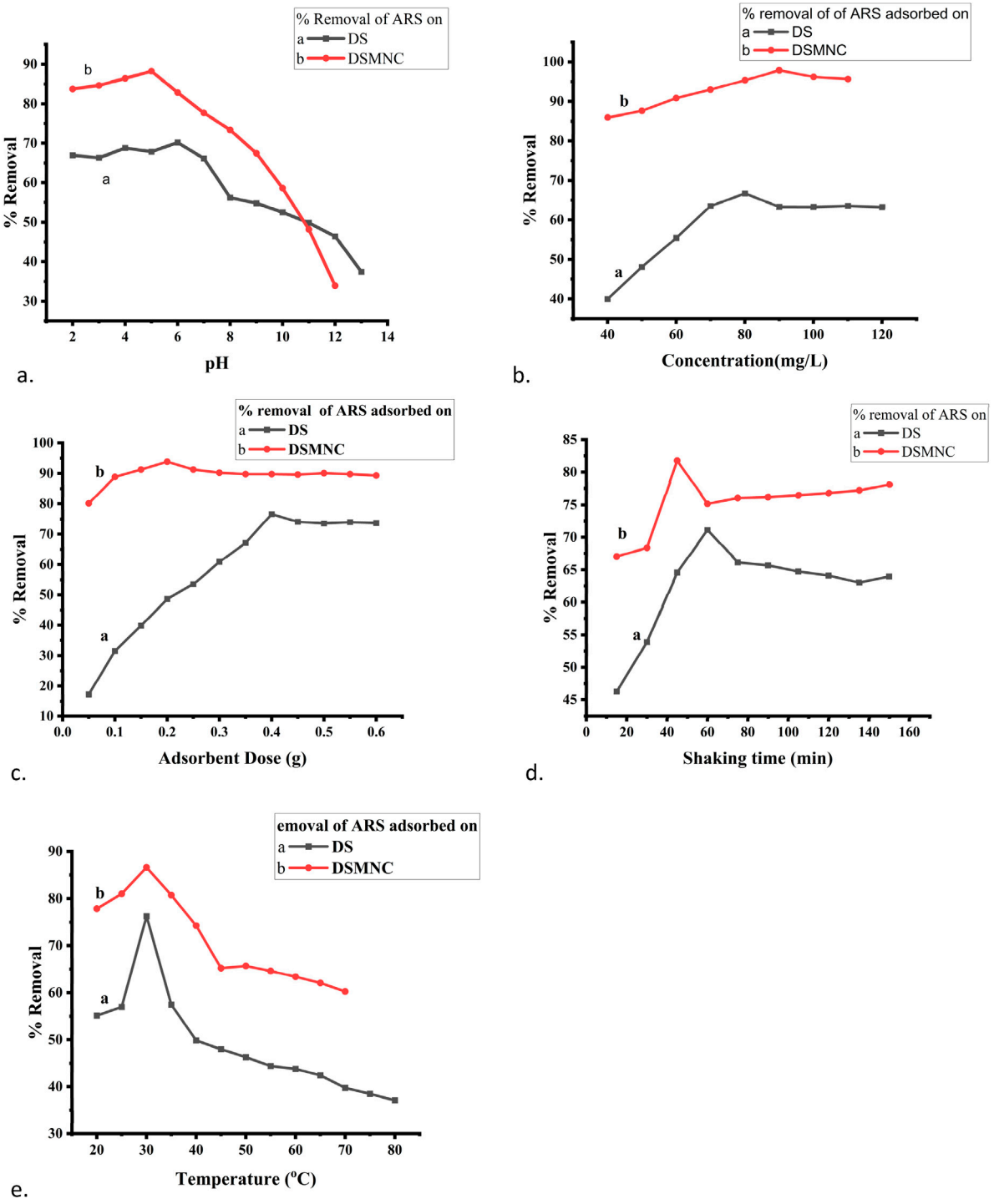

FIGURE 6
Optimization of adsorption parameters: **(A)** pH, **(B)** concentration, **(C)** adsorbent dose, **(D)** shaking time, and **(E)** temperature for adsorption of ARS on DS and DSMNC.

molecules; hence, the amount of ARS per g of adsorbent increases, and increasing the amount of adsorbent may leave some of the adsorbent sites vacant at the same concentration.

Figure 6D illustrates the relationship between the percentage removal and shaking time, from 15 min to 150 min, for the adsorption process of alizarin red S onto both DS and DSMNC. The observed trend indicates a steady increase in percentage removal with increased shaking time, reaching its zenith at 60 min for DS and 45 min for DSMNC. Subsequently, a decline in removal efficiency is observed beyond these contact times. The variation of q_e with shaking time follows the same trend. This phenomenon is primarily attributable to the attainment of the

adsorption–desorption equilibrium, wherein the surface coverage of the adsorbent reaches saturation at a given time interval. Further agitation beyond this equilibrium point leads to mechanical disruption of the already-adsorbed dye molecules, prompting desorption (Kuśmierek and Świątkowski, 2015). Moreover, comparing DS and DSMNC reveals that the latter exhibits a notably higher percentage removal value (increasing from 71.12% to 81.78%), indicating enhanced adsorption efficiency facilitated by the impregnation of magnetic nanoparticles, which provide the advantages of magnetic separation and increase in surface area (Rao and Ramanaiah, 2024). This augmentation underscores the role of magnetic NPs in boosting the adsorptive potential of the adsorbent.

Figure 6E portrays the impact of temperature variation on the percentage removal of alizarin red S by DS and DSMNC. The percentage removal increased from 55.12% at 20°C to 76.24% at 30°C, with a subsequent decrease in percentage removal with further temperature increments. Similar trends were observed for DSMNC, with a notably higher percentage removal of 86% at 30°C. This phenomenon can be attributed to the initial preferment of adsorption by temperature up to 30°C. Beyond this threshold, higher temperatures are hypothesized to favor dye diffusion in the solution phase rather than its adsorption onto the adsorbent (Khalaf et al., 2021). This inference aligns with the exothermic nature of the adsorption phenomenon and is supported by Le Chatelier's principle, which posits that an increase in temperature tends to diminish the equilibrium constant (Kc) associated with adsorption, thereby disadvantaging the adsorption process (Abualnaja et al., 2021).

3.3 Adsorption kinetics study

The adsorption mechanism of alizarin red S onto DS and DSMNC was investigated through batch kinetic biosorption studies (Dehghani et al., 2017). Two 50 mL solutions of alizarin red S were subjected to shaking in the presence of 0.4 g of DS and 0.2 g of DSMNC, respectively, for varying time intervals ranging from 15 to 150 min while maintaining a steady temperature of 30°C throughout the adsorption process. The obtained adsorption data was scrutinized using pseudo-first-order, pseudo-second-order, and the intra-particle diffusion kinetics model equations given as follows:

Pseudo-first-order kinetics:

$$\ln(q_e - q_t) = ln\,q_e - k_1 t. \tag{3}$$

Pseudo-second-order kinetics:

$$\frac{t}{q_t} = \frac{1}{k_2 q_e^2} + \frac{t}{q_e}. \tag{4}$$

Intra-particle diffusion model:

$$q_t = k_{dif} t^{1/2} + C. \tag{5}$$

Liquid diffusion model:

$$\ln\left(1 - \frac{q_t}{q_e}\right) = -k_{fd} t. \tag{6}$$

In the given equations, q_e represents the equilibrium adsorption capacity (mg/g), q_t denotes the adsorption capacity at time t (mg/g), k_1 is the pseudo-first-order equilibrium rate constant (min^{-1}), k_2 is the pseudo-second-order equilibrium rate constant (g/mg/min), k_{dif} is the rate constant of intra-particle diffusion, C is the intercept, and t is the adsorption time (min).

The experimental values of q_t for both DS and DSMNC obtained during the shaking time experiment were subjected to fitting within the pseudo-first-order kinetic model (Equation 3). The resulting plot, depicted in Figure 7A, revealed that the R^2 values obtained from this analysis are 0.695 and 0.81, and values of specific rate constant (k) calculated from slope values are 1.6×10^{-2} min^{-1} and 1.19×10^{-2} min^{-1} for DS and DSMNC, respectively.

Figure 7B illustrates the adsorption behavior of alizarin red S onto the surface of DS and DSMNC over varying shaking intervals, with the data compiled in the pseudo-second-order kinetics (Equation 4). Calculation of the specific rate constants (k) from the slope of the curves reveals k values of 2.53×10^{-2} g. $mg^{-1}.min^{-1}$ for DS and 4.64×10^{-2} $g{\cdot}mg^{-1}{\cdot}min^{-1}$ for DSMNC. This signifies an enhancement in the adsorption rate upon the formation of magnetic nanocomposites from DS. The R^2 values for alizarin red S adsorption on DS and DSMNC are 0.997 and 0.97, respectively.

The value of q_e calculated from the intercept of PFO is 2.01 mg/g for DS and 3.16 mg/g for DSMNC, and from PSO, the values are 7.39 mg/g and 21.55 mg/g. The values obtained experimentally are 9.97 mg/g for DS and 21.35 mg/g for DSMNC, which are in close agreement with the values obtained from second-order kinetics, suggesting that the adsorption process for both DS and DSMNC obeys pseudo-second-order kinetics. This suggestion is also confirmed by a higher R^2 value for PSO, implying that dye molecules and various adsorption sites on a solid substrate randomly bump into each other during a rate-controlling mechanistic phase (Hubbe et al., 2019).

The study utilized both the intra-particle diffusion (Weber–Morris) model (Equation 5) and the liquid film diffusion model (Equation 6), as depicted in Figures 7C, D, to determine the mechanisms of diffusion for adsorption of ARS on DS and DSMNC. It was anticipated that liquid film diffusion, intra-particle diffusion, or a combination of both could serve as the limiting factors in the process (Ahmad et al., 2015). Weber and Morris observed that in many adsorption scenarios, the uptake of adsorbate is nearly linear to the square root of contact time rather than to the contact duration (Alkan et al., 2007). When intra-particle diffusion governs the adsorption process, a plot of q_t against $t^{1/2}$ would be linear. Additionally, if this plot intersects the origin, it suggests that intra-particle diffusion is the only factor limiting the rate. On the other hand, if the straight-line graph of $-\ln(1 - q_t/q_e)$ vs. t has a zero intercept, it implies that the kinetics of adsorption are governed by diffusion via the liquid film neighboring the adsorbent (Hasani et al., 2022).

However, because neither intercept is equal to zero in this case, it is improbable that intra-particle diffusion alone dictates the rate-limiting step. Therefore, the kinetics were influenced by both liquid film and intra-particle diffusion simultaneously.

3.4 Isothermal study of adsorption

Various adsorption isotherm models are employed to comprehensively analyze experimental data and elucidate the adsorption mechanism of alizarin red S onto DS and DSMNC

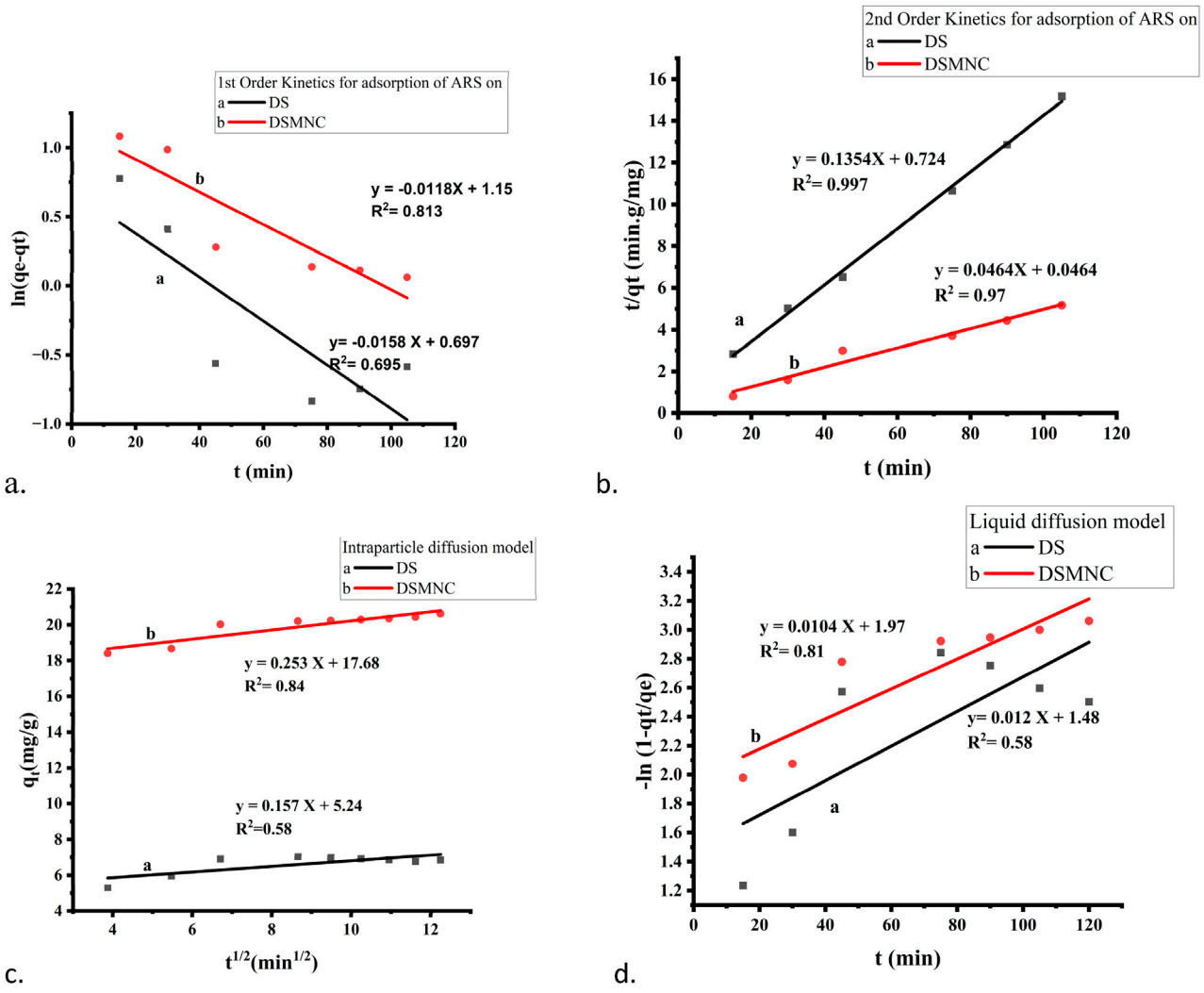

FIGURE 7
Kinetics models for the adsorption of ARS on DS and DSMNC: **(A)** pseudo-first-order, **(B)** pseudo-second-order, **(C)** interparticle diffusion model, and **(D)** liquid diffusion model.

from aqueous solutions. These models, namely, Freundlich, Langmuir, Temkin, and Dubinin–Radushkevich (D–R), offer valuable insights into the interactions between alizarin red S molecules and the adsorbent surface.

The Freundlich isotherm:

$$logqe = \log k + \frac{1}{n} logCe. \tag{7}$$

The Langmuir isotherm:

$$\frac{1}{q_e} = \frac{1}{q_m K_L} + \frac{1}{q_m C_e}. \tag{8}$$

The Temkin isotherm:

$$q_e = \frac{RT}{b} ln\, K_T + \frac{RT}{b} ln\, C_e. \tag{9}$$

The D–R isotherm:

$$ln\, q_e = ln\, q_m - B\varepsilon^2 \tag{10}$$

and

$$\varepsilon^2 = RTln\left(1 + 1/C_e\right). \tag{11}$$

By fitting experimental data to these various adsorption isotherm models shown in Figure 8 and analyzing the resulting parameters, such as equilibrium constants, adsorption capacities, and energy of adsorption, we can elucidate the adsorption mechanism and understand how alizarin red S molecules interact with the surfaces of DS and DSMNC. These insights are crucial for optimizing adsorption processes and designing efficient adsorbents for wastewater treatment or other applications.

Figure 8A depicts the Freundlich isotherm (Equation 7) plot for the adsorption of ARS on DS and DSMNC. The slope of the curve is 1.412 for DS and 1.019 for DSMNC, while the intercept is −1.307 for DS and −0.203 for DSMNC. The R-squared (R^2) values for the adsorption of the dye on both adsorbents are notably high: 0.977 for DS and 0.94 for DSMNC. These high R^2 values indicate a strong fit of the data to the Freundlich isotherm model. The calculated values of

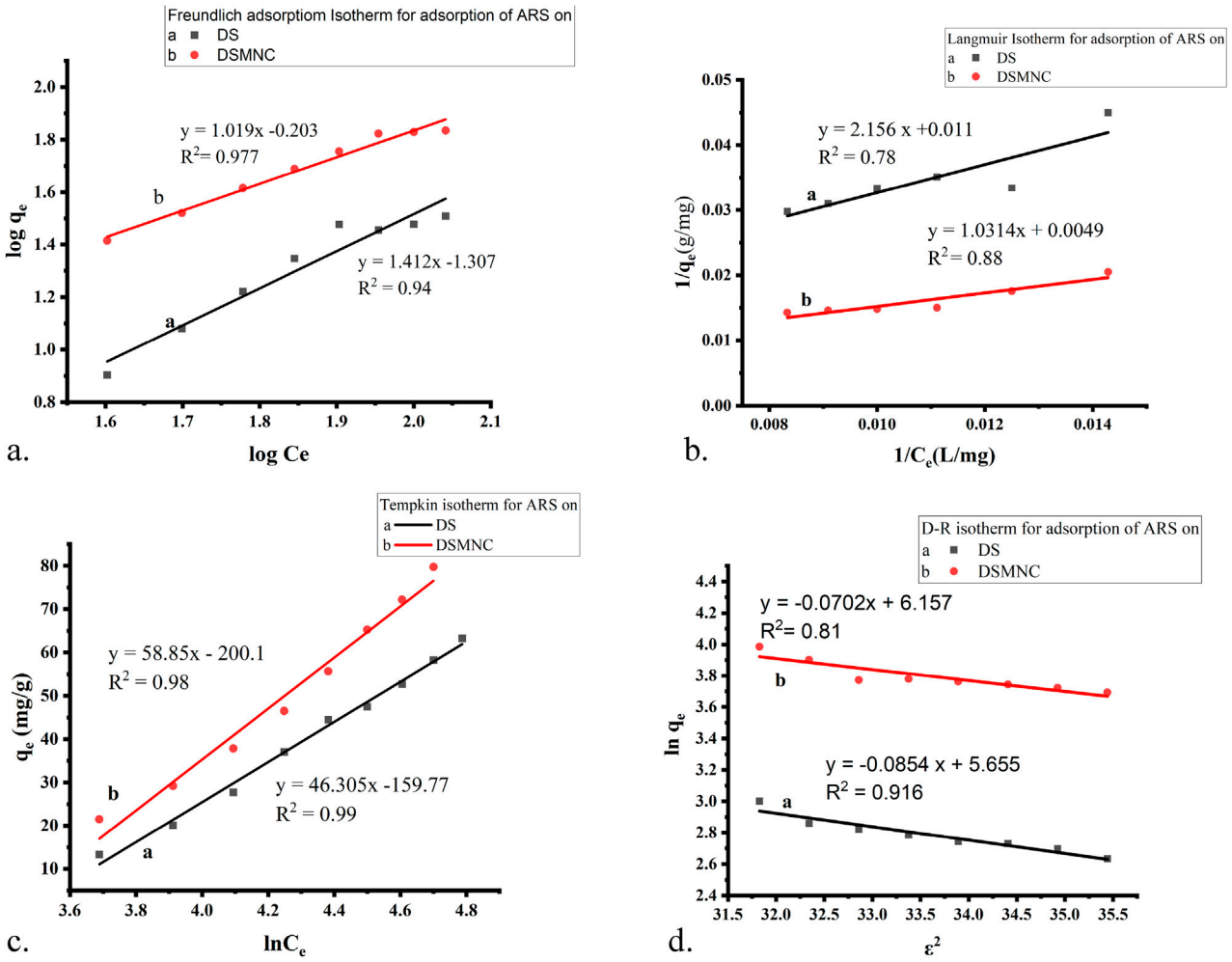

FIGURE 8
Adsorption isotherm models for the adsorption of ARS on DS and DSMNC: **(A)** Freundlich, **(B)** Langmuir, **(C)** Temkin, and **(D)** D–R adsorption isotherm.

the Freundlich isotherm parameters, n, and K_F, which characterize the adsorption behavior of ARS onto DS and DSMNC, are tabulated in Table 2 and provide insight into the affinity and capacity of the adsorbents for the dye.

Figure 8B illustrates a plot depicting the Langmuir adsorption isotherm (Equation 8), showcasing straight lines with slopes of 2.156 and 1.013, along with intercepts of 0.011 and 0.005 for DS and DSMNC, respectively. The corresponding R^2 values stand at 0.78 and 0.88 for the adsorption of ARS onto DS and DSMNC, respectively. Utilizing the slope values, the maximum monolayer capacity (q_m) is determined for DS and DSMNC. Notably, the monolayer capacity experiences a significant increase upon forming a nanocomposite of DS, attributable to the increased surface area resulting from particle size reduction, as confirmed by SEM analysis of the adsorbents. Langmuir constant (K_L) is computed from the curve intercept for DS and DSMNC. Table 2 showcases the calculated q_m and K_L values acquired from the slope and intercept.

Figure 8C illustrates a plot depicting the Temkin isotherm (Equation 9) for the adsorption of ARS on both DS and

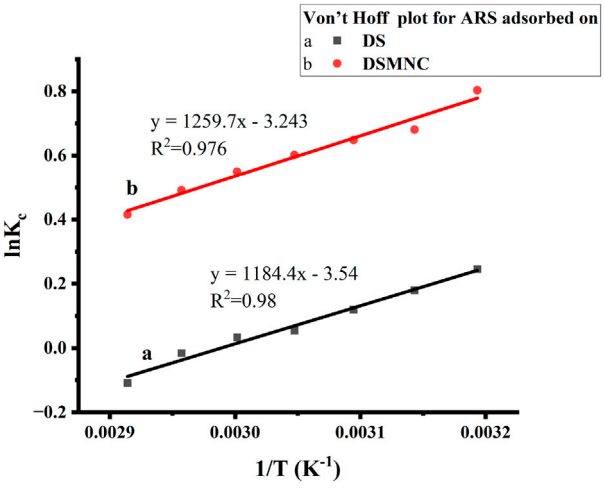

FIGURE 9
Thermodynamics study of adsorption of ARS on DS and DSMNC.

TABLE 1 Summary of kinetics parameters obtained.

Adsorbent used	PFO kinetics			PSO kinetics			Interparticle diffusion model		Liquid film model	
Parameter	R^2	$k_1 \times 10^{-2}$	q_e	R^2	$k_2 \times 10^{-2}$	q_e	R^2	k	R^2	K
DS	0.695	1.6	2.01	0.997	2.53	7.39	0.58	0.157	0.58	0.0102
DSMNC	0.81	1.19	3.16	0.97	4.64	21.55	0.84	0.253	0.81	0.0104

TABLE 2 Values of Langmuir, Freundlich, Temkin, and D–R adsorption isotherm constants for ARS adsorption on DS and DSMNC powder.

Adsorbent used	Freundlich isotherm			Langmuir isotherm			Temkin isotherm			D–R isotherm		
	K_F	n	R^2	q_m mg/g	K_L L/mg	R^2	K_T L/mol	b J/mol	R^2	q_{max} mol/g	E kJ/mol	R^2
DS	0.049	0.71	0.97	0.47	196	0.78	0.031	53.51	0.97	284	2.42	0.81
DSMNC	0.63	0.98	0.94	0.97	210	0.88	0.034	42.1	0.99	473	2.67	0.91

DSMNC; the slopes of the lines are determined to be 46.30 and 58.85, respectively. These slopes indicate that physical adsorption is dominant in both cases. The values of the intercepts obtained from the linear plots are −159.77 and −200.1 for adsorption onto the DS and DSMNC surfaces, respectively. The Temkin isotherm constant (pertaining to the heat of adsorption) and equilibrium binding constants (K_T) can be calculated from the value of slopes and intercepts. The calculated values of K_T for the adsorption of ARS on DS and DSMNC are summarized in Table 2.

These analyses demonstrate the applicability of the Temkin adsorption isotherm in describing the adsorption behavior of ARS onto both DS and DSMNC surfaces, with physical adsorption being the predominant mechanism (Dada et al., 2012).

The D–R isotherm (Equations 10, 11) is predominantly employed to determine the average adsorption-free energy (in kJ mol^{-1}). It provides insights into adsorption behavior, suggesting a physical nature when the value falls within the limit of 1–8 $kJ.mol^{-1}$ and a chemical nature when it resides between 8–16 $kJ.mol^{-1}$ (Dehghani et al., 2017). The R^2 values derived from the plots are 0.91 and 0.81 for the adsorption of ARS onto DS and DSMNC, respectively, indicating a close correlation between the experimental data and the D–R isotherm model.

The average free energy of adsorption (E) is computed by analyzing the obtained values of B from the slope, −0.0853 and −0.0702 for DS and DSMNC, respectively. The result indicates that the adsorption process for both adsorbents is physical in nature. The intercepts, having values of 5.65 and 6.16, are utilized to calculate q_m, the maximum adsorption capacity, for the adsorption of ARS on the surfaces of DS and DSMNC, respectively.

3.5 Adsorption thermodynamics study

Thermodynamic studies of dye biosorption are often conducted (using Equations 12–15) to ascertain the viability of the sorption process. Three key exploratory parameters are the standard entropy change (ΔS), the standard enthalpy change (ΔH), and the Gibbs free energy change (ΔG) (Bilal et al., 2022).

$$\Delta G = -RTlnK_c, \tag{12}$$

$$K_c = \frac{C_{ad}}{C_{after}}, \tag{13}$$

$$\Delta G = \Delta H - T\Delta S, \tag{14}$$

$$\ln K_c = \frac{\Delta S}{R} - \frac{\Delta H}{RT}. \tag{15}$$

Figure 9 depicts a thermodynamic study of the adsorption of alizarin red S on DS and DSMNC at various temperatures.

By plotting ln K_c against 1/T, a linear relationship (Equation 15) is observed, yielding slopes of 1,184.4 and 1,259.7, with intercepts of −3.54 and −3.25, respectively. The high values of R^2 (0.9834 and 0.9767) indicate an excellent correlation between the adsorption data (Elmorsi, 2011). From the slopes, ΔH is calculated to be −9.85 kJ/mol and −10.47 kJ/mol for the adsorption of alizarin red S on DS and DSMNC, respectively. The intercepts give the ΔS as −29.43 J/mol and −26.97 J/mol for DS and DSMNC, respectively. Equation 14 yields the values of ΔG energy as −1072 J/mol and −2427 J/mol for the adsorption of alizarin red S on DS and DSMNC, respectively. These calculations indicate that the process is physical adsorption, enthalpy-driven, and spontaneous (Ebelegi et al., 2020).

4 Conclusion

In the current investigation, we addressed the pressing environmental issue of non-biodegradable organic dyes by exploring the adsorption characteristics of ARS using DS and a DSMN composite. Batch adsorption experiments demonstrated a maximum removal efficiency of 76.63% for DS and 97.89% for DSMNC at 30°C, indicating favorable adsorption onto the heterogeneous surface of the composite. This adsorption process was facilitated by a combination of weak interactive forces. These outcomes suggest that

both DS and DSMNC are potent for the removal of the mutagenic dye, ARS, with DSMNC exhibiting higher removal efficiency.

Data availability statement

The datasets presented in this study can be found in online repositories. The names of the repository/repositories and accession number(s) can be found in the article/Supplementary Material.

Author contributions

SN: formal analysis, investigation, validation, writing–original draft, and writing–review and editing. SMS: supervision, writing–original draft and writing–review and editing. AA: funding acquisition, resources, and writing–review and editing. BA: data curation, investigation, validation, and writing–review and editing. SNS: formal analysis, software, and writing–review and editing. LUR: data curation, formal analysis, resources, and writing–review and editing.

Funding

The authors declare that financial support was received for the research, authorship, and/or publication of this article. Dr. Asad Ali thanks the financial support from Kempe Foundation (SMK21-0011, SMK21-0020) and Lulea university of technology, Sweden.

Conflict of interest

The authors declare that the research was conducted in the absence of any commercial or financial relationships that could be construed as a potential conflict of interest.

Publisher's note

Supplementary material

The Supplementary Material for this article can be found online at: https://www.frontiersin.org/articles/10.3389/fchem.2024.1457265/full#supplementary-material

References

Abualnaja, K. M., Alprol, A. E., Abu-Saied, M. A., Ashour, M., and Mansour, A. T. (2021). Removing of anionic dye from aqueous solutions by adsorption using of multiwalled carbon nanotubes and poly (Acrylonitrile-styrene) impregnated with activated carbon. *Sustainability* 13, 7077–7099. doi:10.3390/su13137077

Adegoke, K. A., and Bello, O. S. (2015). Dye sequestration using agricultural wastes as adsorbents. *Water Resour. Ind.* 12, 8–24. doi:10.1016/j.wri.2015.09.002

Ahmad, M., Bachmann, R. T., Khan, M. A., Edyvean, R. G., Farooq, U., and Athar, M. M. (2015). Dye removal using carbonized biomass, isotherm and kinetic studies. *Desalin. Water Treat.* 53, 2289–2298. doi:10.1080/19443994.2013.867818

Ali, I., Peng, C., Lin, D., Saroj, D. P., Naz, I., Khan, Z. M., et al. (2019). Encapsulated green magnetic nanoparticles for the removal of toxic Pb^{2+} and Cd^{2+} from water: development, characterization and application. *J. Environ. Manage.* 234, 273–289. doi:10.1016/j.jenvman.2018.12.112

Alkan, M., Demirbaş, O., and Doğan, M. (2007). Adsorption kinetics and thermodynamics of an anionic dye onto sepiolite. *Microporous Mesoporous Mater* 101, 388–396. doi:10.1016/j.micromeso.2006.12.007

Aragaw, T. A., and Bogale, F. M. (2021). Biomass-based adsorbents for removal of dyes from wastewater: a review. *Front. Environ. Sci.* 9, 764958–764981. doi:10.3389/fenvs.2021.764958

Bensalah, J., Idrissi, A., El Faydy, M., Doumane, G., Staoui, A., Hsissou, R., et al. (2023). Investigation of the cationic resin as a potential adsorbent to remove MR and CV dyes: kinetic, equilibrium isotherms studies and DFT calculations. *J. Mol. Struct.* 1278, 134849. doi:10.1016/j.molstruc.2022.134849

Bilal, M., Ihsanullah, I., Shah, M., Reddy, A. V. B., and Aminabhavi, T. M. (2022). Recent advances in the removal of dyes from wastewater using low-cost adsorbents. *J. Environ. Manag.* 321, 115981. doi:10.1016/j.jenvman.2022.115981

Chin, Y. P., Raof, S. F. A., Sinniah, S., Lee, V. S., Mohamad, S., and Manan, N. S. A. (2015). Inclusion complex of Alizarin Red S with β-cyclodextrin: synthesis, spectral, electrochemical and computational studies. *J. Mol. Struct.* 1083, 236–244. doi:10.1016/j.molstruc.2014.12.010

Chowdhury, S., Mishra, R., Saha, P., and Kushwaha, P. (2011). Adsorption thermodynamics, kinetics and isosteric heat of adsorption of malachite green onto chemically modified rice husk. *Desalination* 265, 159–168. doi:10.1016/j.desal.2010.07.047

Dada, A. O., Olalekan, A. P., Olatunya, A. M., and Dada, O. J. I. J. C. (2012). Langmuir, Freundlich, Temkin and Dubinin–Radushkevich isotherms studies of equilibrium sorption of Zn^{2+} unto phosphoric acid modified rice husk. *IOSR-JAC.* 3, 38–45. doi:10.9790/5736-0313845

Dehghani, M. H., Dehghan, A., and Najafpoor, A. (2017). Removing Reactive Red 120 and 196 using chitosan/zeolite composite from aqueous solutions: kinetics, isotherms, and process optimization. *J. Ind. Eng. Chem.* 51, 185–195. doi:10.1016/j.jiec.2017.03.001

Dehkhoda, A. M., Ellis, N., and Gyenge, E. (2014). Electrosorption on activated biochar: effect of thermo-chemical activation treatment on the electric double layer capacitance. *J. Appl. Electrochem.* 44, 141–157. doi:10.1007/s10800-013-0616-4

Delpiano, G. R., Tocco, D., Medda, L., Magner, E., and Salis, A. (2021). Adsorption of malachite green and alizarin red s dyes using fe-btc metal organic framework as adsorbent. *Int. J. Mol. Sci.* 22, 788–801. doi:10.3390/ijms22020788

Detpisuttitham, W., Phanthong, C., Ngamchana, S., Rijiravanich, P., and Surareungchai, W. (2020). Electrochemical detection of salicylic acid in pickled fruit/vegetable and juice. *J. Anal. Test.* 4, 291–297. doi:10.1007/s41664-020-00127-y

Ebelegi, A. N., Ayawei, N., and Wankasi, D. (2020). Interpretation of adsorption thermodynamics and kinetics. *Open J. Phys. Chem.* 10, 166–182. doi:10.4236/ojpc.2020.103010

Elmorsi, T. M. (2011). Equilibrium isotherms and kinetic studies of removal of methylene blue dye by adsorption onto miswak leaves as a natural adsorbent. *J. Environ. Prot.* 2, 817–827. doi:10.4236/jep.2011.26093

Elzahar, M. M., and Bassyouni, M. (2023). Removal of direct dyes from wastewater using chitosan and polyacrylamide blends. *Sci. Rep.* 13, 15750–15765. doi:10.1038/s41598-023-42960-y

Fayazi, M., Ghanei-Motlagh, M., and Taher, M. A. (2015). The adsorption of basic dye (Alizarin red S) from aqueous solution onto activated carbon/γ-Fe_2O_3 nano-composite: kinetic and equilibrium studies. *Mater. Sci. Semicond. Process* 40, 35–43. doi:10.1016/j.mssp.2015.06.044

Gautam, P. K., Gautam, R. K., Banerjee, S., Chattopadhyaya, M. C., and Pandey, J. D. (2017). Adsorptive removal of alizarin red S by a novel biosorbent of an invasive weed Mikania micrantha. *Natl. Acad. Sci. Lett.* 40, 113–116. doi:10.1007/s40009-017-0540-y

Gautam, P. K., Shivapriya, P. M., Banerjee, S., Sahoo, A. K., and Samanta, S. K. (2020). Biogenic fabrication of iron nanoadsorbents from mixed waste biomass for aqueous phase removal of alizarin red S and tartrazine: kinetics, isotherm, and thermodynamic investigation. *Environ. Prog. Sustain. Energy* 39, 13326–13338. doi:10.1002/ep13326

Gholivand, M. B., Yamini, Y., Dayeni, M., Seidi, S., and Tahmasebi, E. (2015). Adsorptive removal of alizarin red-S and alizarin yellow GG from aqueous solutions using polypyrrole-coated magnetic nanoparticles. *J. Environ. Chem. Eng.* 3, 529–540. doi:10.1016/j.jece.2015.01.011

Gul, A., Muhammad, S., Nawaz, S., Munir, S., Rehman, K. U., Ahmadm, S., et al. (2021). Ficus religiosa bark an efficient adsorbent for Alizarin Red S dye: equilibrium and kinetic analysis. *J. Iran. Chem. Soc.* 19, 1737–1746. doi:10.1007/s13738-021-02413-7

Hasani, N., Selimi, T., Mele, A., Thaçi, V., Halili, J., Berisha, A., et al. (2022). Theoretical, equilibrium, kinetics and thermodynamic investigations of methylene blue adsorption onto lignite coal. *Molecules* 27, 1856–1874. doi:10.3390/molecules27061856

Hu, S., Yuan, D., Liu, Y., Zhao, L., Guo, H., Niu, Q., et al. (2019). The toxic effects of alizarin red S on catalase at the molecular level. *Rsc. Adv.* 9, 33368–33377. doi:10.1039/c9ra02986a

Hubbe, M. A., Azizian, S., and Douven, S. (2019). Implications of apparent pseudo-second-order adsorption kinetics onto cellulosic materials: a review. *Bioresour* 14, 7582–7626. doi:10.15376/biores.14.3.7582-7626

Ibrahim, S. M., Badawy, A. A., and Essawy, A. (2019). Improvement of dyes removal from aqueous solution by Nanosized cobalt ferrite treated with humic acid during coprecipitation. *J. Nanostructure Chem.* 9, 281–298. doi:10.1007/s40097-019-00318-9

Jawad, A. H., Hum, N. N. M. F., Farhanand, A. M., and Mastuli, M. S. (2020). Biosorption of methylene blue dye by rice (*Oryza sativa* L.) straw: adsorption and mechanism study. *Desalin. Water Treat.* 190, 322–330. doi:10.5004/dwt.2020.25644

Jebli, A., El Amri, A., Hsissou, R., Lebkiri, A., Zarrik, B., Bouhassane, F. Z., et al. (2023). Synthesis of a chitosan@ hydroxyapatite composite hybrid using a new approach for high-performance removal of crystal violet dye in aqueous solution, equilibrium isotherms and process optimization. *J. Taiwan Inst. Chem. Eng.* 149, 105006. doi:10.1016/j.jtice.2023.105006

Kadiri, L., Ouass, A., Hsissou, R., Safi, Z., Wazzan, N., Essaadaoui, Y., et al. (2021). Adsorption properties of coriander seeds: spectroscopic kinetic thermodynamic and computational approaches. *J. Mol. Liq.* 343, 116971. doi:10.1016/j.molliq.2021.116971

Kainth, S., Sharma, P., and Pandey, O. P. (2024). Green sorbents from agricultural wastes: a review of sustainable adsorption materials. *Appl. Surf. Sci. Adv.* 19, 100562–100582. doi:10.1016/j.apsadv.2023.100562

Kamarehie, B., Jafari, A., Ghaderpoori, M., Karami, M. A., Mousavi, K., and Ghaderpoury, A. (2019). Catalytic ozonation process using PAC/γ-Fe_2O_3 to alizarin red S degradation from aqueous solutions: a batch study. *Chem. Eng. Commun.* 206, 898–908. doi:10.1080/00986445.2018.1537266

Khalaf, I. H., Al-Sudani, F. T., AbdulRazak, A. A., Aldahri, T., and Rohani, S. (2021). Optimization of Congo red dye adsorption from wastewater by a modified commercial zeolite catalyst using response surface modeling approach. *Water Sci. Technol.* 83, 1369–1383. doi:10.2166/wst.2021.078

Kumar, A., Singh, R., Upadhyay, S. K., Kumar, S., and Charaya, M. U. (2021). Biosorption: the removal of toxic dyes from industrial effluent using phytobiomass-A review. *Plant Arch.* 21, 1320–1325. doi:10.51470/PLANTARCHIVES.2021.v21.S1.207

Kuśmierek, K., and Świątkowski, A. (2015). The influence of different agitation techniques on the adsorption kinetics of 4-chlorophenol on granular activated carbon. *React. Kinet. Mech. Catal.* 116, 261–271. doi:10.1007/s11144-015-0889-1

Lebkiri, I., Abbou, B., Hsissou, R., Safi, Z., Sadiku, M., Berisha, A., et al. (2023). Investigation of the anionic polyacrylamide as a potential adsorbent of crystal violet dye from aqueous solution: equilibrium, kinetic, thermodynamic, DFT, MC and MD approaches. *J. Mol. Liq.* 372, 121220. doi:10.1016/j.molliq.2023.121220

Mahmoodi, N. M., Taghizadeh, M., Taghizadeh, A., Abdi, J., Hayati, B., and Shekarchi, A. A. (2019). Bio-based magnetic metal-organic framework nanocomposite: ultrasound-assisted synthesis and pollutant (heavy metal and dye) removal from aqueous media. *Appl. Surf. Sci.* 480, 288–299. doi:10.1016/j.apsusc.2019.02.211

Malik, A., Khan, A., Anwar, N., and Naeem, M. (2020). A comparative study of the adsorption of Congo red dye on rice husk, rice husk char and chemically modified rice husk char from aqueous media. *Bull. Chem. Soc. Ethiop.* 34, 41–54. doi:10.4314/bcse.v34i1.4

Murthy, T. K., Gowrishankar, B. S., Krishna, R. H., Chandraprabha, M. N., and Mathew, B. B. (2020). Magnetic modification of coffee husk hydrochar for adsorptive removal of methylene blue: isotherms, kinetics and thermodynamic studies. *J. Environ. Chem. Ecotoxicol.* 2, 205–212. doi:10.1016/j.enceco.2020.10.002

Nistor, M. A., Muntean, S. G., Ianos, R., Racoviceanu, R., Ianași, C., and Cseh, L. (2021). Adsorption of anionic dyes from wastewater onto magnetic nanocomposite powders synthesized by combustion method. *Appl. Sci.* 11, 9236–9255. doi:10.3390/app11199236

Oroujizad, S., Kashi, M. A., and Montazer, A. H. (2023). Fine-tuning magnetic and hyperthermia properties of magnetite (Fe_3O_4) nanoparticles by using ammonia as a reducing agent. *Phys. B Condens. Matter* 671, 415393. doi:10.1016/j.physb.2023.415393

Oyekanmi, A. A., Ahmad, A., Mohd Setapar, S. H., Alshammari, M. B., Jawaid, M., Hanafiah, M. M., et al. (2021). Sustainable durio zibethinus-derived biosorbents for Congo red removal from aqueous solution: statistical optimization, isotherms and mechanism studies. *Sustainability* 13, 13264–13282. doi:10.3390/su132313264

Pal, K., Banthia, A. K., and Majumdar, D. K. (2007). Preparation and characterization of polyvinyl alcohol-gelatin hydrogel membranes for biomedical applications. *Aaps Pharmscitech* 8, E142–E146. doi:10.1208/pt080121

Pirkarami, A., and Olya, M. E. (2017). Removal of dye from industrial wastewater with an emphasis on improving economic efficiency and degradation mechanism. *J. Saudi Chem. Soc.* 21, S179–S186. doi:10.1016/j.jscs.2013.12.008

Rao, V. D., and Ramanaiah, M. (2024). Magnetic activated carbon: a promising approach for the removal of methylene blue from wastewater. *Desalin. Water Treat.* 317, 100146–100156. doi:10.1016/j.dwt.2024.100146

Saha, T. K., Bhoumik, N. C., Karmaker, S., Ahmed, M. G., Ichikawa, H., and Fukumori, Y. (2011). Adsorption characteristics of reactive black 5 from aqueous solution onto chitosan. *Clean–Soil, Air, Water* 39, 984–993. doi:10.1002/clen.201000315

Salari, M. (2022). Optimization by box–Behnken design and synthesis of magnetite nanoparticles for removal of the antibiotic from an aqueous phase. *Adsorpt. Sci. Technol.* 2022, 1–13. doi:10.1155/2022/1267460

Sen, T. K., Afroze, S., and Ang, H. M. (2011). Equilibrium, kinetics and mechanism of removal of methylene blue from aqueous solution by adsorption onto pinecone biomass of pinus radiata. *Wat. Air Soil Poll* 218, 499–515. doi:10.1007/s11270-010-0663-y

Sowjanya, B., Sirisha, U., Juttuka, A. S., Matla, S., King, P., and Vangalapati, M. (2022). Synthesis and characterization of zinc oxide nanoparticles: it's application for the removal of alizarin red S dye. *Mater. Today Proc.* 62, 3968–3972. doi:10.1016/j.matpr.2022.04.576

Sultana, S., Rehan, K., Rehan, I., Arellano, M. C., Farqad, R. O., Shaghnab, M. L., et al. (2023). Nano-clay modified multi-walled carbon nanotube composite as a potential adsorbent towards Eriochrome Black T: a comparative study of isotherm and kinetic models. *Desalin. Water Treat.* 314, 251–262. doi:10.5004/dwt.2023.30103

Wong, S., Ghafar, N. A., Ngadi, N., Razmi, F. A., Inuwa, I. M., Mat, R., et al. (2020). Effective removal of anionic textile dyes using adsorbent synthesized from coffee waste. *Sci. Rep.* 10, 2928–2940. doi:10.1038/s41598-020-60021-6

Yagub, M. T., Sen, T. K., Afroze, S., and Ang, H. M. (2014). Dye and its removal from aqueous solution by adsorption: a review. *Adv. Colloid Interface Sci.* 209, 172–184. doi:10.1016/j.cis.2014.04.002

Zare, K., Gupta, V. K., Moradi, O., Makhlouf, S. H., Sillanpää, M., Nadagouda, M. N., et al. (2015). A comparative study on the basis of adsorption capacity between CNTs and activated carbon as adsorbents for removal of noxious synthetic dyes: a review. *J. Nanostructure Chem.* 5, 227–236. doi:10.1007/s40097-015-0158-x

Zhou, Y., Lu, J., Zhou, Y., and Liu, Y. (2019). Recent advances for dyes removal using novel adsorbents: a review. *Environ. Pollut.* 252, 352–365. doi:10.1016/j.envpol.2019.05.072

frontiers | Frontiers in Chemistry

TYPE Mini Review
PUBLISHED 03 October 2024
DOI 10.3389/fchem.2024.1472284

OPEN ACCESS

EDITED BY
Bin Mu,
Chinese Academy of Sciences (CAS), China

REVIEWED BY
Dimitrios Papoulis,
University of Patras, Greece
Yanfu Wei,
Macau University of Science and Technology, Macao SAR, China

*CORRESPONDENCE
Jong Seto,
jong.seto@asu.edu
Emir Islamovic,
emir.islamovic@basf.com
Carlos Lizandara-Pueyo,
carlos.lizandara@basf.com

RECEIVED 23 August 2024
ACCEPTED 23 September 2024
PUBLISHED 03 October 2024

CITATION
Comes J, Islamovic E, Lizandara-Pueyo C and Seto J (2024) Improvements in the utilization of calcium carbonate in promoting sustainability and environmental health.
Front. Chem. 12:1472284.
doi: 10.3389/fchem.2024.1472284

Improvements in the utilization of calcium carbonate in promoting sustainability and environmental health

Jackson Comes[1], Emir Islamovic[2]*, Carlos Lizandara-Pueyo[3]* and Jong Seto[1,4]*

[1]School for the Engineering of Matter, Transport, and Energy, Center for Biological Physics, Arizona State University, Tempe, AZ, United States, [2]BASF Corporation, Raleigh, NC, United States, [3]BASF SE, Ludwigshafen, Germany, [4]Molecular Foundry, Lawrence Berkeley National Laboratory, Berkeley, CA, United States

Calcium carbonate ($CaCO_3$) is an incredibly abundant mineral on Earth, with over 90% of it being found in the lithosphere. To address the CO_2 crisis and combat ocean acidification, it is essential to produce more $CaCO_3$ using various synthetic methods. Additionally, this approach can serve as a substitute for energy-intensive processes like cement production. By doing so, we have the potential to not only reverse the damage caused by climate change but also protect biological ecosystems and the overall environment. The key lies in maximizing the utilization of $CaCO_3$ in various human activities, paving the way for a more sustainable future for our planet.

KEYWORDS

calcium carbonate, catalysis, carbon capture, agriculture, inorganic materials chemistry

Introduction

The significance of inorganic materials in the chemical industry cannot be overstated. These materials, derived from non-carbon-based compounds, play a foundational role in various processes, applications, and innovations (Gągol et al., 2020; Industrial inorganic chemistry, 2010; Wang and Wang, 2021; Wang et al., 2022; Waris et al., 2021) (Figure 1). As we navigate an era emphasizing sustainability, the importance of inorganic materials in fostering sustainable chemistry becomes increasingly apparent (Huang and Zhai, 2021; Lima et al., 2020; Van Soest et al., 2021). Inorganic materials serve as essential building blocks for countless chemical products, ranging from catalysts and reagents to structural components (Clark and Rhodes, 2000; Furukawa and Komatsu, 2017; Mitzi, 2009; Osterloh, 2008; Schubert and Hüsing, 2019; Song and Lee, 2002; Zheng et al., 2022). Their versatility extends into diverse sectors such as electronics, pharmaceuticals, energy, technology and materials science (Al Zoubi and Ko, 2020; Avouris and Martel, 2010; Boles et al., 2016; Chen and Park, 2018; Chen et al., 2015; Ebadi Jamkhaneh et al., 2021; Fadia et al., 2021; Fan et al., 2021; Moon et al., 2007; Niemeyer, 2001; Qi et al., 2020; Servin and White, 2016; Sun and Rogers, 2007; Vallet-Regí et al., 2007).

Crucially, in the context of sustainable chemistry, inorganic materials contribute to environmentally conscious practices (Caballero-Calero et al., 2021; Mazari et al., 2021; Nelson and Schelter, 2019; Pham et al., 2020). Their role in catalysts (Boles et al., 2016; K.-G; Liu et al., 2021; Shen et al., 2020) and processes designed for cleaner and more energy-efficient production and applications (Kitchen et al., 2014; Zheng et al., 2022) exemplifies their

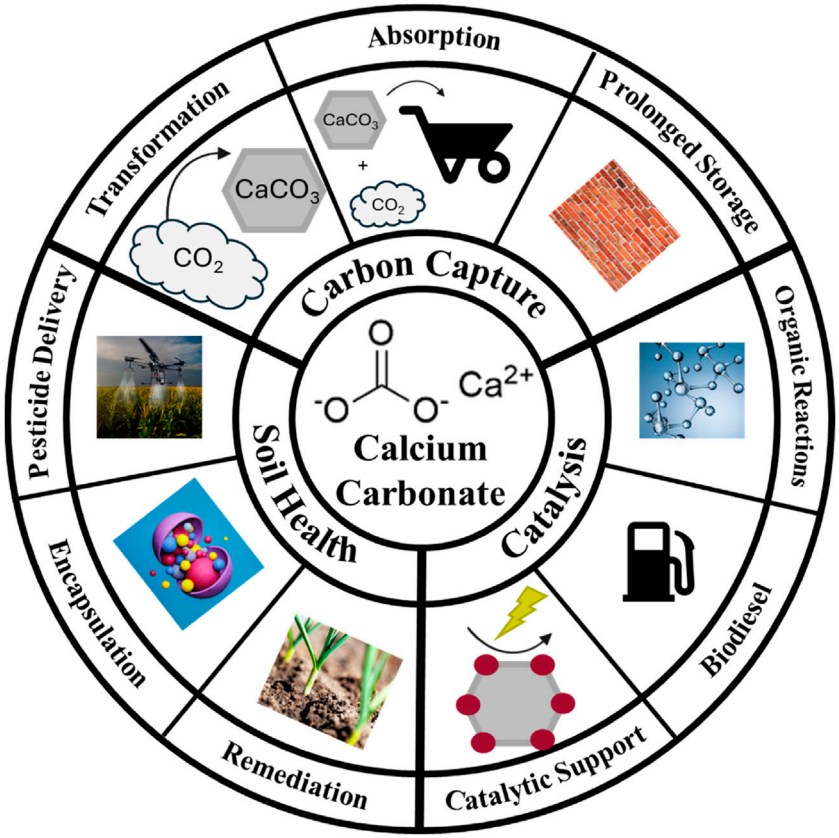

FIGURE 1
Schematic representation of current uses of calcium carbonate discussed in this mini review.

significance. Additionally, their use in energy storage (Cheng et al., 2021; Junaid et al., 2021; Liu et al., 2020; Piątek et al., 2021), renewable energy technologies (Chandrasekaran et al., 2011; Liang et al., 2017), and waste treatment (Goh and Ismail, 2018; Kayvani Fard et al., 2018; Manikandan et al., 2022; Xiang et al., 2022) underscores their pivotal role in addressing global sustainability challenges.

Calcium carbonate serves as a versatile reagent in inorganic chemistry, contributing to various reactions and processes (Al-Hosney and Grassian, 2004; Baltrusaitis et al., 2007; Lin et al., 2020; Salek et al., 2015; Suppes et al., 2001). Moreover, its unique properties such as its porous structure and high surface area (Durand et al., 2018), make it a suitable substrate for anchoring catalytically active components (García-Mota et al., 2011; Liu et al., 2013; Saetan et al., 2017; Schlägl et al., 1987). Calcium carbonate plays a role in the production of biodiesel, catalyzing transesterification of natural oils (Alonso et al., 2010; Chutia and Phukan, 2024; Kouzu et al., 2008; Ling et al., 2019; X; Liu et al., 2021; Ngamcharussrivichai et al., 2010; Suppes et al., 2001; Thangaraj et al., 2019). Calcium carbonate is employed in carbon capture applications as a sorbent for CO_2 removal (Dou et al., 2016; Erans et al., 2016; Florin et al., 2010; Liu et al., 2010; Witoon, 2011). In a process called mineral carbonation, it reacts with carbon dioxide to form stable carbonates, contributing to carbon capture and storage efforts (Abanades, 2002; Bewernitz et al., 2024; Erans et al., 2020; Gadikota, 2021; Gambhir and Tavoni, 2019; Levey et al., 2024; Olajire, 2013; Sanna et al., 2014; Sanz-Pérez et al., 2016). Like in biological materials, various mineral phases of $CaCO_3$ can be processed to obtain customized chemical reactivity and functionality (Briegel and Seto, 2012; Cho et al., 2019; Seto et al., 2014; 2013). This method aids in mitigating greenhouse gas emissions and addresses climate change concerns (Neeraj and Yadav, 2020; Snæbjörnsdóttir et al., 2020; Thonemann et al., 2022). Understanding these diverse properties unveils calcium carbonate's significance in addressing environmental concerns.

This material emerges as a linchpin for fostering robust soil health, vibrant plant growth, and bountiful crop yields (Hamdan et al., 2017; Soon et al., 2014; Wang et al., 2015; Xie et al., 2024). From soil pH adjustment in acidic terrains (Neina, 2019) to serving as a vital calcium supplement for plants (Shabtai et al., 2023), calcium carbonate's agricultural significance is underscored by its ability to rectify deficiencies that may impede the optimal development of crops. Furthermore, its impact extends beneath the surface, where it actively participates in enhancing soil structure (Dou et al., 2023). By promoting aggregation, calcium carbonate facilitates improved water retention and drainage, creating an environment conducive to the flourishing of roots (Figure 1).

As an additive in fertilizers, it takes on the role of a nourishing component, supplying essential calcium that supports the formation of robust cell walls and overall plant structure (Abo-Sedera, 2016; Hua et al., 2015). Acting as a buffering agent, calcium carbonate becomes a guardian of soil pH stability, curbing rapid fluctuations that could detrimentally affect plant health (McFarland et al., 2020; Zhang et al., 2016). Beyond the crop fields, its practical application

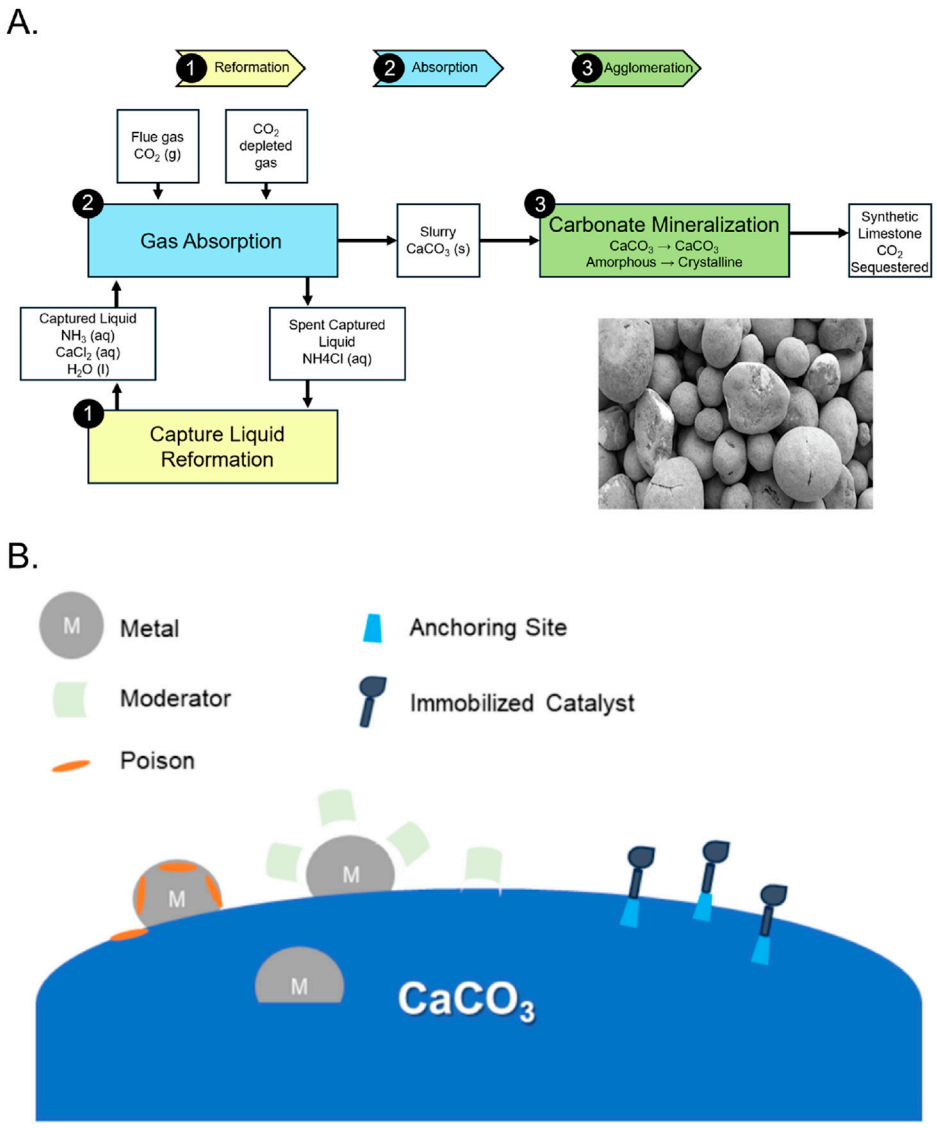

FIGURE 2
Diverse methods of utilizing $CaCO_3$ at various length-scales. **(A)** By utilizing a biogeomimetic mineralization route, recycled geomass can be harvested to make tonnes of aggregates. [inset: $CaCO_3$ aggregates formed] (images courtesy of Blue Planet Systems, Inc). **(B)** $CaCO_3$ can serve as catalysts with specific functional groups to enhance the formation of chemical feedstocks. (conceptual graph inspired by, among others, Lindlar and Dubuis, 2003; Senra et al., 2008; Lizandara-Pueyo et al., 2021).

even extends to dust control in agricultural settings, where it contributes to creating a more comfortable environment, particularly in livestock farming (Hamdan and Kavazanjian, 2016; Meyer et al., 2011; Song et al., 2020). In essence, the diverse applications of calcium carbonate in agriculture stand as a testament to its integral role in promoting soil fertility, sustaining healthy plant growth, and ultimately cultivating agricultural landscapes that thrive (Figure 1).

$CaCO_3$ in carbon capture and mineralization applications

Carbon capture, utilization, and storage (CCUS) technologies aim to decrease the greenhouse gas effect by capturing emitted carbon and transforming it for long term storage or chemical utility (Chang et al., 2017). Industrial mineralization of carbon dioxide to produce calcium carbonate is a promising CCUS method with high economic potential (Chang et al., 2017; Teir et al., 2016). These reaction pathways valorize waste streams from processes such as steelmaking and cement production while reducing energy consumption (Jin et al., 2022; Katsuyama et al., 2005; Marin Rivera and Van Gerven, 2020; Teir et al., 2016). By utilizing chemicals in waste flue gas, steelmaking slag and cement powder, calcium carbonate production provides a green alternative to disposal and storage of carbon dioxide (Czaplicka and Konopacka-Łyskawa, 2020; Teir et al., 2016) (Figure 2). There are many methods to precipitate calcium carbonate from CO_2 streams such as microbially induced precipitation, ultrasonication of supercritical carbon dioxide, and other methods, most of which

TABLE 1 Publications related to calcium carbonate sustainability arranged by year.

Application	Topic	Scope	Year published	Author(s)
Carbon capture	Transformation	Carbonation	2002	Abanades, J.C
		Sorbent	2010	FlorinN.H.
		Sorbent	2010	Liu, W. et al
		Sorbent	2019	Gambhir, A
		MICP	2020	Chuo, S.C. et al
		Carbonation	2020	Czaplicka, N. et al
		Carbonation	2020	Yadav, S
		Mineralization	2020	Marin Rivera, R. et al
		Mineralization	2021	Gadikota, G
		Chemical looping	2022	Jin, Z. et al
		Liquid condensed phase	2024	Bewernitz, M.A. et al
	Absorption	Biomineralization	2013	Dhami, N.K et al
		Sorbent	2016	Erans, M
		Carbonation	2016	Sanz-Pérez, E.S. et al
		Sorbent	2020	Erans, M
	Prolonged storage	Scale up	2011	HerzogH.J.
		Carbonation	2017	Chang, R. et al
		Carbonation	2020	Snæbjörnsdóttir, S.Ó. et al
		Carbonation	2021	Campo, F.P et al
		Cement	2021	Hargis, C.W. et al
		Cement	2023	Hanifa, M. et al
		Cement	2024	Levey, C. et al
Catalysis	Biodiesel	Transesterification	2008	Kouzu, M. et al
		Transesterification	2010	Alonso, D.M. et al
		Transesterification	2010	Ngamcharussrivichai, C. et al
		Transesterification	2010	Liu, X. et al
		Transesterification	2024	Chutia, G.P. et al
	Catalytic support	Selective hydrogenation	1987	Schlägl, R. et al
		Selective hydrogenation	2008	Senra, J.D. et al
		Selective hydrogenation	2011	García-Mota, M. et al
		Cross coupling reactions	2013	Liu, H. et al
		Cross coupling reactions	2017	Saetan, T. et al
		Selective hydrogenation	2020	Laverdura, U.P. et al
		Asymmetric Michael addition	2021	Lizandara-Pueyo, C. et al
		Selective hydrogenation	2022	Ballesteros-Soberanas, J. et al
	Organic reactions	Alcoholysis	2001	Suppes, G.J. et al
		Intermediate surface reactions	2004	Al-Hosney, H.A. et al
		Sulfur dioxide reactions	2007	Baltrusaitis, J. et al

(Continued on following page)

TABLE 1 (*Continued*) Publications related to calcium carbonate sustainability arranged by year.

Application	Topic	Scope	Year published	Author(s)
Soil health	Pesticide delivery	Nanoparticles	2018	Zhao, X. et al
		Fungicide	2022	Zhou, Z. et al
		Sporopollenin	2023	Xiang, S. et al
	Encapsulation	Sunflower pollen	2016	Mundargi, R.C. et al
		Slow release	2023	Abhiram, G. et al
	Remediation	Pond soil	2004	Queiroz, J.F.D. et al
		MICP	2011	Meyer, F.D. et al
		MICP	2014	Soon, N.W. et al
		MICP	2020	Song, J.Y. et al
		pH control	2015	Salek, S. et al
		pH control	2016	Juang, Y. et al
		pH control	2018	Gentili, R. et al
		pH control	2020	McFarland, C. et al
		Foliar spray	2016	Abo-Sedera, F
		Dust control	2016	Hamdan, N. et al
		Denitrification	2017	Hamdan, N. et al
		Improved tomato yield	2018	Patanè, C. et al
		Metal remediation	2019	Bashir, M.A. et al
		Metal remediation	2020	Lin, P.-Y. et al
		Cauliflower development	2020	Santos, C.A.D. et al
		Carbon regulation	2023	Dou, X. et al
		Improved wheat yield	2023	Gao, Y. et al
		Pathogen elimination	2023	Liu, Q. et al

*MICP, microbially induced calcium carbonate precipitation.

are based on biomimetics or CO_2 bubbling (Boyjoo et al., 2014; Chuo et al., 2020; López-Periago et al., 2010). When using sorbent technology, a compromise must be made between sorbent performance and the increasing cost (Erans et al., 2016). Modified materials and advanced chemical reactors increase sorbent utility, but can be vastly more expensive than their simpler counterparts. Also, the activity of sorbents decay over time due to sintering and attrition, further limiting utility (Erans et al., 2016).

In recent years, chemical looping and mineralization has been gaining attention as a promising CCSU technology, with publications such as those from Jin, Z. et al. and Bewernitz, M.A. et al. (Table 1). $CaCO_3$ aggregates can be used to replace cementitious products (Hargis et al., 2021; Pu et al., 2021). Through an exponential increase in the built environment, cement production has become an ever-increasing source of CO_2 and dust pollution. It approximately accounts for 8% of the anthropogenic CO_2 produced per year and is a process with very little technical improvement since its utilization from Roman times (Stefaniuk et al., 2023). Only through recent advances like replacements with clinker as well as new formulations with lower energy substitutes (Martinez et al., 2023) as well as aggregates (Hanifa et al., 2023). can we envision a world with more infrastructure, but without the pollution attached to building it (Figure 2).

It is indisputable that the indiscriminate emissions of greenhouse gas have resulted in increased surface temperature on Earth and environmental degradation (Yoro and Daramola, 2020). Given the tremendous amount of CO_2 in Earth's atmosphere, CCUS technology would have to make gigaton-scale changes to have a meaningful impact on the global scale (Figure 3). Through reduction of emissions and increasing global CCUS usage, humanity has been trying to reduce the impact of climate change caused by anthropogenic CO_2 emissions (Dey and Dhal, 2019; Huisingh et al., 2015; Sanna et al., 2014).

The relationship between average surface temperature and CO_2 concentration is directly proportional (Humlum et al., 2013). Ice core records indicate that CO_2 concentration has varied with temperature over long time scales for the past 420,000 years or even longer (Humlum et al., 2013; Lüthi et al., 2008). Also, it is suggested that rising atmospheric CO_2 levels amplify or even precede global temperature changes initiated by Milankovitch

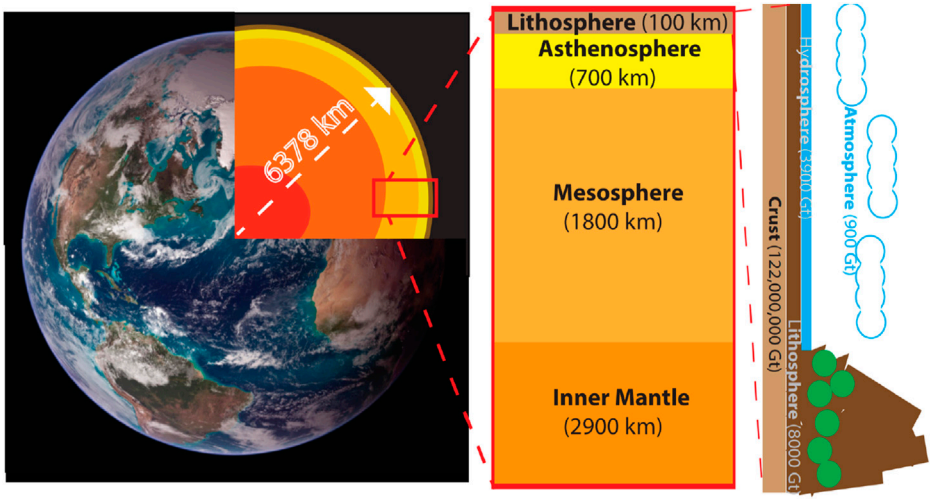

FIGURE 3
The geological composition of the Earth **(A)**. The various segments from the core to the surface of the planet **(B)**. The diverse composition of the Earth's mantle **(C)**. The majority of carbon (in the form of carbonates and CO_2) stored in the diverse surface layers of Earth (image courtesy of NASA).

cycles (Humlum et al., 2013; Shakun et al., 2012; Toggweiler and Lea, 2010). With these facts in mind, data from the National Center for Environmental Information (NOAA National Centers for Environmental Information, 2024; U.S. Global Change Research Program et al., 2017) was plotted and regression was performed to derive Equation 1, describing the relationship between global average surface temperature (as compared to the 1901–200 average), time, and atmospheric CO_2 concentration.

$$T = (1 - \alpha \times t)\left(3.5 \times 10^{-26}\right) exp\,(0.029 \times t) \quad (1)$$

The factor $(1 - \alpha \times t)$ in Equation 1 accounts for humanity's intervention and efforts to halt the rising global temperatures. The variable α is proportional to the amount of CO_2 being captured and removed from the atmosphere. With a higher amount of CCS technology used globally, α would increase proportionally. If no changes are made to humanity's current emission rates, $(1 - \alpha \times t) = 1$, and the current trend is expected to continue, increasing surface temperatures and further harming global ecosystems (Ainsworth et al., 2020; Karnosky, 2003; Moore et al., 2021; Prakash, 2021; U.S. Global Change Research Program et al., 2017). Improving CCS technology has the potential to slow this temperature increase, but not enough to see impactful differences at current rates (Davis, 2017). Even if carbon dioxide emission was completely halted, and all emitted CO_2 were captured and stored, the Earth's temperature is expected to remain the same or continue increasing at a very slow rate for centuries (Frölicher et al., 2014). Such a carbon neutral state can only be accomplished through radical improvements to CCS technologies, and drastically decreasing reliance on fossil fuels (Budinis et al., 2018; Stone et al., 2009). CCS technology will only become a reasonable solution to rising surface temperatures through sequestering billions of metric tons (gigatons) of carbon dioxide per year (Herzog, 2011; Valone, 2023) (Figure 4).

Given Earth's tremendously large surface area, and high water content, it takes an enormous amount of energy to raise the average surface temperature even by a small amount. Though 1°C may seem like an insignificant change, the global effects are drastic due to the tremendous amount of trapped heat (Lindsey and Dahlman, 2024; NOAA National Centers for Environmental Information, 2024; U.S. Global Change Research Program et al., 2017). If dramatic industrial and legal changes are not made, the disastrous effects may be irreversible (Armstrong McKay et al., 2022; Ridley et al., 2010).

$CaCO_3$ in chemical catalysis

One of the most relevant processes in the chemical industry is the selective partial hydrogenation of alkynes to alkenes; this transformation is usually enabled by the Lindlar Catalyst (Lindlar and Dubuis, 2003). The use of calcium carbonate in the Lindlar Catalyst dates back to the 1980s when authors such as Schlägl, R. et al. released publications detailing its structure and activity (Table 1). This catalyst is based on palladium supported on calcium carbonate and passivated with lead acetate and quinoline. This catalytic system has a broad application in natural product synthesis (Ballesteros-Soberanas et al., 2022) or in the upgrading of vegetable oils (Laverdura et al., 2020). This catalyst allows the reaction to be performed at high temperatures (200°C), increasing conversion rates while simultaneously increasing the cost required to run such a system (Suppes et al., 2001). The versatility and inertness of calcium carbonate as support, allows the fine tuning of the surfaces. Accordingly, an efficient and selective catalytic system using hydroxypropylated cyclodextrins and palladium on calcium carbonate has been presented by Senra et al. (2008) for a ligand-free aqueous Heck reactions. In this case, the catalyst was not only active and selective but also immobilized. Most recently, calcium carbonate has been used as a support for the immobilization of asymmetric catalysts using biomineralization concepts and click chemistry. A calcium

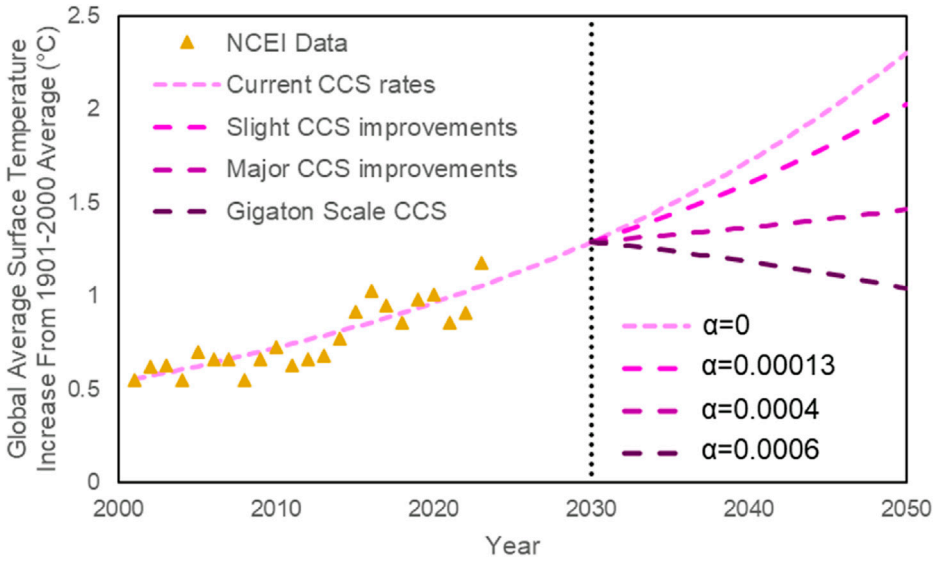

FIGURE 4
Global average surface temperature increase from 1901 to 2000 average based on data from the National Centers for Environmental Information (triangles) (NOAA National Centers for Environmental information, 2024).

carbonate-supported α,α-diarylprolinol silyl ether prepared in this manner catalyzed Michael addition of aldehydes to trans-β-nitrostyrenes with very high diastereo- and enantioselectivity. By utilizing calcium carbonate as a heterogenous support, organocatalysis can be immobilized which reduces the cost and energy requirement of downstream separations (Lizandara-Pueyo et al., 2021). Additionally, this method allows for the used organocatalysis to be recycled and reused (Benaglia, 2009) (Figure 2). The catalyst can be recovered for reuse by simple decantation or used in a continuous flow reactor, increasing productivity five-fold as compared to batch processes (Lizandara-Pueyo et al., 2021).

Recycling catalysts is a sustainable process, but sometimes a certain portion of the catalyst cannot be recovered. A small amount of the catalyst can dissolve into the reaction mixture, and potentially escape into the environment. Calcium is extremely common in the environment as compared to other catalytic chemicals. The miniscule amounts of calcium carbonate which escape into the environment would generally cause no effect because calcium is already present (Suppes et al., 2001).

Remarkably, calcium carbonate is highly recyclable and utilization of recycled calcium carbonate enables a boost in the recycled content found in compounds and final polymer applications, thereby aiding customers in achieving their circular economy objectives. Utilization of pre-consumer and post-consumer recycled calcium carbonate is on rise thus adding another benefit of calcium carbonate as a part of a product (Cunningham et al., 2021).

$CaCO_3$ in agricultural applications

With an increasing global population (Gu et al., 2021), food security is of the utmost importance (Molotoks et al., 2021). Between 2010 and 2050, there is an anticipated increase in global food demand ranging from 35% to 56%. Simultaneously, the population at risk of hunger is projected to undergo a change ranging from a reduction of 91% to an increase of 8% during the same period (Van Dijk et al., 2021). The looming threat of food scarcity heightens humanity's need to protect and ensure a bountiful supply of healthy crops in the coming years (Anderson et al., 2020; Devaux et al., 2021; Fukase and Martin, 2020; Hasegawa et al., 2021; Zhao et al., 2021). Calcium carbonate offers various solutions to some issues farmers are facing (Liu et al., 2023; Patanè et al., 2018; Santos et al., 2020). By utilizing the unique chemical, physical and material properties of $CaCO_3$, humanity can nourish the agricultural industry in a sustainable way, while potentially avoiding the projected food insecurities.

Soils play a vital role in meeting the food and feed requirements of an expanding global population. The addition of calcium carbonate to soil can have a beneficial effect on plant health. Traditionally, it is commonly used as a liming agent to reduce soil acidity, meaning that calcium carbonate acts as a neutralizing agent for acidic soils by increasing the soil's pH level, making it more suitable for plant growth. Furthermore, it helps to enhance soil aggregation, water retention, and nutrient availability, making the soil more conducive to plant growth. Interestingly, doping soil with calcium carbonate has alleviated poisoning caused by heavy metal pollution in Hunan, China (Zeng et al., 2015). A field study conducted in Tehsil Lahore City, Punjab, Pakistan further confirmed that concentrations of heavy metals were negatively correlated with calcium carbonate concentrations (Bashir et al., 2019).

Calcium carbonate is often used as a filler in fertilizers to improve their physical properties. It helps to prevent caking and improve the flowability of granular fertilizers, making them easier to handle and apply (Abhiram et al., 2023). Calcium is an essential nutrient for plant growth and development. Calcium carbonate is

used as a source of calcium to supplement the soil and provide plants with this vital nutrient. It helps in strengthening the cell walls of plants, improving their overall structure and resilience (Gao et al., 2023).

Plant diseases have a substantial effect on crop yields and quality, leading to considerable economic losses and requiring significant management inputs each year for crops, landscapes, and forests in the United States, amounting to billions of dollars (Fones et al., 2020; Ristaino et al., 2021). Plant sporopollenin has recently emerged as an environmentally friendly drug carrier (Mundargi et al., 2016). The sporopollenin capsule modified with calcium carbonate can be loaded with drugs or pesticides and used for controlled release of pesticide (Xiang et al., 2023). The engineered sporopollenin can then be mixed with soil used to grow plants. This process allows for the slow release of drugs, pesticides and calcium carbonate while remaining environmentally friendly and increasing crop yield.

Microcapsule based controlled release formulations are promising alternatives to conventional pesticide. By preparing double shelled calcium carbonate capsules, many adverse effects caused by traditional pesticide can be avoided. Approximately 90% of the liquid-based pesticide is lost to run-off and evaporation (Zhao et al., 2018). The controlled release of pesticides through microcapsules is a promising method to solve such issues (Zhou et al., 2022). Though environmentally favorable, the preparation of pesticide loaded calcium carbonate microcapsules is expensive, due to the large amount or organic substances required (Zhou et al., 2022). Therefore, developing a cheap and efficient production process is needed.

Starch doped porous calcium carbonate can also be used as a pesticide delivery mechanism. Calcium carbonate microspheres fabricated through coprecipitation regulated by soluble starch can be used as drug carriers for plants (Xiang et al., 2018). Porous calcium carbonate microspheres with intercalated soluble starch molecules were used as carriers for Prometryn, a typical herbicide (Xiang et al., 2018). Due to electrostatic attractions and hydrogen bonding, the herbicide is slowly released, controlling migration of the chemical while increasing its utility (Xiang et al., 2018). This method can potentially be expanded to include the use of other chemical herbicides as well.

For agricultural applications, the approval and regulations regarding calcium carbonate microcapsules depend on the specific application and the country in which it is being used. In general, calcium carbonate itself is commonly used and considered safe for various agricultural applications. However, if calcium carbonate is used as a carrier or encapsulating agent for other substances, such as pesticides or fertilizers, the regulations may vary. Nevertheless, this application will be more explored and it will gain more interest in the future in comparison to more traditional calcium carbonate applications (Table 1).

Regulatory bodies, such as the Environmental Protection Agency (EPA) in the United States or the European Chemicals Agency (ECHA) in the European Union, assess and approve the use of carriers and encapsulating technologies based on their specific applications and potential risks. These bodies evaluate factors such as the effectiveness, safety, and environmental impact of the carried or encapsulated substances. Calcium carbonate is a naturally occurring mineral that is not derived from plastic and does not pose the same environmental concerns as microplastics. Calcium carbonate is biologically and chemically distinct from plastics and is not classified as a microplastic.

Naturally, calcium carbonate exists in the form of limestone, a rock that contains a minimum of 50% calcium carbonate. Limestone deposits can be found worldwide and are extracted through quarrying or mining processes. The United States stands as a prominent producer of calcium carbonate, with minimal risk of supply disruption. Presently, the cost of lime for agricultural applications, like non-irrigated corn farming in South Georgia, stands at $55 per ton, amounting to $13.73 per acre or $0.16 per bushel. Although this may appear relatively high, investing in lime can yield returns within two to 3 years (University of Georgia, 2024). However, one should be careful in applying lime in the field as the pH of the soil is an important factor that can be regarded as a crucial variable because of its impact on various other soil properties and processes that ultimately affect the growth of plants. The activity of microorganisms, as well as the solubility and availability of nutrients, are among the vital processes that rely on soil pH. For example, pH has a significant influence on various plant characteristics or traits, including height, lateral spread, biomass, flower size and quantity, pollen production, and more (Gentili et al., 2018; Jiang et al., 2017).

Conclusion

$CaCO_3$ is a mineral with a diversity of utilization throughout the built environment. With increasing atmospheric CO_2 to ocean and soil acidification, methods to mitigate pollution are ever more required for a sustainable environment. Specifically, these activities include CO_2 sequestration, chemical catalysis and utilization, precise agricultural applications and essential soil amendments, as well as formation of light weight aggregates in cement replacement applications; all of which will provide noticeable improvements for a more sustainable future. We show an evolution of diverse applications that have been and are using $CaCO_3$ however, with time these applications with $CaCO_3$ will also multiply and its utility will be invaluable in the near future.

Author contributions

JC: Conceptualization, Data curation, Formal Analysis, Funding acquisition, Investigation, Methodology, Project administration, Resources, Software, Supervision, Validation, Visualization, Writing–original draft, Writing–review and editing. EI: Conceptualization, Data curation, Formal Analysis, Funding acquisition, Investigation, Methodology, Project administration, Resources, Software, Supervision, Validation, Visualization, Writing–original draft, Writing–review and editing. CL-P: Conceptualization, Data curation, Formal Analysis, Funding acquisition, Investigation, Methodology, Project administration, Resources, Software, Supervision, Validation, Visualization, Writing–original draft, Writing–review and editing. JS: Conceptualization, Data curation, Formal Analysis, Funding acquisition, Investigation, Methodology, Project administration,

Resources, Software, Supervision, Validation, Visualization, Writing–original draft, Writing–review and editing.

Funding

The author(s) declare that no financial support was received for the research, authorship, and/or publication of this article.

Conflict of interest

Author EI was employed by BASF Corporation. Author CL-P was employed by BASF SE.

The remaining authors declare that the research was conducted in the absence of any commercial or financial relationships that could be construed as a potential conflict of interest.

Publisher's note

All claims expressed in this article are solely those of the authors and do not necessarily represent those of their affiliated organizations, or those of the publisher, the editors and the reviewers. Any product that may be evaluated in this article, or claim that may be made by its manufacturer, is not guaranteed or endorsed by the publisher.

References

Abanades, J. C. (2002). The maximum capture efficiency of CO_2 using a carbonation/calcination cycle of CaO/$CaCO_3$. *Chem. Eng. J.* 90, 303–306. doi:10.1016/S1385-8947(02)00126-2

Abhiram, G., Bishop, P., Jeyakumar, P., Grafton, M., Davies, C. E., and McCurdy, M. (2023). Formulation and characterization of polyester-lignite composite coated slow-release fertilizers. *J. Coat. Technol. Res.* 20, 307–320. doi:10.1007/s11998-022-00670-6

Abo-Sedera, F. (2016). Effect of organic fertilizer and foliar spray with some safety compounds on growth and productivity of snap bean. *Ann. Agric. Sci. Moshtohor* 54, 105–118. doi:10.21608/assjm.2016.103931

Ainsworth, E. A., Lemonnier, P., and Wedow, J. M. (2020). The influence of rising tropospheric carbon dioxide and ozone on plant productivity. *Plant Biol.* 22, 5–11. doi:10.1111/plb.12973

Al-Hosney, H. A., and Grassian, V. H. (2004). Carbonic acid: an important intermediate in the surface chemistry of calcium carbonate. *J. Am. Chem. Soc.* 126, 8068–8069. doi:10.1021/ja0490774

Alonso, D. M., Vila, F., Mariscal, R., Ojeda, M., Granados, M. L., and Santamaría-González, J. (2010). Relevance of the physicochemical properties of CaO catalysts for the methanolysis of triglycerides to obtain biodiesel. *Catal. Today* 158, 114–120. doi:10.1016/j.cattod.2010.05.003

Al Zoubi, W., and Ko, Y. G. (2020). Chemical stability of synergistic inorganic materials for enhancing electrochemical performance. *Compos. Sci. Technol.* 199, 108383. doi:10.1016/j.compscitech.2020.108383

Anderson, R., Bayer, P. E., and Edwards, D. (2020). Climate change and the need for agricultural adaptation. *Curr. Opin. Plant Biol.* 56, 197–202. doi:10.1016/j.pbi.2019.12.006

Armstrong McKay, D. I., Staal, A., Abrams, J. F., Winkelmann, R., Sakschewski, B., Loriani, S., et al. (2022). Exceeding 1.5°C global warming could trigger multiple climate tipping points. *Science* 377, eabn7950. doi:10.1126/science.abn7950

Avouris, P., and Martel, R. (2010). Progress in carbon nanotube electronics and photonics. *MRS Bull.* 35, 306–313. doi:10.1557/mrs2010.553

Ballesteros-Soberanas, J., Hernández-Garrido, J. C., Cerón-Carrasco, J. P., and Leyva-Pérez, A. (2022). Selective semi-hydrogenation of internal alkynes catalyzed by Pd–$CaCO_3$ clusters. *J. Catal.* 408, 43–55. doi:10.1016/j.jcat.2022.02.020

Baltrusaitis, J., Usher, C. R., and Grassian, V. H. (2007). Reactions of sulfur dioxide on calcium carbonate single crystal and particle surfaces at the adsorbed water carbonate interface. *Phys. Chem. Chem. Phys.* 9, 3011. doi:10.1039/b617697f

Bashir, M. A., Rehim, A., Liu, J., Imran, M., Liu, H., Suleman, M., et al. (2019). Soil survey techniques determine nutrient status in soil profile and metal retention by calcium carbonate. *CATENA* 173, 141–149. doi:10.1016/j.catena.2018.10.015

M. Benaglia (2009). *Recoverable and recyclable catalysts*. 1st ed. (Hoboken, N.J: Wiley).

Bewernitz, M. A., Ginder-Vogel, M., Wolf, S. E., Seto, J., and Constantz, B. R. (2024). A bicarbonate-rich liquid condensed phase in non-saturated solutions in the absence of divalent cations. *Front. Bioeng. Biotechnol.* 12, 1382047. doi:10.3389/fbioe.2024.1382047

Boles, M. A., Engel, M., and Talapin, D. V. (2016). Self-assembly of colloidal nanocrystals: from intricate structures to functional materials. *Chem. Rev.* 116, 11220–11289. doi:10.1021/acs.chemrev.6b00196

Boyjoo, Y., Pareek, V. K., and Liu, J. (2014). Synthesis of micro and nano-sized calcium carbonate particles and their applications. *J. Mater Chem. A* 2, 14270–14288. doi:10.1039/C4TA02070G

Briegel, C., and Seto, J. (2012). Single amino acids as additives modulating $CaCO_3$ mineralization. *Adv. Top. Biominer.*, 33–48.

Budinis, S., Krevor, S., Dowell, N. M., Brandon, N., and Hawkes, A. (2018). An assessment of CCS costs, barriers and potential. *Energy Strategy Rev.* 22, 61–81. doi:10.1016/j.esr.2018.08.003

Caballero-Calero, O., Ares, J. R., and Martín-González, M. (2021). Environmentally friendly thermoelectric materials: high performance from inorganic components with low toxicity and abundance in the Earth. *Adv. Sustain. Syst.* 5, 2100095. doi:10.1002/adsu.202100095

Chandrasekaran, J., Nithyaprakash, D., Ajjan, K. B., Maruthamuthu, S., Manoharan, D., and Kumar, S. (2011). Hybrid solar cell based on blending of organic and inorganic materials—an overview. *Renew. Sustain. Energy Rev.* 15, 1228–1238. doi:10.1016/j.rser.2010.09.017

Chang, R., Kim, S., Lee, S., Choi, S., Kim, M., and Park, Y. (2017). Calcium carbonate precipitation for CO_2 storage and utilization: a review of the carbonate crystallization and polymorphism. *Front. Energy Res.* 5, 17. doi:10.3389/fenrg.2017.00017

Chen, J., and Park, N.-G. (2018). Inorganic hole transporting materials for stable and high efficiency perovskite solar cells. *J. Phys. Chem. C* 122, 14039–14063. doi:10.1021/acs.jpcc.8b01177

Chen, K., Song, S., and Xue, D. (2015). Beyond graphene: materials chemistry toward high performance inorganic functional materials. *J. Mater. Chem. A* 3, 2441–2453. doi:10.1039/C4TA06989G

Cheng, X., Liu, H., Yuan, H., Peng, H., Tang, C., Huang, J., et al. (2021). A perspective on sustainable energy materials for lithium batteries. *SusMat* 1, 38–50. doi:10.1002/sus2.4

Cho, K. R., Kulshreshtha, P., Wu, K. J. J., Seto, J., Qiu, S. R., and De Yoreo, J. J. (2019). The effects of different types of additives on growth of biomineral phases investigated by *in situ* atomic force microscopy. *J. Cryst. Growth* 509, 8–16. doi:10.1016/j.jcrysgro.2018.12.021

Chuo, S. C., Mohamed, S. F., Mohd Setapar, S. H., Ahmad, A., Jawaid, M., Wani, W. A., et al. (2020). Insights into the current trends in the utilization of bacteria for microbially induced calcium carbonate precipitation. *Materials* 13, 4993. doi:10.3390/ma13214993

Chutia, G. P., and Phukan, K. (2024). Biomass derived heterogeneous catalysts used for sustainable biodiesel production: a systematic review. *Braz. J. Chem. Eng.* 41, 23–48. doi:10.1007/s43153-023-00371-6

Clark, J., and Rhodes, C. (2000). "Clean synthesis using porous inorganic solid catalysts and supported reagents," in *RSC Clean technology monographs*. Cambridge: Royal Society of Chemistry [distributor] RSC Distribution Services].

Cunningham, P. R., Green, P. G., and Miller, S. A. (2021). Utilization of post-consumer carpet calcium carbonate (PC4) from carpet recycling as a mineral resource in concrete. *Resour. Conserv. Recycl.* 169, 105496. doi:10.1016/j.resconrec.2021.105496

Czaplicka, N., and Konopacka-Łyskawa, D. (2020). Utilization of gaseous carbon dioxide and industrial Ca-rich waste for calcium carbonate precipitation: a review. *Energies* 13, 6239. doi:10.3390/en13236239

Davis, W. (2017). The relationship between atmospheric carbon dioxide concentration and global temperature for the last 425 million years. *Climate* 5, 76. doi:10.3390/cli5040076

Devaux, A., Goffart, J.-P., Kromann, P., Andrade-Piedra, J., Polar, V., and Hareau, G. (2021). The potato of the future: opportunities and challenges in sustainable agri-food systems. *Potato Res.* 64, 681–720. doi:10.1007/s11540-021-09501-4

Dey, S., and Dhal, G. C. (2019). Materials progress in the control of CO and CO_2 emission at ambient conditions: an overview. *Mater. Sci. Energy Technol.* 2, 607–623. doi:10.1016/j.mset.2019.06.004

Dou, B., Wang, C., Song, Y., Chen, H., Jiang, B., Yang, M., et al. (2016). Solid sorbents for *in-situ* CO_2 removal during sorption-enhanced steam reforming process: a review. *Renew. Sustain. Energy Rev.* 53, 536–546. doi:10.1016/j.rser.2015.08.068

Dou, X., Zhang, J., Zhang, C., Ma, D., Chen, L., Zhou, G., et al. (2023). Calcium carbonate regulates soil organic carbon accumulation by mediating microbial communities in northern China. *CATENA* 231, 107327. doi:10.1016/j.catena.2023.107327

Durand, N., Monger, H. C., Canti, M. G., and Verrecchia, E. P. (2018). "Calcium carbonate features," in *Interpretation of micromorphological features of soils and regoliths* (Elsevier), 205–258. doi:10.1016/B978-0-444-63522-8.00009-7

Ebadi Jamkhaneh, M., Ahmadi, M., and Shokri Amiri, M. (2021). Sustainable reuse of inorganic materials in eco-friendly clay bricks: special focus on mechanical and durability assessment. *J. Mater. Civ. Eng.* 33, 04021111. doi:10.1061/(ASCE)MT.1943-5533.0003737

Erans, M., Manovic, V., and Anthony, E. J. (2016). Calcium looping sorbents for CO_2 capture. *Appl. Energy* 180, 722–742. doi:10.1016/j.apenergy.2016.07.074

Erans, M., Nabavi, S. A., and Manović, V. (2020). Carbonation of lime-based materials under ambient conditions for direct air capture. *J. Clean. Prod.* 242, 118330. doi:10.1016/j.jclepro.2019.118330

Fadia, P., Tyagi, S., Bhagat, S., Nair, A., Panchal, P., Dave, H., et al. (2021). Calcium carbonate nano- and microparticles: synthesis methods and biological applications. *3 Biotech.* 11, 457. doi:10.1007/s13205-021-02995-2

Fan, L.-Z., He, H., and Nan, C.-W. (2021). Tailoring inorganic–polymer composites for the mass production of solid-state batteries. *Nat. Rev. Mater.* 6, 1003–1019. doi:10.1038/s41578-021-00320-0

Florin, N. H., Blamey, J., and Fennell, P. S. (2010). Synthetic CaO-based sorbent for CO_2 capture from large-point sources. *Energy fuels.* 24, 4598–4604. doi:10.1021/ef100447c

Fones, H. N., Bebber, D. P., Chaloner, T. M., Kay, W. T., Steinberg, G., and Gurr, S. J. (2020). Threats to global food security from emerging fungal and oomycete crop pathogens. *Nat. Food* 1, 332–342. doi:10.1038/s43016-020-0075-0

Frölicher, T. L., Winton, M., and Sarmiento, J. L. (2014). Continued global warming after CO_2 emissions stoppage. *Nat. Clim. Change* 4, 40–44. doi:10.1038/nclimate2060

Fukase, E., and Martin, W. (2020). Economic growth, convergence, and world food demand and supply. *World Dev.* 132, 104954. doi:10.1016/j.worlddev.2020.104954

Furukawa, S., and Komatsu, T. (2017). Intermetallic compounds: promising inorganic materials for well-structured and electronically modified reaction environments for efficient catalysis. *ACS Catal.* 7, 735–765. doi:10.1021/acscatal.6b02603

Gadikota, G. (2021). Carbon mineralization pathways for carbon capture, storage and utilization. *Commun. Chem.* 4, 23. doi:10.1038/s42004-021-00461-x

Gągol, M., Cako, E., Fedorov, K., Soltani, R. D. C., Przyjazny, A., and Boczkaj, G. (2020). Hydrodynamic cavitation based advanced oxidation processes: studies on specific effects of inorganic acids on the degradation effectiveness of organic pollutants. *J. Mol. Liq.* 307, 113002. doi:10.1016/j.molliq.2020.113002

Gambhir, A., and Tavoni, M. (2019). Direct air carbon capture and sequestration: how it works and how it could contribute to climate-change mitigation. *One Earth* 1, 405–409. doi:10.1016/j.oneear.2019.11.006

Gao, Y., Chen, S., Li, Y., and Shi, Y. (2023). Effect of nano-calcium carbonate on morphology, antioxidant enzyme activity and photosynthetic parameters of wheat (*Triticum aestivum* L.) seedlings. *Chem. Biol. Technol. Agric.* 10, 31. doi:10.1186/s40538-023-00404-9

García-Mota, M., Gómez-Díaz, J., Novell-Leruth, G., Vargas-Fuentes, C., Bellarosa, L., Bridier, B., et al. (2011). A density functional theory study of the 'mythic' Lindlar hydrogenation catalyst. *Theor. Chem. Acc.* 128, 663–673. doi:10.1007/s00214-010-0800-0

Gentili, R., Ambrosini, R., Montagnani, C., Caronni, S., and Citterio, S. (2018). Effect of soil pH on the growth, reproductive investment and pollen allergenicity of ambrosia artemisiifolia L. *Front. Plant Sci.* 9, 1335. doi:10.3389/fpls.2018.01335

Goh, P. S., and Ismail, A. F. (2018). A review on inorganic membranes for desalination and wastewater treatment. *Desalination* 434, 60–80. doi:10.1016/j.desal.2017.07.023

Gu, D., Andreev, K., and Dupre, E. (2021). Major trends in population growth around the world, 3, 604–613. doi:10.46234/ccdcw2021.160

Hamdan, N., and Kavazanjian, E. (2016). Enzyme-induced carbonate mineral precipitation for fugitive dust control. *Géotechnique* 66, 546–555. doi:10.1680/jgeot.15.P.168

Hamdan, N., Kavazanjian, E., Rittmann, B. E., and Karatas, I. (2017). Carbonate mineral precipitation for soil improvement through microbial denitrification. *Geomicrobiol. J.* 34, 139–146. doi:10.1080/01490451.2016.1154117

Hanifa, M., Agarwal, R., Sharma, U., Thapliyal, P. C., and Singh, L. P. (2023). A review on CO_2 capture and sequestration in the construction industry: emerging approaches and commercialised technologies. *J. CO_2 Util.* 67, 102292. doi:10.1016/j.jcou.2022.102292

Hargis, C. W., Chen, I. A., Devenney, M., Fernandez, M. J., Gilliam, R. J., and Thatcher, R. P. (2021). Calcium carbonate cement: a carbon capture, utilization, and storage (CCUS) technique. *Materials* 14, 2709. doi:10.3390/ma14112709

Hasegawa, T., Sakurai, G., Fujimori, S., Takahashi, K., Hijioka, Y., and Masui, T. (2021). Extreme climate events increase risk of global food insecurity and adaptation needs. *Nat. Food* 2, 587–595. doi:10.1038/s43016-021-00335-4

Herzog, H. J. (2011). Scaling up carbon dioxide capture and storage: from megatons to gigatons. *Energy Econ.* 33, 597–604. doi:10.1016/j.eneco.2010.11.004

Hua, K.-H., Wang, H.-C., Chung, R.-S., and Hsu, J.-C. (2015). Calcium carbonate nanoparticles can enhance plant nutrition and insect pest tolerance. *J. Pestic. Sci.* 40, 208–213. doi:10.1584/jpestics.D15-025

Huang, M.-T., and Zhai, P.-M. (2021). Achieving Paris Agreement temperature goals requires carbon neutrality by middle century with far-reaching transitions in the whole society. *Adv. Clim. Change Res.* 12, 281–286. doi:10.1016/j.accre.2021.03.004

Huisingh, D., Zhang, Z., Moore, J. C., Qiao, Q., and Li, Q. (2015). Recent advances in carbon emissions reduction: policies, technologies, monitoring, assessment and modeling. *J. Clean. Prod.* 103, 1–12. doi:10.1016/j.jclepro.2015.04.098

Humlum, O., Stordahl, K., and Solheim, J.-E. (2013). The phase relation between atmospheric carbon dioxide and global temperature. *Glob. Planet. Change* 100, 51–69. doi:10.1016/j.gloplacha.2012.08.008

Jiang, Y., Li, Y., Zeng, Q., Wei, J., and Yu, H. (2017). The effect of soil pH on plant growth, leaf chlorophyll fluorescence and mineral element content of two blueberries. *Acta Hortic.*, 269–276. doi:10.17660/ActaHortic.2017.1180.36

Jin, Z., Yu, C., Wang, R., Wei, W., Jing, Y., and Wang, Q. (2022). Preparation of precipitated calcium carbonate using wollastonite and CO2 from industrial exhaust. *Braz. J. Chem. Eng.* 39, 661–669. doi:10.1007/s43153-021-00200-8

Junaid, M. F., Rehman, Z. U., Čekon, M., Čurpek, J., Farooq, R., Cui, H., et al. (2021). Inorganic phase change materials in thermal energy storage: a review on perspectives and technological advances in building applications. *Energy Build.* 252, 111443. doi:10.1016/j.enbuild.2021.111443

Karl Heinz, B., Hans-Heinrich, M., and Dietmar, W. (2010). *Industrial inorganic chemistry, 2nd, completed rev.* Weinheim: Wiley VCH.

Karnosky, D. F. (2003). Impacts of elevated atmospheric CO_2 on forest trees and forest ecosystems: knowledge gaps. *Environ. Int.* 29, 161–169. doi:10.1016/S0160-4120(02)00159-9

Katsuyama, Y., Yamasaki, A., Iizuka, A., Fujii, M., Kumagai, K., and Yanagisawa, Y. (2005). Development of a process for producing high-purity calcium carbonate ($CaCO_3$) from waste cement using pressurized CO_2. *Environ. Prog.* 24, 162–170. doi:10.1002/ep.10080

Kayvani Fard, A., McKay, G., Buekenhoudt, A., Al Sulaiti, H., Motmans, F., Khraisheh, M., et al. (2018). Inorganic membranes: preparation and application for water treatment and desalination. *Materials* 11, 74. doi:10.3390/ma11010074

Kitchen, H. J., Vallance, S. R., Kennedy, J. L., Tapia-Ruiz, N., Carassiti, L., Harrison, A., et al. (2014). Modern microwave methods in solid-state inorganic materials chemistry: from fundamentals to manufacturing. *Chem. Rev.* 114, 1170–1206. doi:10.1021/cr4002353

Kouzu, M., Kasuno, T., Tajika, M., Sugimoto, Y., Yamanaka, S., and Hidaka, J. (2008). Calcium oxide as a solid base catalyst for transesterification of soybean oil and its application to biodiesel production. *Fuel* 87, 2798–2806. doi:10.1016/j.fuel.2007.10.019

Laverdura, U. P., Rossi, L., Ferella, F., Courson, C., Zarli, A., Alhajyoussef, R., et al. (2020). Selective catalytic hydrogenation of vegetable oils on lindlar catalyst. *ACS Omega* 5, 22901–22913. doi:10.1021/acsomega.0c02280

Levey, C., Reed, J., Sanchez, C., Schneider, J., and Constantz, B. R. (2024). Calorimetry of amorphous calcium carbonate is correlated with its lithification and durability as synthetic stone—implications for CO_2 storage and utilization. *Front. Mater.* 11, 1365217. doi:10.3389/fmats.2024.1365217

Liang, K., Li, L., and Yang, Y. (2017). Inorganic porous films for renewable energy storage. *ACS Energy Lett.* 2, 373–390. doi:10.1021/acsenergylett.6b00666

Lima, M. A., Mendes, L. F. R., Mothé, G. A., Linhares, F. G., De Castro, M. P. P., Da Silva, M. G., et al. (2020). Renewable energy in reducing greenhouse gas emissions: reaching the goals of the Paris agreement in Brazil. *Environ. Dev.* 33, 100504. doi:10.1016/j.envdev.2020.100504

Lin, P.-Y., Wu, H.-M., Hsieh, S.-L., Li, J.-S., Dong, C., Chen, C.-W., et al. (2020). Preparation of vaterite calcium carbonate granules from discarded oyster shells as an adsorbent for heavy metal ions removal. *Chemosphere* 254, 126903. doi:10.1016/j.chemosphere.2020.126903

Lindlar, H., and Dubuis, R. (2003). "Palladium catalyst for partial reduction of acetylenes," in *Organic syntheses*. Editors A. S. Kende and J. P. Freeman (Wiley), 89. doi:10.1002/0471264180.os046.27

Lindsey, R., and Dahlman, L., 2024. Climate change: global temperature.

Ling, J. S. J., Tan, Y. H., Mubarak, N. M., Kansedo, J., Saptoro, A., and Nolasco-Hipolito, C. (2019). A review of heterogeneous calcium oxide based catalyst from waste for biodiesel synthesis. *SN Appl. Sci.* 1, 810. doi:10.1007/s42452-019-0843-3

Liu, H., Cao, C.-Y., Wei, F.-F., Jiang, Y., Sun, Y.-B., Huang, P.-P., et al. (2013). Fabrication of macroporous/mesoporous carbon nanofiber using $CaCO_3$ nanoparticles as dual purpose template and its application as catalyst support. *J. Phys. Chem. C* 117, 21426–21432. doi:10.1021/jp4078807

Liu, K.-G., Sharifzadeh, Z., Rouhani, F., Ghorbanloo, M., and Morsali, A. (2021). Metal-organic framework composites as green/sustainable catalysts. *Coord. Chem. Rev.* 436, 213827. doi:10.1016/j.ccr.2021.213827

Liu, L., Diao, X., He, Z., Yi, Y., Wang, T., Wang, M., et al. (2020). High-performance all-inorganic portable electrochromic Li-ion hybrid supercapacitors toward safe and smart energy storage. *Energy Storage Mater.* 33, 258–267. doi:10.1016/j.ensm.2020.08.023

Liu, Q., He, X., and Li, D. (2023). Unearthing the mechanisms underlying calcium carbonate therapies for eliminating pathogens during composting. *Chem. Eng. J.* 451, 139087. doi:10.1016/j.cej.2022.139087

Liu, W., Low, N. W., Feng, B., Wang, G., and Diniz Da Costa, J. C. (2010). Calcium precursors for the production of CaO sorbents for multicycle CO_2 capture. *Environ. Sci. Technol.* 44, 841–847. doi:10.1021/es902426n

Liu, X., Xing, S., Yang, L., Fu, J., Lv, P., Zhang, X., et al. (2021). Highly active and durable Ca-based solid base catalyst for biodiesel production. *Fuel* 302, 121094. doi:10.1016/j.fuel.2021.121094

Lizandara-Pueyo, C., Fan, X., Ayats, C., and Pericàs, M. A. (2021). Calcium carbonate as heterogeneous support for recyclable organocatalysts. *J. Catal.* 393, 107–115. doi:10.1016/j.jcat.2020.11.013

López-Periago, A. M., Pacciani, R., García-González, C., Vega, L. F., and Domingo, C. (2010). A breakthrough technique for the preparation of high-yield precipitated calcium carbonate. *J. Supercrit. Fluids* 52, 298–305. doi:10.1016/j.supflu.2009.11.014

Lüthi, D., Le Floch, M., Bereiter, B., Blunier, T., Barnola, J.-M., Siegenthaler, U., et al. (2008). High-resolution carbon dioxide concentration record 650,000–800,000 years before present. *Nature* 453, 379–382. doi:10.1038/nature06949

Manikandan, S., Subbaiya, R., Saravanan, M., Ponraj, M., Selvam, M., and Pugazhendhi, A. (2022). A critical review of advanced nanotechnology and hybrid membrane based water recycling, reuse, and wastewater treatment processes. *Chemosphere* 289, 132867. doi:10.1016/j.chemosphere.2021.132867

Marin Rivera, R., and Van Gerven, T. (2020). Production of calcium carbonate with different morphology by simultaneous CO2 capture and mineralisation. *J. CO_2 Util.* 41, 101241. doi:10.1016/j.jcou.2020.101241

Martinez, D. M., Horvath, A., and Monteiro, P. J. M. (2023). Comparative environmental assessment of limestone calcined clay cements and typical blended cements. *Environ. Res. Commun.* 5, 055002. doi:10.1088/2515-7620/acccd8

Mazari, S. A., Ali, E., Abro, R., Khan, F. S. A., Ahmed, I., Ahmed, M., et al. (2021). Nanomaterials: applications, waste-handling, environmental toxicities, and future challenges – a review. *J. Environ. Chem. Eng.* 9, 105028. doi:10.1016/j.jece.2021.105028

McFarland, C., Shiwakoti, S., Carpenter-Boggs, L., Schroeder, K., Brown, T., and Huggins, D. R. (2020). Evaluating buffer methods for determining lime requirement on acidified agricultural soils of the Palouse. *Soil Sci. Soc. Am. J.* 84, 1769–1781. doi:10.1002/saj2.20111

Meyer, F. D., Bang, S., Min, S., Stetler, L. D., and Bang, S. S. (2011). "Microbiologically-induced soil stabilization: application of sporosarcina pasteurii for fugitive dust control," in *Geo-frontiers 2011. Presented at the geo-frontiers congress 2011, American society of civil engineers* (Dallas, Texas, United States), 4002–4011. doi:10.1061/41165(397)409

Mitzi, D. B. (2009). *Solution processing of inorganic materials*. Hoboken, New Jersey: Wiley.

Molotoks, A., Smith, P., and Dawson, T. P. (2021). Impacts of land use, population, and climate change on global food security. *Food Energy Secur* 10, e261. doi:10.1002/fes3.261

Moon, H. Y., Shin, D. G., and Choi, D. S. (2007). Evaluation of the durability of mortar and concrete applied with inorganic coating material and surface treatment system. *Constr. Build. Mater.* 21, 362–369. doi:10.1016/j.conbuildmat.2005.08.012

Moore, C. E., Meacham-Hensold, K., Lemonnier, P., Slattery, R. A., Benjamin, C., Bernacchi, C. J., et al. (2021). The effect of increasing temperature on crop photosynthesis: from enzymes to ecosystems. *J. Exp. Bot.* 72, 2822–2844. doi:10.1093/jxb/erab090

Mundargi, R. C., Potroz, M. G., Park, S., Shirahama, H., Lee, J. H., Seo, J., et al. (2016). Natural sunflower pollen as a drug delivery vehicle. *Small* 12, 1167–1173. doi:10.1002/smll.201500860

Neeraj, D., and Yadav, S. (2020). Carbon storage by mineral carbonation and industrial applications of CO2. *Mater. Sci. Energy Technol.* 3, 494–500. doi:10.1016/j.mset.2020.03.005

Neina, D. (2019). The role of soil pH in plant nutrition and soil remediation. *Appl. Environ. Soil Sci.* 2019, 1–9. doi:10.1155/2019/5794869

Nelson, J. J. M., and Schelter, E. J. (2019). Sustainable inorganic chemistry: metal separations for recycling. *Inorg. Chem.* 58, 979–990. doi:10.1021/acs.inorgchem.8b01871

Ngamcharussrivichai, C., Nunthasanti, P., Tanachai, S., and Bunyakiat, K. (2010). Biodiesel production through transesterification over natural calciums. *Fuel Process. Technol.* 91, 1409–1415. doi:10.1016/j.fuproc.2010.05.014

Niemeyer, C. M. (2001). Nanoparticles, proteins, and nucleic acids: biotechnology meets materials science. *Angew. Chem. Int. Ed.* 40, 4128–4158. doi:10.1002/1521-3773(20011119)40:22<4128::aid-anie4128>3.3.co;2-j

NOAA National Centers for Environmental information (2024). Climate at a glance: global time series, published july. Available at: https://www.ncei.noaa.gov/access/monitoring/climate-at-a-glance/global/time-series.

Olajire, A. A. (2013). A review of mineral carbonation technology in sequestration of CO_2. *J. Pet. Sci. Eng.* 109, 364–392. doi:10.1016/j.petrol.2013.03.013

Osterloh, F. E. (2008). Inorganic materials as catalysts for photochemical splitting of water. *Chem. Mater.* 20, 35–54. doi:10.1021/cm7024203

Patanè, C., Pellegrino, A., and Di Silvestro, I. (2018). Effects of calcium carbonate application on physiology, yield and quality of field-grown tomatoes in a semi-arid Mediterranean climate. *Crop Pasture Sci.* 69, 411. doi:10.1071/CP17424

Pham, P. T., Federico-Perez, R. A., Fine, K. L., Matzek, L. W., Carter, K. E., Palomino, A. M., et al. (2020). Sustained release of persulfate from inert inorganic materials for groundwater remediation. *Chemosphere* 259, 127508. doi:10.1016/j.chemosphere.2020.127508

Piątek, J., Afyon, S., Budnyak, T. M., Budnyk, S., Sipponen, M. H., and Slabon, A. (2021). Sustainable Li-ion batteries: chemistry and recycling. *Adv. Energy Mater.* 11, 2003456. doi:10.1002/aenm.202003456

Prakash, S. (2021). Impact of climate change on aquatic ecosystem and its biodiversity: an overview. *Int. J. Biol. Innov. 03* 03. doi:10.46505/IJBI.2021.3210

Pu, Y., Li, L., Wang, Q., Shi, X., Luan, C., Zhang, G., et al. (2021). Accelerated carbonation technology for enhanced treatment of recycled concrete aggregates: a state-of-the-art review. *Constr. Build. Mater.* 282, 122671. doi:10.1016/j.conbuildmat.2021.122671

Qi, W., Zhou, X., Li, J., Cheng, J., Li, Y., Ko, M. J., et al. (2020). Inorganic material passivation of defects toward efficient perovskite solar cells. *Sci. Bull.* 65, 2022–2032. doi:10.1016/j.scib.2020.07.017

Ridley, J., Gregory, J. M., Huybrechts, P., and Lowe, J. (2010). Thresholds for irreversible decline of the Greenland ice sheet. *Clim. Dyn.* 35, 1049–1057. doi:10.1007/s00382-009-0646-0

Ristaino, J. B., Anderson, P. K., Bebber, D. P., Brauman, K. A., Cunniffe, N. J., Fedoroff, N. V., et al. (2021). The persistent threat of emerging plant disease pandemics to global food security. *Proc. Natl. Acad. Sci.* 118, e2022239118. doi:10.1073/pnas.2022239118

Saetan, T., Lertvachirapaiboon, C., Ekgasit, S., Sukwattanasinitt, M., and Wacharasindhu, S. (2017). Palladium nanoparticles immobilized on individual calcium carbonate plates derived from mussel shell waste: an ecofriendly catalyst for the copper-free sonogashira coupling reaction. *Chem. – Asian J.* 12, 2221–2230. doi:10.1002/asia.201700537

Salek, S. S., Van Turnhout, A. G., Kleerebezem, R., and Van Loosdrecht, M. C. M. (2015). pH control in biological systems using calcium carbonate. *Biotechnol. Bioeng.* 112, 905–913. doi:10.1002/bit.25506

Sanna, A., Uibu, M., Caramanna, G., Kuusik, R., and Maroto-Valer, M. M. (2014). A review of mineral carbonation technologies to sequester CO_2. *Chem. Soc. Rev.* 43, 8049–8080. doi:10.1039/C4CS00035H

Santos, C. A. D., Carmo, M. G. F. D., Bhering, A. D. S., Costa, E. S. P., and Amaral Sobrinho, N. M. B. D. (2020). Use of limestone and agricultural gypsum in cauliflower crop management and clubroot control in mountain farming. *Acta Sci. Agron.* 42, e42494. doi:10.4025/actasciagron.v42i1.42494

Sanz-Pérez, E. S., Murdock, C. R., Didas, S. A., and Jones, C. W. (2016). Direct capture of CO_2 from ambient air. *Chem. Rev.* 116, 11840–11876. doi:10.1021/acs.chemrev.6b00173

Schlägl, R., Noack, K., Zbinden, H., and Reller, A. (1987). The microstructure of selective palladium hydrogenation catalysts supported on calcium carbonate and modified by lead (lindlar catalysts), studied by photoelectron spectroscopy, thermogravimetry, X-ray diffraction, and electron microscopy. *Helv. Chim. Acta* 70, 627–679. doi:10.1002/hlca.19870700317

Schubert, U., and Hüsing, N. (2019). *Synthesis of inorganic materials*. Fourth edition. Weinheim: Wiley VCH.

Senra, J. D., Malta, L. F. B., Souza, A. L. F., Aguiar, L. C. S., and Antunes, O. A. C. (2008). Palladium on calcium carbonate combined to 2-Hydroxypropyl-α/β-cyclodextrins: a selective catalytic system for aqueous Heck coupling and hydroarylation. *Adv. Synth. Catal.* 350, 2551–2558. doi:10.1002/adsc.200800472

Servin, A. D., and White, J. C. (2016). Nanotechnology in agriculture: next steps for understanding engineered nanoparticle exposure and risk. *NanoImpact* 1, 9–12. doi:10.1016/j.impact.2015.12.002

Seto, J., Azaïs, T., and Cölfen, H. (2013). Formation of aragonitic layered structures from kaolinite and amorphous calcium carbonate precursors. *Langmuir* 29, 7521–7528. doi:10.1021/la400442j

Seto, J., Picker, A., Chen, Y., Rao, A., Evans, J. S., and Cölfen, H. (2014). Nacre protein sequence compartmentalizes mineral polymorphs in solution. *Cryst. Growth Des.* 14, 1501–1505. doi:10.1021/cg401421h

Shabtai, I. A., Wilhelm, R. C., Schweizer, S. A., Höschen, C., Buckley, D. H., and Lehmann, J. (2023). Calcium promotes persistent soil organic matter by altering microbial transformation of plant litter. *Nat. Commun.* 14, 6609. doi:10.1038/s41467-023-42291-6

Shakun, J. D., Clark, P. U., He, F., Marcott, S. A., Mix, A. C., Liu, Z., et al. (2012). Global warming preceded by increasing carbon dioxide concentrations during the last deglaciation. *Nature* 484, 49–54. doi:10.1038/nature10915

Shen, Q., Li, X., Li, R., and Wu, Y. (2020). Application of metal–organic framework materials and derived porous carbon materials in catalytic hydrogenation. *ACS Sustain. Chem. Eng.* 8, 17608–17621. doi:10.1021/acssuschemeng.0c06849

Snæbjörnsdóttir, S. Ó., Sigfússon, B., Marieni, C., Goldberg, D., Gislason, S. R., and Oelkers, E. H. (2020). Carbon dioxide storage through mineral carbonation. *Nat. Rev. Earth Environ.* 1, 90–102. doi:10.1038/s43017-019-0011-8

Song, C. E., and Lee, S. (2002). Supported chiral catalysts on inorganic materials. *Chem. Rev.* 102, 3495–3524. doi:10.1021/cr0103625

Song, J. Y., Sim, Y., Jang, J., Hong, W.-T., and Yun, T. S. (2020). Near-surface soil stabilization by enzyme-induced carbonate precipitation for fugitive dust suppression. *Acta Geotech.* 15, 1967–1980. doi:10.1007/s11440-019-00881-z

Soon, N. W., Lee, L. M., Khun, T. C., and Ling, H. S. (2014). Factors affecting improvement in engineering properties of residual soil through microbial-induced calcite precipitation. *J. Geotech. Geoenvironmental Eng.* 140, 04014006. doi:10.1061/(ASCE)GT.1943-5606.0001089

Stefaniuk, D., Hajduczek, M., Weaver, J. C., Ulm, F. J., and Masic, A. (2023). Cementing CO_2 into C-S-H: a step toward concrete carbon neutrality. *PNAS Nexus* 2, pgad052. doi:10.1093/pnasnexus/pgad052

Stone, E. J., Lowe, J. A., and Shine, K. P. (2009). The impact of carbon capture and storage on climate. *Energy Env. Sci.* 2, 81–91. doi:10.1039/B807747A

Sun, Y., and Rogers, J. A. (2007). Inorganic semiconductors for flexible electronics. *Adv. Mater.* 19, 1897–1916. doi:10.1002/adma.200602223

Suppes, G. J., Bockwinkel, K., Lucas, S., Botts, J. B., Mason, M. H., and Heppert, J. A. (2001). Calcium carbonate catalyzed alcoholysis of fats and oils. *J. Am. Oil Chem. Soc.* 78, 139–146. doi:10.1007/s11746-001-0234-y

Teir, S., Kotiranta, T., Pakarinen, J., and Mattila, H.-P. (2016). Case study for production of calcium carbonate from carbon dioxide in flue gases and steelmaking slag. *J. CO_2 Util.* 14, 37–46. doi:10.1016/j.jcou.2016.02.004

Thangaraj, B., Solomon, P. R., Muniyandi, B., Ranganathan, S., and Lin, L. (2019). Catalysis in biodiesel production—a review. *Clean. Energy* 3, 2–23. doi:10.1093/ce/zky020

Thonemann, N., Zacharopoulos, L., Fromme, F., and Nühlen, J. (2022). Environmental impacts of carbon capture and utilization by mineral carbonation: a systematic literature review and meta life cycle assessment. *J. Clean. Prod.* 332, 130067. doi:10.1016/j.jclepro.2021.130067

Toggweiler, J. R., and Lea, D. W. (2010). Temperature differences between the hemispheres and ice age climate variability: ice age climate variability. *Paleoceanography* 25. doi:10.1029/2009PA001758

University of Georgia (2024). *Dep. Agric. and Appl. Econ. Budgets*.

U.S. Global Change Research ProgramWuebbles, D. J., Fahey, D. W., Hibbard, K. A., Dokken, D. J., Stewart, B. C., and Maycock, T. K. (2017). Climate science special report: fourth national climate assessment, volume I. *U.S. Glob. Change Res. Program*. doi:10.7930/J0J964J6

Vallet-Regí, M., Balas, F., Colilla, M., and Manzano, M. (2007). Bioceramics and pharmaceuticals: a remarkable synergy. *Solid State Sci.* 9, 768–776. doi:10.1016/j.solidstatesciences.2007.03.026

Valone, T. F. (2023). Gigatonne carbon dioxide removal can reverse global heating trend. . *Environ. Ecol.* 20, 42–58. doi:10.9734/ajee/2023/v20i2436

Van Dijk, M., Morley, T., Rau, M. L., and Saghai, Y. (2021). A meta-analysis of projected global food demand and population at risk of hunger for the period 2010–2050. *Nat. Food* 2, 494–501. doi:10.1038/s43016-021-00322-9

Van Soest, H. L., Den Elzen, M. G. J., and Van Vuuren, D. P. (2021). Net-zero emission targets for major emitting countries consistent with the Paris Agreement. *Nat. Commun.* 12, 2140. doi:10.1038/s41467-021-22294-x

Wang, C., Li, W., Yang, Z., Chen, Y., Shao, W., and Ji, J. (2015). An invisible soil acidification: critical role of soil carbonate and its impact on heavy metal bioavailability. *Sci. Rep.* 5, 12735. doi:10.1038/srep12735

Wang, J., and Wang, S. (2021). Effect of inorganic anions on the performance of advanced oxidation processes for degradation of organic contaminants. *Chem. Eng. J.* 411, 128392. doi:10.1016/j.cej.2020.128392

Wang, L., Zhang, J., Zhang, Y., Yu, H., Qu, Y., and Yu, J. (2022). Inorganic metal-oxide photocatalyst for H_2O_2 production. *Small* 18, 2104561. doi:10.1002/smll.202104561

Waris, A., Din, M., Ali, A., Ali, M., Afridi, S., Baset, A., et al. (2021). A comprehensive review of green synthesis of copper oxide nanoparticles and their diverse biomedical applications. *Inorg. Chem. Commun.* 123, 108369. doi:10.1016/j.inoche.2020.108369

Witoon, T. (2011). Characterization of calcium oxide derived from waste eggshell and its application as CO_2 sorbent. *Ceram. Int.* 37, 3291–3298. doi:10.1016/j.ceramint.2011.05.125

Xiang, S., Kang, H., Chai, A., Shi, Y., Xie, X., Li, L., et al. (2023). Calcium carbonate-modified plant sporopollen capsule as an eco-friendly microvehicle for controlled release of pesticide. *Pest Manag. Sci.* 79, 1604–1614. doi:10.1002/ps.7333

Xiang, Y., Han, J., Zhang, G., Zhan, F., Cai, D., and Wu, Z. (2018). Efficient synthesis of starch-regulated porous calcium carbonate microspheres as a carrier for slow-release herbicide. *ACS Sustain. Chem. Eng.* 6, 3649–3658. doi:10.1021/acssuschemeng.7b03973

Xiang, Y., Liu, H., Zhu, E., Yang, K., Yuan, D., Jiao, T., et al. (2022). Application of inorganic materials as heterogeneous cocatalyst in Fenton/Fenton-like processes for wastewater treatment. *Sep. Purif. Technol.* 295, 121293. doi:10.1016/j.seppur.2022.121293

Xie, J., Gao, J., Cao, H., Li, J., Wang, X., Zhang, J., et al. (2024). Calcium carbonate promotes the formation and stability of soil macroaggregates in mining areas of China. *J. Integr. Agric.* 23, 1034–1047. doi:10.1016/j.jia.2023.09.015

Yoro, K. O., and Daramola, M. O. (2020). "CO2 emission sources, greenhouse gases, and the global warming effect," in *Advances in carbon capture* (Elsevier), 3–28. doi:10.1016/B978-0-12-819657-1.00001-3

Zeng, W.-A., Li, F., Zhou, H., Qin, X.-L., Zou, Z.-J., Tian, T., et al. (2015). Effect of calcium carbonate on cadmium and nutrients uptake in tobacco (Nicotiana tabacum L.) planted on contaminated soil. *J. Environ. Biol.* 37, 163–168.

Zhang, Y., Zhang, S., Wang, R., Cai, J., Zhang, Y., Li, H., et al. (2016). Impacts of fertilization practices on pH and the pH buffering capacity of calcareous soil. *Soil Sci. Plant Nutr.* 62, 432–439. doi:10.1080/00380768.2016.1226685

Zhao, H., Chang, J., Havlík, P., Van Dijk, M., Valin, H., Janssens, C., et al. (2021). China's future food demand and its implications for trade and environment. *Nat. Sustain.* 4, 1042–1051. doi:10.1038/s41893-021-00784-6

Zhao, X., Cui, H., Wang, Y., Sun, C., Cui, B., and Zeng, Z. (2018). Development strategies and prospects of nano-based smart pesticide formulation. *J. Agric. Food Chem.* 66, 6504–6512. doi:10.1021/acs.jafc.7b02004

Zheng, B., Fan, J., Chen, B., Qin, X., Wang, J., Wang, F., et al. (2022). Rare-earth doping in nanostructured inorganic materials. *Chem. Rev.* 122, 5519–5603. doi:10.1021/acs.chemrev.1c00644

Zhou, Z., Gao, Y., Tang, G., Tian, Y., Li, Y., Wang, H., et al. (2022). Facile preparation of pH/pectinase responsive microcapsules based on $CaCO_3$ using fungicidal ionic liquid as a nucleating agent for sustainable plant disease management. *Chem. Eng. J.* 446, 137073. doi:10.1016/j.cej.2022.137073

frontiers | Frontiers in Chemistry

TYPE Original Research
PUBLISHED 25 October 2024
DOI 10.3389/fchem.2024.1467810

OPEN ACCESS

EDITED BY
Richard Villanneau,
Sorbonne Université, France

REVIEWED BY
Andrea Mezzetta,
University of Pisa, Italy
María Salomé Álvarez,
University of Vigo, Spain

*CORRESPONDENCE
Marina Cvjetko Bubalo,
marina.cvjetko.bubalo@pbf.unizg.hr

RECEIVED 20 July 2024
ACCEPTED 10 October 2024
PUBLISHED 25 October 2024

CITATION
Logarušić M, Šubar K, Nikolić M, Jurinjak Tušek A, Damjanović A, Radović M, Radojčić Redovniković I, Žnidaršič-Plazl P, Kroutil W and Cvjetko Bubalo M (2024) Harnessing the potential of deep eutectic solvents in biocatalysis: design strategies using CO_2 to formate reduction as a case study. *Front. Chem.* 12:1467810. doi: 10.3389/fchem.2024.1467810

Harnessing the potential of deep eutectic solvents in biocatalysis: design strategies using CO_2 to formate reduction as a case study

Marijan Logarušić[1], Karla Šubar[1], Maja Nikolić[1], Ana Jurinjak Tušek[1], Anja Damjanović[1], Mia Radović[1], Ivana Radojčić Redovniković[1], Polona Žnidaršič-Plazl[2], Wolfgang Kroutil[3] and Marina Cvjetko Bubalo[1]*

[1]Faculty of Food Technology and Biotechnology, University of Zagreb, Zagreb, Croatia, [2]Faculty of Chemistry and Chemical Technology, University of Ljubljana, Ljubljana, Slovenia, [3]Institute of Chemistry, University of Graz, Field of Excellence BioHealth, BioTechMed Graz, Graz, Austria

Introduction: Deep eutectic solvents (DESs) have emerged as green solvents with versatile applications, demonstrating significant potential in biocatalysis. They often increase the solubility of poorly water-soluble substrates, serve as smart co-substrates, modulate enzyme stereoselectivity, and potentially improve enzyme activity and stability. Despite these advantages, screening for an optimal DES and determining the appropriate water content for a given biocatalytic reaction remains a complex and time-consuming process, posing a significant challenge.

Methods: This paper discusses the rational design of DES tailored to a given biocatalytic system through a combination of experimental screening and computational tools, guided by performance targets defined by solvent properties and process constraints. The efficacy of this approach is demonstrated by the reduction of CO_2 to formate catalyzed by NADH-dependent formate dehydrogenase (FDH). By systematically analyzing FDH activity and stability, NADH stability (both long-term and short-term stability after solvent saturation with CO_2), and CO_2 solubility in initially selected glycerol-based DESs, we were able to skillfully guide the DES screening process.

Results and discussion: Considering trade-offs between experimentally determined performance metrics of DESs, 20% solution of choline chloride: glycerol in phosphate buffer (ChCl:$Gly_{80\%B}$) was identified as the most promising solvent system for a given reaction. Using ChCl:Gly as a co-solvent resulted in an almost 15-fold increase in FDH half-life compared to the reference buffer and stabilized the coenzyme after the addition of CO_2. Moreover, the 20% addition of ChCl:Gly to the buffer improved the volumetric productivity of FDH-catalyzed CO_2 reduction in a batch system compared to the reference buffer. The exceptional stability of the enzyme in this co-solvent system shows great potential for application in continuous operation, which can significantly improve process productivity. Additionally, based on easily measurable physicochemical solvent properties and molecular descriptors derived from

COSMO-RS, QSAR models were developed, which successfully predicted enzyme activity and stability, as well as coenzyme stability in selected solvent systems with DESs.

KEYWORDS

deep eutectic solvents, rational design, biocatalysis, mathematical modelling, QSAR, formate dehydrogenase, NADH, CO_2 conversion

1 Introduction

Medium engineering is one of the main components of biocatalysis engineering, which also includes substrate engineering, protein (enzyme) engineering, biocatalyst (formulation) engineering, biocatalytic cascade engineering, and reactor engineering (Sheldon and Pereira, 2017). Its purpose is to enhance the performance of biocatalysts, improve substrate solubility, and positively influence reaction equilibrium, so it has been a significant research focus for over the past 30 years (Castillo et al., 2016; Sheldon and Pereira, 2017; Sheldon et al., 2023). Accordingly, numerous enzymatic syntheses have been developed in both aqueous and non-aqueous media, including organic solvents, supercritical fluids, ionic liquids (ILs) and, more recently, deep eutectic solvents (DESs). The latter two, ILs and DESs, are of particular interest due to their high tunability as they can fulfil specific process requirements and meet "green solvent" criteria (Lozano et al., 2010; Villa et al., 2019; Panić et al., 2021; van Schie et al., 2021; Žnidaršič-Plazl, 2021a; Sheldon et al., 2023; Zhang et al., 2024). Eutectic systems have long been known as multi-component mixtures used in materials chemistry and engineering. However, in 2003 Abbott et al. coined the term "deep eutectic solvents" to describe mixtures that solidify at temperatures well below (*deeper*) than the crystallization points of their individual components, such that these compositions remain liquid even at room temperature (Abbott et al., 2003). In general, these solvents are formed by mixing two or more compounds that are normally solid at room temperature; when combined in certain molar ratios, they form a liquid solution due to molecular interactions (mainly hydrogen bonds) that lower the melting point of the mixture. In practice, DES can be easily prepared by combining hydrogen bond acceptors (HBAs) such as choline chloride and betaine with hydrogen bond donors (HBDs) such as polyols (e.g., glycerol, ethylene glycol, sorbitol), organic acids (e.g., citric, malic, oxalic acid), amino acids (e.g., alanine, proline), sugars (e.g., glucose, sucrose, trehalose) or amide urea with an atom economy of 100%. These combinations lead to different DESs, which almost always contain water to reduce the viscosity or to adjust certain properties of the DES (Hansen et al., 2021). The diversity of DES-forming components has led to many new and structurally different DESs, refining the initial definition by Abbott's group. Recently, a (deep) eutectic solvent/system has been defined as a liquid system with eutectic properties that remains liquid at a given temperature, even if one component would normally be solid (Abranches and Coutinho, 2022). The wide range of their possible structural combinations, coupled with their sustainability and their distinctive physicochemical properties (non-volatility, non-flammability, easy and clean preparation, low to moderate toxicity), as well as the ability to fine-tune their solvent properties, make them ideal candidates for the development of efficient and sustainable processes or products (Cvjetko Bubalo et al., 2015).

In 2008, Gorke et al. published a pioneering work in which they demonstrated the potential of DESs as solvents or co-solvents for biocatalytic reactions (Gorke et al., 2008). It was shown that the media composed of urea, a strong HBD, with choline chloride, a HBA, does not denature hydrolases and even increases enzyme activity. Their study revealed that the components of DESs are significantly less denaturizing agents than expected, suggesting that the hydrogen bonding network in DESs lowers the chemical potential of the components. Since then, interest in the use of these solvents for various biocatalytic reactions has surged, as evidenced by the exponential growth in related publications over the past decade (according to Web of Science, more than 250 scientific papers have been published on this topic since 2009). DESs have shown considerable potential in enhancing biocatalysis through various mechanisms. These solvents can improve substrate solubility, act as smart co-substrates, and influence enzyme stereoselectivity. Furthermore, they are noted for their ability to improve enzyme activity and especially operational stability in reaction media (Zhang et al., 2024). In a recent study, a hydrophilic DES was used to tailor the properties of a copolymeric hydrogel utilized for enzyme immobilization. This addition not only exhibited superior mechanical properties of DES-infused hydrogel but also increased permeability to the specific substrate in a given biocatalytic reaction (Menegatti et al., 2024). Stabilization of enzymes, whether in homogeneous reactions or through enzyme immobilization, remains one of the major challenges in the development of long-term continuous biocatalytic processes. Overcoming this challenge is crucial as it can greatly increase the total turnover number and thus efficiency of biocatalysts, leading to the intensification of biocatalytic processes (Žnidaršič-Plazl, 2021b).

Despite the numerous advantages of DESs, the modification of the conventional aqueous medium with these solvents can significantly affect various aspects of a reaction, sometimes in undesirable ways. Therefore, finding the optimal DES for a given reaction remains a challenge. A promising method for rationally designing solvents for a specific biocatalytic system involves a complementary approach that integrates experimental screening with computational tools. If such an approach is successful, it would be possible to realize the full potential of these solvents while avoiding some problems associated with their use, such as high viscosity, product recovery issues and still quite unexplored methods of DES recovery and recycling. In this paper, we briefly review the current literature on DES-assisted biocatalysis and emphasize the need for strategic design of DESs for a given reaction. Furthermore, we propose and discuss complementary

experimental and *in silico* methods to tackle the complexity of DES screening. Finally, this approach is illustrated by a case study of CO_2 reduction catalyzed by formate dehydrogenase.

2 Optimizing the synergy between DES and biocatalysis: the quest for the ideal solvent

The synergy between DESs and biocatalysis is ideally suited for the efficient and sustainable production of commercially important products (Sheldon et al., 2023; Zhang et al., 2024). Biocatalysis, which is known to enable complex transformations with high regio-, chemo-, and enantioselectivity under mild and cost-effective conditions, could be greatly enhanced by DESs. These tunable solvents with their wide range of structural possibilities could be a particularly valuable aid in processes facing challenges such as enzyme stability/activity, cofactor stability, substrate solubility, product inhibition, and negative environmental impact. To date, a variety of DES-assisted biocatalytic reactions have been developed using versatile enzymes such as hydrolases (e.g., lipase, epoxide hydrolases, dehalogenases), oxidoreductases (e.g., alcohol dehydrogenases, laccases, peroxidases, monooxygenases), lyases (e.g., benzaldehyde lyase, phenolic acid decarboxylase), and transferases (e.g., amine transaminases) (Panić et al., 2021; Domingues et al., 2024; Zhang et al., 2024). In these reactions, DESs primarily act as (co-) solvents or additives. In some cases, they fulfil a dual function by acting as both solvents and (co-) substrates (Mourelle-Insua et al., 2019; Pätzold et al., 2019b). It should be noted that when DESs act as solvents, they are rarely used in their pure form. Instead, they are usually mixed with water, which is tightly incorporated into the DES cavities up to a proportion of about 50%. For example, Hammond et al. studied the effect of water on DES choline chloride:urea nanostructure, finding that it remains stable up to about 42% water (w/w) due to solvophobic sequestration of water into nanostructured domains around the cholinium cation. At 51% water (w/w), the structure disrupts, and water–water and DES–water interactions prevail, making the mixture resemble an aqueous solution of DES components (Hammond et al., 2017), which was later confirmed by Sapir and Harries (Sapir and Harries, 2020). Moreover, Nolasco et al. observed that in the same DES system containing <30% water (w/w), water molecules promote a strengthening of hydrogen bonds between choline chloride and urea (Nolasco et al., 2022). In biocatalysis, DES-water mixtures, whether in a water-in-DES or DES-in-water state, have been shown to be beneficial. These mixtures not only meet the enzyme's hydration needs but also reduce the inherent viscosity of DESs to a more practical level (Sanchez-Fernandez et al., 2022).

One of the most prominent advantages of using DESs in biocatalysis is their versatility and tunability. By varying the component, an HBD and an HBA, and fine-tuning the water content, DESs can be tailored to the specific needs of biocatalytic processes. It used to be estimated that there are about 10^6 possible structural variations of DESs (Panić et al., 2021) but with the continuous reporting of new DES components, multicomponent DESs, and various possible molar ratios of components (including water), the number of possible structural combinations appears to be unlimited. This vast chemical space offers enormous potential for solvent design, but also poses a major challenge: How to identify the "ideal" DES that fulfils the various criteria of a given biocatalytic system? Obviously, this task is time-consuming and sometimes leads to contradictory results in DES performance with respect to specific targets that are not easy to reconcile. For example, when Wu et al. tested different cholinium chloride- and cholinium acetate-based DESs with four HBDs (urea, glycerol, acetamide, ethylene glycol) in three molar ratios and at different water contents for the activity and stability of horseradish peroxidase, it was found that increasing the DES concentration as a co-solvent in aqueous media made the enzyme much more stable but less active than in the reference buffer (Wu et al., 2014). This pattern has been confirmed in numerous cases: DESs that stabilize enzymes (usually co-solvents with low water content) are often poor media for catalytic reactions due to the reduced enzyme activity and high solvent viscosities, resulting in slow reaction rates (Taklimi et al., 2023). Additionally, our extensive experience with these solvents has taught us that hydrophobic substrates are readily soluble in acidic DESs containing organic acids as HBDs or in hydrophobic DESs based on terpenes and fatty acids, which are generally less suitable media for enzymes than hydrophilic DESs based on polyols, sugar alcohols and sugars (with the exception of lipases, which work well in hydrophobic DES (Elgharbawy et al., 2023; Ma et al., 2024). All of this implies that it is crucial to strike a perfect balance, which essentially means finding the DES candidate that satisfies all relevant factors for the application, such as stabilization and activation of enzymes or improved substrate solubility, in a balanced manner.

Traditionally, navigating this vast design space to determine an optimal DES for specific applications has mostly relied on trial-and-error methods (e.g., measuring rection rates and calculating reaction yields in different DESs), without systematic exploration of the influence of DES on specific reaction targets (e.g., enzyme behavior and substrate solubility in these solvents), and with structure-property relationships using available computational tools. This has hindered the strategic design of these inherently tailored solvents. In addition, the understanding of intermolecular interplay between DES components, water and reactants is still in its infancy although our comprehension of these solvents has evolved over the last decade.

To fully exploit the potential of DESs and accelerate the design of a DES with optimal properties, several important steps are required: (*i*) Obtaining a thorough understanding of the DES structure at the molecular level and its corresponding properties; (*ii*) Understanding the interactions of DES with reacting compounds (biocatalyst, substrate(s)/product(s), cofactor(s), co-substrate(s)) at the molecular level by combining experimental and computational approaches; (*iii*) Comprehensive experimental screening of promising DES candidates with respect to factors relevant to the process of interest (solubility and stability of reacting compounds, enzyme activity, and product/substrate inhibition); (*iv*) Utilizing computational tools to establish relationships between DES composition and desired properties, and possibly develop predictive Quantitative Structure-Property Relationships (QSPRs); (*v*) Development of sustainable methods for product recovery, and recycle/reuse of DES (Figure 1). In addition to the above steps, green chemistry principles should be considered when selecting DES, including consideration of the environmental footprint of the solvent, cost and ease of recycling (Abildskov

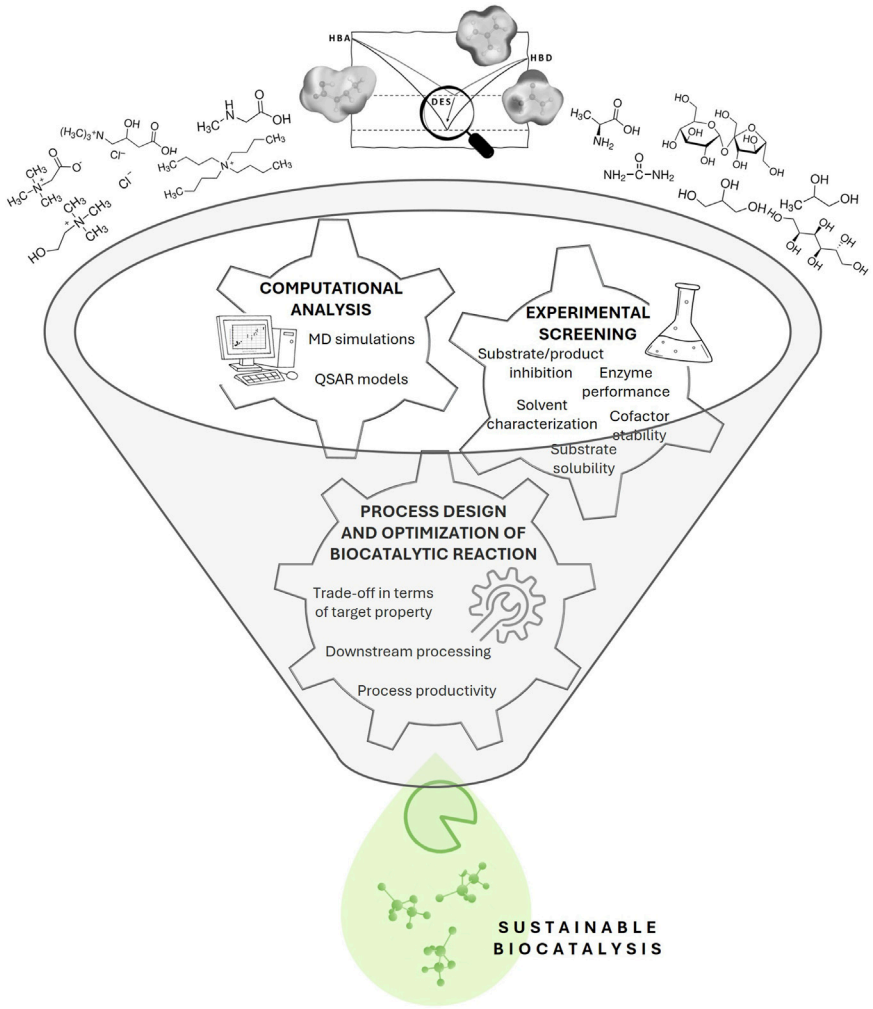

FIGURE 1
Rational design of DES for sustainable biocatalysis.

et al., 2013). By favoring sustainable and non-toxic DESs, we could minimize environmental impact while optimizing the biocatalytic processes.

Molecular dynamics simulations have proven to be powerful in understanding thermodynamic and transport processes in DESs at the atomic level, providing insights into fundamental phenomena that may not be accessible through experiments (Bittner et al., 2024). Another computational tool, the Conductor-like Screening Model for Real Solvents (COSMO-RS), provides a computational approach to generate σ-profiles (molecular descriptors) of DESs, which provide essential information on hydrogen bonding, and electrostatic and dispersion interactions in solutions (Klamt, 2005). These descriptors enable the quantification of structural changes and are widely used for high-throughput screening of DES candidates regarding the solubility of organic and inorganic molecules in DESs, but are also very useful in development of QSPR models and machine learning to predict the physicochemical properties of DESs (Benguerba et al., 2019; Lemaoui et al., 2020; Lemaoui et al., 2022). Recently, we developed a robust and reliable QSPR model based on artificial neural networks to predict the ability of DESs to stabilize dehydrogenase (Radović et al., 2024). Thus, we have shown for the first time that such models with their high prediction accuracy provide a reliable means for *in silico* screening of DESs, obviating the need for labor-intensive experimental screening and paving the way for rational design of tailored solvents. In general, mathematical and simulation models allow for the exploration of a vast chemical space of DESs that would be impossible to capture experimentally, making them essential for optimizing these solvents for industrial applications. However, accurately modeling and simulating DESs at the molecular level is challenging due to the simultaneous occurrence of multiple interactions (Lemaoui et al., 2020). Concerning the ecological footprint of DESs, they generally exhibit low to moderate toxicity to vertebrates, invertebrates, and various animal cell lines (Lomba et al., 2021). Several authors reported that DESs produced from natural metabolites can be classified as "biodegradable" according to OECD guidelines (Radošević et al., 2015; Torregrosa-Crespo et al., 2020). This means that as long as natural metabolites such as choline, betaine,

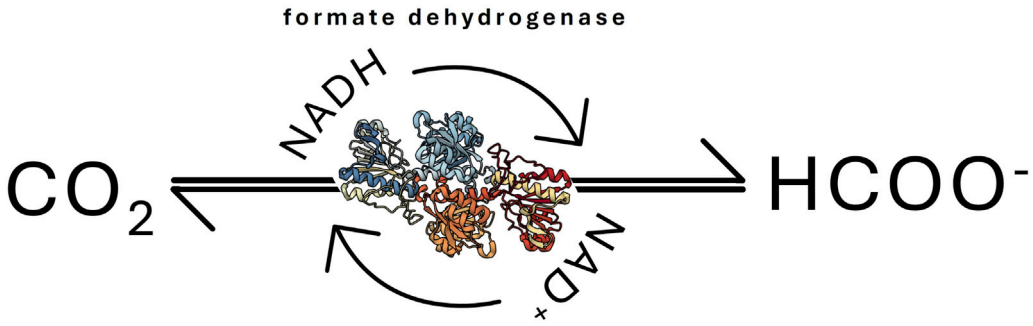

FIGURE 2
Formate dehydrogenase (FDH)-catalysed CO_2 conversion to formate.

polyols, sugars, and amino acids are used in the preparation of DESs, these solvents are expected to have a low environmental impact. In terms of cost, DESs are generally easy and inexpensive to prepare from readily available and renewable materials with 100% atom economy. Depending on their primary constituents, the cost of DESs ranges from €7 to €100 kg^{-1}, which is comparable to organic solvents (Panić et al., 2021). The cost flexibility allows solvent selection that matches the price of the product, making DESs an attractive option for large-scale applications (Rente et al., 2022).

It should be noted that the downstream processes of the biocatalytic reactions in DESs, which are often the most complex and costly part of the whole process, are not yet sufficiently addressed. One of the major challenges in DES-assisted biocatalytic reactions is the isolation of the product as well as the regeneration and reuse of the DES. In this context, an advantageous property of DESs — their non-volatility — becomes a problem unless the products are volatile and can be removed by evaporation, as has already been shown for the recovery of butyl butyrate from ILs (Pohar et al., 2012). Due to their low vapor pressure, it is practically impossible to remove DESs by evaporation. Therefore, various techniques have been proposed for the recovery of target compounds and recycling of DESs, including liquid-liquid extraction with a different solvent, solid-liquid extraction with macroporous resins, and the use of antisolvents (Panić et al., 2021; Zhang et al., 2024).

In this field, two studies stand out as they offer new perspectives for downstream processes with these solvents. First, Maugeri et al. showed the separation of alcohol and ester in DES after kinetic resolution, with the ester forming a separate phase, a viable method when the product or substrate is insoluble in DES (Maugeri et al., 2012). Secondly, in the study by Pätzold et al., DES compounds (menthol and dodecanoic acid) acted simultaneously as substrates and reaction solvent in lipase-catalyzed esterification for the synthesis of (-)-methyl dodecanoate, where the product was separated from the DES reaction mixture by a vacuum distillation step, and a second esterification reaction could be performed with the recovered (-)-menthol (Pätzold et al., 2019a). Both studies show that through innovative thinking in downstream processing, the unique properties of these solvents can be utilized, making them very attractive for sustainable biocatalysis.

3 Navigating DES screening complexity: enzymatic CO_2 conversion to formate as a case study

Given the demonstrated potential of DESs as versatile media for biocatalysis, our study aimed to illustrate effective strategies for screening these solvents using the case of formate dehydrogenase (FDH)-catalyzed reduction of CO_2.

The reduction of CO_2 — whether by electrochemical or (bio) catalytic means — produces formate, the first stable intermediate product in the conversion of CO_2. The resulting formate can be further converted to valuable chemicals such as formaldehyde and methanol through additional enzymatic reactions involving aldehyde dehydrogenase and alcohol dehydrogenase. However, formate is now increasingly recognized as an energy source in its own right (Reda et al., 2008; Villa et al., 2023). It is known that the enzyme FDH is able to reduce CO_2 to formic acid using a coenzyme such as NADH or NADPH (Figure 2) (Villa et al., 2023). The complexity of this reaction arises from several limitations: (*i*) the low concentration of CO_2 available for the enzyme, leading to a low reaction rate, (*ii*) the relative instability of FDH and the NADH coenzyme in aqueous environments, (*iii*) the acidification of the reaction medium, firstly by the dissolution of CO_2 and secondly by formic acid formation, can cause further FDH inhibition and NADH degradation (Zhang et al., 2018; Calzadiaz-Ramirez and Meyer, 2022).

Removing these limitations is critical to making FDH-catalyzed reduction of CO_2 to formate a practical and economically viable process for industrial and environmental applications. Among other approaches, switching to unconventional media could help solve the problems stated above. Zhang et al. were the first to show that ILs can act as cosolvents for enhanced conversion of CO_2 to methanol catalyzed by NADH-dependent FDH: the 67.1% conversion achieved in 1-butyl-3-methylimidazolium tetrafluoroborate was more than twice that in phosphate buffer (24.3%) (Zhang et al., 2018). Later, the same group demonstrated the advantages of introducing DES, L-serine:glycerol at a molar ratio of 1:6, into the electro-enzymatic conversion of CO_2 and achieved a 16-fold higher reaction yield compared to the control reaction in the buffer (Zhang et al., 2022).

Instead of the traditional approach of performing the reaction and then testing for suitability, which would be extremely complex given the vast number of possible DES candidates, here we set a performance targets defined by solvent properties and process constraints. By identifying DES that fulfil these predefined goals in a balanced way, we can significantly reduce the number of trials required and allow for a more strategic allocation of resources (Abildskov et al., 2013). Based on the above considerations, the design of the solvent system with DES was divided into several phases. First, we narrowed down the list of DES candidates based on the data available in the literature on dehydrogenase performance in these solvents as well as their sustainability attributes. Then, to gain a better understanding of DES potential in overcoming the limitations associated with the reaction, the influence of selected DESs on FDH activity and stability, NADH stability, and CO_2 solubility was systematically investigated. A computational analysis was further performed to gain insight into the DES structure and the corresponding physicochemical properties affecting the measured parameters. For the most promising DES candidates, further experiments were performed to investigate NADH stability under acidification at CO_2 saturation. Finally, considering the trade-offs between the results in different solvent systems with DESs in terms of performance objectives, the most suitable DES candidate was proposed. This solvent system was then tested for the reaction and compared with the results in the reference buffer. At this point, it should be mentioned that for the purpose of this study, we excluded *in situ* cofactor regeneration, e.g., based on chemical, electrochemical, photochemical, or enzymatic processes (Wichmann and Vasic-Racki, 2005) to maintain methodological clarity and to avoid potential confounding effects from new reactants.

3.1 DESs selection and characterization

Ensuring the stability of enzymes is crucial for their industrial implementation, as it increases operational stability, prolong activity and thus increases total turnover number, and improve cost-efficiency of the process (Žnidaršič-Plazl, 2021b; Woodley, 2022). To systematically evaluate DES candidates for performance goals, we first narrowed the list to those documented in the literature as beneficial for dehydrogenases, focusing specifically on those known to stabilize FDH. Studies suggest that polyol-based DESs, containing either choline chloride or betaine as HBA, are the most effective stabilizing media for various dehydrogenases, including FDH (Bittner et al., 2022; Gajardo-Parra et al., 2023). First, seven polyol-based DESs with either choline chloride or betaine as HBA were tested at three water contents (up to 50%, w/w) for their ability to stabilize FDH. It was confirmed that glycerol-based DES containing both tested HBAs are optimal candidates for stabilizing the enzyme upon prolonged incubation at room temperature (data not shown).

Glycerol-based DESs were recently demonstrated to stabilize NAD coenzymes (Radović et al., 2022). Besides, Leron and Li (2013), Leron et al. (2013) and Biswas et al. (2023) reported that among several choline chloride-based DES containing urea, ethylene glycol, and glycerol as HBDs, the one with glycerol had the highest CO_2 solubility. The above studies also emphasize that water plays a crucial role in enzyme performance and CO_2 solubility. Finally, concerning the toxicological footprint, glycerol-based DES are considered non-toxic and biodegradable (Radošević et al., 2015).

Based on the above considerations, we selected two glycerol (Gly)-based DESs, with choline chloride (ChCl) or betaine (B) as HBA in a molar ratio of 1:2, and prepared the corresponding solutions in water (10%–90%, w/w). In parallel, we also prepared solutions in 50 mM potassium phosphate buffer (pH 7.5) to keep the pH close to the enzyme's optimal value and to possibly prevent a pH drop when CO_2 is added to the reaction medium. As previously mentioned, DESs diluted with more than 50% water (w/w) can be considered aqueous solutions of DES components (Hammond et al., 2017). Nevertheless, these mixtures were included in the study, as a high water content within DES is often essential for enzymes to sustain their catalytic activity (Taklimi et al., 2023).

A total of 20 DES-based solvents were prepared and characterized for their physicochemical properties (pH, density, and viscosity) relevant to the reaction (Table 1). As expected, the densities and viscosities of the DES aqueous solutions were strongly influenced by the water/buffer content, peaking at mixtures with 10% water (up to 1.21 g cm^{-3} and 353.70 mPa s for B:$Gly_{10\%W}$, and 1.17 g cm^{-3} and 82.63 mPa s for ChCl:$Gly_{10\%B}$). In general, B:Gly-based mixtures were denser and more viscous than their ChCl:Gly-based counterparts. All mixtures tested had pH values ranging from 5.3 to 9.2, with betaine-based mixtures being more acidic than ChCl-based ones. Dissolving DES in buffer generally maintained the solutions at pH values between 7.5 and 8. All DES mixtures remained stable for 3 months under laboratory conditions and showed no signs of contamination or precipitation.

For statistical analysis and mathematical modelling (Section 3.4.), the identification of a molecular representation that converts the component structures into descriptive features for numerical evaluation is essential (Venkatraman et al., 2018). An advanced and accurate molecular representation is the σ-profile (sigma profile), an unnormalized histogram of the screened surface charge of a molecule (Klamt, 2005). σ-profiles are distinguished from other representations by the fact that they capture nuanced effects such as polarizability and electron density asymmetry (Abranches et al., 2022). The σ-profile can be divided into three key regions: (*i*) the HBD region with negative charge densities, (*ii*) the non-polar region with nearly neutral charge densities, and (*iii*) the HBA region with positive charge densities (Figure 3A). This division is based on the fact that each atom in an HBA or HBD molecule is identifiable by a distinct peak with a specific screening charge density (σ) value (Lemaoui et al., 2020).

Here, the σ-profile of each DES-based mixture was calculated using BOVIA COSMOtherm software: the σ-profile curves for each HBA and HBD were divided into 10 regions, and the area under each region was calculated considering the molar ratios of the components and the water content (Supplementary Table S1). For glycerol, the σ-profile reveals peaks at negative polar coordinates (left side) corresponding to the positively polar H atoms in the -OH group, while peaks at positive polar coordinates (right side) correspond to the O atoms in the -OH group (Figure 3A) (Cheng et al., 2018). These polar regions interact

TABLE 1 List of DES solutions in water/buffer (10%–90%, w/w) and buffer (50 mM potassium phosphate buffer pH 7.5) used for experimental screening, together with physicochemical properties and corresponding concentration of dissolved CO_2 (c_s), pH of CO_2 saturated solutions (pH*), first-order degradation rate constant of NADH in CO_2 saturated solutions (k_{NADH}*), and residual FDH activity (A_{Res}) (c_{FDH} = 12.8 mg mL^{-1}, t = 14 days, T = 30°C).

		Abbrev.	pH	η (mPa s)	ρ (g cm^{-3})	c_s (mg L^{-1})	k_{NADH}* (min^{-1})	pH*	A_{Res} (%)
			Physicochemical properties			CO_2 solubility and NADH stability			FDH
Choline chloride-based DESs	Water dissolutions	ChCl:Gly$_{10\%w}$	7.51	77.88	1.17	282	0.004	6.95	0.0
		ChCl:Gly$_{30\%w}$	6.60	18.98	1.14	480	0.000	6.03	47.6
		ChCl:Gly$_{50\%w}$	7.12	4.16	1.09	702	0.009	5.68	42.1
		ChCl:Gly$_{80\%w}$	6.48	2.27	1.03	825	0.009	4.89	52.0
		ChCl:Gly$_{90\%w}$	6.25	1.48	1.02	965	0.000	4.8	0.0
	Buffer dissolutions	ChCl:Gly$_{10\%B}$	9.19	82.63	1.17	465	0.000	6.88	0.0
		ChCl:Gly$_{30\%B}$	8.75	19.61	1.14	727	0.000	6.89	95.1
		ChCl:Gly$_{50\%B}$	8.33	5.74	1.11	913	0.003	6.79	11.8
		ChCl:Gly$_{80\%B}$	7.75	2.50	1.06	1,057	0.000	6.53	70.7
		ChCl:Gly$_{90\%B}$	7.67	1.31	1.04	1,149	0.000	6.49	40.3
Betaine-based DESs	Water dissolutions	B:Gly$_{10\%w}$	6.48	353.70	1.21	311	0.000	4.73	33.3
		B:Gly$_{30\%w}$	5.96	20.86	1.15	618	0.001	4.26	70.0
		B:Gly$_{50\%w}$	5.33	8.84	1.13	829	0.006	3.87	51.5
		B:Gly$_{80\%w}$	5.29	2.27	1.04	1,101	0.008	3.75	11.9
		B:Gly$_{90\%w}$	5.47	1.31	1.03	1,112	0.005	3.77	0.0
	Buffer dissolutions	B:Gly$_{10\%B}$	7.85	219.05	1.21	509	0.003	6.39	60.0
		B:Gly$_{30\%B}$	7.46	32.87	1.17	586	0.000	6.26	59.8
		B:Gly$_{50\%B}$	7.45	6.45	1.13	765	0.001	6.24	65.0
		B:Gly$_{80\%B}$	7.49	2.27	1.06	1,027	0.009	6.24	58.5
		B:Gly$_{90\%B}$	7.47	1.19	1.04	1,010	0.000	6.31	48.3
		buffer	7.50	1.39	1.02	1,029	0.003	6.49	0.0

Abbreviations: choline chloride (ChCl), betaine (B), glycerol (Gly).

with opposite polar segments in a solution. The σ-profile's extension into strongly polar regions (-0.022 e/Å^2 < σ < -0.01 e/Å^2 on the left and 0.01 e/Å^2 < σ < 0.013 e/Å^2 on the right) is asymmetric, indicating that glycerol has a larger positive polarity surface area. This electrostatic misfit suggests that glycerol tends to act as a HBD and thus shows greater affinity for HBA in a solution (Cui et al., 2021). In contrast, the σ-profile of water extends more symmetrically into strongly polar regions, indicating its balanced ability to act as both a HBD and HBA. Finally, for ChCl, as well as for betaine (Radović et al., 2024), the strongest peak appears in the non-polar region, corresponding to the cholinium cation, followed by a peak in the HBA region, associated with the Cl^- anion. Figure 3A illustrates the sigma surfaces of the DES components (choline chloride, glycerol and water) generated by TmoleX19. The colors represent a calculated charge gradient, ranging from charge-deficient to charge-dense regions: HBD regions are labelled as deep blue and HBA regions as deep red on the surface. Non-polar regions are marked in green (Quaid and Reza, 2023). Figure 3B shows that even small changes in the ChCl:Gly mixture, such as increasing the water content from 10% to 90%, result in solvents with different polarity distributions. This demonstrates that the software is capable of capturing nuanced phenomena, which is crucial for exploring the chemical landscape of these solvents and understanding their potential impact on enzyme and coenzyme behavior, as well as the solubility of reaction participants. We have recently demonstrated the same ability of the software for the system betaine:ethylene glycol with 3 water proportions (10, 30, 50% water, w/w) (Radović et al., 2024).

3.2 Activity and long-term stability of FDH in DESs

The activity of FDH in the reference buffer and in aqueous solutions of DESs at different concentrations were measured by

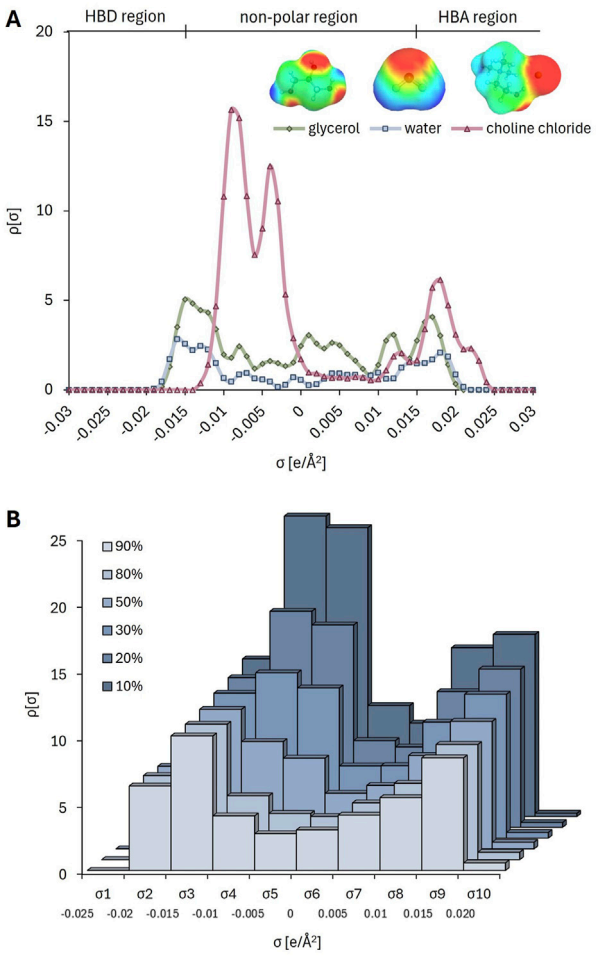

FIGURE 3
σ-surface **(A)** and σ-profiles **(B)** of individual DES constituents (choline chloride, glycerol and water), and σ-profile of corresponding DES solutions in buffer (10%–90%, w/w).

monitoring the oxidation of sodium formate. For the stability test, enzyme solutions were incubated in selected solvent systems at 30°C for 14 days and residual enzyme activity (A_{Res}) was measured at regular intervals (Table 1). Both in the reference buffer and in the mixtures with DESs, FDH inactivation followed first-order kinetics, allowing us to use this kinetic model to calculate the FDH half-life ($t_{1/2,\ FDH}$) (Figure 4).

As anticipated, FDH showed little or no activity in the DES mixtures containing ≤50% (w/w) water or buffer, while the activity increased with the addition of water and peaked in the highly diluted mixtures (90% water, w/w), although the values were still lower than those observed in the buffer (residual activities, A_R, between 44% and 92%). Interestingly, it appears that dilutions with water generally resulted in better enzyme activity than their counterparts diluted with buffer, although buffered systems are closer to the enzyme's optimal pH of 7.5 (determined experimentally, data not shown). For example, ChCl:Gly with 90% water content (ChCl:$Gly_{90\%W}$) with a pH of only 6.3 had an A_R of about 92%, while its counterpart with the buffer (ChCl:$Gly_{90\%B}$) with a pH of 7.5, yielded the A_R of only 44.5%.

DESs with a water/buffer content in the range of 30% - 80% (w/w) showed the best ability to stabilize the enzyme, with half-lives of up to 64 days, which is much higher than in the reference buffer, where $t_{1/2,\ FDH}$ was 2.1 days (Figure 4). On the other hand, highly diluted DESs (90% water/buffer, w/w) demonstrated a stabilizing effect on the enzyme comparable to that of the reference buffer.

The stability of FDH in buffered DES solutions (80% buffer, w/w) was also significantly increased compared to the reference buffer, with $t_{1/2,\ FDH}$ of 65.6 days and 29.9 days for B:$Gly_{80\%B}$ and ChCl:$Gly_{80\%B}$, respectively. Again, DESs solutions with a water/buffer content of only 10% led to a faster destabilization of the enzyme. These results are consistent with previous findings that most dehydrogenases require more than 10% water content in DES to maintain their structural integrity. DESs absorb water in their hydrogen bonding network, reducing the availability of free water molecules required for enzyme hydration. This reduction in water activity can lead to dehydration and irreversible denaturation of the enzyme (Mourelle-Insua et al., 2019; Bittner et al., 2022; Radović et al., 2024). Overall, solvent systems with 80% buffer (w/w) exhibited an optimal balance between FDH activity and stability, which was particularly evident for B:$Gly_{80\%B}$, where the A_R was 51.7% (Figure 4).

3.3 CO_2 solubility and NADH stability in DESs

The saturated dissolved CO_2 concentrations (c_s) in various DES solutions with water/buffer were evaluated after introduction of CO_2 at a flow rate of 100 mL min^{-1} until saturation. The results are presented in Table 1. All DESs mixtures with ≤50% water or buffer were poor media for dissolving CO_2, with c_s values between 282 and 913 mg L^{-1}, which is lower than those observed in the reference buffer (1,029 mg L^{-1}). Highly diluted DESs led to similar CO_2 solubilities as in the buffer, with the highest improvements observed in ChCl:$Gly_{90\%B}$ and B:$Gly_{90\%W}$, with values of 1,149 and 1,112 mg L^{-1}, respectively.

To investigate the long-term stability of the NADH coenzyme, the changes in the UV-Vis absorption spectra of NADH were observed during a 14-day incubation at 25°C in the solvent systems described above. During incubation, the absorbance loss at 340 nm followed the first-order kinetics used to calculate the NADH half-lives shown in Figure 4. The results clearly show that DES composition plays an important role in the coenzyme degradation rate. Virtually all DES aqueous solutions, except ChCl:$Gly_{90\%B}$ ($t_{1/2,\ NADH}$ = 2.9 days) and B:$Gly_{90\%W}$ ($t_{1/2,\ NADH}$ = 0.8 days), stabilized the coenzyme compared to the reference buffer ($t_{1/2,\ NADH}$ = 4.6 days). In general, ChCl-based DESs were more suitable for coenzyme stabilization than betaine-based DESs. This was particularly pronounced for DESs with 10% buffer content (e.g., for ChCl:$Gly_{10\%B}$, $t_{1/2,\ NADH}$ was 44.2 days, while for B:$Gly_{10\%B}$, $t_{1/2,\ NADH}$ was 17.5 days). As evident from Figure 4, a higher DES content had a positive effect on the ability of solvent systems to stabilize the coenzyme for all DESs tested. This was most evidenced for B:Gly solutions in water, where the $t_{1/2,\ NADH}$ for B:$Gly_{30\%W}$ and B:$Gly_{90\%W}$ was 65.7 and 0.8 days, respectively.

To further navigate the DES screening, the short-term NADH stability in DES aqueous solutions saturated with CO_2 was investigated. The presence of dissolved CO_2 not only affects the

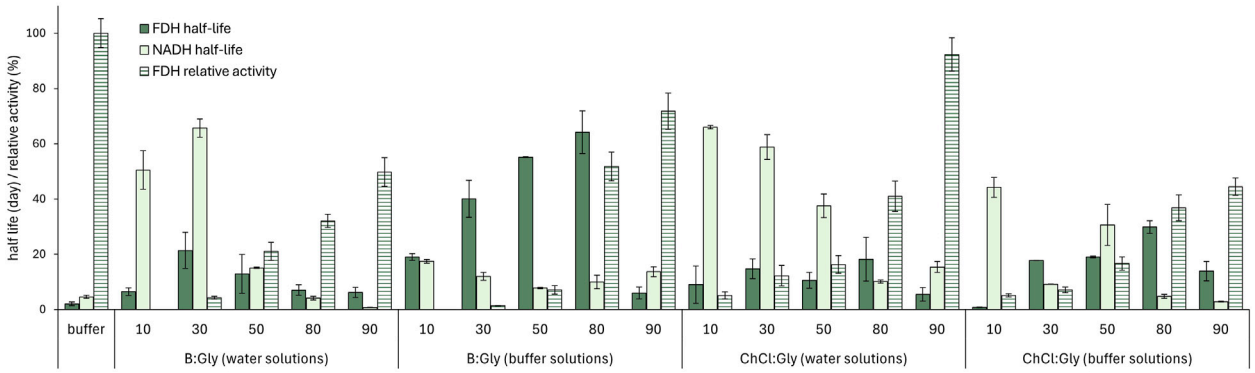

FIGURE 4
FDH relative activity (c_{FDH} = 1.5 mg mL^{-1}; c_{NADH} = 0.1 mg mL^{-1}; $c_{formate}$ = 10 mg mL^{-1}, T = 25°C) and half-life (c_{FDH} = 12.8 mg mL^{-1}, T = 30°C), along with NADH half-life (c_{NADH} = 0.03 mg mL^{-1}, T = 25°C) in B:Gly and ChCl:Gly solutions in water/buffer (10%–90%, w/w) and the reference 50 mM potassium phosphate buffer (pH 7.5). FDH relative activities in DES mixtures are expressed as a percentage of the activity measured in the reference buffer.

intrinsic properties of the DESs but also the behavior of the system after substrate addition. It has been previously reported that the acidification of the reaction medium by dissolving CO_2 leads to enhanced NADH degradation, which directly affects the conversion of CO_2 to formic acid (Zhang et al., 2018). Therefore, NADH solutions in the solvent systems described above were monitored over a period of 90 min, and the corresponding degradation constants (k_{NADH^*}) were calculated using a first-order kinetic model (Table 1). In general, buffer-diluted DESs were equally or more successful in stabilization of the coenzyme over the tested period ($k_{NADH^*} \leq 0.003$ min^{-1}) than the reference buffer (k_{NADH^*} = 0.003 min^{-1}), while water-based solvent systems with DESs were poor media in this regard, especially at high water contents (k_{NADH^*} up to 0.009 min^{-1}). This effect is directly related to the inability of water-diluted DESs to maintain pH close to neutral. For example, after the introduction of CO_2 into B:Gly$_{80\%W}$, pH decreased to 3.75, resulting in the highest observed k_{NADH^*} value of 0.008 min^{-1}. Moreover, buffered solutions of ChCl-based DESs maintained a higher pH than betaine-based DES solutions after CO_2 saturation, resulting in complete stabilization of NADH over the time tested, except for ChCl:Gly$_{50\%B}$ (k_{NADH^*} = 0.003 min^{-1}).

3.4 Statistical analysis of data and development of mathematical models

The correlations between the physicochemical properties (pH, viscosity and density) of the DESs used, the DES descriptors (σ-profiles), FDH performance, long-term NADH stability and CO_2 solubility were analyzed using the Spearman correlation matrix, which was selected due to the non-normal data distribution. The analysis confirmed our above assumptions and findings from the experimental screening: the targeted properties of the reaction affected by the DES composition led to contradictory results (Table 2). First, both FDH activity and stability in tested solvent systems showed negative correlations with NADH stability. In addition, FDH activity values demonstrated negative correlations with all analyzed variables except CO_2 solubility, favouring aqueous/buffered media over DES solutions with lower amounts of aqueous phase. Besides, negative correlations were found also for FDH and NADH stability with CO_2 solubility (Table 2).

The Spearman correlation matrix shown in Table 2 highlights the complex interplay between the physicochemical properties of DES (pH, density, viscosity) and the DES descriptors with the performance characteristics of FDH and the stability of its cofactor NADH. As expected, significant negative correlations were observed between FDH activity and DES density/viscosity, likely due to the lower mobility and diffusion of substrates and enzymes. Conversely, NADH stability showed significant positive correlation with the density/viscosity of the solvent systems with DESs, which can be attributed to the slower overall dynamics of the solvents providing a less detrimental environment for dissolved NADH.

FDH activity and NADH stability are significantly impacted by pH value, while for FDH stability there is no correlation with this chemical property. It is well-established that enzyme activity (Bisswanger, 2017) and NADH stability (Zachos et al., 2019) are pH-dependent. However, the consistent reports on pH-independent ability of DESs to stabilize various enzymes remains puzzling. This intriguing observation hints at other mechanisms, such as direct interactions between DES components and proteins or with nearby water molecules, potentially altering the medium's water activity (Damjanović et al., 2024).

Furthermore, the analysis revealed that nearly all DES descriptors significantly impacted the targeted properties. Specifically, S^1_{mix} and S^2_{mix} (HBD region, medium polarity), S^3_{mix} - S^5_{mix} (nonpolar region, positive charges), S^6_{mix} – S^8_{mix} (nonpolar region, negative charges) and S^9_{mix} (HBA region) (Lemaoui et al., 2020), all demonstrated a significant influence on the properties being studied. FDH activity exhibited a negative correlation with all the descriptors, except for S^2_{mix}, which showed a positive correlation. Conversely, both FDH stability and NADH stability demonstrated positive correlations with all the descriptors, except for S^2_{mix}, which displayed a negative correlation. Interestingly, the analysis suggests an inverse relationship between enzyme activity and stability in DESs: solvents rich in HBA and non-polar domains stabilize the enzyme (and coenzyme), while HBD-rich solvents enhance enzyme activity but may lead to destabilization. These findings emphasize

TABLE 2 Spearman correlation matrix.

	A_R	$t_{1/2,\ FDH}$	$t_{1/2,\ NADH}$	c_S	ρ	η	pH	S^1_{mix}	S^2_{mix}	S^3_{mix}	S^4_{mix}	S^5_{mix}	S^6_{mix}	S^7_{mix}	S^8_{mix}	S^9_{mix}	S^{10}_{mix}
A_R	1.000																
$t_{1/2,\ FDH}$	-0.146	1.000															
$t_{1/2,\ NADH}$	**-0.577**	-0.045	1.000														
c_S	**0.887**	**-0.028**	**-0.603**	1.000													
ρ	**-0.939**	**0.199**	**0.635**	**-0.866**	1.000												
η	**-0.944**	**0.142**	**0.663**	**-0.902**	**0.942**	1.000											
pH	**-0.323**	**0.063**	-0.104	-0.159	**0.461**	**0.301**	1.000										
S^1_{mix}	**-0.953**	**0.146**	**0.679**	**-0.908**	**0.964**	**0.974**	**0.316**	1.000									
S^2_{mix}	**0.953**	**-0.146**	**-0.679**	**0.908**	**-0.964**	**-0.974**	**-0.316**	-1.000	1.000								
S^3_{mix}	**-0.906**	**0.101**	**0.727**	**-0.882**	**0.909**	**0.957**	0.170	**0.948**	**-0.948**	1.000							
S^4_{mix}	**-0.906**	**0.101**	**0.727**	**-0.882**	**0.909**	**0.957**	0.170	**0.948**	**-0.948**	1.000	1.000						
S^5_{mix}	**-0.953**	**0.146**	**0.679**	**-0.908**	**0.964**	**0.974**	**0.316**	1.000	-1.000	**0.948**	**0.948**	1.000					
S^6_{mix}	**-0.932**	**0.110**	**0.694**	**-0.900**	**0.948**	**0.964**	**0.286**	**0.990**	**-0.990**	**0.958**	**0.958**	**0.990**	1.000				
S^7_{mix}	**-0.906**	**0.101**	**0.727**	**-0.882**	**0.909**	**0.957**	0.170	**0.948**	**-0.948**	1.000	1.000	**0.948**	**0.958**	1.000			
S^8_{mix}	**-0.906**	**0.101**	**0.727**	**-0.882**	**0.909**	**0.957**	0.170	**0.948**	**-0.948**	1.000	1.000	**0.948**	**0.958**	1.000	1.000		
S^9_{mix}	**-0.906**	**0.101**	**0.727**	**-0.882**	**0.909**	**0.957**	0.170	**0.948**	**-0.948**	1.000	1.000	**0.948**	**0.958**	1.000	1.000	1.000	
S^{10}_{mix}	-0.202	0.249	-0.139	-0.072	0.177	0.099	**0.439**	0.144	-0.144	-0.144	-0.144	0.144	0.044	-0.144	-0.144	-0.144	1.000

Abbreviations: FDH relative activity (A_R), FDH half-life ($t_{1/2,\ FDH}$), NADH half-life ($t_{1/2,\ NADH}$), CO_2 saturated dissolved concentration (c_s), DES descriptors (S^1_{mix} – S^{10}_{mix}).
Correlations significant at $p<0.05$ are marked in bold.

10.3389/fchem.2024.1467810

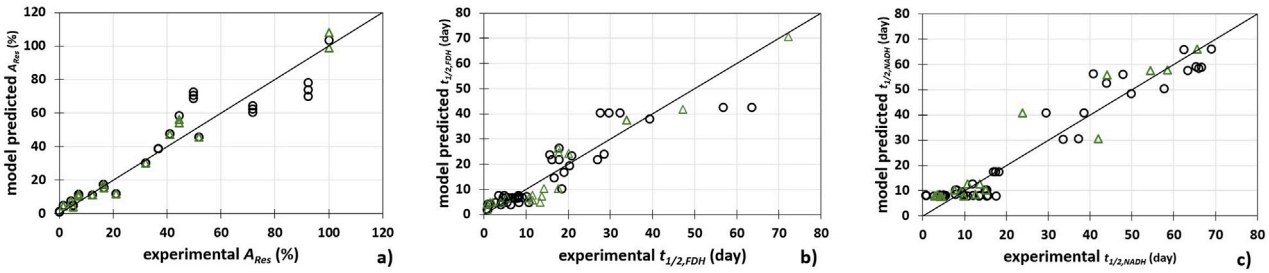

FIGURE 5
Comparison between experimental data and piecewise linear model predicted data for **(A)** FDH activity (A_{Res}), **(B)** FDH half-life ($t_{1/2,\ FDH}$) and **(C)** NADH half-life ($t_{1/2,\ NADH}$). (O) calibration data set (Δ) prediction data set.

the delicate balance between enzyme activity and stability in DESs, driven by their specific compositional properties (as described by σ-descriptors). Similar interplay between the enzyme's active and stable (but inactive) states, influenced by the water content in DESs, has been confirmed in our recent study on lysozyme behaviour in DESs based on various naturally occurring osmolytes (Damjanović et al., 2024). Insights into this relationship could guide the rational design of DESs for optimized biocatalysis applications: by performing similar statistical analyses on a larger set of DESs, it may be possible to predict an ideal σ-profile shape, and thereby identify or design the most suitable DES for a specific purpose.

According to discussed above, our next step was to see if it was possible to develop a simple QSAR model to summarize the relationship between the targeted properties (FDH activity, FDH stability, and NADH stability) and the DES descriptors (Figure 3; Supplementary Table S1) along with the physicochemical properties (Table 1) of the DESs using piecewise linear regression (PLR) (Figure 5). The latter is a powerful tool for modelling complex relationships in a simple and interpretable way, especially when the relationship between variables changes at a certain point. The input variables of the PLR models were selected based on the significant correlations in the Spearman correlation matrix. The relationship between the observed data and model predictions was also estimated using the coefficient of determination for prediction (R_{pred}^2), the adjusted coefficient of determination for calibration ($R_{pred}{}^2{}_{adj}$), the root mean square error of prediction (*RMSEP*), the ratio of prediction to deviation (*RPD*) and the ratio of the error range (*RER*).

As shown in Table 3 and Figure 5, the developed models describe the experimental data with high precision. The best agreement between the experimental data and the data predicted by the model was obtained for the FDH activity (Figure 5A) (R_{cal}^2 = 0.914, $R_{cal}{}^2{}_{adj}$ = 0.913, *RMSEC* = 7.203%, R_{pred}^2 = 0.905, $R_{pred}{}^2{}_{adj}$ = 903, *RMSEP* = 7.379%, *RPD* = 5.589, *RER* = 18.324). On the other hand, the largest scatter between the model and experimental data was found for the FDH half-life (Figure 5B) (R_{cal}^2 = 0.829, $R_{cal}{}^2{}_{adj}$ = 0.827, *RMSEC* = 4.775 days, R_{pred}^2 = 0.738, $R_{pred}{}^2{}_{adj}$ = 0.731, *RMSEP* = 4.944%, *RPD* 3.292, *RER* = 10.456).

According to Hussain et al., an R^2 value of 0.75 is considered significant, an R^2 value of 0.50 is considered moderate, and an R^2 value of 0.26 is considered weak (Hussain et al., 2018). Furthermore, models with *RPD* < 1.4 are considered non-reliable, those with *RPD* in the range from 1.4 to 2 are considered fair, while models with *RPD* > 2 are described as excellent models (Chang et al., 2001). Models with *RER* > 4 are acceptable for data screening, models with *RER* > 10 can be used for quality control, while models with *RER* > 15 can be used for quantification (Sim et al., 2023). Therefore, the PLR models developed for the prediction of FDH activity and NADH half-life based on R_{pred}^2 can be considered substantial, while the model developed for the prediction of FDH half-life can be considered moderate. Based on the *RPD* values, all three models developed can be considered reliable. And based on the *RER* values, the model developed for the prediction of FDH activity can be used for quantification (*RER* = 18.324), while the other two modes can be used for quality control. Therefore, it can be concluded that the feasibility of mathematical models for predicting targeted properties or applications of DES using easily measurable physicochemical properties and chemical descriptors, as demonstrated here, could be valuable for both industrial applications and research efforts focusing on these solvents. Additionally, utilizing these QSPR models may not only assist in predicting the properties of interest but also provide valuable insights into the relationship between the structure of the DES and its measurable properties. By analyzing how various structural features influence the targeted properties, these models can help unravel the underlying mechanisms driving behavior of biomolecules in DESs. This understanding can inform the design and optimization of DESs, leading to more effective and tailored applications in various fields.

3.5 Trade-off between the performance of DESs with respect to target properties

We have demonstrated that the evaluation of different targets related to the tested reaction often leads to contradictory results regarding the optimal DES. For example, the enzyme dissolved in B:$Gly_{30\%B}$ showed remarkable stability with a half-life of 40.1 days, while its relative activity was less than 2% of that in the buffer. This DES also showed average performance in the long-term stability of the coenzyme, with a half-life of 12.1 days. In contrast, the enzyme dissolved in B:$Gly_{90\%B}$ maintained a high relative activity, which was 71.2% of that in the reference buffer, but was one of the worst candidates for enzyme stabilization with a half-life of only 6.0 days. In general, "concentrated" DESs (<50% water/buffer, w/w), with η > 18 mPa s showed high efficacy in stabilizing both the enzyme and the

TABLE 3 Pricewise linear regression models for prediction of FDH stability, FDH activity and NADH stability based on the specific input variables. (Coefficient of determination for calibration (R_{cal}^2), the adjusted coefficient of determination for calibration (R_{cal}^2 adj), the root mean square error for calibration (*RMSEC*), the coefficient of determination for prediction (R_{pred}^2), the adjusted coefficient of determination for calibration (R_{pred}^2 adj), the root mean square error of prediction (*RMSEP*), the ratio of prediction to deviation (*RPD*),the ratio of the error range (*RER*)).

Output variable	Input variables	Model equation	R_{cal}^2 R_{cal}^2 adj	*RMSEC*	R_{pred}^2 R_{pred}^2 adj	*RMSEP*	*RPD*	*RER*
FDH activity	Viscosity (X_1) Density (X_2) pH (X_3) DES descriptors 1–9 (X_4-X_{12})	Y_1 = (31.635 + 0.024 X_1-81.589 X_2-0.257 X_3+0.382 X_4+41.465 X_5-98.311 X_6-93.683 X_7+8.822 X_8+201.025 X_9+123.045 X_{10} + 80.146 X_{11} + 46.359 X_{12}) (for $Y_1 \leq 30.081$) + (25.079 + 35.851 X_1+1782.264 X_2-25.075 X_3+0.080 X_4+42.087 X_5-99.096 X_6-67.368 X_7-36.899 X_8+22.587 X_9+29.178 X_{10}-29.264 X_{11}-70.624 X_{12}) (for $Y_1 > 30.081$)	0.914 0.913	7.203	0.905 0.903	7.379	5.589	18.324
FDH half-life	Viscosity (X_1) Density (X_2) pH (X_3) DES descriptors 1–9 (X_4-X_{12})	Y_2 = (3.489-0.015 X_1-7.078 X_2-1.359 X_3+0.113 X_4+7.413 X_5-6.365 X_6-6.827 X_7+2.733 X_8+12.839 X_9+8.943 X_{10} + 2.277 X_{11}-3.795 X_{12}) (for $Y_2 \leq 14.041$) + (4.429-0.229 X_1-285.320 X_2+11.223 X_3+0.109 X_4+19.063 X_5+10.294 X_6-10.294 X_7-10.649 X_8+9.620 X_9+12.795 X_{10} + 8.317 X_{11} + 1.174 X_{12}) (for $Y_2 > 14.041$)	0.829 0.827	4.775	0.738 0.731	4.944	3.292	10.456
NADH half-life	Viscosity (X_1) Density (X_2) DES descriptors 1-9 (X_3-X_{11})	Y_3= (11.199 + 0.001 X_1+4.581 X_2+0.121 X_3+21.634 X_4-26.329 X_5-10.074 X_6-0.219 X_7+29.394 X_8+25.508 X_9+11.581 X_{10}-11.355 X_{11}) (for $Y_3 \leq 23.872$) + (−0.217-0.175 X_1+691.395 X_2+0.157 X_3-30.392 X_4-58.475 X_5-3.406 X_6-7.604 X_7+28.916 X_8+14.168 X_9+28.553 X_{10}-24.523 X_{11}) (for $Y_3 > 22.872$)	0.930 0.929	4.789	0.856 0.853	6.150	3.595	14.193

coenzyme, but also high viscosity, which poses significant challenges for scaling up processes with these solvents. Based on these observations, it is crucial to reconcile these results by finding a DES that optimally fulfils the desired properties and thus contributes to the overall efficiency of the process. A graphical representation shown in Figures 6A, B illustrates the trade-off between the performance of ChCl:Gly and B:Gly, respectively, with different buffer proportions with respect to the targeted property values (FDH activity/stability, CO_2 solubility, NADH stability in saturated CO_2 solutions, and compared to the reference buffer). The radar chart is bounded by the respective lower and upper limits of each target property, with ratings, ranging from 0 to 100, reflecting the performance of DES-based solvents relative to the best candidate for each target property. At this point, DESs diluted with water were omitted due to their poor ability to stabilise NADH after acidification of the medium due to CO_2 introduction (Table 1).

As can be seen from Figure 6A, ChCl:$Gly_{80\%B}$ has a balanced distribution across all target property values, which is crucial for the simultaneous optimization of the reaction where all design objectives are equally important. In particular, this DES, which in this case could be considered an additive rather than a solvent (Hammond et al., 2017), had the highest values for all target properties except for FDH activity, where the reference buffer resulted in the highest values. It should be emphasized that ChCl:$Gly_{80\%B}$ had an almost 15-fold higher $t_{1/2,\ FDH}$ value compared to the buffer and stabilized the coenzyme more effectively when CO_2 was dissolved in the solvent system. B:$Gly_{80\%B}$ also showed similar balanced behavior to ChCl:$Gly_{80\%B}$, but was ineffective in stabilizing NADH after dissolving CO_2.

3.6 FDH-catalyzed CO_2 conversion to formate in the most promising solvent system

Since ChCl:Gly dissolved with 80% (w/w) buffer (ChCl:$Gly_{80\%B}$) was found as the most promising solvent system for the FDH-catalyzed conversion of CO_2 to formate, the reaction was performed in a medium pre-saturated with CO_2 and product formation was monitored over time. The amount of formate produced by the enzymatic CO_2 reduction in the selected solvent system and in the reference buffer is shown in Figure 7. The reaction performed in the DES-supplemented medium yielded 26.5 μmol mL^{-1} of formate with a volumetric productivity of 6.6 μmol $mL^{-1}{\cdot}h^{-1}$, while the reaction in the buffer yielded 22.7 μmol mL^{-1} with a volumetric productivity of 5.6 μmol $mL^{-1}{\cdot}h^{-1}$. These differences can be attributed to the slightly lower solubility of CO_2 in the buffer and the pronounced degradation of NADH in the buffer due to acidification by dissolved CO_2 (Wu et al., 1986).

NADH stability was monitored in a separate experiment without enzyme addition: after 4 h (corresponding to the reaction time), the NADH concentration in the buffer decreased to 78% of its initial value, while in the DES medium the NADH concentration remained above 98% (data not shown). The shape of the concentration vs. time curve reflects the interplay of several factors, including enzyme activity, CO_2 solubility and availability, and NADH degradation dynamics. The variations in formate concentration between the two solvents observed during the first

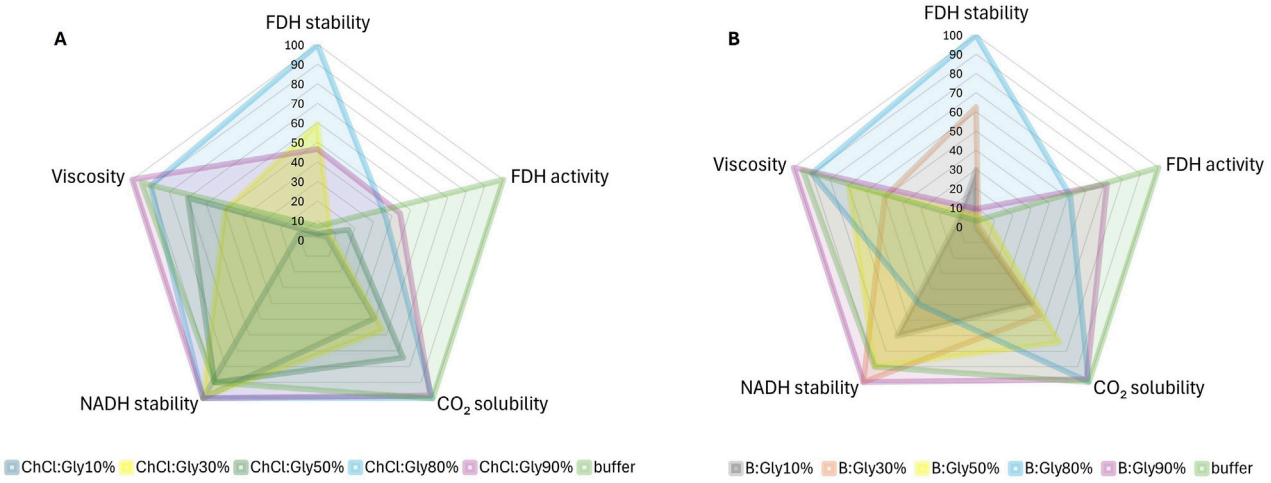

FIGURE 6
Radar plot evaluating ChCl:Gly **(A)** and B:Gly **(B)** and their corresponding solutions in buffer (10%–90%, w/w) in terms of target properties (FDH activity and stability, CO_2 solubility in DES systems, stability of NADH after solvent saturation with CO_2, and DES systems' viscosity). The radar chart is bounded by the specific lower and upper limits for each target property. Ratings, ranging from 0 to 100, reflect the performance of DES-based solvents relative to the best candidate for each target property.

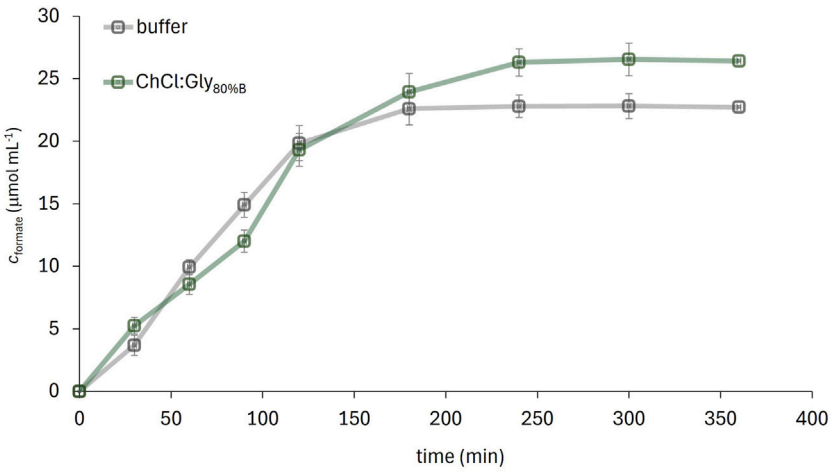

FIGURE 7
FDH-catalysed CO_2 conversion to formate in ChCl:$Gly_{80\%B}$ (20%, w/w) solution of ChCl:Gly in potassium phosphate buffer) and the reference 50 mM potassium phosphate buffer (pH 7.5) (c_{FDH} = 28.8 mg mL^{-1}, c_{NADH} = 16.4 mg mL^{-1}, T = 25°C).

120 min may be attributed, on one hand, to the higher enzyme activity in the buffer compared to ChCl:$Gly_{80\%B}$, and, on the other hand, to the enhanced CO_2 solubility and NADH stability provided by the DES. It is presumed that this dynamic interplay results in the reaction rate being sometimes higher in the buffer and at other times in the DES.

In addition to improving volumetric productivity, the true potential of using ChCl:$Gly_{80\%B}$ lies in its ability to stabilize FDH and thus extend the enzyme's half-life by up to 15-fold compared to the buffer. Although this DES property is not fully utilized in a reaction lasting only 4 h, it is of great advantage in a continuous process (e.g., using an enzymatic membrane reactor). Under steady-state conditions, the volumetric productivity of the DES-assisted process could be significantly increased, as the productivity inversely correlates with the enzyme's deactivation rate constant. Therefore, the productivity of the selected process under study was estimated for continuous operation mode comprising the enzyme inactivation rate. Considering the following assumptions: (*i*) that the process runs under steady-state conditions, (*ii*) that the enzyme is continuously deactivated over time according to first-order kinetics, and (*iii*) that the substrate concentration remains relatively constant, the reaction performed in buffer over 10-day period would yield 185.7 μmol mL^{-1} formate, while the reaction carried out in ChCl:$Gly_{80\%B}$ over the same period would yield 639.0 μmol mL^{-1} formate, which is approximately a 3.5-fold

improvement. The calculation of overall productivity included estimation of the Michaelis–Menten kinetic parameters by fitting the NADH concentration profiles to the differential equation describing the change in substrate concentration over time. The results showed that both the maximum reaction rate (v_{max}) and the NADH saturation constant (K_s) were higher for the solvent system with DES. In the buffer, the constant values were v_{max} = 0.091 μmol mL^{-1} min^{-1} and K_s = 6.746 μmol mL^{-1}, while for the systems with DES, the constants were v_{max} = 0.133 μmol mL^{-1} min^{-1} and K_s = 12.133 μmol mL^{-1}.

Finally, downstream processing was not part of this study. Nevertheless, based on the available literature, liquid–liquid extraction with the green solvent 2-methyltetrahydrofuran (Slater et al., 2016; Laitinen et al., 2021) appears to be a promising option for the separation of dilute aqueous formate solutions in the context of developing sustainable formic acid production.

4 Conclusion

DESs offer considerable potential for improving biocatalytic processes. Finding the ideal solvent requires a balanced approach that considers all relevant factors, from the behavior of all reaction participants in the medium to downstream processing and the overall economic and environmental sustainability of the process. This paper presents a complementary strategy that integrates experimental screening with computational tools. By using performance targets defined by solvent properties and process constraints, this approach aims to facilitate the rational design of DESs tailored to specific biocatalytic systems. The effectiveness of the proposed approach is demonstrated using a case study of the NADH-dependent formate dehydrogenase-catalyzed reduction of CO_2 to formate.

By systematically analyzing the performance of 20 DES-based solvents in terms of enzyme stability, activity, co-enzyme stability, and product solubility, we successfully navigated the DES screening process. It has been shown that certain DESs are highly efficient in stabilizing FDH and the coenzyme NADH, while none of the DES candidates were able to improve enzyme activity or the solubility of CO_2. Additionally, we have demonstrated that the evaluation of different targets related to the tested reaction often leads to contradictory results regarding the optimal DES. By analyzing the data using Spearman correlation coefficients and evaluating trade-offs between the performance of DES-based solvents with respect to target properties, we identified a candidate, ChCl:Gly$_{80\%B}$, that exhibited a balanced distribution across all target property values. Moreover, this DES displayed an almost 15-fold higher FDH half-life value compared to the buffer and was more effective in stabilizing the coenzyme after addition of CO_2. In the FDH-catalyzed reduction of CO_2, ChCl:Gly$_{80\%B}$ outperformed the conventionally used buffered media in terms of volumetric productivity in a batch process. This solvent candidate proved to be suitable for use in continuous process due to the exceptional stability of FDH in this solvent. Furthermore, we developed a simple QSAR model to summarize the relationship between the targeted properties and the DES characteristics. These models demonstrate the feasibility of mathematical models for predicting the specific performances of DESs based on easily measurable physicochemical properties and molecular descriptors of the solvent.

However, to fully realize the benefits of DESs in biocatalysis, further research and development of computational tools and sustainable methods for product recovery is crucial. Finally, our combined experimental and computational approach increases reliability, optimizes resources, and accelerates DES-based solvent development for enzyme stabilization, as well as for other industrial applications of these green solvents. This approach improves the scalability and cost-effectiveness of DESs and represents a significant advance in DES-based industrial processes.

5 Materials and methods

5.1 Materials

For the enzymatic reactions performed in this study, the NADH-dependent formate dehydrogenase (FDH) from *Pseudomonas sp. 101* was used (see Supplementary Information) (Tishkov et al., 1993). Carbon dioxide (CO_2) with a purity of 99.5% was acquired from Messer Croatia Plin (Zaprešić, Croatia), while all other chemicals were purchased from Sigma-Aldrich (St. Louis, Missouri, United States). All materials had a purity of at least 99% and were used as received without further purification.

5.2 DES preparation and physicochemical characterization

For the preparation of DESs based on betaine (B) and choline chloride (ChCl), the hydrogen bond acceptor (HBA) and the hydrogen bond donor (HBD) were mixed in a molar ratio of 1: 2 with water or 50 mM potassium phosphate buffer (pH 7.5) in defined proportions (Table 1). Prior to use, ChCl was dried in a vacuum concentrator at 60°C for 24 h. The mixtures were stirred and heated to 60°C until a colourless and homogeneous liquid was formed. All prepared DESs were stored in sealed bottles until further use. The pH values of the prepared DESs were measured using a pH glass electrode (Mettler Toledo, Greifensee, Switzerland). The properties of the prepared DESs (pH, density and viscosity) were determined at 25°C. Density was determined using the pycnometric method and the viscosity using a rotary viscometer (Anton Paar ViscoQC 300, Ashland, Virginia, United States). All measurements were performed in triplicates. The σ-descriptors of the DESs were calculated according to Panić et al. (2022) (Supplementary Table S1).

5.3 FDH activity and stability assays

To determine FDH activity, the FDH enzyme, NAD^+ coenzyme, and formate substrate were added sequentially to various solvent systems to achieve final concentrations of 1.5 mg mL^{-1}, 0.1 mg mL^{-1}, and 10 mg mL^{-1}, respectively. The total working volume of the assay

was 250 µL. The NADH formation rate was measured immediately in a 96-well plate for 5 min at 340 nm using a UV-Vis spectrophotometer (SpectraMax® ABS Plus, Molecular Devices, San Jose, CA, United States).

To evaluate FDH stability, stock solutions of the enzyme (12.8 mg mL^{-1}) were prepared in the tested DES solutions and the reference buffer. These solutions were stored in sealed vials at 30°C in the dark. Aliquots were taken at regular intervals over a 14-day period and analyzed for FDH activity using the method described above.

The first-order deactivation rate constant (k_{FDH}, day^{-1}) was evaluated from the first-order kinetic model for the decrease of residual enzymatic activity over time (A_{Res} (t)) (Equation 1):

$$k_{FDH} = \frac{1}{t} ln\left(\frac{A_{Res,0}}{A_{Res\ (t)}}\right) \quad (1)$$

where A_{Res} is residual enzyme activity (either at time zero, $A_{R,0}$, or at time t, $A_R(t)$). The kinetic parameters were estimated by fitting the experimental data to the nonlinear equation using the Levenberg–Marquardt algorithm implemented in WR Mathematica 10.0 (Wolfram Research, Champaign, United States).

The half-life of the enzyme ($t_{1/2,\ FDH}$, day) was calculated using the previously determined k_{FDH} (Equation 1), according to Equation 2:

$$t_{1/2,FDH} = \frac{\ln 2}{k_{FDH}} \quad (2)$$

5.4 NADH stability assay

Measurements of the stability of the coenzyme NADH in various solvent systems (0.03 mg mL^{-1}) were monitored for up to 14 days. The samples were stored in the dark at 25°C and the absorption spectra in the range from 230 to 400 nm were recorded regularly using a UV-Vis spectrophotometer (SpectraMax® ABS Plus, Molecular Devices, San Jose, CA, United States). Each measurement was carried out in triplicate. The absorption spectrum of NADH shows a characteristic peak with an absorption maximum at 260 nm, which is due to the adenosine monophosphate moiety, and another peak at 340 nm, which is due to the neutral nicotinamide moiety. The decrease in absorbance at 340 nm followed first-order kinetics (Equation 3):

$$k_{NADH} = \frac{1}{t} ln\left(\frac{A_0}{A_t}\right) \quad (3)$$

where k_{NADH} is the first-order degradation rate constant (day^{-1}), A is the absorbance at 340 nm, either at time zero, A_0, or at time t, A_t (Wu et al., 1986).

The NADH half-life ($t_{1/2,\ NADH}$, day) was calculated using the previously determined k_{NADH} (Equation 3), according to Equation 4:

$$t_{1/2,NADH} = \frac{\ln 2}{k_{NADH}} \quad (4)$$

Moreover, the stability of NADH (25 mg mL^{-1}), added in tested solvent systems after their saturation with CO_2, was assessed to evaluate the impact of dissolved CO_2 on the coenzyme. Monitoring was accomplished by measuring the absorbance decrease at 340 nm using a UV-Vis spectrophotometer for 90 min. The absorbance decrease at 340 nm followed the first-order kinetics, and the first-order rate degradation constants (k_{NADH^*}, day^{-1}) were calculated in the same manner as described above. For the FDH-catalyzed reduction of CO_2 in the reference buffer and ChCl:$Gly_{80\%B}$, NADH stability was monitored throughout the entire course of the reaction (6 h).

5.5 CO_2 solubility measurements

The CO_2 solubility measurement, based on the setup described by Obert and Dave (Obert and Dave, 1999) was conducted in a glass tube where CO_2 was bubbled through the tested solvent systems with DESs and the reference buffer (V = 5 mL) for 90 min (time sufficient to reach a saturation point) at a flow rate of 100 mL min^{-1}. The gas was introduced using a small nozzle with an approximate diameter of 1 mm. To prevent CO_2 loss, the glass tube was sealed with parafilm. The concentration of CO_2 was continuously monitored using a Mettler Toledo (Greifensee, Switzerland) CO_2 sensor InPro 5000i/120.

5.6 FDH-catalysed reduction of CO_2

Prior to the reaction initiation, both 50 mM potassium phosphate buffer (pH 7.5) and ChCl:$Gly_{80\%B}$ were saturated with CO_2 by bubbling both solvents for 90 min, resulting in CO_2 dissolved concentrations of 1,029 mg mL^{-1} and 1,057 mg mL^{-1}, respectively. The enzymatic reaction was initiated by adding NADH and FDH to the CO_2-saturated buffer or ChCl:$Gly_{80\%B}$ to reach final concentrations of 16.4 mg mL^{-1} and 28.8 mg mL^{-1}, respectively. The reactions occurred at a room temperature using a magnetic stirrer in small tubes with a working volume of 250 µL. Aliquots were sampled at specific intervals to monitor NADH consumption, which was measured spectrophotometrically at 340 nm, indicating enzyme activity in reducing CO_2. To validate the results and assess the stability of NADH under experimental conditions, control reactions were conducted without the FDH enzyme. These control mixtures allowed us to monitor NADH stability in both the buffer and ChCl:$Gly_{80\%B}$ throughout the reaction period, as described in Section 5.4. To verify that the consumed NADH was utilized for formate synthesis, the concentration of formate was additionally determined using the method described by Lang and Lang (Singh et al., 2018). Briefly, samples (25 µL) containing formate were mixed with 50 µL of solution A, 2.5 µL of solution B, and 175 µL of 100% acetic anhydride. The mixture was incubated at 50°C for 2 h with occasional mixing. Formation of red color was subsequently measured spectrophotometrically at 515 nm using the SpectraMax® ABS Plus (Molecular Devices, San Jose, CA, United States). Solution A was prepared by dissolving 0.5 g of citric acid and 10 g of acetamide in 100 mL of isopropanol; solution B was prepared by dissolving 30 g of sodium acetate in 100 mL of water. For standard calibration, sodium formate dissolved in 50 mM potassium phosphate buffer (pH 7.5) was used.

5.7 Piecewise linear regression modelling

It was assumed that FDH activity, FDH and NADH stability can be described as a function of the DES physical properties and σ-profile of the mixture, expressed by a set of S^i_{mix} descriptors:

$$A_R \text{ or } t_{1/2,FDH} \text{ or } t_{1/2,NADH} = f\left(\rho, \eta, pH, S^1_{mix}, S^2_{mix}, S^3_{mix}, S^4_{mix}, S^5_{mix}, S^6_{mix}, S^7_{mix}, S^8_{mix}, S^9_{mix}, S^{10}_{mix}\right)$$

Piecewise linear regression (PLR) models have been used to describe the relationship between input and output variables. Input variables were selected based on the Spearman correlation matrix (Equation 5).

$$\begin{aligned} &A_R \text{ or } t_{1/2,FDH} \text{ or } t_{1/2,NADH} \\ &\quad = (b_{01} + b_{11}\cdot\rho + b_{21}\cdot\eta + b_{31}\cdot pH \\ &\quad + b_{41}\cdot S^1_{mix} + b_{51}\cdot S^2_{mix} + b_{61}\cdot S^3_{mix} + b_{71}\cdot S^4_{mix} \\ &\quad + b_{81}\cdot S^5_{mix} + b_{91}\cdot S^6_{mix} + b_{101}\cdot S^7_{mix} + b_{111} \\ &\quad \cdot S^8_{mix} + b_{121}\cdot S^9_{mix} + b_{131}\cdot S^{10}_{mix}) \\ &\quad \cdot \left(A_R \text{ or } t_{1/2,FDH} \text{ or } t_{1/2,NADH} \le b_n\right) \\ &\quad + (b_{02} + b_{12}\cdot\rho + b_{22}\cdot\eta + b_{32}\cdot pH \\ &\quad + b_{42}\cdot S^1_{mix} + b_{52}\cdot S^2_{mix} + b_{62}\cdot S^3_{mix} + b_{72} \\ &\quad \cdot S^4_{mix} + b_{82}\cdot S^5_{mix} + b_{92}\cdot S^6_{mix} + b_{102} \\ &\quad \cdot S^7_{mix} + b_{112}\cdot S^8_{mix} + b_{122}\cdot S^9_{mix} + b_{132}\cdot S^{10}_{mix}) \\ &\quad \cdot \left(A_R \text{ or } t_{1/2,FDH} \text{ or } t_{1/2,NADH} > b_n\right) \end{aligned} \quad (5)$$

The PLR technique is based on estimating the parameters of two linear regression equations: one for dependent variable values (Y) less than or equal to the breakpoint (b_n) and the other for dependent variable values (Y) higher than the breakpoint. The PLR parameters were estimated using the Levenberg-Marquardt algorithm implemented in the software Statistica 14.0 (Tibco Software Inc., Palo Alto, United States). The data set (63 data points for each output variable) was randomly split 70:30 into a calibration and a prediction data set. The applicability of the developed calibration models was estimated using the coefficient of determination for calibration (R_{cal}^2), the adjusted coefficient of determination for calibration ($R_{cal}^2{}_{adj}$), and cosmo (*RMSEC*). Predictive performance of the models was estimated using the coefficient of determination for prediction (R_{pred}^2), the adjusted coefficient of determination for calibration ($R_{pred}^2{}_{adj}$), the root mean square error of prediction (*RMSEP*), the ratio of prediction to deviation (*RPD*) and the ratio of the error range (*RER*) (Fearn, 2002).

5.8 Estimation of the productivity of the biocatalytic process

The productivity of the FDH-catalysed CO_2 conversion to formate was estimated based on the enzyme reaction kinetics including the enzyme inactivation rate (Bisswanger, 2017). Michaelis–Menten kinetic parameters were estimated by fitting the NADH concentration profiles to the differential equation (Equation 6) using WR Mathematica 10.0 (Wolfram Research, Champaign, United States). The change in substrate concentration over time without enzyme inactivation reads:

$$\frac{dc_{NADH}}{dt} = -\frac{v_{max}\cdot c_{NADH}}{K_S + c_{NADH}} \quad (6)$$

Considering enzyme inactivation, the following expression for the reaction rate $v(t)$ (Equation 7) is obtained:

$$v(t) = \frac{v_{max}\cdot c_{NADH}}{K_S + c_{NADH}}\cdot e^{-k_{FDH}\cdot t} \quad (7)$$

The productivity of the FDH-catalyzed CO_2 conversion to formate can be calculated by integrating (Equation 7) from the beginning of the reaction ($t = 0$) to its end ($t = t_f$) to obtain (Equation 8):

$$\begin{aligned} productivity &= \int_0^{t_f} \frac{v_{max}\cdot c_{NADH}}{K_S + c_{NADH}}\cdot e^{-k_{FDH}\cdot t}dt \\ &= \frac{v_{max}\cdot c_{NADH}}{K_S + c_{NADH}}\cdot\left(\frac{1 - e^{-k_{FDH}\cdot t_f}}{k_{FDH}}\right) \end{aligned} \quad (8)$$

Data availability statement

The original contributions presented in the study are included in the article/Supplementary Material, further inquiries can be directed to the corresponding author.

Author contributions

ML: Conceptualization, Data curation, Formal Analysis, Investigation, Methodology, Writing–original draft, Writing–review and editing. KŠ: Data curation, Investigation, Writing–review and editing. MN: Data curation, Investigation, Writing–review and editing. AT: Writing–review and editing, Conceptualization, Formal Analysis, Methodology, Software. AD: Writing–review and editing, Investigation, Visualization. MR: Investigation, Writing–review and editing, Visualization. IR: Writing–review and editing, Data curation. PŽ-P: Writing–review and editing, Funding acquisition, Resources, Supervision. WK: Writing–review and editing, Resources. MC: Resources, Writing–original draft, Writing–review and editing, Conceptualization, Data curation, Formal Analysis, Funding acquisition, Methodology, Supervision, Visualization.

Funding

The author(s) declare that financial support was received for the research, authorship, and/or publication of this article. This research was funded by the Croatian Science Foundation (grant number IPS- 2022-02-3938), and the Slovenian Research and Innovation Agency through Grants J4-4562 and P2-0191. PŽ-P was also supported through the Interreg Central Europe project

CE0200857 GreenChemForCE, co-funded by the European Union.

Acknowledgments

The authors are grateful for the continuous support of the Croatian Science Foundation for the research related to the application of deep eutectic solvents in biotechnology.

Conflict of interest

The authors declare that the research was conducted in the absence of any commercial or financial relationships that could be construed as a potential conflict of interest.

Publisher's note

Supplementary material

The Supplementary Material for this article can be found online at: https://www.frontiersin.org/articles/10.3389/fchem.2024.1467810/full#supplementary-material

References

Abbott, A. P., Capper, G., Davies, D. L., Rasheed, R. K., and Tambyrajah, V. (2003). Novel solvent properties of choline chloride/urea mixtures. *Chem. Commun.*, 70–71. doi:10.1039/B210714G

Abildskov, J., Van Leeuwen, M. B., Boeriu, C. G., and Van Den Broek, L. A. M. (2013). Computer-aided solvent screening for biocatalysis. *J. Mol. Catal. B Enzym.* 85 (86), 200–213. doi:10.1016/J.MOLCATB.2012.09.012

Abranches, D. O., and Coutinho, J. A. P. (2022). Type V deep eutectic solvents: design and applications. *Curr. Opin. Green Sustain. Chem.* 35, 100612. doi:10.1016/J.COGSC.2022.100612

Abranches, D. O., Zhang, Y., Maginn, E. J., and Colón, Y. J. (2022). Sigma profiles in deep learning: towards a universal molecular descriptor. *Chem. Commun.* 58, 5630–5633. doi:10.1039/D2CC01549H

Benguerba, Y., Alnashef, I. M., Erto, A., Balsamo, M., and Ernst, B. (2019). A quantitative prediction of the viscosity of amine based DESs using Sσ-profile molecular descriptors. *J. Mol. Struct.* 1184, 357–363. doi:10.1016/J.MOLSTRUC.2019.02.052

Bisswanger, H. (2017). *Enzyme kinetics*. doi:10.1002/9783527806461

Biswas, R., Metya, A. K., Abebe, K. M., Gedf, S. A., and Melese, B. T. (2023). Carbon dioxide solubility in choline chloride-based deep eutectic solvents under diverse conditions. *J. Mol. Model.* 29, 236. doi:10.1007/S00894-023-05643-Z

Bittner, J. P., Smirnova, I., and Jakobtorweihen, S. (2024). Investigating biomolecules in deep eutectic solvents with molecular dynamics simulations: current state, challenges and future perspectives. *Molecules* 29, 703. doi:10.3390/MOLECULES29030703

Bittner, J. P., Zhang, N., Huang, L., Domínguez De María, P., Jakobtorweihen, S., and Kara, S. (2022). Impact of deep eutectic solvents (DESs) and individual des components on alcohol dehydrogenase catalysis: Connecting experimental data and molecular dynamics simulations. *Green Chem.* 24, 1120–1131. doi:10.1039/d1gc04059f

Calzadiaz-Ramirez, L., and Meyer, A. S. (2022). Formate dehydrogenases for CO_2 utilization. *Curr. Opin. Biotechnol.* 73, 95–100. doi:10.1016/J.COPBIO.2021.07.011

Castillo, E., Casas-Godoy, L., and Sandoval, G. (2016). Medium-engineering: a useful tool for modulatinglipase activity and selectivity. *Biocatalysis* 1, 178–188. doi:10.1515/boca-2015-0013

Chang, C.-W., Laird, D. A., Mausbach, M. J., and Hurburgh, C. R. (2001). Near-Infrared reflectance spectroscopy–principal components regression analyses of soil properties. *Soil Sci. Soc. Am. J.* 65, 480–490. doi:10.2136/SSSAJ2001.652480X

Cheng, H., Liu, C., Zhang, J., Chen, L., Zhang, B., and Qi, Z.(2018). Screening deep eutectic solvents for extractive desulfurization of fuel based on COSMO-RS model.*Chem. Eng. Process. - Process Intensif.*125, 246–252. doi:10.1016/J.CEP.2018.02.006

Cui, Z., Enjome Djocki, A. V., Yao, J., Wu, Q., Zhang, D., Nan, S., et al. (2021). COSMO-SAC-supported evaluation of natural deep eutectic solvents for the extraction of tea polyphenols and process optimization. *J. Mol. Liq.* 328, 115406. doi:10.1016/j.molliq.2021.115406

Cvjetko Bubalo, M., Vidović, S., Radojčić Redovniković, I., and Jokić, S. (2015). Green solvents for green technologies. *J. Chem. Technol. Biotechnol.* 90, 1631–1639. doi:10.1002/jctb.4668

Damjanović, A., Logarušić, M., Tumir, L.-M., Andreou, T., Bubalo, M. C., and Redovniković, I. R. (2024). Enhancing protein stability under stress: osmolyte-based deep eutectic solvents as a biocompatible and robust stabilizing medium for lysozyme under heat and cold shock. *Phys. Chem. Chem. Phys.* 26, 21040–21051. doi:10.1039/D4CP02275K

Domingues, L., Duarte, A. R. C., and Jesus, A. R. (2024). How can deep eutectic systems promote greener processes in medicinal chemistry and drug discovery? *Pharmaceuticals* 17, 221. doi:10.3390/PH17020221

Elgharbawy, A. A. M., Syed Putra, S. S., Khan, H. W., Azmi, N. A. N., Sani, M. S. A., Ab llah, N., et al. (2023). Menthol and fatty acid-based hydrophobic deep eutectic solvents as media for enzyme activation. *Process* 11, 547. doi:10.3390/PR11020547

Fearn, T. (2002). Assessing calibrations: SEP, RPD, RER and R2. *NIR News*, 13, 12–13. doi:10.1255/NIRN.689

Gajardo-Parra, N. F., Rodríguez, G., Arroyo-Avirama, A. F., Veliju, A., Happe, T., Canales, R. I., et al. (2023). Impact of deep eutectic solvents on kinetics and folding stability of formate dehydrogenase. *Processes* 11, 2815. doi:10.3390/pr11102815

Gorke, J. T., Srienc, F., and Kazlauskas, R. J. (2008). Hydrolase-catalyzed biotransformations in deep eutectic solvents. *Chem. Commun.*, 1235–1237. doi:10.1039/B716317G

Hammond, O. S., Bowron, D. T., Edler, K. J., Hammond, S., Edler, K. J., and B owron, D. T. (2017). The effect of water upon deep eutectic solvent nanostructure: an unusual transition from ionic mixture to aqueous solution. *Angew. Chem. Int. Ed.* 56, 9782–9785. doi:10.1002/ANIE.201702486

Hansen, B. B., Spittle, S., Chen, B., Poe, D., Zhang, Y., Klein, J. M., et al. (2021). Deep eutectic solvents: a review of fundamentals and applications. *Chem. Rev.* 121, 1232–1285. doi:10.1021/acs.chemrev.0c00385

Hussain, S., Fangwei, Z., Siddiqi, A. F., Ali, Z., and Shabbir, M. S. (2018). Structural equation model for evaluating factors affecting quality of social infrastructure projects. *Sustain* 10, 1415. doi:10.3390/SU10051415

Klamt, A. (2005). COSMO-RS: from quantum chemistry to fluid phase thermodynamics and drug design. *Chem. Eng. Data* 51 (4)–1480. doi:10.1021/je0602317

Laitinen, A. T., Parsana, V. M., Jauhiainen, O., Huotari, M., Van Den Broeke, L. J. P., De Jong, W., et al. (2021). Liquid-liquid extraction of formic acid with 2-methyltetrahydrofuran: experiments, process modeling, and economics. *Ind. Eng. Chem. Res.* 60, 5588–5599. doi:10.1021/acs.iecr.1c00159

Lemaoui, T., Boublia, A., Darwish, A. S., Alam, M., Park, S., Jeon, B. H., et al. (2022). Predicting the surface tension of deep eutectic solvents using artificial neural networks. *ACS Omega* 7, 32194–32207. doi:10.1021/acsomega.2c03458

Lemaoui, T., Darwish, A. S., Hammoudi, N. E. H., Abu Hatab, F., Attoui, A., Alnashef, I. M., et al. (2020). Prediction of electrical conductivity of deep eutectic solvents using COSMO-RS sigma profiles as molecular descriptors: a quantitative structure-property relationship study. *Ind. Eng. Chem. Res.* 59, 13343–13354. doi:10.1021/ACS.IECR.0C02542

Leron, R. B., Caparanga, A., and Li, M. H. (2013). Carbon dioxide solubility in a deep eutectic solvent based on choline chloride and urea at T = 303.15–343.15 K and moderate pressures. *J. Taiwan Inst. Chem. Eng.* 44, 879–885. doi:10.1016/J.JTICE.2013.02.005

Leron, R. B., and Li, M. H. (2013). Solubility of carbon dioxide in a choline chloride–ethylene glycol based deep eutectic solvent. *Thermochim. Acta* 551, 14–19. doi:10.1016/J.TCA.2012.09.041

Lomba, L., Ribate, M. P., Zaragoza, E., Concha, J., Garralaga, M. P., Errazquin, D., et al. (2021). Deep eutectic solvents: are they safe? *Appl. Sci.* 11, 10061. doi:10.3390/APP112110061

Lozano, P., Diego, T. D., and Iborra, J. L. (2010). Biocatalytic processes using ionic liquids and supercritical carbon dioxide. *Handb. Green Chem.*, 51–73. doi:10.1002/9783527628698.HGC027

Ma, G., Zhang, Z., Lu, Z., Qi, Y., Nian, B., and Hu, Y. (2024). Hydrophobic deep eutectic solvents-lipase synergistically catalyze the synthesis of Vitamin E succinate via hydrogen bonds. *J. Mol. Liq.* 394, 123711. doi:10.1016/J.MOLLIQ.2023.123711

Maugeri, Z., Leitner, W., and Domínguez De María, P. (2012). Practical separation of alcohol–ester mixtures using Deep-Eutectic-Solvents. *Tetrahedron Lett.* 53, 6968–6971. doi:10.1016/J.TETLET.2012.10.044

Menegatti, T., Kopač, T., and Žnidaršič-Plazl, P. (2024). Tuning mechanical characteristics and permeability of alginate hydrogel by polyvinyl alcohol and deep eutectic solvent addition. *Bioengineering* 11, 371. doi:10.3390/bioengineering11040371

Mourelle-Insua, Á., Lavandera, I., and Gotor-Fernández, V. (2019). A designer natural deep eutectic solvent to recycle the cofactor in alcohol dehydrogenase-catalysed processes. *Green Chem.* 21, 2946–2951. doi:10.1039/C9GC00318E

Nolasco, M. M., Pedro, S. N., Vilela, C., Vaz, P. D., Ribeiro-Claro, P., Rudić, S., et al. (2022). Water in deep eutectic solvents: new insights from inelastic neutron scattering spectroscopy. *Front. Phys.* 10, 834571. doi:10.3389/fphy.2022.834571

Obert, R., and Dave, B. C. (1999). Enzymatic conversion of carbon dioxide to methanol: enhanced methanol production in silica sol-gel matrices. *J. Am. Chem. Soc.* 121, 12192–12193. doi:10.1021/ja991899r

Panić, M., Cvjetko Bubalo, M., and Radojčić Redovniković, I. (2021). Designing a biocatalytic process involving deep eutectic solvents. *J. Chem. Technol. Biotechnol.* 96, 14–30. doi:10.1002/JCTB.6545

Panić, M., Radović, M., Cvjetko Bubalo, M., Radošević, K., Rogošić, M., Coutinho, J. A. P., et al. (2022). Prediction of pH value of aqueous acidic and basic deep eutectic solvent using COSMO-RS σ profiles' molecular descriptors. *Mol* 27, 4489. doi:10.3390/MOLECULES27144489

Pätzold, M., Burek, B. O., Liese, A., Bloh, J. Z., and Holtmann, D. (2019a). Product recovery of an enzymatically synthesized (−)-menthol ester in a deep eutectic solvent. *Bioprocess Biosyst. Eng.* 42, 1385–1389. doi:10.1007/s00449-019-02125-6

Pätzold, M., Weimer, A., Liese, A., and Holtmann, D. (2019b). Optimization of solvent-free enzymatic esterification in eutectic substrate reaction mixture. *Biotechnol. Rep.* 22, e00333. doi:10.1016/J.BTRE.2019.E00333

Pohar, A., Žnidaršič-Plazl, P., and Plazl, I. (2012). Integrated system of a microbioreactor and a miniaturized continuous separator for enzyme catalyzed reactions. *Chem. Eng. J.* 189–190, 376–382. doi:10.1016/J.CEJ.2012.02.035

Quaid, T., and Reza, T. (2023). COSMO prediction of siloxane compounds absorption on type 3 and type 5 deep eutectic solvents. *Chem. Eng. J. Adv.* 14, 100489. doi:10.1016/J.CEJA.2023.100489

Radošević, K., Cvjetko Bubalo, M., Gaurina Srček, V., Grgas, D., Landeka Dragičević, T., and Radojčić, R. I. (2015). Evaluation of toxicity and biodegradability of choline chloride based deep eutectic solvents. *Ecotoxicol. Environ. Saf.* 112, 46–53. doi:10.1016/J.ECOENV.2014.09.034

Radović, M., Hok, L., Panić, M., Cvjetko Bubalo, M., Vianello, R., Vinković, M., et al. (2022). Deep eutectic solvents as a stabilising medium for NAD coenzyme: unravelling the mechanism behind coenzyme stabilisation effect. *Green Chem.* 24, 7661–7674. doi:10.1039/d2gc02656b

Radović, M., Jurinjak Tušek, A., Kroutil, W., Reiter, T., Radojčić Redovniković, I., and Cvjetko Bubalo, M. (2024). Rational design of deep eutectic solvents for the stabilization of dehydrogenases: an artificial neural network prediction approach. *Front. Chem.* 12, 1436049. doi:10.3389/FCHEM.2024.1436049

Reda, T., Plugge, C. M., Abram, N. J., and Hirst, J. (2008). Reversible interconversion of carbon dioxide and formate by an electroactive enzyme. *Proc. Natl. Acad. Sci. U. S. A.* 105, 10654–10658. doi:10.1073/pnas.0801290105

Rente, D., Cvjetko Bubalo, M., Panić, M., Paiva, A., Caprin, B., Radojčić Redovniković, I., et al. (2022). Review of deep eutectic systems from laboratory to industry, taking the application in the cosmetics industry as an example. *J. Clean. Prod.* 380, 135147. doi:10.1016/J.JCLEPRO.2022.135147

Sanchez-Fernandez, A., Basic, M., Xiang, J., Prevost, S., Jackson, A. J., and Dicko, C. (2022). Hydration in deep eutectic solvents induces non-monotonic changes in the conformation and stability of proteins. *J. Am. Chem. Soc.* 144, 23657–23667. doi:10.1021/jacs.2c11190

Sapir, L., and Harries, D. (2020). Restructuring a deep eutectic solvent by water: the nanostructure of hydrated choline chloride/urea. *J. Chem. Theory Comput.* 16, 3335–3342. doi:10.1021/acs.jctc.0c00120

Sheldon, R. A., Bode, M. L., and Mathebula, N. (2023). Green and sustainable solvents for biocatalytic oxidations. *Curr. Opin. Green Sustain. Chem.* 39, 100741. doi:10.1016/J.COGSC.2022.100741

Sheldon, R. A., and Pereira, P. C. (2017). Biocatalysis engineering: the big picture. *Chem. Soc. Rev.* 46, 2678–2691. doi:10.1039/C6CS00854B

Sim, J., McGoverin, C., Oey, I., Frew, R., and Kebede, B. (2023). Near-infrared reflectance spectroscopy accurately predicted isotope and elemental compositions for origin traceability of coffee. *Food Chem.* 427, 136695. doi:10.1016/J.FOODCHEM.2023.136695

Singh, R. K., Singh, R., Sivakumar, D., Kondaveeti, S., Kim, T., Li, J., et al. (2018). Insights into cell-free conversion of CO2 to chemicals by a multienzyme cascade reaction. *ACS Catal.* 8, 11085–11093. doi:10.1021/acscatal.8b02646

Slater, C. S., Savelski, M. J., Hitchcock, D., and Cavanagh, E. J. (2016). Environmental analysis of the life cycle emissions of 2-methyl tetrahydrofuran solvent manufactured from renewable resources. *J. Environ. Sci. Health. A. Tox. Hazard. Subst. Environ. Eng.* 51, 487–494. doi:10.1080/10934529.2015.1128719

Taklimi, S. M., Divsalar, A., Ghalandari, B., Ding, X., Di Gioia, M. L., Omar, K. A., et al. (2023). Effects of deep eutectic solvents on the activity and stability of enzymes. *J. Mol. Liq.* 377, 121562. doi:10.1016/J.MOLLIQ.2023.121562

Tishkov, V. I., Galkin, A. G., Marchenko, G. N., Egorova, O. A., Sheluho, D. V., Kulakova, L. B., et al. (1993). Catalytic properties and stability of a Pseudomonas sp.101 formate dehydrogenase mutants containing cys-255-ser and cys-255-met replacements. *Biochem. Biophys. Res. Commun.* 192, 976–981. doi:10.1006/BBRC.1993.1511

Torregrosa-Crespo, J., Marset, X., Guillena, G., Ramón, D. J., and María Martínez-Espinosa, R. (2020). New guidelines for testing "Deep eutectic solvents" toxicity and their effects on the environment and living beings. *Sci. Total Environ.* 704, 135382. doi:10.1016/J.SCITOTENV.2019.135382

van Schie, M. M. C. H., Spöring, J. D., Bocola, M., Domínguez de María, P., and Rother, D. (2021). Applied biocatalysis beyond just buffers – from aqueous to unconventional media. Options and guidelines. *Green Chem.* 23, 3191–3206. doi:10.1039/D1GC00561H

Venkatraman, V., Evjen, S., Knuutila, H. K., Fiksdahl, A., and Alsberg, B. K. (2018). Predicting ionic liquid melting points using machine learning. *J. Mol. Liq.* 264, 318–326. doi:10.1016/J.MOLLIQ.2018.03.090

Villa, R., Alvarez, E., Porcar, R., Garcia-Verdugo, E., Luis, S. V., and Lozano, P. (2019). Ionic liquids as an enabling tool to integrate reaction and separation processes. *Green Chem.* 21, 6527–6544. doi:10.1039/C9GC02553G

Villa, R., Nieto, S., Donaire, A., and Lozano, P. (2023). Direct biocatalytic processes for CO2 capture as a green tool to produce value-added chemicals. *Mol* 28, 5520. doi:10.3390/MOLECULES28145520

Wichmann, R., and Vasic-Racki, D. (2005). Cofactor regeneration at the lab scale. *Adv. Biochem. Eng. Biotechnol.* 92, 225–260. doi:10.1007/B98911

Woodley, J. M. (2022). Ensuring the sustainability of biocatalysis. *ChemSusChem* 15, e202102683. doi:10.1002/CSSC.202102683

Wu, B. P., Wen, Q., Xu, H., and Yang, Z. (2014). Insights into the impact of deep eutectic solvents on horseradish peroxidase: activity, stability and structure. *J. Mol. Catal. B. Enzym. Complete* 101, 101–107. doi:10.1016/J.MOLCATB.2014.01.001

Wu, J. T., Wu, L. H., and Knight, J. A. (1986). Stability of NADPH: effect of various factors on the kinetics of degradation. *Clin. Chem.* 32, 314–319. doi:10.1093/CLINCHEM/32.2.314

Zachos, I., Nowak, C., and Sieber, V. (2019). Biomimetic cofactors and methods for their recycling. *Curr. Opin. Chem. Biol.* 49, 59–66. doi:10.1016/J.CBPA.2018.10.003

Zhang, N., Domínguez de María, P., and Kara, S. (2024). Biocatalysis for the synthesis of active pharmaceutical ingredients in deep eutectic solvents: state-of-the-art and prospects. *Catal* 14, 84. doi:10.3390/CATAL14010084

Zhang, Z., Wang, H., Nie, Y., Zhang, X., and Ji, X. (2022). Natural deep eutectic solvents enhanced electro-enzymatic conversion of CO2 to methanol. *Front. Chem.* 10, 1–8. doi:10.3389/fchem.2022.894106

Zhang, Z., Xu, B. H., Luo, J., Von Solms, N., He, H., Zhang, Y., et al. (2018). Ionic liquids as bifunctional cosolvents enhanced co2 conversion catalysed by nadh-dependent formate dehydrogenase. *Catalysts* 8, 304. doi:10.3390/catal8080304

Žnidaršič-Plazl, P. (2021a). Let the biocatalyst flow. *Acta Chim. Slov.* 68, 1–16. doi:10.17344/ACSI.2020.6488

Žnidaršič-Plazl, P. (2021b). Biocatalytic process intensification via efficient biocatalyst immobilization, miniaturization, and process integration. *Curr. Opin. Green Sustain. Chem.* 32, 100546. doi:10.1016/J.COGSC.2021.100546

Glossary

DES	Deep eutectic solvent
FDH	Formate dehydrogenase
NADH	Nicotinamide adenine dinucleotide
HBA	Hydrogen bond acceptor
HBD	Hydrogen bond donor
ChCl	Choline chloride
B	Betaine
Gly	Glycerol
$_{\%W}$	% (w/w) of water
$_{\%B}$	% (w/w) of buffer
η	Dynamic viscosity
ρ	Density
S^{i}_{mix}	σ-profile of the mixture
COSMO-RS	Conductor-like Screening Model for Real Solvents
QSPR	Quantitative structure property relationships
c_s	concentration of dissolved CO_2
A_R	relative enzyme activity
A_{Res}	residual enzyme activity
$t_{1/2,\ FDH}$	FDH half-life
$t_{1/2,\ NADH}$	NADH half-life
k_{FDH}	first-order degradation rate constant of FDH
k_{NADH}	first-order degradation rate constant of NADH
k_{NADH^*}	first-order degradation rate constant of NADH in CO_2 saturated solutions
v_{max}	maximum reaction rate
K_s	NADH saturation constant
$v(t)$	reaction rate
PLR	piecewise linear regression
R_{pred}^2	coefficient of determination for prediction
$R_{pred\ adj}^2$	adjusted coefficient of determination for prediction
RMSEP	root mean square error of prediction
RPD	ratio of prediction to deviation
RER	ratio of the error range
R_{cal}^2	coefficient of determination for calibration
$R_{cal\ adj}^2$	adjusted coefficient of determination for calibration
RMSEC	root mean square error for calibration

Frontiers in Chemistry

Explores all fields of chemical science across the periodic table

Advances our understanding of how atoms, ions, and molecules come together and come apart. It explores the role of chemistry in our everyday lives - from electronic devices to health and wellbeing.

Discover the latest Research Topics

See more →

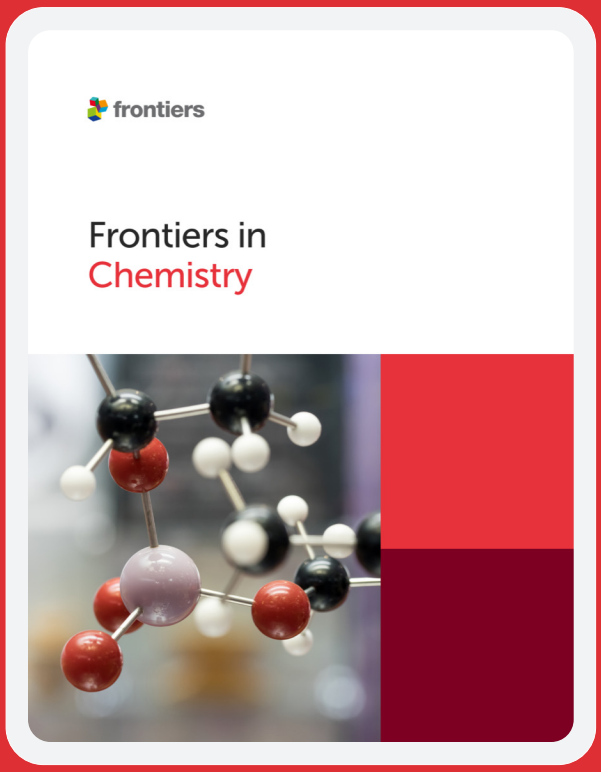

Frontiers

Avenue du Tribunal-Fédéral 34
1005 Lausanne, Switzerland
frontiersin.org

Contact us

+41 (0)21 510 17 00
frontiersin.org/about/contact